

# A Micromechanical Frequency-Selective Power Amplifier

*Clark Nguyen  
Wei-chang Li*



Electrical Engineering and Computer Sciences  
University of California at Berkeley

Technical Report No. UCB/EECS-2017-171

<http://www2.eecs.berkeley.edu/Pubs/TechRpts/2017/EECS-2017-171.html>

December 1, 2017

Copyright © 2017, by the author(s).  
All rights reserved.

Permission to make digital or hard copies of all or part of this work for personal or classroom use is granted without fee provided that copies are not made or distributed for profit or commercial advantage and that copies bear this notice and the full citation on the first page. To copy otherwise, to republish, to post on servers or to redistribute to lists, requires prior specific permission.

**A Micromechanical Frequency-Selective Power Amplifier**

by

Wei-Chang Li

A dissertation submitted in partial satisfaction of the  
requirements for the degree of  
Doctor of Philosophy

in

Engineering – Electrical Engineering and Computer Sciences

in the

Graduate Division

of the

University of California, Berkeley

Committee in charge:

Professor Clark T.-C. Nguyen, Chair  
Professor Elad Alon  
Professor Roya Maboudian

Fall 2015

The dissertation of Wei-Chang Li, titled A Micromechanical Frequency-Selective Power Amplifier, is approved:

Chair	_____	Date	_____
	_____	Date	_____
	_____	Date	_____

University of California, Berkeley

# **A Micromechanical Frequency-Selective Power Amplifier**

Copyright 2015  
by  
Wei-Chang Li

## Abstract

A Micromechanical Frequency-Selective Power Amplifier

by

Wei-Chang Li

Doctor of Philosophy in Engineering – Electrical Engineering and Computer Sciences

University of California, Berkeley

Professor Clark T.-C. Nguyen, Chair

This dissertation describes a MEMS-based frequency-selective power amplifier that performs both signal filtering and power amplification, while consuming zero power when there is no input, i.e., zero-quiescent power consumption. The frequency-selective power amplifier employs a micromechanical resonant switch (resoswitch) as a key building block similar to those recently used for zero-quiescent power radio receivers, but capable of handling higher powers. This document details the design, fabrication, and characterization of these higher frequency and higher power micromechanical resoswitches, and employs them as power amplifiers. Here, the mechanical  $Q$  of the resoswitch largely governs the threshold input level that instigates power gain. Theoretical and experimental studies of  $Q$ , as well as  $Q$  enhancement techniques and high- $Q$  structural design, are discussed. Further, post-fabrication laser trimming addresses the frequency accuracy of the vibrating devices. A model that replaces laser blasted holes with stiffness-modifying cracks captures well the frequency shift dependence on laser blast location. The accuracy of this theory further enables a deterministic trimming protocol that specifies the laser targeting sequence needed to achieve a required amount of frequency tuning with minimal  $Q$  reduction.

The resoswitch used to demonstrate the frequency-selective power amplifier employs slots to engineer stiffness along orthogonal axes of a wine-glass disk resonator structure. The slots realize displacement amplification—a larger displacement magnitude along the output than the input axis—allowing impact switching only to the output electrodes, not the input, all of which improves reliability. A finite element analysis (FEA)-based model predicts the displacement gain as a function of disk size and slot dimension/location.

To improve impact contact resistance, this work employs metal for the slotted-disk resoswitch, achieved via a CMOS-compatible surface micromachining process that essentially replaces normally-used polysilicon material with aluminum metal, which serves as both structural and interconnect material. This not only improves contact resistance, but also reduces parasitic resistance, which in turn reduces feedthrough currents. When embedded in a switched-mode power amplifier circuit, the Al displacement-amplifying resoswitch performs signal filtering and power amplification that first filters an incoming signal with channel-like

selectivity and then amplifies the signal with a power gain of 13.8 dB. More importantly, unlike transistor-based circuits, the resoswitch-based frequency-selective power amplifier consumes zero power while in standby.

Measurements indicate that sputtered aluminum has high mechanical  $Q$  at low frequencies, as a folded-beam capacitive-comb-driven micromechanical resonator fabricated via the aforementioned process achieved a  $Q$  up to  $\sim 20,000$ . Unfortunately, the higher frequency slotted-disk used in the displacement amplifier did not fare as well, as its  $Q$  was only on the order of 1,000. An effort to study the  $Q$  limits of different resoswitch designs included an experimental study of intrinsic loss mechanisms using cryogenic operation to enhance resonator  $Q$  and better elucidate important energy loss mechanisms. Here, operation of a 61-MHz wine-glass disk resonator at temperatures as low as 5K reduces temperature-dependent energy loss and raises  $Q$  to as high as 362,000, likely devoid of thermoelastic friction. On the other hand, introduction of slots into a wine-glass disk structure (to effect displacement gain) reduces  $Q$  by introducing thermoelasting damping, which this document models in detail. A displacement-amplifying elliptic disk solves this problem by deriving gain-induced stiffness differences from geometric ratioing rather than  $Q$ -degrading slots, which permits simultaneous displacement gain and high- $Q$ .

Finally, this work includes a study of laser trimming to trim power amplifier frequency to a desired range. Here, laser trimming offers flexible bidirectional frequency tuning with minimal effect on  $Q$ . Unlike other frequency tuning methods, laser trimming does not require added process steps, e.g., sputtering of frequency-shifting metal materials on structures. Rather, laser trimming offers precise post-fabrication frequency adjustment via blasts of controlled size and location on a given resonator. A model that captures the frequency shift dependency on laser blast location shows good agreement with measured results on micromechanical clamped-clamped (CC)-beam resonators. The theory provides a modeling framework for laser trimming applicable to other types of beam resonators—e.g., free-free beams, cantilevers, and even disks or rings—by altering the boundary condition matrices.

*To my parents*

# Contents

<b>Contents</b>	<b>ii</b>
<b>List of Figures</b>	<b>v</b>
<b>List of Tables</b>	<b>xii</b>
<b>1 Introduction</b>	<b>1</b>
1.1 Motivation: Towards Zero-Quiescent Power Radio Front-Ends . . . . .	1
1.2 Issues of Current Technologies . . . . .	2
1.2.1 Transistor-Based Switches . . . . .	2
1.2.2 Conventional MEMS Switches . . . . .	4
1.3 Approach: Micromechanical Resonant Switches . . . . .	5
1.4 Overview . . . . .	6
<b>2 Micromechanical Displacement-Amplifying Resonant Switches</b>	<b>8</b>
2.1 Slotted-Disk Displacement Amplifier . . . . .	9
2.1.1 Structure and Operation . . . . .	9
2.1.2 Single-Stage Slotted-Disks . . . . .	10
2.1.3 Slotted-Disk Arrays . . . . .	11
2.1.4 Negative-Capacitor Equivalent Circuit Model . . . . .	13
2.2 Slotted-Disk Displacement Amplifier Design Procedure . . . . .	15
2.2.1 Semi-Empirical Model of Displacement Gain . . . . .	15
2.2.2 Semi-Empirical Model of Resonance Frequency and Stiffness . . . . .	16
2.2.3 Determine the Slot Span Angle $\theta_s$ and Radius-to-Slot “Beam” Width Ratio $R/w_b$ . . . . .	18
2.2.4 Determine the Disk Radius $R$ and Slot “Beam” Width $w_b$ . . . . .	18
2.3 Experimental Results of Slotted-Disk Displacement Amplifiers . . . . .	19
2.3.1 Mixing Technique for Measuring Displacement Gain . . . . .	19
2.3.2 Single-Slotted-Disk Displacement Amplifiers . . . . .	21
2.3.3 Slotted-Disk Array . . . . .	26
2.4 Elliptic-Disk Displacement Amplifiers . . . . .	27
2.4.1 Advantages over Previous Resoswitches . . . . .	28

2.4.2	Displacement Gain Modeling . . . . .	29
2.4.3	Experimental Results . . . . .	31
2.5	Conclusions . . . . .	32
<b>3</b>	<b>Metal Micromechanical Frequency-Selective Power Amplifiers</b>	<b>35</b>
3.1	Structure and Operation . . . . .	35
3.2	Fabrication Process . . . . .	38
3.2.1	Sputtering Deposition of Al Structural Material . . . . .	38
3.2.2	Etching of Al Structural Material . . . . .	39
3.2.3	Process Flow for Al Comb-Driven Resonators . . . . .	42
3.2.4	Process Flow for Al Disk Resonators/Displacement Amplifiers . . . . .	43
3.3	Experimental Results . . . . .	44
3.3.1	Al Comb-Driven Resonators . . . . .	44
3.3.2	Al Disk Resonators/Displacement Amplifiers . . . . .	45
3.3.3	Al Switched-Mode Filter-Power Amplifiers . . . . .	47
3.4	Conclusions . . . . .	50
<b>4</b>	<b>Quality Factor of Micromechanical Resonators and Resoswitches</b>	<b>51</b>
4.1	Quality Factor Fundamentals . . . . .	51
4.2	Cryogenic Operation to Raise $Q$ . . . . .	53
4.2.1	Test Devices–Wine-Glass Disk Resonators . . . . .	53
4.2.2	Cryogenic Measurement . . . . .	54
4.2.3	Measurement vs. Theory . . . . .	57
4.3	Annealing to Raise $Q$ . . . . .	58
4.3.1	Test Devices–Nickel Comb-Driven Resonators . . . . .	58
4.4	Material Approach to Raise $Q$ : Polysilicon-Filled CNT Structural Material . . . . .	59
4.4.1	Fabrication Process Flow . . . . .	60
4.4.2	As-Fabricated Polysilicon-Filled CNT Material Properties . . . . .	64
4.4.3	<i>In Situ</i> Localized Annealing to Raise $Q$ . . . . .	68
4.4.4	Conclusions . . . . .	69
4.5	Quality Factor of Slotted-Disk Displacement Amplifiers . . . . .	71
4.5.1	Quality Factors vs. Varying Slot Geometry . . . . .	71
4.5.2	Energy Losses in Slotted Disks . . . . .	71
4.5.3	Theoretical versus Measured $Q_{TED}$ . . . . .	77
4.5.4	Conclusions . . . . .	78
4.6	Quality Factor of Elliptic-Disk Displacement Amplifiers . . . . .	79
4.6.1	Quality Factor vs. Varying Ellipse Aspect Ratio $AR$ . . . . .	79
4.6.2	$AR$ -Dependent Anchor Loss . . . . .	79
<b>5</b>	<b>Laser Frequency Trimming of Micromechanical Resonant Devices</b>	<b>81</b>
5.1	Overview . . . . .	81
5.2	Frequency Trimming Fundamentals . . . . .	83

5.3	Modeling of Laser Trimming of CC-Beam Resonators . . . . .	85
5.3.1	Stiffness Change—a Rotational Spring Model . . . . .	86
5.3.2	Combining Trimmed and Un-trimmed Beam Portions . . . . .	92
5.3.3	Mass Change . . . . .	95
5.4	Experimental Results . . . . .	96
5.4.1	Location-Dependent Frequency Trimming . . . . .	97
5.4.2	Symmetrical Trimming to Preserve $Q$ . . . . .	100
5.4.3	Deterministic Trimming of a CC-beam Resonator . . . . .	101
5.5	Laser Trimming of Micromechanical Wine-Glass Disk Resonators . . . . .	104
5.5.1	Experimental Results of Laser Trimming of Disk Resonators . . . . .	105
5.6	Conclusions . . . . .	108
<b>6</b>	<b>Conclusions</b>	<b>109</b>
6.1	Future Research Directions . . . . .	111
6.1.1	Reliability . . . . .	111
6.1.2	Resoswitch-Based Switched-Mode Power Amplifiers . . . . .	111
6.1.3	Integrated Resoswitch-Based Radios . . . . .	112
6.1.4	Laser Frequency Trimming of Other Types of Resonators . . . . .	112
6.2	Conclusion Remarks . . . . .	112
	<b>Appendix A: All-Al Disk Process Outline</b>	<b>113</b>
	<b>Bibliography</b>	<b>119</b>

# List of Figures

1.1	Wireless sensor networks (WSNs) enables Internet of Things (IoT) that connects billions or even trillions of sensors to the Internet for structural monitoring, transportation management, smart grid, smart homes, and even personal health monitoring. . . . .	2
1.2	(a) A schematic of a transistor-based Class-E PA. (b) The theoretical amounts of value for the reactive components shown in (a) required to achieve the non-overlapped current and voltage waveforms across the switch device. (c) Simulated (ideal) switching current and voltage waveforms, showing the product of current times voltage is zero at any times. . . . .	3
1.3	Comparison of effects on switching waveforms and dissipated energy per cycle by using (a) an ideal value of $C_1$ and (b) a larger value of capacitance of $C_1$ dominated by the parasitic. . . . .	4
1.4	Schematic of a resoswitch-enabled zero-quiescent power receiver architecture. . .	6
2.1	(a) Schematic for a wine glass disk resonant switch and its transistor analogue operating as a switch. (b) Periodic switching between two phased cycles, showing a larger gap at input is needed to prevent the input port from impacting. . . . .	9
2.2	Schematic of a slotted displacement amplifying disk resonator, which yields a larger displacement along the output axis than that along the input and in turn prevents input from impacting without the need of larger gap spacing. . . . .	10
2.3	Slot opening design of (a) rectangular; (b) arc; and (c) elliptic slots. . . . .	11
2.4	CoventorWare <sup>®</sup> FEA simulation compares the mode shape of (a) a conventional wine glass disk resonator and (b) a slotted displacement amplifying disk resonator of $(R, w_b, w_s, \theta_s) = (32 \mu\text{m}, 8 \mu\text{m}, 2 \mu\text{m}, 45^\circ)$ , presenting an identical radial displacement along the two orthogonal axes in a conventional disk resonator while the slotted disk first follows the mode shape of the conventional counterpart but then rapidly increases its displacement as $\phi$ increases. . . . .	12
2.5	Schematic of two slotted disk array to illustrate boundary conditions set by the coupler to achieve a larger displacement gain. . . . .	13

2.6	(a) FEA-simulated mode shape of a slotted-disk array achieved by coupling two displacement amplifying resonators with a zero-length of coupler. (b) The normalized radial displacement for each of the disks. Note that each of the slotted disks has the same displacement gain (i.e., $G = 3.45$ ) from the non-slotted axis to the slotted axis, together with the coupler which forces the coupled locations to have identical displacement, yield an overall displacement gain of $G_2 (= 11.9)$ .	14
2.7	A negative-Capacitor based equivalent circuit model for slotted disk displacement amplifier. . . . .	15
2.8	Displacement gain estimated by the simplified fitting model of (2.2) and (2.3). . . . .	17
2.9	Displacement gain estimated by the complete fitting model of (2.4) and (2.5). . . . .	17
2.10	Schematics of device cross-sections via (a) conventional disk process and (b) thick-polysilicon-interconnect process, showing that the modified process uses a $\sim 3\times$ thicker polysilicon layer, $1.5\ \mu\text{m}$ versus $0.4\ \mu\text{m}$ , for reduced interconnect resistances.	19
2.11	Schematic of mixing measurement set-up that is used to measure separately the motional currents from the input and output ports. . . . .	20
2.12	Measured mixed powers from input and output electrodes of a disk with rectangle slots as seen in [11] and the difference of two measured powers presents a displacement gain of $2.34\times$ achieved by this single slotted disk structure. . . . .	22
2.13	SEM images of overview and close view for a fabricated displacement amplifying disk with arc slots sized as $(R, w_b, w_s, \theta_s) = (32\ \mu\text{m}, 8\ \mu\text{m}, 2\ \mu\text{m}, 47.5^\circ)$ . . . . .	22
2.14	Measured mixed powers from input and output electrodes of the arc-slot disk in Fig. 2.13 and the difference of two measured powers presents a displacement gain of $3.72\times$ achieved by this single slotted disk structure. . . . .	23
2.15	SEM images of overview and close view for a fabricated displacement amplifying disk with elliptic slots sized as $(R, w_b, a_s, b_s) = (32\ \mu\text{m}, 8\ \mu\text{m}, 7\ \mu\text{m}, 1\ \mu\text{m})$ . . . . .	24
2.16	Measured mixed powers from input and output electrodes of the elliptic slot disk in Fig. 2.15 and the difference of two measured powers represents a displacement gain of $1.86\times$ achieved by this single slotted disk structure. . . . .	24
2.17	Measured mixed powers from input and output electrodes of a disk with rectangle slots as seen in [6] and the difference of two measured powers presents an overall displacement gain of $6.09\times$ and $2.45\times$ achieved by each of the individual slotted-disks. . . . .	25
2.18	SEM of a two-stage ellipse-slot disk array with a zero-wavelength coupling beam.	25
2.19	Measured mixed powers from input and output electrodes of the two-stage array in Fig. 2.18 composed by two single ellipse-shaped slotted-disks and a half-wavelength coupling beam. The difference of two measured powers represents an overall displacement gain of $2.19\times$ achieved by this two-stage array ( $1.48\times$ for each of the disks). . . . .	26
2.20	Descriptions of (a) array; (b) slotted-disk; and (c) elliptic-disk displacement amplifiers, along with a table comparing their performance, where the elliptic-disk displacement amplifier clearly presents the highest $Q$ . . . . .	27

2.21	FEM simulated mode shapes comparing displacements along input and output axes for (a) a conventional wine-glass disk resonator; (b) a slotted-disk displacement amplifier; and (c) an elliptic displacement-amplifying disk. . . . .	29
2.22	(a) SEM of a fabricated polysilicon elliptic disk with an $AR = 1.6$ . Measurement set-up for extracting displacement gain is indicated. (b) Measured transmissions obtained via the device and set-up in (a), exhibiting a displacement gain $\sim 2.04$ and a measured $Q$ over 100,000. . . . .	30
2.23	Comparison of displacement gains as a function of aspect ratio obtained from measurement, FEA, and prediction using (2.11). . . . .	31
2.24	Measured frequency shifts with tuning voltages applied on input ( $V_{B1}$ ) versus on output ( $V_{B2}$ ), where the lower mechanical stiffness along the output axis yields a larger tuning range. . . . .	32
2.25	Measured input to output frequency response spectra as a function of input drive voltage, showing flattening and bandwidth widening of the response at the onset of impacting. . . . .	33
2.26	Measured $Q$ versus aspect ratio from three dies. Here, $AR = 1$ corresponds to a circular disk, while higher $AR$ 's indicate ellipses. $AR = 1.2$ presents the lowest $Q$ while $AR > 1.6$ seems to be able to recover $Q$ back to that of a circular disk. . . . .	34
3.1	Schematic of the displacement-amplifying Al resoswitch-based filter-PA used in a FSK-based RF receiver chain, showing a highly nonlinear amplification while all other out-of-channel signals have been eliminated/filtered. . . . .	36
3.2	Illustrations of displacement amplifier operation that as the displacement of the vibrating structure is much higher and conventional disks and limited by the gap as of (a), the disk would close the gap and deliver power from the bias applied on the structure to the output around a small bandwidth of resonance frequency as of (b). In this switching bandwidth, a time domain waveform can be then measured, with a much higher amplitude than the capacitively vibrating ac signals as shown in (c). . . . .	37
3.3	Cross-section of Al films deposited in (a) a contaminated conventional DC magnetron sputtering system and in (b) a clean S-gun sputtering system with an optimized recipe. . . . .	38
3.4	Cross-section of Al film etched in varying process pressures (RF/Bias Power = 800/100 W, $Cl_2/BCl_3 = 90/45$ sccm). . . . .	39
3.5	Cross-section of Al film etched with varying $Cl_2/BCl_3$ ratios (RF/Bias Power = 800/100 W, process pressure = 4 mTorr) . . . . .	40
3.6	Cross-section of Al film etched with varying $Cl_2/BCl_3$ ratio (Cont'd) (RF/Bias Power = 800/100 W, process pressure = 4 mTorr). . . . .	41
3.7	Cross-section of Al film etched with varying RF bias (RF power = 800 W, process pressure = 4 mTorr). . . . .	41

3.8	One-mask fabrication process flow used to achieve the folded-beam comb-driven micromechanical Al resonator, where the Si substrate was first doped and deposited a 2- $\mu\text{m}$ sacrificial oxide as in (a), followed by a 2- $\mu\text{m}$ Al sputtering of (b). The Al was then photolithographed and etched as in (c) and finally, a timed release of (d) was performed in a commercial Al-compatible solution to remain the oxide isolation island under the anchor areas. . . . .	42
3.9	Surface micromachined fabrication process used to achieve the slotted Al displacement amplifiers. . . . .	43
3.10	SEM images of (a) the fabricated Al comb-drive and (b) a zoom-in view on the comb structures. . . . .	44
3.11	Measured frequency response of the Al comb-drive showing a high mechanical $Q$ in Al structural material up to $\sim 20,000$ . . . . .	45
3.12	SEM of a fabricated Al slotted disk displacement amplifier. . . . .	46
3.13	Schematic of the measurement setup that was used to characterize the motional currents simultaneously from two different electrodes of the slotted disk. . . . .	47
3.14	Measured frequency responses from the input and output ports of a slotted displacement-amplifying Al disk. . . . .	48
3.15	Measured frequency responses from the input and output ports of a non-slotted Al wine glass disk. . . . .	48
3.16	Schematic of the demonstrated Al filter-power amplifier together with the measurement setup. . . . .	49
3.17	Measured hot switching waveform of the Al filter-power amplifier using the measurement setup of Fig. 3.16. . . . .	49
4.1	Schematic pictorially summarizing important loss mechanisms that constrain the $Q$ of a wine-glass disk resonator. . . . .	52
4.2	(a) Schematic of a wine-glass disk micromechanical resonator in a preferred two-port bias, excitation, and sense configuration. (b) SEM photo of a wine-glass disk resonator test device. (c) Wine-glass mode shape simulated via finite element analysis showing the locations of quasi-nodal points. . . . .	54
4.3	Schematic of wine-glass disk micromechanical resonators using various support configurations to vary anchor losses in this work: (a) four 1- $\mu\text{m}$ supports; (b) two 1.5- $\mu\text{m}$ supports oriented $180^\circ$ ; and (c) two 1.5- $\mu\text{m}$ $90^\circ$ -oriented support beams. . . . .	55
4.4	Photo of the Suss MicroTec PMC150 probe station used to measure micromechanical resonators at cryogenic temperatures. . . . .	55
4.5	Measured frequency response for a 32 $\mu\text{m}$ -radius wine-glass disk with two asymmetric supports at room temperatures and at cryogenic temperatures with $V_P = 3$ V. . . . .	56
4.6	Measured $Q$ vs. temperature for 32 $\mu\text{m}$ -radius wine-glass disks with varying numbers and orientations of support beams. . . . .	57
4.7	Plot of measured $Q$ versus temperature alongside theoretical $Q$ limits imposed by various loss mechanisms. . . . .	58

4.8	SEM and measured frequency spectrum of a micromechanical electroplated nickel folded-beam comb-driven resonator. . . . .	59
4.9	Measured frequency responses of the comb-driven resonator shown in 4.8 before and after a rapid thermal annealing for 2 mins at 400°, showing $Q$ substantially increases from 561 to >10,000. . . . .	60
4.10	Fabrication process flow for folded-beam comb-driven microstructures in polysilicon-filled CNT material. . . . .	61
4.11	SEMs of CNT structures grown (a) with and (b) without the oxide mold, before and after polysilicon-filling. . . . .	63
4.12	SEM of polysilicon-filled CNT clamped-clamped and cantilever beam arrays immediately after release, showing little or no curling or buckling. . . . .	63
4.13	(a) Overview and (b) zoom-in SEMs of a fabricated polySi-filled CNT comb-driven resonator. . . . .	65
4.14	Electrically measured frequency response of the resonator of Fig. 4.13 before in situ localized annealing. . . . .	66
4.15	Zoom-in SEM of the cross-section view of a released structure showing the voids inside the material. . . . .	67
4.16	Curve fitting to extract the acoustic velocity of polysilicon-filled CNT material from frequency information. . . . .	68
4.17	Setup for <i>in situ</i> localized annealing and measurement of frequency characteristics. . . . .	69
4.18	Measured frequency characteristics before and after in situ localized annealing under $V_a = 4$ V. . . . .	70
4.19	(a) SEMs of unannealed and annealed parts; and (b)-(c) respective zoom-in views. . . . .	70
4.20	Measured $Q$ 's for conventional non-slotted resonators and displacement amplifiers with elliptic and arc slots with varying support scheme as labeled. . . . .	72
4.21	Simulated vibration-induced temperature deviations in (a) a CC-beam; (b) an elliptic-slot disk; (c) an arc-slot disk; and (d) rectangular-slot disk, illustrating the postulation of the thermoelastic loss in the slot region. . . . .	73
4.22	Schematic of a slotted disk used to calculate the thermoelastic damping in which the slotted disk is approximated as a composite of a partial wine-glass disk and CC-beams. . . . .	74
4.23	Theoretical $Q_{TED}$ vs. extracted $Q_{TED}$ showing that for a larger displacement gain suffers higher thermoelastic damping and thus, a lower $Q_{TED}$ magnitude and that disks with rectangular slots exhibit higher TED compared to disks with other slot designs. . . . .	77
4.24	Measured $Q$ versus aspect ratio from three dies. Here, $AR=1$ corresponds to a circular disk, while higher ARs indicate ellipses. $AR=1.2$ presents the lowest $Q$ while $AR > 1.6$ seems to be able to recover $Q$ back to that of a circular disk. (Reprint of Fig. 2.26) . . . . .	78

4.25	(a) Schematic of an elliptic disk dissipating energy into the substrate while vibrating. (b) FEA-simulated deformation of the center stem bottom (substrate is not shown for clarity). (c) Illustration of z displacement components versus rotating angle along the circumference at the bottom of the center stem when the elliptic disk vibrates in the wine glass mode shape. . . . .	79
4.26	FEA-simulated z-displacement components versus aspect ratio, indicating a large vibration magnitude along the z axis when $AR = 1.2$ . . . . .	80
5.1	Schematic of laser trimming on micromechanical CC-beam resonators. . . . .	82
5.2	(a) Schematic of a CC-beam micromechanical resonator in a favored 2-terminal measurement setup. (b) Mode shape of fundamental transverse vibration by finite element analysis. . . . .	83
5.3	Effective mass and stiffness for a CC-beam ( $(l, w, h) = (40 \mu\text{m}, 10 \mu\text{m}, 2 \mu\text{m})$ ), showing a trimming hole generates location-dependent stiffness and mass deviations and therefore a location-dependent frequency shift. . . . .	84
5.4	Schematic of a trimmed CC-beam where the CC-beam is decomposed by two intact CC-beams and one CC-beam that has the trimming holes across the width. . . . .	86
5.5	Schematic of a trimmed CC-beam and its mechanical model, where the trimming spots are modeled as cracks. Three cracks are shown in this example with depths of $a_1, a_2$ , and $a_3$ , at locations $x_1, x_2$ , and $x_3$ , respectively. Each of the cracks is modeled as a rotational spring ( $k_1, k_2$ , and $k_3$ ). . . . .	87
5.6	Frequency shift (relative to a crack-free version) versus crack location for a CC-beam resonator with dimensions of $(l, w, h) = (40 \mu\text{m}, 10 \mu\text{m}, 2 \mu\text{m})$ estimated by the analytical model. . . . .	91
5.7	Comparison of frequency shift versus crack location using the analytical model and CoventorWare FEA for a CC-beam resonator with dimensions of $(l, w, h) = (40 \mu\text{m}, 10 \mu\text{m}, 2 \mu\text{m})$ . . . . .	92
5.8	Stress intensity factor test specimen used to estimate the adjusting factors for partial-width trimming holes: (a) a partial-width central hole compared to (b) an edge hole. . . . .	93
5.9	Adjusting factors (inverse) for partial-width trimming holes for varying crack depth, showing factors due to area and edge effects. . . . .	93
5.10	Frequency shift versus trimming location in a CC-beam ( $(l, w, h) = (40 \mu\text{m}, 10 \mu\text{m}, 2 \mu\text{m})$ ) resonator with a 1- $\mu\text{m}$ -diameter 0.5- $\mu\text{m}$ -deep circular hole estimated by FEA and the analytical model (only considering stiffness change). . . . .	94
5.11	Frequency shift pattern using the analytical model added with mass removal effects, showing positive frequency shifts (i.e., trim-up) regions. . . . .	95
5.12	Photograph of the apparatus used to trim micromechanical CC-beam resonators. . . . .	96
5.13	Measured frequency response of a fabricated CC-beam resonator with dimensions of $(l, w, h) = (40 \mu\text{m}, 10 \mu\text{m}, 2 \mu\text{m})$ . . . . .	97

5.14	SEM of the trimmed CC-beam resonator with dimensions of $(l, w, h) = (40 \mu\text{m}, 10 \mu\text{m}, 2 \mu\text{m})$ , showing regions ablated by the applied laser pulses and with a inset of zoom-in view of the laser trimming spot. . . . .	98
5.15	Measured frequency shift versus trimming location for the CC-beam resonator of Fig. 5.14 alongside with that obtained from the analytical model and FEA simulation. . . . .	98
5.16	SEM of the trimmed CC-beam resonator with dimensions of $(l, w, h) = (49 \mu\text{m}, 10 \mu\text{m}, 2 \mu\text{m})$ . . . . .	99
5.17	Measured frequency shift versus trimming location for the CC-beam resonator of Fig. 5.16 alongside with that obtained from the analytical model and FEA simulation. . . . .	99
5.18	Measured $Q$ versus laser pulse sequence for the device of Fig. 5.16, illustrating how symmetric trimming maintains the CC-beam $Q$ . . . . .	100
5.19	FEA-simulated mode shapes of vertical z-displacement at either ends of a CC-beam ( $(l, w, h) = (40 \mu\text{m}, 10 \mu\text{m}, 2 \mu\text{m})$ ) with (a) no trimming holes; (b) a single trimming hole at midpoint; (c) a single trimming hole away from midpoint by $15 \mu\text{m}$ , and (d) two trimming holes symmetrically away from midpoint by $15 \mu\text{m}$ . . . . .	101
5.20	SEM of a CC-beam ( $(l, w, h) = (40 \mu\text{m}, 10 \mu\text{m}, 2 \mu\text{m})$ ) labeled with the sequence of applied pulses that is used to demonstrate deterministic trimming from its initial resonance frequency of 10.27612 MHz to the 10-MHz target frequency. . . . .	102
5.21	Resonance frequency and the corresponding $Q$ as a function of the applied laser pulse number for the deterministic trimming of the CC-beam resonator of Fig. 5.20 towards a 10-MHz target frequency. . . . .	102
5.22	(a) Schematic of a center stem supported disk resonator showing the measurement setup and targeted trimming locations. (b) The FEM simulated wine glass mode shape showing a hole on the disk solid model (mass removal) to imitate the trimmed spot. . . . .	104
5.23	Measured frequency shift versus the trim location measured from the center of disk, presenting a good matching against the FEM simulated data. The SEM of the trimmed disk is shown in the inset with pulse sequence number labeled. . . . .	105
5.24	Measured $Q$ s versus the pulse number that has been applied sequentially, exhibiting $Q$ degradation for trims of #1 and #2, which are closest to the center. . . . .	106
5.25	FEM simulation for comparison of vertical displacement (shown as the color legend) for trimming location occurred at (a) $8 \mu\text{m}$ , and (b) $2 \mu\text{m}$ from the center, illustrating unbalanced movement/stress was introduced by a close-to-center laser pulse. . . . .	106
5.26	Measured frequencies and $Q$ s for a trimming sequence with all pulses being applied on the edge of disk, verifying the postulation that $Q$ can be kept as long as pulses are away from the center. . . . .	107

# List of Tables

2.1	Summary of Elliptic Disk Designs . . . . .	29
4.1	Expressions estimating the $Q$ limits imposed by various loss mechanisms in micromechanical resonators . . . . .	52
4.2	Deposition rate and resistivity comparison between CVD polySiC and polySi-filled CNT grass . . . . .	62
4.3	Summary data for devices used in acoustic velocity extraction . . . . .	66
5.1	Pulse sequence used for deterministic trimming of a CC-beam resonator targeted to a desired frequency of 10 MHz . . . . .	103

## Acknowledgments

First, I would like to thank my advisor, Professor Clark T.-C. Nguyen, who has guided, inspired, and encouraged me through the past eight years. His pay-attention-to-detail and challenging-the-impossible attitude will continuously influence me throughout the rest of my life.

I am grateful to Professor Elad Alon, Professor Ali Javey, and Professor Roya Maboudian for their valuable advice to my research. I thank Professor Ali Javey and Professor Ana Arias, and of course, Professor Clark Nguyen for choosing me as the Head GSI of EE143. It was a wonderful experience working with you all.

I am grateful to the staff in BSAC for organizing IAB meetings and seminars. I thank NanoLab Staff (formerly Microlab), especially Joe Donnelly and Jay Morford for their incredible work on keeping the critical tools up and running. Without them, I won't be able to finish the most critical parts of my process. I also thank Dr. Xiaofan Meng for the help of metal deposition, especially the last Al run that saved my process!

Early collaborations with Dr. Wen-Lung Huang, Dr. Bongsang Kim, Dr. Tommi Riekkinen, and of course, Zeying Ren taught me the essential fundamentals and disciplines about microfabrication, which benefit me a lot along the way. I'd also like to thank Dr. Yang Lin for all of the times we worked together on developing "resoswitches".

In addition, thanks for inspiring conversations and all of the help and support along the road from my labmates and friends Mehmet Akgul, Thura Lin Naing, Tristan Rocheleau, Henry Barrow, Bobby Schneider, Lingqi Wu, Turker Beyazoglu, Ruonan Liu, Alper Ozgurluk, Chih-Ming Lin, Yenhao Chen, Jun-Chau Chien, Yung-Kan Chen, Wei-Chen Lien, Jack Yaung, Chao-Shiun Wang, Chung-Hsun Lin, Tsung-Te Liu, Long You, Yingqi Jiang, Peng Zheng, Yuji Takabayashi, Eric Zheng, Cary Lin, and Melanie Chang. I am especially grateful for all the encouragement given by Yi-Chin Chiang and Dr. Yu-Ting Kuo, my best friends for 20+ years. That indeed means a lot to me.

According to NanoLab Manager Bill Flounder, I hold the record of the most semesters of serving the EE143 Head GSI in the history—Spring'10, Fall'13, Spring'14, Fall'14, and Spring'15. Thanks to all the students (and GSI's!) for behaving well in the lab and not getting me into any troubles. It was absolutely fun teaching this class, and most of all I had my name engraved on the mask together with Kirt Williams, Jack Judy, Katalin Voros, and Matthew Last! (What an achievement!)

I am grateful to my former M.S. advisor Professor C.-k. Wang for his continued encouragement and advise. I also want to thank Professor Sheng-Shian Li and Professor Weileun Fang for the encouraging conversations.

I thank my family for their boundless support throughout these years. I am especially grateful to my parents, for their unconditional love and early attitude that they instilled in me that led to all of this.

Words can not describe my gratitude to Matilda Yun-Ju Lai. I am very lucky to have Matilda's company through these tough yet sweet years. I will never forget those days and

nights that we spent together fabricating devices in the Nanolab. Thank you for always being supportive and lighting up my life.

# Chapter 1

## Introduction

To date, billions of sensors installed ubiquitously in the environment are playing a key role to make a better world. Those sensors are connected to the Internet via wireless sensor networks (WSNs) to enable the Internet of Things (IoT) concept that embraces seemingly unbounded possibilities such as (1) structural health monitoring; (2) unmanned vehicles; (3) environmental sensing; and (4) personal health monitoring (*cf.* Fig. 1.1). In fact, the success of IoT would heavily depend on the amount of sensors available in the network—the more sensors distributed in the environment, the more powerful and accurate information that can be retrieved. While being driven by demand, the speed how fast more sensors can be deployed is a direct consequence of the progress of cost reduction for production and maintenance of individual wireless sensor modules.

### 1.1 Motivation: Towards Zero-Quiescent Power Radio Front-Ends

Particularly, wireless sensor modules are distributed with no intention of returning to replace their power sources (to reduce maintenance cost), thereby spurring an obvious need to minimize their power consumption.

Among components in a sensor node, the wireless communication radio module is very often a major power hog. Within this module, transmit power is critical, especially when sleep strategies are utilized to greatly reduce the average receive power consumption that might otherwise dominate the battery drain.

To minimize transmit power, the efficiency of the power amplifier (PA) is paramount. Among high efficiency PA topologies, the switched-mode Class-E design theoretically delivers the highest drain efficiency—ideally 100%—by shaping the switching waveform so that no power dissipates across the switch [1].

When sleep strategies cannot be employed, e.g., in cellular networks, receive power can actually overshadow transmit energy consumption, since receive path electronics must remain “on” over periods to listen for interrogating signals. Thus, it is important that front-end RF

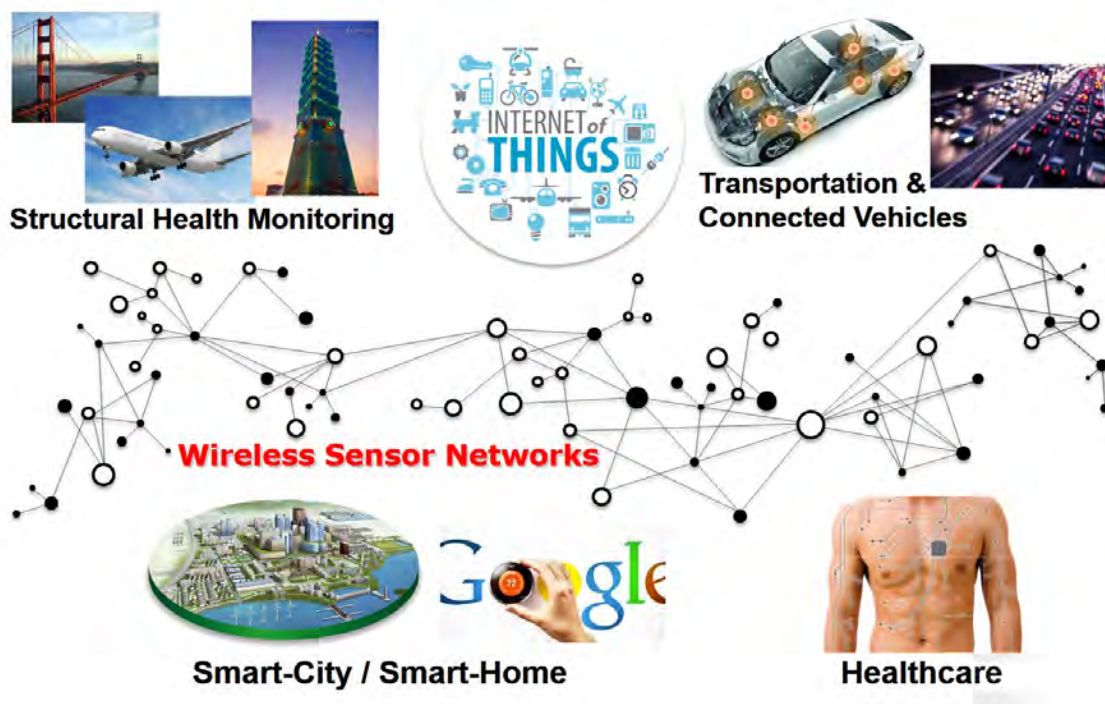


Figure 1.1: Wireless sensor networks (WSNs) enables Internet of Things (IoT) that connects billions or even trillions of sensors to the Internet for structural monitoring, transportation management, smart grid, smart homes, and even personal health monitoring.

receive path circuits, e.g., the low noise amplifier (LNA) and mixer, operate with very low standby power consumption.

## 1.2 Issues of Current Technologies

### 1.2.1 Transistor-Based Switches

To date, unfortunately, large parasitic capacitances associated with transistor-based switches dramatically degrades the circuit performance that otherwise would be much higher. Take Class-E switched-mode power amplifier for example. Class-E switched-mode power amplifier was first demonstrated that theoretically can achieve 100% drain efficiency by managing to realize non-overlapped voltage and current waveforms across the switch component [1]. Fig. 1.2 (a) presents a conventional transistor-based switched-mode power amplifier whereby the transistor is operated as a switch, together with the right amounts of reactive components (i.e.,  $C_1$ ,  $C_2$ , and  $L_1$ ) as listed in Fig. 1.2 (b), to shape the current and voltage such as shown in Fig. 1.2 (c).

However, in order to attend low turn-on resistance  $R_{on}$ , the transistor component needs to be relatively wide (i.e.,  $R_{on}^{-1} \propto$  transistor width) and in turn rises the parasitic capacitance to

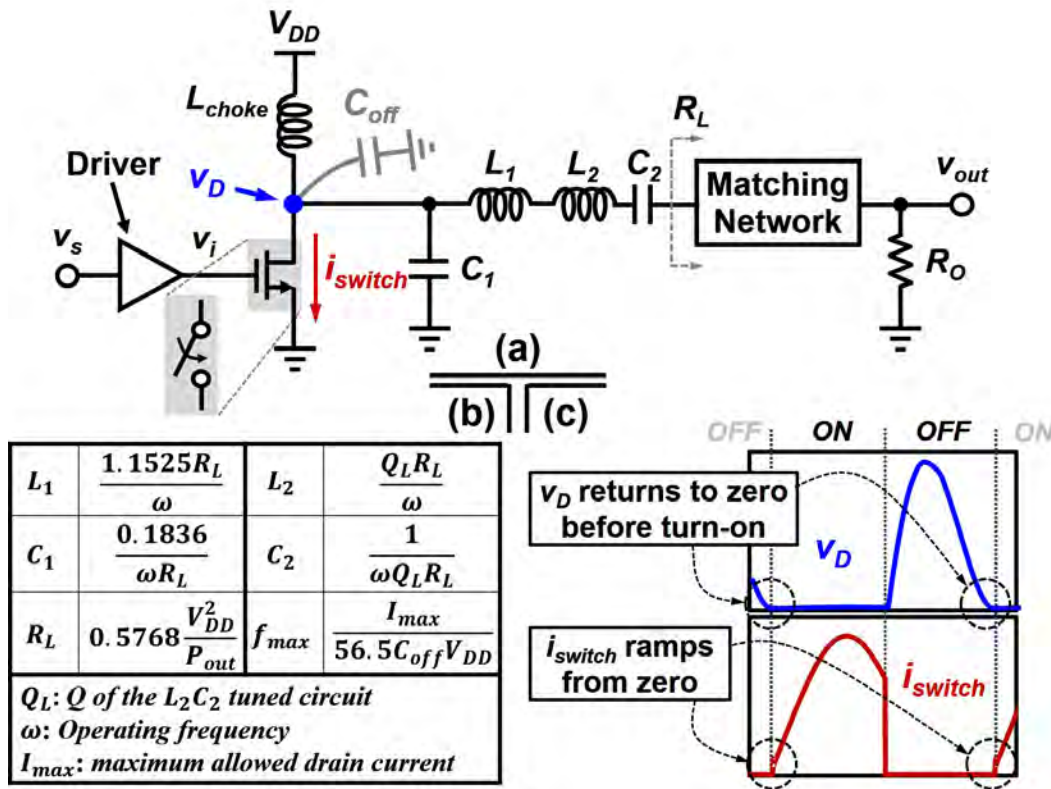


Figure 1.2: (a) A schematic of a transistor-based Class-E PA. (b) The theoretical amounts of value for the reactive components shown in (a) required to achieve the non-overlapped current and voltage waveforms across the switch device. (c) Simulated (ideal) switching current and voltage waveforms, showing the product of current times voltage is zero at any times.

a point where the right value of  $C_1$  no longer can be used. This is one of the major issues that prevent switched-mode power amplifiers using current transistor technologies from reaching the theoretical 100% efficiency especially for those high frequency applications up to GHz range [2].

To better elucidate the resoswitch-induced benefits, Fig. 1.3 presents simulations of switch voltage and current in a typical Class-E PA for two cases: (a) a transistor switch with very large  $C_{off} \sim 1.1$  pF; and (b) a MEMS resoswitch that allows the right value of  $C_1$ . As expected, when  $C_1$  takes on the right value, very little energy per cycle is wasted. On the other hand, when  $C_{off} \sim 1.1$  pF, large currents spike during turn-on that dissipate sizable energy per cycle, thereby dramatically degrading efficiency. Clearly, if use of a resoswitch allows the right  $C_{off}$ , it should also greatly reduce transmit power consumption.

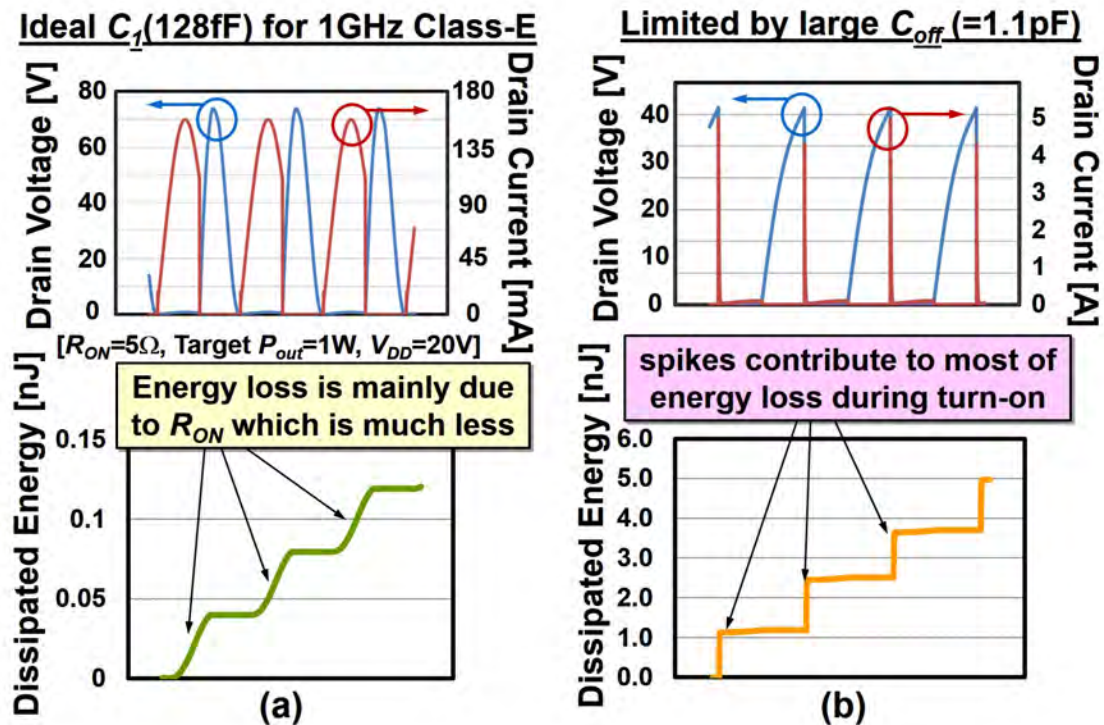


Figure 1.3: Comparison of effects on switching waveforms and dissipated energy per cycle by using (a) an ideal value of  $C_1$  and (b) a larger value of capacitance of  $C_1$  dominated by the parasitic.

## 1.2.2 Conventional MEMS Switches

Micromechanical switches operating at radio frequencies (RF) have exhibited superior performance over transistor-based counterparts in insertion loss, isolation, and power handling capability [3]. In particular, the small parasitic capacitances of MEMS switches offers switch figure of merits (FOM's<sup>1</sup>) several orders better than transistor counterparts, which could substantially enhance the efficiency of periodic switch applications, such as power amplifiers and converters. However, the majority of MEMS switches demonstrated so far still suffer from slow switching speeds, large actuation voltages (i.e., on the order of 20-80 V), and poor long-term reliability. These unsolved issues greatly limit the use of these devices in RF applications, e.g., phased-array antennas, and outright prevents them from addressing higher volume switched-mode power amplifier or power converter applications.

<sup>1</sup>FOM =  $\frac{1}{R_{on}C_{off}}$

### 1.3 Approach: Micromechanical Resonant Switches

The receive chain of a wireless sensor module needs to remain on when sleep mode technique cannot be utilized, which in turn requires a finite standby power to consume the battery drain if transistor circuits are used. In order to reduce the power consumed by the receiver front-ends, RF channel selection technique can be first employed prior to the front-end circuits. As covered in [4], if RF channel selection were available to remove all incoming blockers before they reach front-end electronics, then the local oscillator phase noise and dynamic ranges of the LNA and mixer in any RF front-end could be relaxed enormously, to the point where highly nonlinear (and thus, low power) designs of these functions become permissible. In fact, an ultimate yet simpler solution could be enabled by MEMS resonant switches (“resoswitch”) that allow simultaneous signal filtering and amplification when equipped in a switched-mode power amplifier circuit (*cf.* Fig. 1.4).

Micromechanical resonant switch (“resoswitch”) harnesses the resonance and nonlinear dynamic properties of micromechanical resonators to greatly increase switching speed and cycle count and lower the needed actuation voltage with much lower parasitic capacitances. In particular, when at resonance, the displacement of mechanical structures enhances by  $Q$  times and therefore, actuation voltages are small even though the stiffness of the device can be quite large. The large stiffness in turn allows very fast operation (because of high resonance frequency) and very reliable operation, since large stiffness generates large restoring forces against any sticking phenomenon.

The first resoswitch demonstrated in [5] based on a polysilicon wine-glass disk resonator yielded a switching frequency of 61 MHz (i.e., a switching time of  $\sim 4$  ns) with an actuation voltage of 2.5 V. This device, however, suffered from impacting at input port since the symmetrical structure exhibits the same displacement along the input and the output axes which have the same gap spacing. Another revised version of resonant switch demonstrated in [6] utilized asymmetrical mechanical structural design to yield different magnitudes of stiffness and so as displacement along the input and the output axes. By preventing the input port from impacting, the displacement-amplifying resonant switch posted a cycle lifetime of 173 trillion hot-switched cycles. The two resoswitches above, however, were constructed in doped polysilicon, which compromised their ability to achieve power gain, since the high series and contact resistances loaded down its FOM. To solve this, work in [7] introduced a resoswitch in nickel metal to lower the  $R_{on}$  to less than  $1 \Omega$  with varying gap spacing along the input and the output axes achieved by intentionally sputtering the sidewall sacrificial material with varying thickness. When embedded in a simple switched-mode power amplifier circuit, the device generate 17.7 dB of sustained electrical power at 25 MHz, marking the first successful demonstration of RF power gain using a micromechanical resoswitch device.

The recent demonstration of a wireless receiver employing a micromechanical resoswitch to permit continuous listening while consuming no power until a valid input signal arrives [8] has sparked renewed interest in ultra-low power sensor networks that dispense with the complexity of sleep/wake cycles and remain awake and listening at all times. Indeed, such a zero-quiescent power receiver, with block diagram pictured in Fig. 1.4, obviates the need

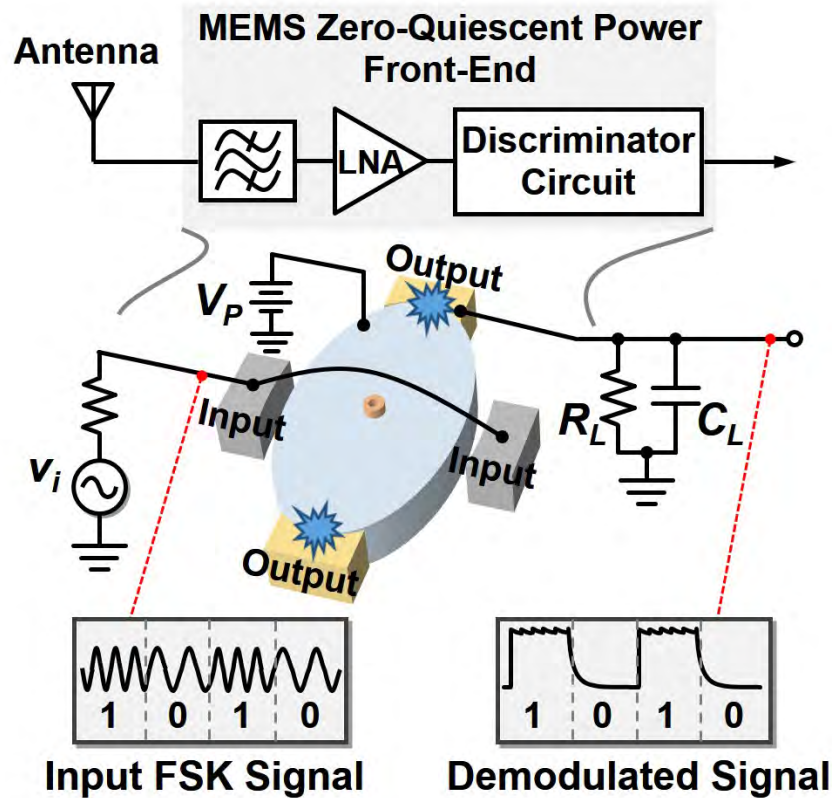


Figure 1.4: Schematic of a resoswitch-enabled zero-quiescent power receiver architecture.

for real-time clocks to synchronize the wake-up times of networked sensor motes, thereby eliminating their cost and power consumption.

## 1.4 Overview

This dissertation will focus upon design issues of MEMS-based filter-power amplifiers using micromechanical resonant switches. It starts in Chapter 2 with discussion of micromechanical displacement-amplifying resonant switches, from design, to modeling, to experimental verification. Next, Chapter 3 discusses an aluminum resoswitch embedded filter-power amplifier circuit based on the displacement-amplifying resonant switch. The detailed fabrication process flow, experimental results, and utility of the filter-power amplifier in the receive path. Next, Chapter 4 addressed one of the most important attributes of micromechanical resonant switch— $Q$ —that would affect the receiving signal sensitivity. Several techniques will be discussed and demonstrated to raise  $Q$  of micromechanical vibrating resonators. Chapter 5 then addresses yet another important attribute: frequency accuracy. Laser trimming technique that preserves high- $Q$  with bidirectional frequency tuning will be demonstrated on

CC-beam and wine-glass disk resonators as demonstrate vehicles and an analytical model for location-dependent frequency shift will be detailed. Finally, Chapter 6 finishes with some conclusions and possible future research directions.

## Chapter 2

# Micromechanical Displacement-Amplifying Resonant Switches

Although the -60dBm sensitivity demonstrated in [8] is already sufficient for many short range wireless sensor applications, its 20-kHz frequency relegates it to low bit rate long-range applications, e.g., time transfer from an atomic reference (perhaps at NIST) to a portable clock thousands of miles away that receives atomic time via radio transmission in the 60-kHz LF WWVB band [9][10]. To address more abundant higher bit rate applications, operation at higher frequencies spanning 60 MHz to 5.8 GHz is desirable.

This chapter will describe two designs of VHF micromechanical displacement-amplifying resonant switches that dispense the need for additional process step used in [7] and rather utilize a design-centric approach—directional stiffness engineering—to effect displacement amplification in the switch structure. In Design#1, introducing slots into the wine glass disk resonator structure generates difference stiffness along the orthogonal axes, thereby different displacement amplitudes—larger displacements along its output axis than its input, so that impact occurs only at the output electrodes. Although Design#1 nicely provides displacement gain, it does so at the expense of  $Q$  via concentrated stress as well as excessive thermoelastic damping (details will be discussed in Chapter 4) at the corners of its slots. To solve this, Design#2 uses ellipse geometry that provides stiffness differences by geometric ratioing rather than  $Q$ -degrading slots, where the smaller stiffness along the longer axis (i.e., the major axis of the ellipse) yields a larger displacement than that along its shorter, hence stiffer, input minor axis. The elliptic disk avoids the energy-consuming stress corners of slots, allowing itself to retain high  $Q$ .

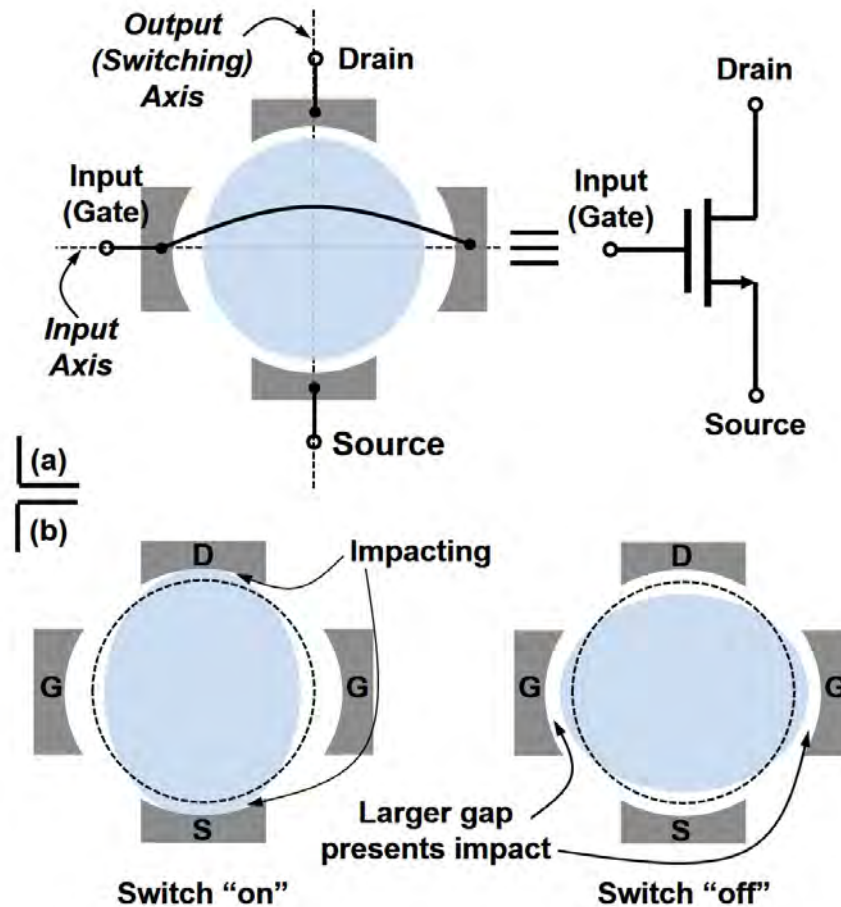


Figure 2.1: (a) Schematic for a wine glass disk resonant switch and its transistor analogue operating as a switch. (b) Periodic switching between two phased cycles, showing a larger gap at input is needed to prevent the input port from impacting.

## 2.1 Slotted-Disk Displacement Amplifier

### 2.1.1 Structure and Operation

Fig. 2.1 (a) presents a micromechanical resoswitch based on a conventional wine glass disk resonator and its equivalent transistor switch circuit. Note that the gap spacing along the input axis is wider than that along the output axis to prevent the disk from impacting the input electrodes. As shown in Fig. 2.1 (b), during the first half cycle of vibration while the disk expands along its output axis, the disk provides a short path, i.e., switching "on", between the two output electrodes (i.e., as the drain and source terminals in a transistor) when the displacement is large enough. In the next half cycle while the disk expands towards the input electrodes with the same displacement magnitude as that in the previous half cycle, a larger gap spacing that prevents the input electrodes from impacting ensures the driving

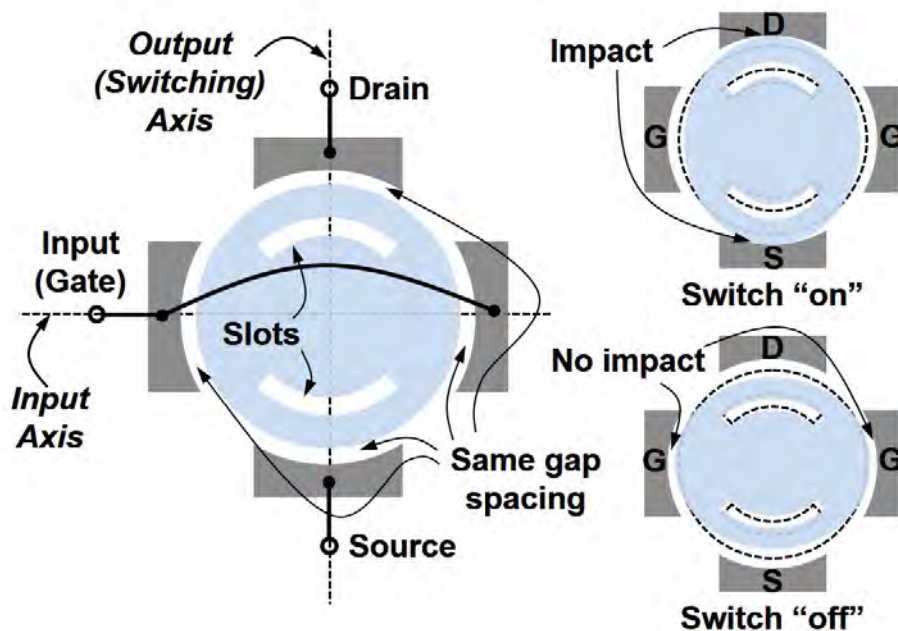


Figure 2.2: Schematic of a slotted displacement amplifying disk resonator, which yields a larger displacement along the output axis than that along the input and in turn prevents input from impacting without the need of larger gap spacing.

signal remains intact.

One possible way to achieving the desirable different gap spacings along the two axes is the use of uneven sidewall sacrificial layer as demonstrated in [7]. Particularly, intentional tilting of the substrate with respect to the sputtering flux during sidewall sacrificial layer deposition yields a non-uniform—wider along the input axis than along the output axis—gap spacings between the disk and electrodes. As a consequence of the added complex process, this technique suffers from repeatability and greatly increases cost.

### 2.1.2 Single-Stage Slotted-Disks

Fig. 2.2 plots the schematic of a slotted disk, where two slots cut along the output axis of the conventional disk structure effectively lower the stiffness of the disk along the output axis, resulting in a larger displacement along the output axis than the input axis when vibrating under the wine glass mode. By doing so, even with identical gap spacing along the two axes, the displacement difference only allows impact between the disk and output electrodes. Thus, there no longer exists a need for varying gaps, nor the special processing that would entail.

Fig. 2.3 plots the schematics of slotted disks with (a) rectangular- (as seen in [11]); (b) arc-; and (c) elliptic-slots. Fig. 2.4 illustrates the displacement filed between (a) a conventional

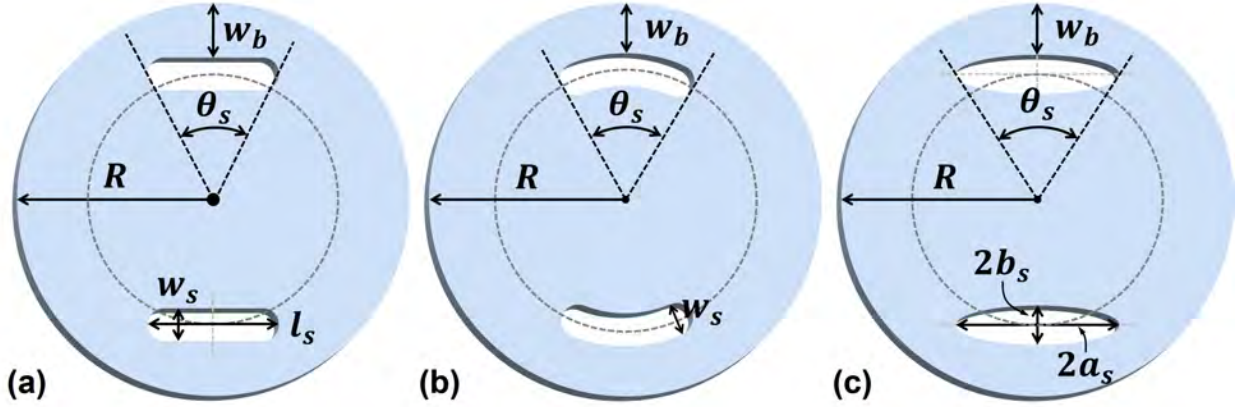


Figure 2.3: Slot opening design of (a) rectangular; (b) arc; and (c) elliptic slots.

disk (i.e., with no slots) and (b) an arc-slotted disk sized as  $(R, w_b, w_s, \theta_s) = (32 \text{ } \mu\text{m}, 8 \text{ } \mu\text{m}, 2 \text{ } \mu\text{m}, 45^\circ)$ . The conventional disk resonator exhibits a maximum displacement along the two orthogonal axes (input and output), at equal displacement magnitudes (both in red). In contrast, the slotted resonator of Fig. 2.4 (b) yields a larger displacement (red) along the output axis than that along the input (blue), for a total displacement amplifying gain of  $3.45\times$ . Fig. 2.4 (c) plot the normalized radial displacement as a function of angular location along the perimeter  $\phi$ , where both devices exhibit similar movement for  $\phi$  below  $60^\circ$ . For  $\phi$  above  $60^\circ$ , the conventional disk exhibits a symmetric mode shape along the quasi-node point at  $\phi = 45^\circ$  (same magnitude with opposite signs). The slotted disk, however, exhibits a larger radial displacement magnitude and for this particular slot dimension, yields a  $3.45\times$  displacement gain between the output axis ( $\phi = 90^\circ$ ) and the input axis ( $\phi = 0^\circ$ ).

### 2.1.3 Slotted-Disk Arrays

Use of a slotted disk array, composed of multiple such individual slotted disks coupled via beam couplers, can provide further displacement amplification when needed [12]. Such beam couplers present the greatest efficiency when their lengths equal multiples of half wavelengths at the disk resonance frequency. The following defines the relationship

$$L_{\text{coupler}} = i \times \frac{\lambda}{2}, i = 0, 1, 2, \dots \quad (2.1)$$

where  $\lambda$  represents the extensional-mode wavelength, at which point the beam couplers' dynamic stiffnesses become virtually infinite. This “infinite” stiffness forces the two coupled locations to move with the same amount, as shown in Fig. 2.5, in opposite directions for odd numbered  $i$ , and in the same direction for even numbered  $i$ .

Fig. 2.5 also illustrates how a two-stage array produces a higher displacement gain. In particular, the coupler attached to the small displacement point (i.e., input) of one disk and to the large displacement point (i.e., output) of another disk enforces identical displacement

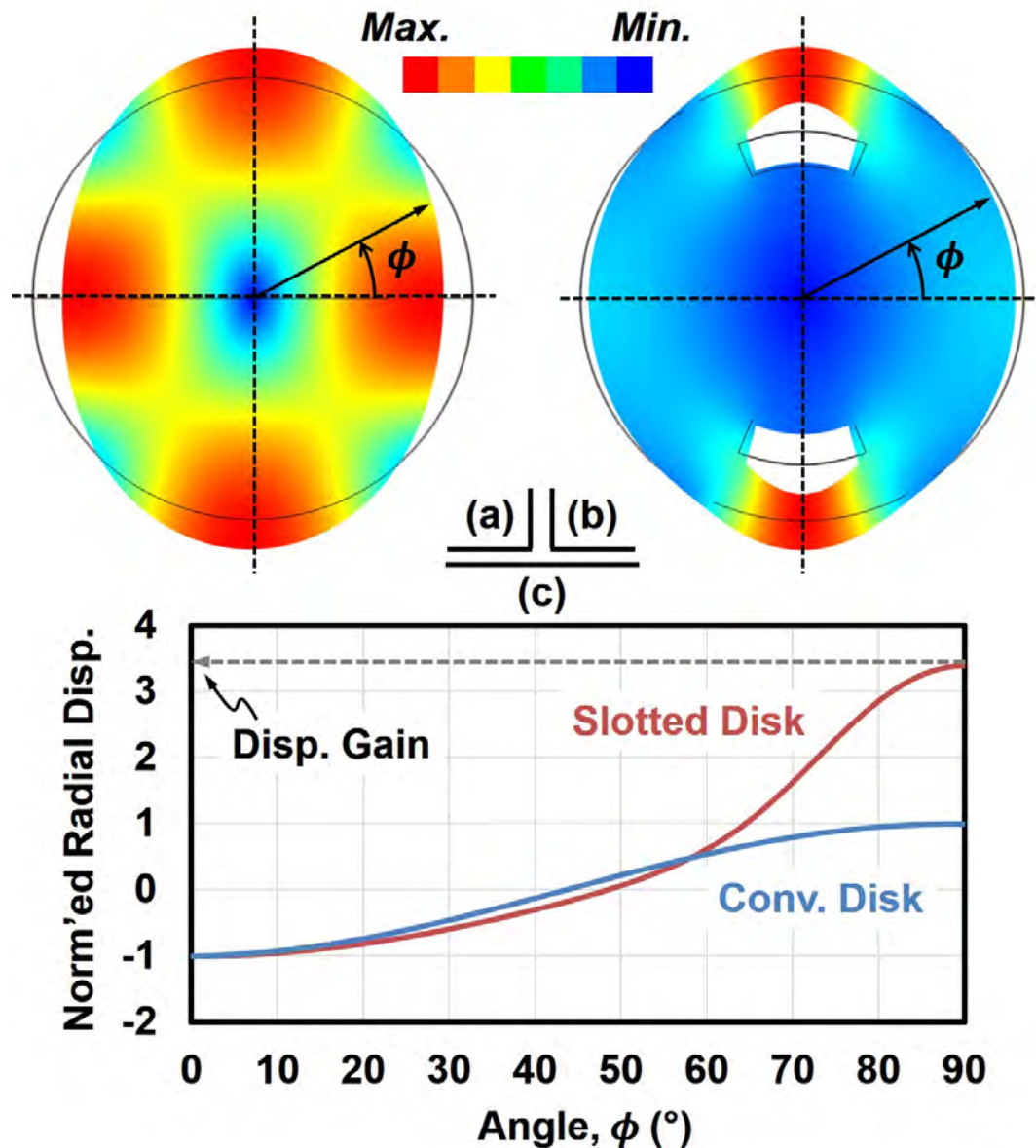


Figure 2.4: CoventorWare<sup>®</sup> FEA simulation compares the mode shape of (a) a conventional wine glass disk resonator and (b) a slotted displacement amplifying disk resonator of  $(R, w_b, w_s, \theta_s) = (32 \mu\text{m}, 8 \mu\text{m}, 2 \mu\text{m}, 45^\circ)$ , presenting an identical radial displacement along the two orthogonal axes in a conventional disk resonator while the slotted disk first follows the mode shape of the conventional counterpart but then rapidly increases its displacement as  $\phi$  increases.

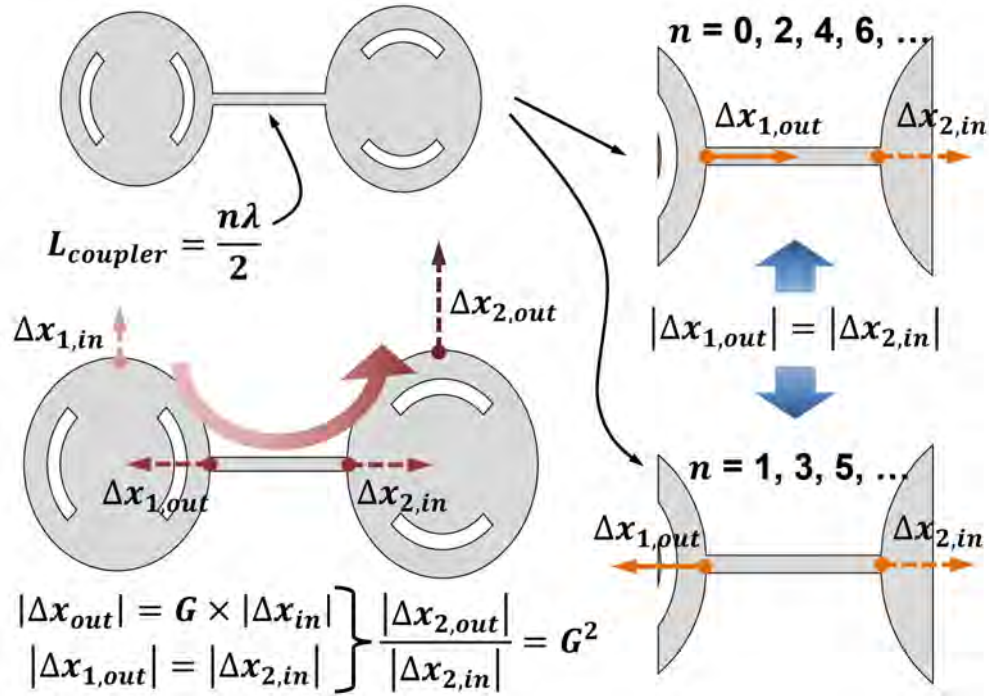


Figure 2.5: Schematic of two slotted disk array to illustrate boundary conditions set by the coupler to achieve a larger displacement gain.

at the two coupled locations. This connection allows the displacement gain  $G$  of each individual slotted disk to combine with the others for an overall gain of  $G^n$  (where  $n$  is the number of stages). Fig. 2.6 (a) presents the simulated mode shape for a two-slotted-disk array composed of two identical slotted disks and a zero-length coupler. Fig. 2.6 (b) plots normalized displacement as a function of angular location along the perimeter  $\phi$  for each of the disks in the two-stage array. As expected, cascading two slotted disks both with a displacement gain of  $3.45\times$  achieves a larger overall displacement gain of  $11.9\times (= (3.45\times)^2)$ .

#### 2.1.4 Negative-Capacitor Equivalent Circuit Model

Fig. 2.7 presents a negative-capacitor equivalent circuit of displacement-amplifying slotted disks, in which the mechanical impedance transformer with a turn ratio of  $\eta_c$  captures displacement amplification. The mechanical impedance transformer effectively yields an asymmetrical network with a lower impedance seen from the output port than from the input port.

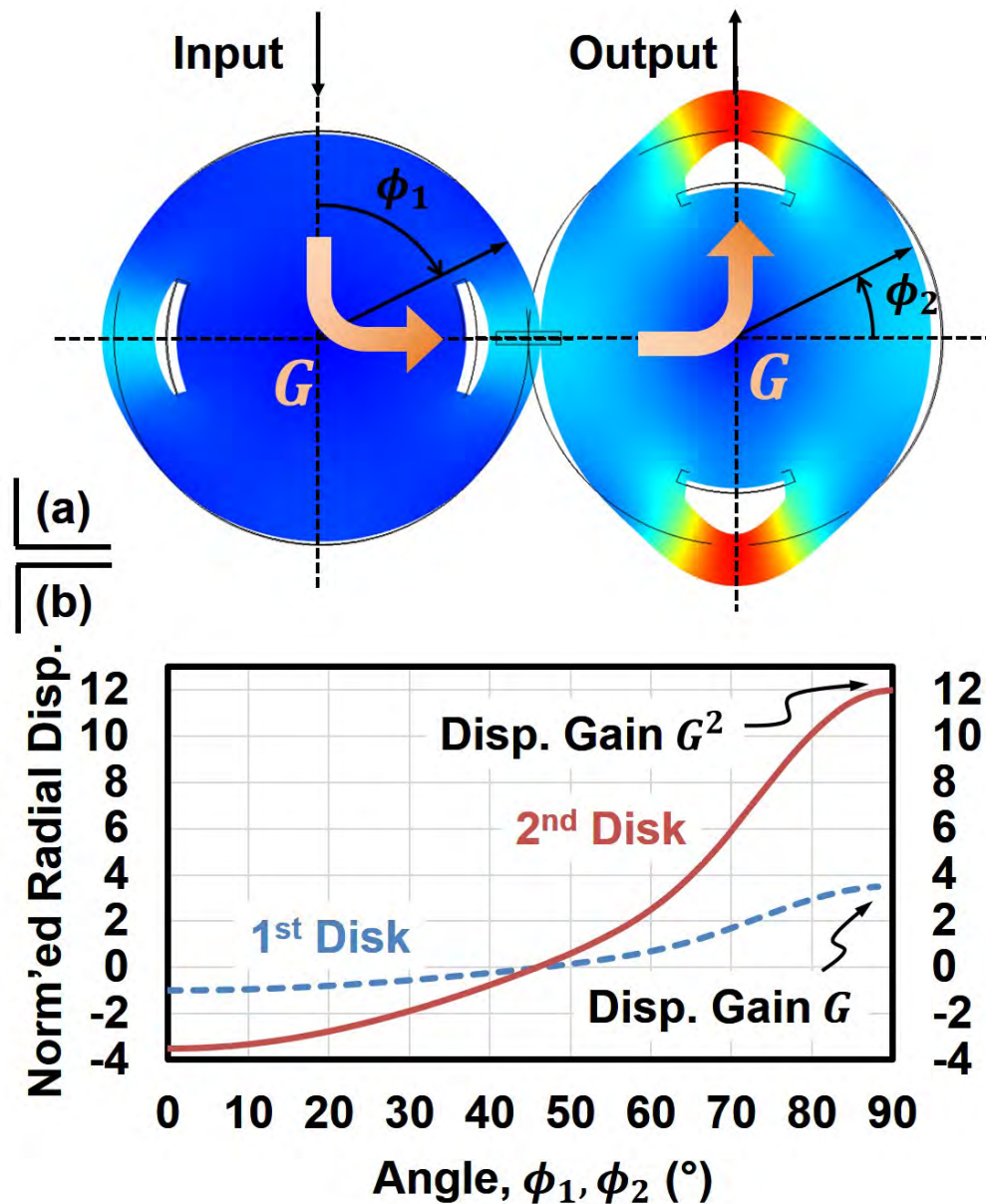


Figure 2.6: (a) FEA-simulated mode shape of a slotted-disk array achieved by coupling two displacement amplifying resonators with a zero-length of coupler. (b) The normalized radial displacement for each of the disks. Note that each of the slotted disks has the same displacement gain (i.e.,  $G = 3.45$ ) from the non-slotted axis to the slotted axis, together with the coupler which forces the coupled locations to have identical displacement, yield an overall displacement gain of  $G_2 (= 11.9)$ .

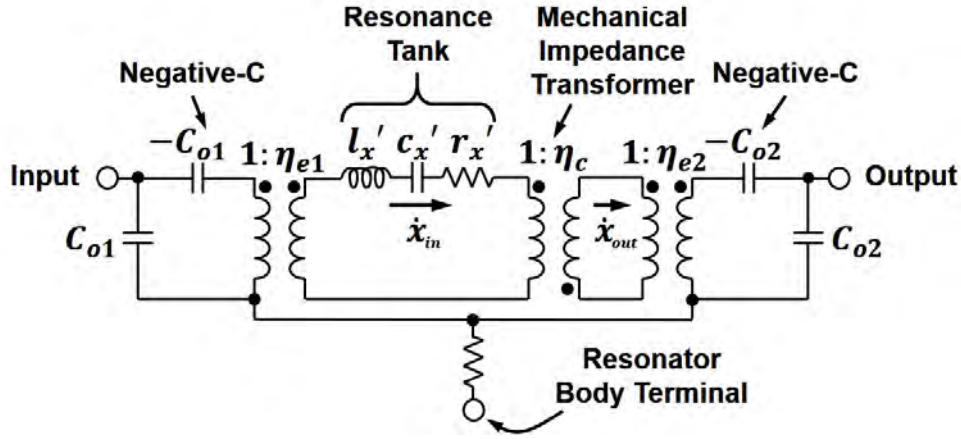


Figure 2.7: A negative-Capacitor based equivalent circuit model for slotted disk displacement amplifier.

## 2.2 Slotted-Disk Displacement Amplifier Design Procedure

The following outlines the design procedure for displacement amplifying slotted disks:

### 2.2.1 Semi-Empirical Model of Displacement Gain

Considering the case of zero slot angle ( $\theta_s = 0$ ) or the “beam” width equaling the radius ( $w_b = R$ ), where the displacement gain  $G_{disp} = 1$ , a semi-empirical displacement gain model based on FEA for given dimensions of  $R$ ,  $w_b$ , and  $\theta_s$  takes the form

$$G_{disp} = [\cos(\theta_s)]^{1-R/w_b}, \quad 0 \leq \theta_s \leq \frac{\pi}{4}. \quad (2.2)$$

$$G_{disp} = G_{disp}|_{\theta_s=\frac{\pi}{4}} + [1 - 0.4(\frac{R}{w_b})^2] \cos(2\theta_s), \quad \frac{\pi}{4} \leq \theta_s \leq \frac{\pi}{2}. \quad (2.3)$$

Note that (2.2) and (2.3) neglects the displacement gain dependency on slot width  $w_s$  since, according to FEA simulation, displacement gains show insensitive to varying slot width. For instance, a variation of  $\pm 1 \mu\text{m}$  for a typical slot width of  $2.5 \mu\text{m}$  (on  $32\text{-}\mu\text{m}$  radius disks) would merely lead to a displacement gain variation less than 4% for all slot angles of interest. Fig. 2.8 plots the displacement gain for a  $32\text{-}\mu\text{m}$ -radius disk with varying  $\theta_s$  for different  $w_b$  values by the modeling formulas and FEA. If higher precision is necessary, (2.2) and (2.3) can include more dimension variables including the slot width  $w_s$  that provides better match with FEA predictions (*cf.* Fig. 2.9):

$$G_{disp} = [\cos(\theta_s)]^{f(R/w-b,\theta_s) \times (1-R/w_b)}, \quad 0 \leq \theta_s \leq \frac{\pi}{4}. \quad (2.4)$$

where  $f(R/w_b, \theta_s)$  is

$$f(R/w_b, \theta_s) = \alpha_3 \theta_s^3 + \alpha_2 \theta_s^2 + \alpha_1 \theta_s + \alpha_0$$

where

$$\alpha_3 = -0.223 \left(\frac{R}{w_b}\right)^2 + 1.303 \left(\frac{R}{w_b}\right) - 3.595$$

$$\alpha_2 = 0.366 \left(\frac{R}{w_b}\right)^2 - 2.403 \left(\frac{R}{w_b}\right) + 5.891$$

$$\alpha_1 = -0.256 \left(\frac{R}{w_b}\right)^2 + 2.397 \left(\frac{R}{w_b}\right) - 5.762$$

$$\alpha_0 = 0.096 \left(\frac{R}{w_b}\right)^2 - 1.164 \left(\frac{R}{w_b}\right) + 4.08$$

and

$$G_{\text{disp}} = G_{\text{disp}}|_{\theta_s=\frac{\pi}{4}} + p \left(\frac{w_s}{R}\right) q \left(\frac{R}{w_b}\right) \cos(2\theta_s)^{g(R/w_b)}, \quad \frac{\pi}{4} \leq \theta_s \leq \frac{\pi}{2}. \quad (2.5)$$

where

$$p\left(\frac{w_s}{R}\right) = -2.272 \left(\frac{w_s}{R}\right) + 1.178$$

$$q\left(\frac{R}{w_b}\right) = 0.455 \left(\frac{R}{w_b}\right)^2 - 0.398 \left(\frac{R}{w_b}\right) - 0.446$$

$$g\left(\frac{R}{w_b}\right) = -0.0122 \left(\frac{R}{w_b}\right)^2 + 0.0476 \left(\frac{R}{w_b}\right) + 1.061$$

## 2.2.2 Semi-Empirical Model of Resonance Frequency and Stiffness

Slot-induced resonance frequency shifts as a function of slot span angle  $\theta_s$  and beam width  $w_b$  can be approximated as

$$f' = f_o h(R/w_b, \theta_s),$$

$$h(R/w_b, \theta_s) = \beta_4 (1 - \cos \theta_s)^4 + \beta_3 (1 - \cos \theta_s)^3 + \beta_2 (1 - \cos \theta_s)^2 + \beta_1 (1 - \cos \theta_s) + 1, \quad (2.6)$$

where

$$\beta_4 = -0.1513 \left(\frac{R}{w_b} - 1\right)^2 - 0.13 \left(\frac{R}{w_b} - 1\right) + 0.3801,$$

$$\beta_3 = 0.2091 \left(\frac{R}{w_b} - 1\right)^2 + 0.8404 \left(\frac{R}{w_b} - 1\right) - 1.2402,$$

$$\beta_2 = -0.0513 \left(\frac{R}{w_b} - 1\right)^2 - 1.013 \left(\frac{R}{w_b} - 1\right) + 1.2458,$$

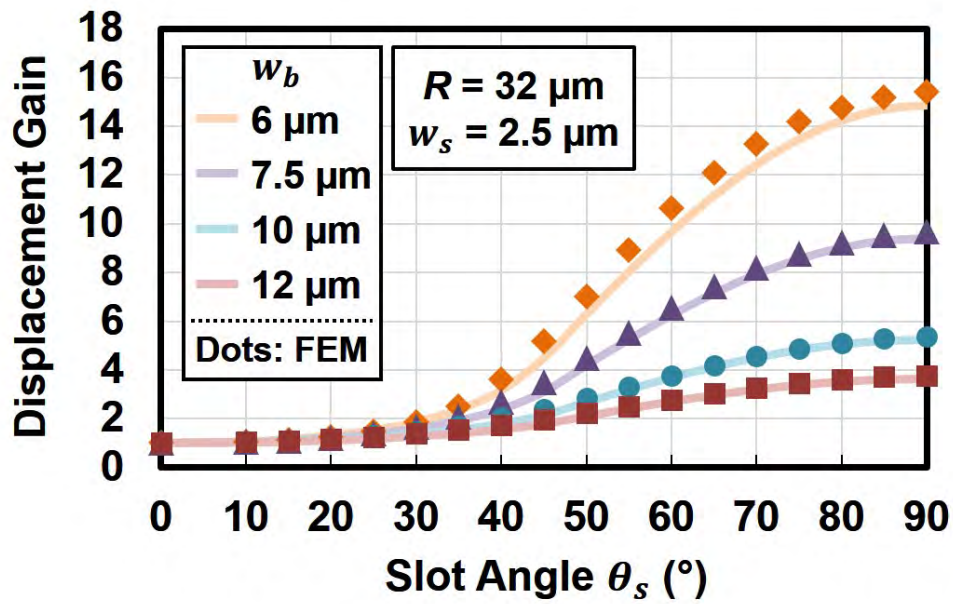


Figure 2.8: Displacement gain estimated by the simplified fitting model of (2.2) and (2.3).

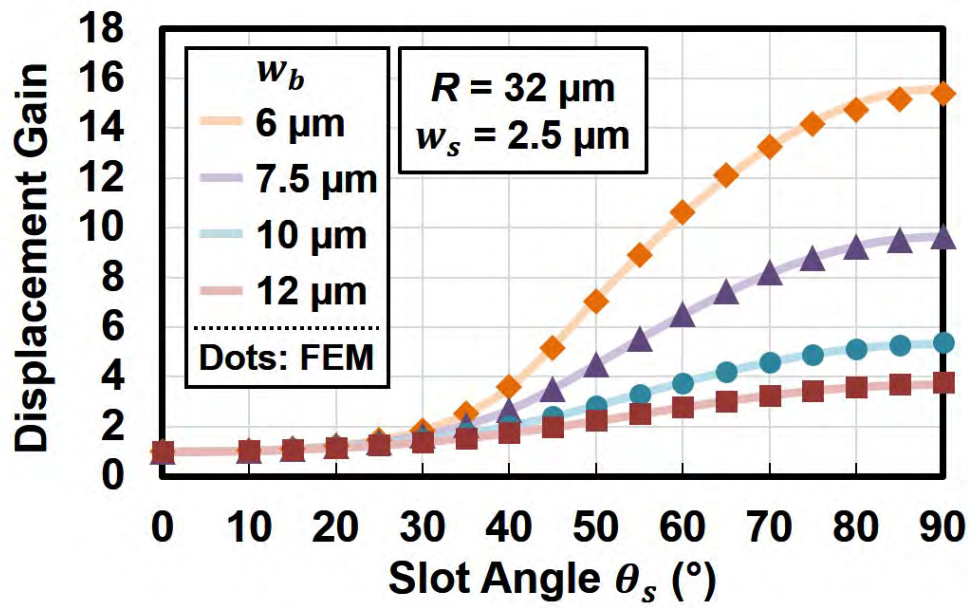


Figure 2.9: Displacement gain estimated by the complete fitting model of (2.4) and (2.5).

$$\text{and } \beta_1 = -0.006 \left( \frac{R}{w_b} - 1 \right)^2 + 0.2188 \left( \frac{R}{w_b} - 1 \right) - 0.567.$$

Note that the function format of  $h(R/w_b, \theta_s)$  again derives from the fact that  $G_{disp} = 1$  when  $\theta_s = 0^\circ$ .

Additionally, slots induce higher input stiffnesses compared to that of conventional wine glass disks with a factor  $\gamma_{in}$  derived by FEA:

$$\begin{aligned} k_{m,in} &= \gamma_{in} k_m, k_{m,out} = \gamma_{in} k_m / G_{disp} \\ \gamma_{in} &= \left( \frac{1 + G_{disp}}{2} \right) \exp \left( -T(\theta_s) \times \frac{R}{w_b} \right), \end{aligned} \quad (2.7)$$

where

$$\begin{aligned} T(\theta_s) &= 8.1415 (1 - \cos \theta_s)^5 - 24.047 (1 - \cos \theta_s)^4 + 26.735 (1 - \cos \theta_s)^3 \\ &\quad - 13.327 (1 - \cos \theta_s)^2 + 2.6038 (1 - \cos \theta_s) - 0.1107 \end{aligned}$$

### 2.2.3 Determine the Slot Span Angle $\theta_s$ and Radius-to-Slot “Beam” Width Ratio $R/w_b$

First, we select a value for either the slot span angle  $\theta_s$ , or the disk radius-to-beam width  $R/w_b$  ratio, and then determine the magnitude of the other parameter by solving (2.4) and (2.5) for a desirable displacement gain. Although the magnitude of  $w_s$  exhibits little influence on the resulting displacement gain, as will be discussed later, it effects  $Q$ —a relatively small magnitude of  $w_s$  is preferable for a higher  $Q$ . For example, when  $w_s/R$  and  $\theta_s$  are 0.1 and  $47.5^\circ$ , respectively, an  $R/w_b$  ratio of 2.55 from (2.5) is calculated for a target displacement gain  $G_{disp}$  of 2.

### 2.2.4 Determine the Disk Radius $R$ and Slot “Beam” Width $w_b$

Next determines the magnitudes of the disk radius  $R$  and slot “beam” width  $w_b$  based on the target operating frequency. The resonance frequencies of slotted disks differ from that of conventional non-slotted wine glass disks by a multiplying factor of  $\gamma_{in}$ , which is a function of  $R/w_b$  and  $\theta_s$  modeled in 2.2.2. Here, the design example in the previous section yields a frequency reduction factor 0.892. Taking a target resonance frequency of 100 MHz for example, a disk radius  $R$  of 17.14  $\mu\text{m}$  is needed to achieve a resonance frequency of 112.23 MHz (100/0.891 MHz) as if for a conventional wine glass disk [13]. Finally,  $w_b$  can be obtained to be 6.72  $\mu\text{m}$ .

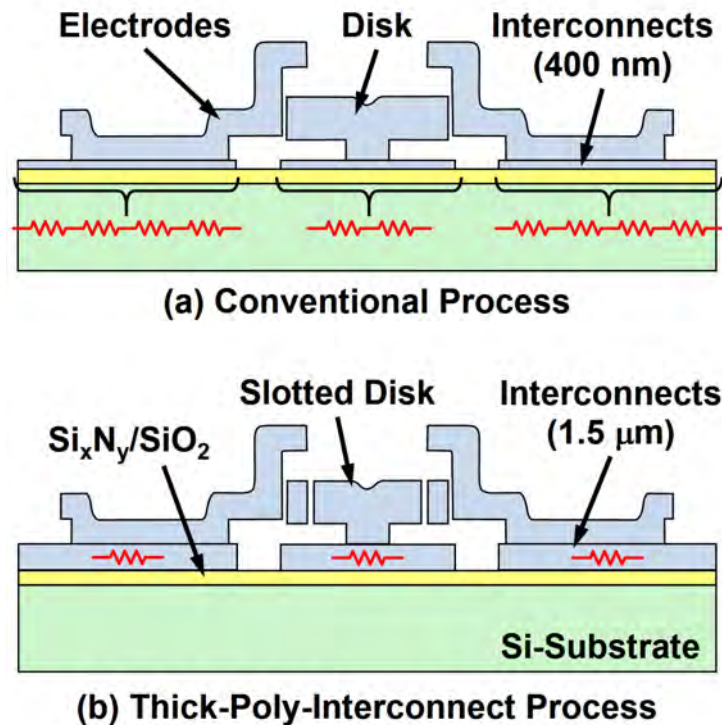


Figure 2.10: Schematics of device cross-sections via (a) conventional disk process and (b) thick-polysilicon-interconnect process, showing that the modified process uses a  $\sim 3\times$  thicker polysilicon layer,  $1.5\ \mu\text{m}$  versus  $0.4\ \mu\text{m}$ , for reduced interconnect resistances.

## 2.3 Experimental Results of Slotted-Disk Displacement Amplifiers

Fabrication of slotted-disk displacement amplifiers with varying slot design followed a process flow similar to that of [13], but used a thicker polysilicon interconnect layer, from  $400\ \text{nm}$  to  $1.5\ \mu\text{m}$ , resulting in a interconnect sheet resistance of  $1.6\ \Omega/\text{sq}$ . As illustrated in Fig. 2.10, the reduced series resistance of thicker polysilicon interconnects minimizes the parasitic resistive loading effect when presented on the device measurement.

### 2.3.1 Mixing Technique for Measuring Displacement Gain

The motional current for a vibrating capacitive-gap transducer under a fixed bias and a small vibration amplitude takes the form The measurement set-up for obtaining displacement gain, as shown in Fig. 2.11, utilizes a mixing measurement technique that apply an ac voltage of frequency  $\omega_{RF}$  on the input electrodes and an ac voltage of frequency  $\omega_{LO}$  on the structure. Capacitive gaps convert the electrical field between the input electrodes and disk structure to mechanical force via a square-law transfer function. The frequency components of the

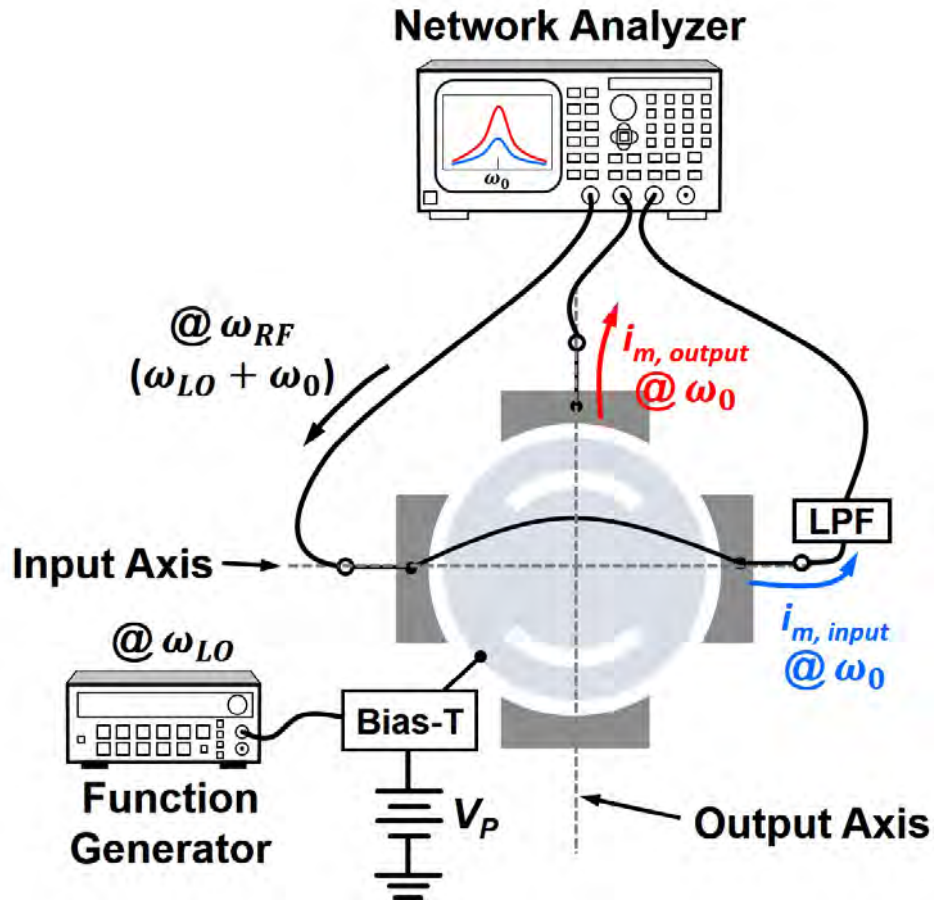


Figure 2.11: Schematic of mixing measurement set-up that is used to measure separately the motional currents from the input and output ports.

force reside at  $\omega_{IF} = (\omega_{RF} - \omega_{LO})$  and  $(\omega_{RF} + \omega_{LO})$ . When one of these components matches the resonant frequency  $\omega_0$ , the force component at this frequency drives the displacement amplifier into vibration. This mechanical vibration produces time-varying gap spacings and thus time-varying capacitance, which finally yields electrical ac currents at  $\omega_0$  with a magnitude of

$$i_m \cong V_P \frac{\epsilon A}{d^2} \omega_o X, \quad (2.8)$$

where  $V_P$  is the dc bias applied to the structure from a bias-T circuit,  $A$  and  $d$  are the electrode-to-resonator overlap area and gap spacing, respectively, and  $X$  is the amplitude of vibration. Spectrum analyzers then capture these motional currents flowing to the input and the output ports. However, as illustrated in Fig. 2.11, the frequency offset function in a network analyzer allows one to capture the motional currents as a spectrum analyzer. Implementation of this set-up requires connection of the network analyzer to the displacement

amplifier in a standard two-port measurement fashion. Next, the network analyzers driving port (e.g., Port 1) sends a signal to the input electrodes at frequency  $\omega_{RF}$ , away from the resonance frequency  $\omega_0$  by a magnitude of  $\omega_{LO}$ . The network analyzers other two receive ports (e.g., Port 2 and 3) measure the signal frequency responses from both the input and output electrodes by turning on S-parameter measurements.

Given identical gap spacings and overlap area along the in-put and output axes, the amplitudes of motional current collected from the two orthogonal electrodes depend upon the integral of displacement magnitude across the angles covered by the electrodes along each axis. It is reasonable to assume that the input and output ports both move as the wine glass mode shape but with different amplitudes characterized by the displacement gain. Thus, the motional currents from the two axes take the form

$$\begin{aligned} i_{m,input} &\propto |X| \\ i_{m,output} &\propto G_{disp} |X|, \end{aligned} \tag{2.9}$$

where  $G_{disp}$  is the displacement gain defined as the ratio of displacement amplitude along two axes. Measured power magnitudes finally estimate the magnitude of the displacement gain  $G_{disp}$  via

$$G = \frac{X_{output}}{X_{input}} = \frac{i_{m,output}}{i_{m,input}} = \frac{\sqrt{P_{output}}}{\sqrt{P_{input}}} \tag{2.10}$$

## 2.3.2 Single-Slotted-Disk Displacement Amplifiers

### Rectangular Slot

Fig. 2.12 plots the measured power of motional current from the input and output electrodes of the rectangle-slot displacement amplifying disk as seen in [6], for which the slots are sized as  $(R, w_b, w_s, l_s) = (32 \mu\text{m}, 10 \mu\text{m}, 5 \mu\text{m}, 15.5 \mu\text{m})$  by using the mixing testing set-up in Fig. 2.11. Here, the output port receives an additional power of 7.4 dB, corresponding to a displacement gain of  $2.34\times$  by (2.10). In this case, the rectangle slots measure an equivalent slot opening angle  $\theta_S \sim 43.35^\circ$  (i.e.,  $2 \times \tan^{-1}(7.75 \mu\text{m}/19.5 \mu\text{m})$ ) and plugging the values into (2.4) predicts a gain of  $2.28\times$ . Although the fitting model of (2.4) established previously was for arc-slot displacement amplifiers, it still predicts fairly well for the rectangular-slot disk within 3% off from the measured value.

### Arc Slot

Fig. 2.13 presents the SEM of a fabricated single disk with arc-shaped slots displacement amplifying resonator with dimensions of  $(R, w_b, w_s, \theta_s) = (32 \mu\text{m}, 8 \mu\text{m}, 2 \mu\text{m}, 47.5^\circ)$ . Note that the slots are intentionally finished with rounded edges to minimize slot-induced stress concentrated at corners. Fig. 2.14 plots the measured mixing power for the two axes, presenting a displacement gain of  $3.68\times$ . Note that for this particular device the input has two symmetrical electrodes while the output only has a single electrode and thus, a factor of 2

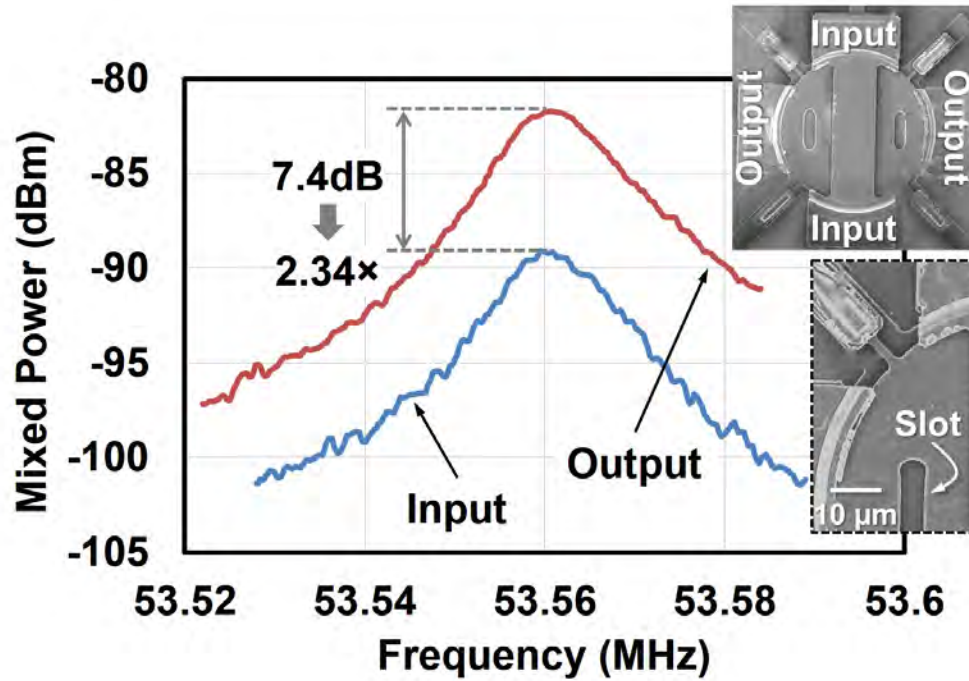


Figure 2.12: Measured mixed powers from input and output electrodes of a disk with rectangle slots as seen in [11] and the difference of two measured powers presents a displacement gain of  $2.34\times$  achieved by this single slotted disk structure.

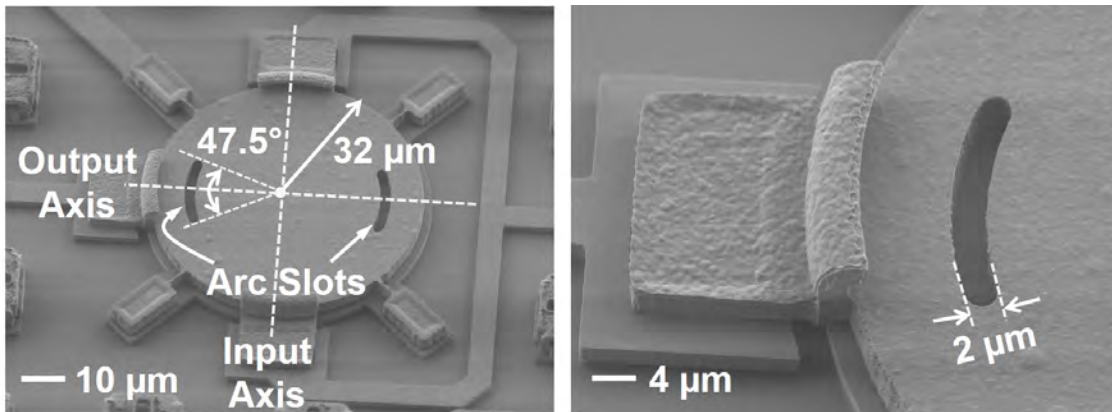


Figure 2.13: SEM images of overview and close view for a fabricated displacement amplifying disk with arc slots sized as  $(R, w_b, w_s, \theta_s) = (32 \mu\text{m}, 8 \mu\text{m}, 2 \mu\text{m}, 47.5^\circ)$ .

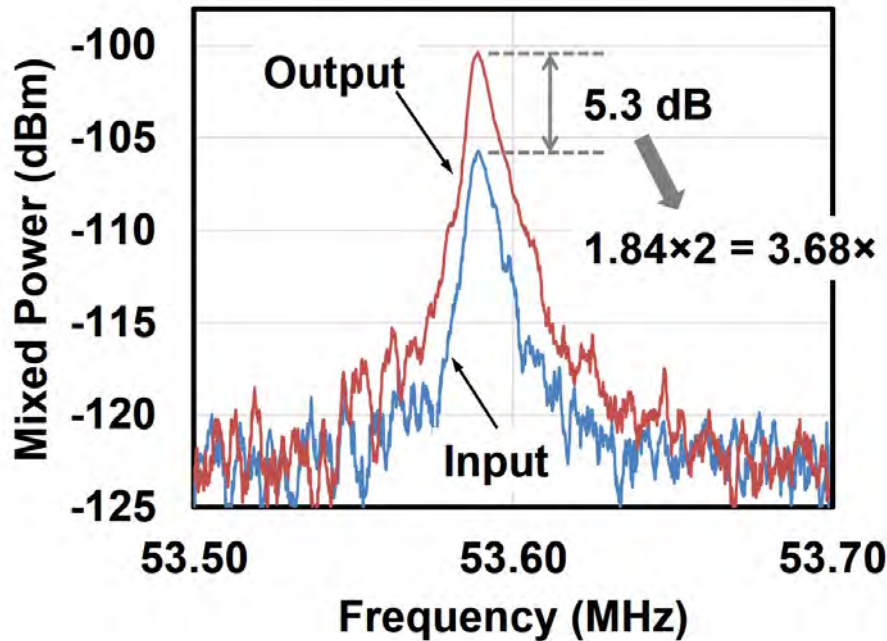


Figure 2.14: Measured mixed powers from input and output electrodes of the arc-slot disk in Fig. 2.13 and the difference of two measured powers presents a displacement gain of  $3.72\times$  achieved by this single slotted disk structure.

is required for the displacement gain calculation by (2.10). With given structural dimensions, the fitting model of (2.4) predicts a displacement gain of  $3.62\times$ , which corresponds a negligible  $<2\%$  discrepancy compared to the measured value.

### Elliptic Slot

Fig. 2.15 presents the SEM of an ellipse-slot version of displacement amplifying resonator with dimensions of  $(R, w_b, a_s, b_s) = (32\ \mu\text{m}, 8\ \mu\text{m}, 7\ \mu\text{m}, 1\ \mu\text{m})$ . Fig. 2.16 shows the measured output and input mixed frequency spectrums, where again the input has two times larger electrode area than the output and therefore even though the input axis has measured power slightly higher than that from the output axis, the disk with elliptic slot design still achieves a measured displacement gain of  $1.86\times$ . Similarly, plugging the dimensions including an equivalent slot angle  $\theta_S \sim 33.86^\circ$  (i.e.,  $2 \times \tan^{-1}(7\ \mu\text{m}/23\ \mu\text{m})$ ) in the model of (2.4) gives an estimation of displacement gain of  $1.89\times$ ,  $<2\%$  higher than the measured value.

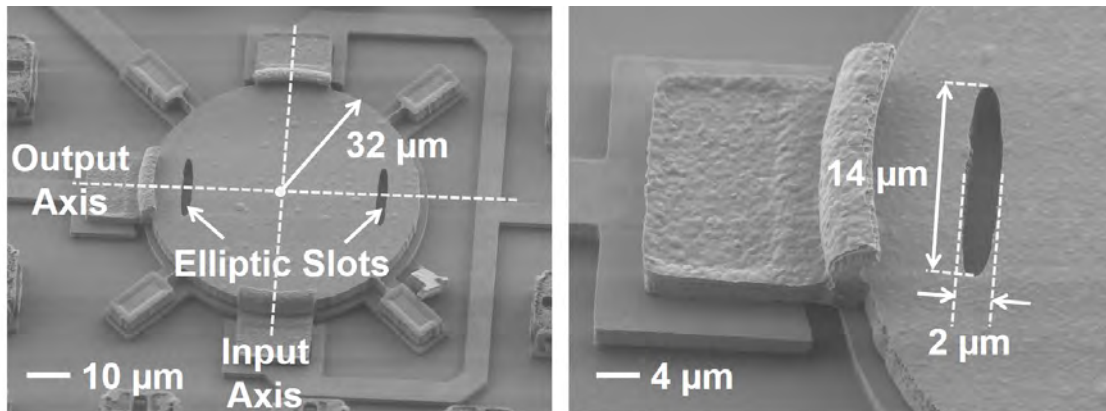


Figure 2.15: SEM images of overview and close view for a fabricated displacement amplifying disk with elliptic slots sized as  $(R, w_b, a_s, b_s) = (32 \mu\text{m}, 8 \mu\text{m}, 7 \mu\text{m}, 1 \mu\text{m})$ .

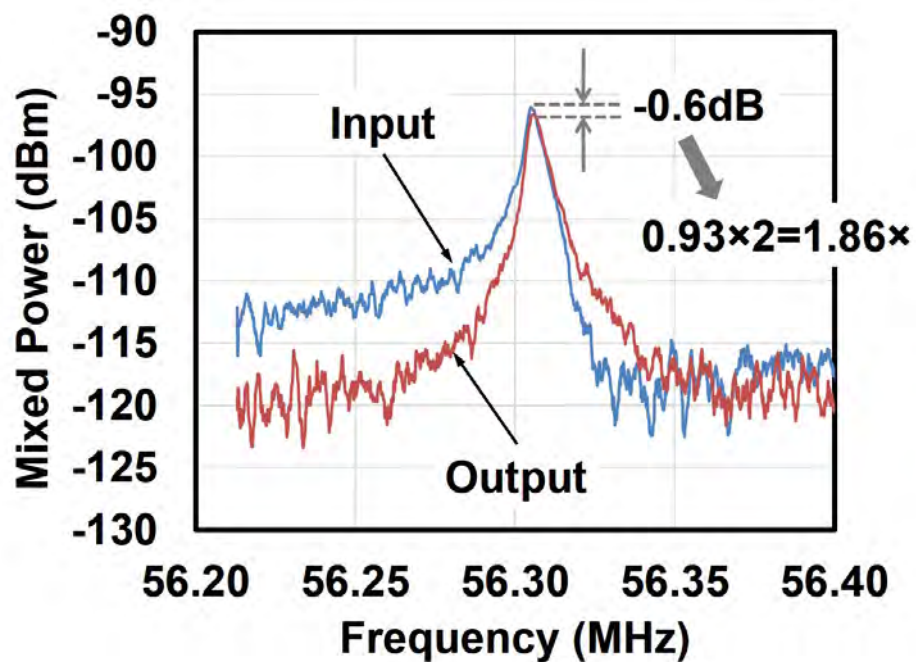


Figure 2.16: Measured mixed powers from input and output electrodes of the elliptic slot disk in Fig. 2.15 and the difference of two measured powers represents a displacement gain of  $1.86\times$  achieved by this single slotted disk structure.

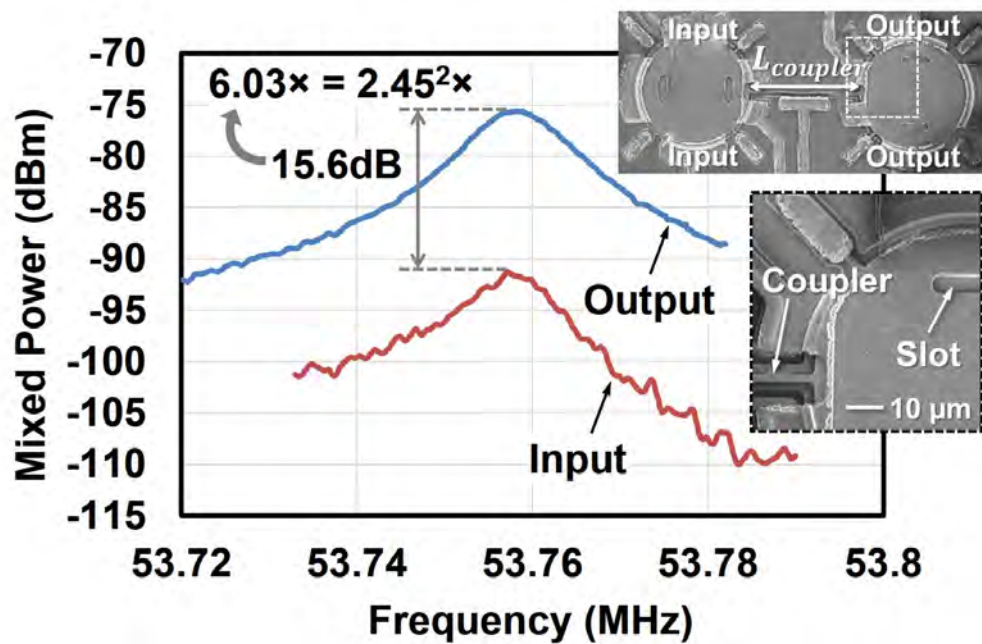


Figure 2.17: Measured mixed powers from input and output electrodes of a disk with rect-angle slots as seen in [6] and the difference of two measured powers presents an overall displacement gain of  $6.09\times$  and  $2.45\times$  achieved by each of the individual slotted-disks.

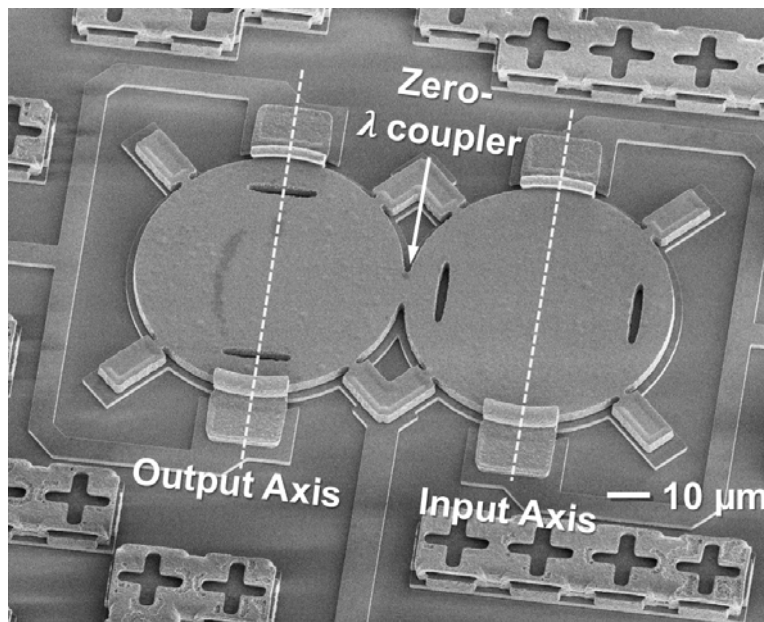


Figure 2.18: SEM of a two-stage ellipse-slot disk array with a zero-wavelength coupling beam.

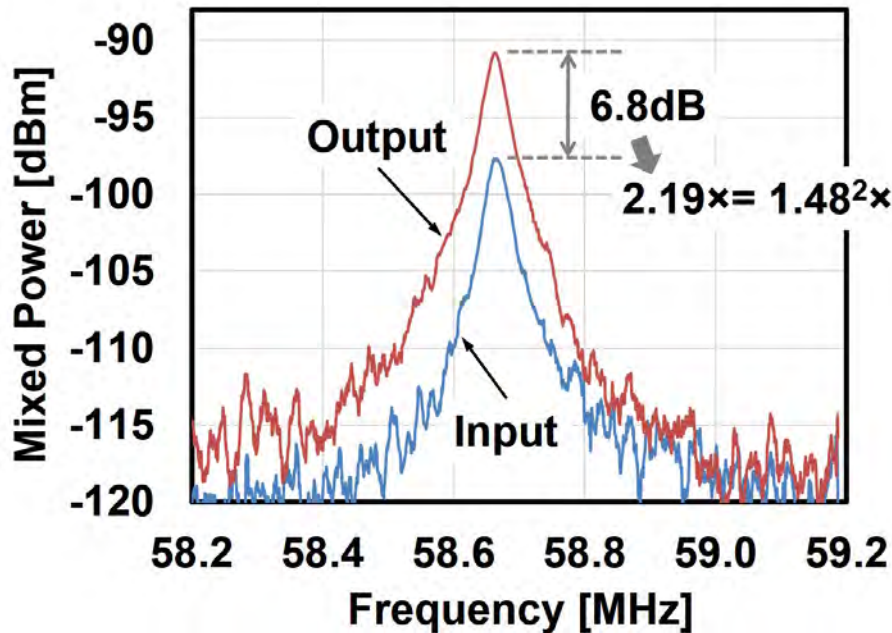


Figure 2.19: Measured mixed powers from input and output electrodes of the two-stage array in Fig. 2.18 composed by two single ellipse-shaped slotted-disks and a half-wavelength coupling beam. The difference of two measured powers represents an overall displacement gain of  $2.19\times$  achieved by this two-stage array ( $1.48\times$  for each of the disks).

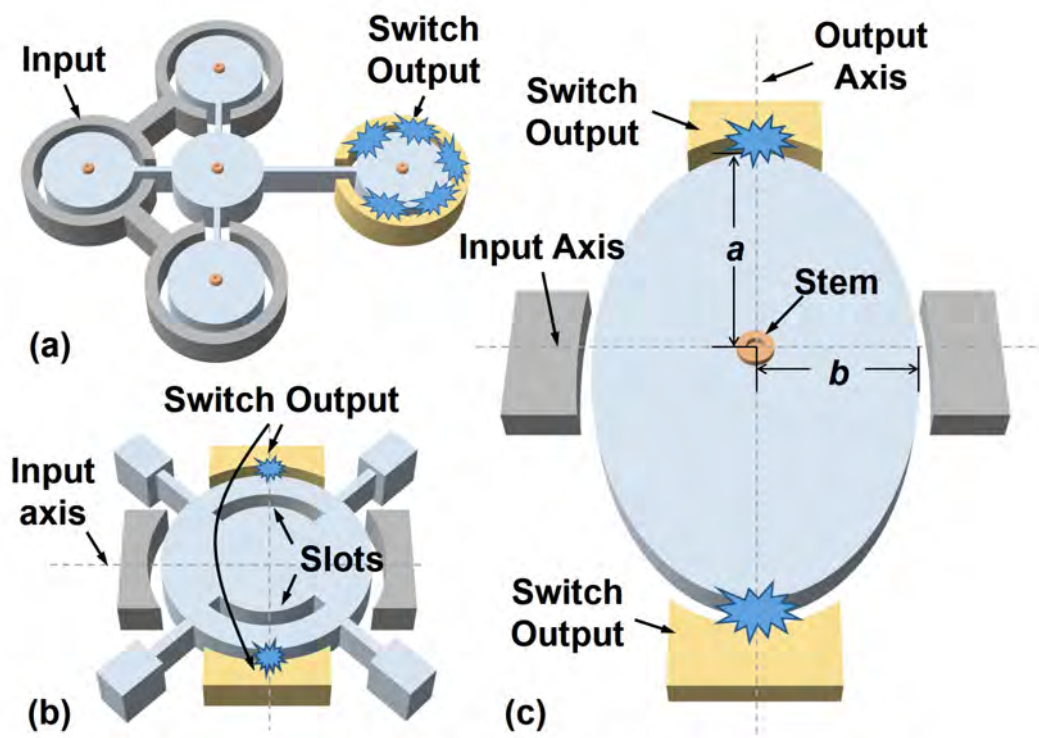
### 2.3.3 Slotted-Disk Array

#### Rectangular-Slot Disk Arrays

To verify the idea of increasing the displacement gain by arraying multiple individual slotted-disks, Fig. 2.17 plots the measured power from the input and output ports of a two-stage displacement amplifiers with rectangle slots, where two slotted disks identical to the device of Fig. 2.12 are coupled by a half-wavelength ( $L_{coupler} = \lambda/2$ ) coupling beam [6]. Here, a displacement gain of  $2.45\times$  by each of the single slotted-disk yields an overall  $6.03\times$  ( $2.45 \times 2.45$ ) displacement gain.

#### Elliptic-Slot Disk Arrays

Fig. 2.18 presents the SEMs of a two-stage displacement amplifier array consisted of a zero-wavelength coupler and two elliptic-slot disks sized as  $(R, w_b, a_s, b_s) = (32 \mu\text{m}, 8 \mu\text{m}, 7 \mu\text{m}, 1 \mu\text{m})$ . Fig. 2.19 plots the measured mixing frequency responses, identifying an overall displacement gain of  $2.19\times$  achieved by two stages (i.e., implying that  $1.48\times$  by each of the individual slotted disks). Compared to the single slotted-disk as shown in Fig: 2.16, the two-stage version of displacement amplifier measures a lower displacement gain and it is



Type	Disp. Gain	Freq.	$Q$
(a) Array	2	153 MHz	$\sim 10,500$
(b) Slotted-Disk	1.86	57 MHz	$\sim 5,000$
(c) Elliptic-Disk	2.04	89 MHz	$\sim 101,600$

Figure 2.20: Descriptions of (a) array; (b) slotted-disk; and (c) elliptic-disk displacement amplifiers, along with a table comparing their performance, where the elliptic-disk displacement amplifier clearly presents the highest  $Q$ .

mainly caused by the imperfection of photolithography that in fact yielded a smaller  $\theta_s$ .

## 2.4 Elliptic-Disk Displacement Amplifiers

Since (as shown in [8]) the sensitivity of a resowtch-embedded receiver like that of Fig. 1.4 is proportional to frequency and inversely proportional to the  $Q$  of its resowtch, the  $Q$  of 10,500 achieved in [6] must rise to at least 100,000 if reasonable sensitivity is to be maintained at frequencies in the 80-100 MHz range. In addition, displacement amplification is desirable to not only prevent input impacting while promoting output impacting [5], but also to improve impedance matching and in some cases further improve sensitivity. Unfortunately,

previously demonstrated displacement amplifying resoswitches in this frequency range suffer  $Q$  degradation, negating any sensitivity advantages. In particular, energy-balancing array-based resoswitches post  $Q$ 's of only 10,500 [6], while slotted-disk ones on the order of only 5,000 [11], the latter far lower than the  $>100,000$  normally exhibited by their base resonator designs. In effect, these devices sacrifice  $Q$  to attain displacement gain.

Pursuant to breaking the apparent  $Q$  versus displacement gain trade-off, an 89-MHz micromechanical elliptic-disk displacement amplifying resoswitch preserves  $Q$  by 1) generating gain-inducing axial stiffness differences from ellipse geometry rather than previous  $Q$ -degrading slots; and 2) using an elliptic resonance strain field that better negates energy loss at a center anchor, allowing for  $Q$ 's in some cases even higher than circular disks. These strategies together permit a displacement gain of 2.04 with a  $Q$  of 101,600 more than  $9\times$  higher than that of previous array-based [6] and slotted-disk [11][14] approaches. Measurements reveal that the  $Q$ 's of elliptic disks vary with ellipse aspect ratio ( $AR$ ) defined as the major axis length  $a$  to the minor axis  $b$ , shown in Fig. 2.20(c). Specifically, a 95-MHz ellipse with  $AR = 1.2$  ( $a/b = 21.91\mu\text{m}/18.26\mu\text{m}$ ) exhibits the lowest  $Q$ , while one with  $AR = 1.6$  and beyond restores the  $Q$  to equal or sometimes exceed that of a circular disk with  $AR = 1$ .

### 2.4.1 Advantages over Previous Resoswitches

Fig. 2.20 compares the present elliptic design in (c) with previously-demonstrated displacement amplifying methods based on (a) energy-balanced coupling of asymmetric disk array-composites [6]; and (b) stiffness engineering via strategic geometrical cuts [11][14].

The disk array resoswitch of Fig. 2.20(a) generates displacement gain by coupling an input disk array-composite to an output one (using a single disk in Fig. 2.20(a)) via a quarter-wavelength beam that effectively balances the energy on both sides. Since the stiffness of the 4-disk half-wavelength-coupled input array ( $n_{in} = 4$ ) in Fig. 2.20(a) is four times larger than that of the single output disk ( $n_{out} = 1$ ), the output disk must move more than the input ones to possess equal energy specifically,  $\sqrt{n_{in}/n_{out}} = 2\times$  more—thereby providing displacement gain. So far, the only demonstrated such mechanical circuit of [6] utilized radial mode disk resonators, which constrained its  $Q$  to only 10,500. Based on [13], a wine-glass disk based version should do much better, but this has yet to be demonstrated.

On the other hand, the slotted-disk of Fig. 2.20(b) generates displacement gain by cutting slots along one axis (i.e., the output axis) of a wine glass disk thereby lowering the stiffness in that direction, hence raising its displacement relative to that along the orthogonal input axis. The result: displacement amplification in a single mechanical structure. Unfortunately, the slots induce higher energy losses at the slot-induced stressed corners, which degrade  $Q$  to  $\sim 10,000$ , which is many times smaller than commonly exhibited by non-slotted wine-glass disks.

The elliptic resoswitch of Fig. 2.20(c) basically engineers stiffness in a similar manner as the device of Fig. 2.20(b), except without the use of slots. Instead, it effects differences in orthogonal axial stiffness via geometric ratioing of the ellipse aspect ratio  $AR$  ( $a/b$ ), where the smaller stiffness along its longer output axis yields a larger displacement than that along

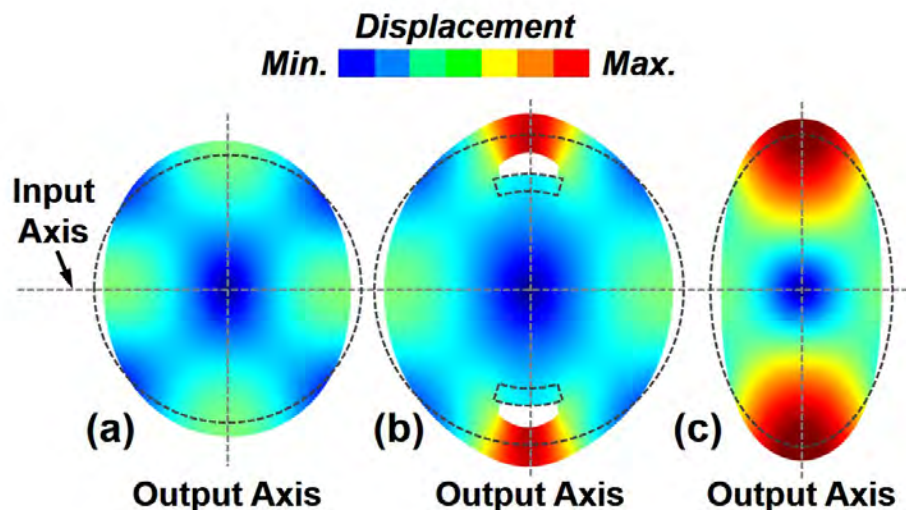


Figure 2.21: FEM simulated mode shapes comparing displacements along input and output axes for (a) a conventional wine-glass disk resonator; (b) a slotted-disk displacement amplifier; and (c) an elliptic displacement-amplifying disk.

$a, b$ ( $\mu\text{m}^2$ )	$ab = 400$					
Thickness $h$ ( $\mu\text{m}$ )	3					
Stem Radius ( $\mu\text{m}$ )	1					
Stem Height ( $\mu\text{m}$ )	0.7					
Aspect Ratio $AR$	1	1.2	1.4	1.6	1.8	2
Frequency (MHz)	96.49	95.36	92.68	89.31	85.79	82.40

Table 2.1: Summary of Elliptic Disk Designs

its shorter, hence stiffer, input axis. Unlike the slotted disk, the elliptic disk avoids the energy-consuming stress corners of slots, allowing it to retain high  $Q$ . Fig. 2.21 compares the FEM-simulated mode shapes of the new design in (c) with those of (a) a conventional wine-glass disk and (b) the slotted disk, showing no displacement gain in (a), but (by red coloring) ample output displacement gain for both the slotted and the elliptic disks.

## 2.4.2 Displacement Gain Modeling

Unlike a slotted-disk, for which displacement gain depends on the size, location, as well as shape of its slots, making modeling very complex; the elliptic disk presents a much simpler structure, for which displacement gain depends only on its geometric aspect ratio  $AR$  and the Poisson ratio  $\nu$  of its structural material. A semi-empirical model based on FEA that

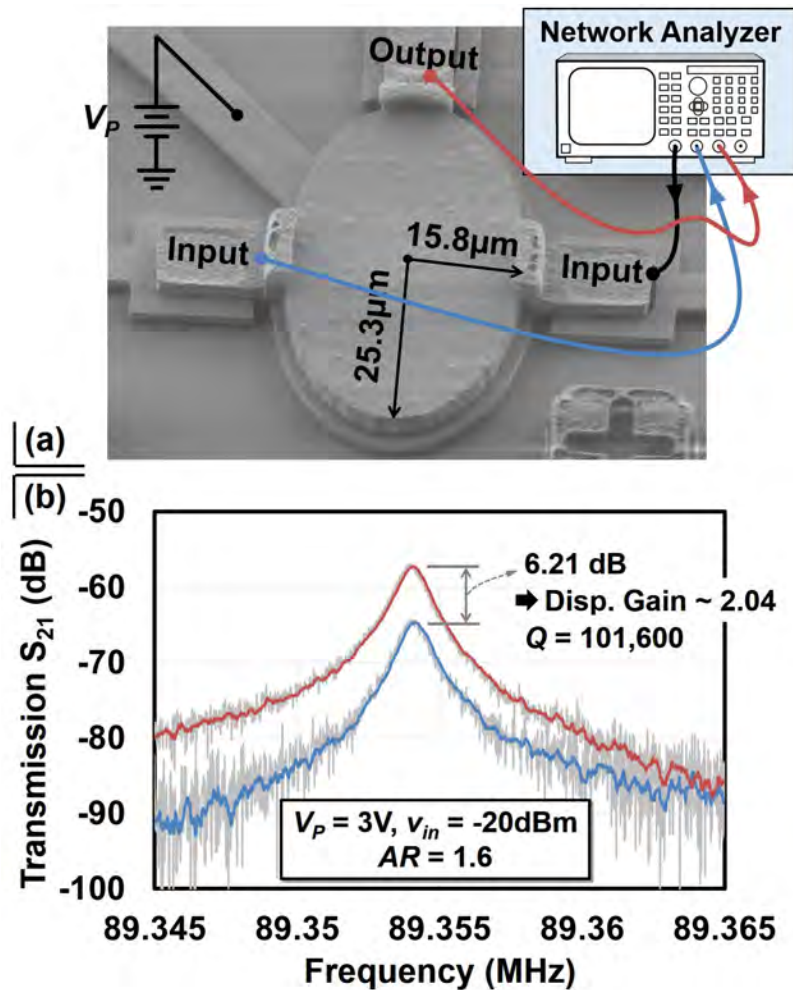


Figure 2.22: (a) SEM of a fabricated polysilicon elliptic disk with an  $AR = 1.6$ . Measurement set-up for extracting displacement gain is indicated. (b) Measured transmissions obtained via the device and set-up in (a), exhibiting a displacement gain  $\sim 2.04$  and a measured  $Q$  over 100,000.

predicts the displacement gain as a function of these two parameters takes the form

$$G_{disp} = AR^{-4.73\nu+2.626} \quad (2.11)$$

The basic form of (2.11) derives from knowledge that a purely circular disk ( $AR = 1$ ) has an orthogonal axis displacement gain of one regardless of the value of Poisson ratio. Note that the displacement gain modeling provided here is merely for a quick estimation of displacement gain. A pure analytical method, e.g., the Ritz method, would enable a more universal model. Work towards this continues.

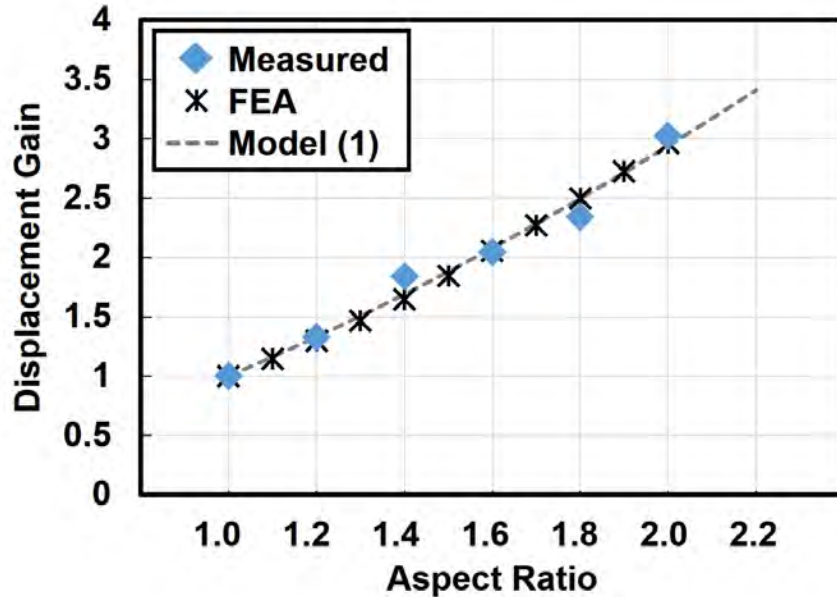


Figure 2.23: Comparison of displacement gains as a function of aspect ratio obtained from measurement, FEA, and prediction using (2.11).

### 2.4.3 Experimental Results

Elliptic displacement amplifiers were fabricated using a polysilicon surface micromachining process similar to that of [13]. Table 2.1 summarizes the designs, which span  $AR$  values from 1 to 2. Note that all elliptic disk designs have a fixed ellipse area of  $400\pi \mu\text{m}^2$  (i.e.,  $\pi ab$ ) and their resultant resonance frequencies span from 96.5 MHz for  $AR = 1$  to 82.4 MHz for  $AR = 2$ . Fig. 2.22(a) presents the SEM of one such fabricated elliptic device with  $AR = 1.6$ .

Devices like this were measured under  $10^{-5}$  Torr vacuum provided by a turbo pump using the indicated circuit, where one input electrode is connected to port 1, and the other input electrode and the output electrode are connected to port 2 and 3, respectively. Fig. 2.22(b) presents measured frequency transmissions between two input ports (S21) (blue) and between the input and output ports (S31) (red) of an elliptic disk with  $AR = 1.6$ , where the transmitted power difference between the two peaks indicates a displacement gain of 2.04.

Fig. 2.23 plots measured displacement gain as a function of aspect ratio  $AR$  varying from 1 (a purely circular disk) to 2 alongside predictions by FEA and Eq. (2.11) (with  $\nu = 0.226$ ), showing good agreement. Here, a single elliptic disk with  $AR = 2$  achieves a displacement gain up to  $\sim 3$ .

Fig. 2.24 plots the frequency shift versus electrical-stiffness tuning voltage applied at the input electrode ( $V_{B1}$ , blue curve) and the output electrode ( $V_{B2}$ , red curve), where the larger frequency shift of the latter confirms lower stiffness along the output axis. Fig. 2.25 presents measured frequency responses taken at the output electrode of an 89-MHz elliptic resoswitch as a function of increasing input voltage, showing the expected peak flattening as the elliptic

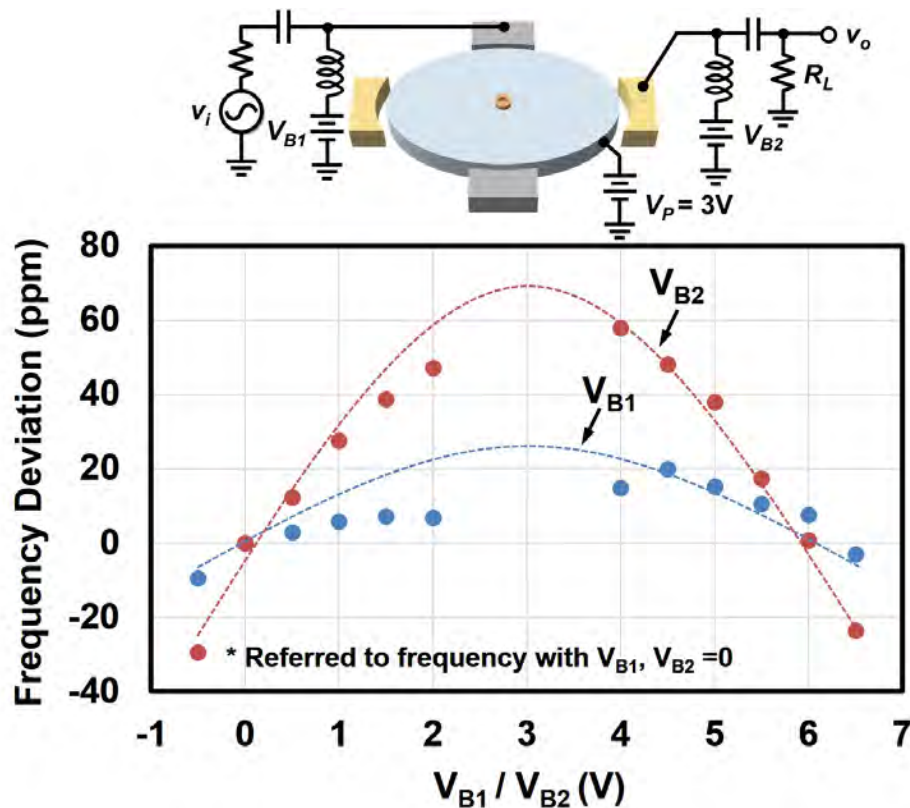


Figure 2.24: Measured frequency shifts with tuning voltages applied on input ( $V_{B1}$ ) versus on output ( $V_{B2}$ ), where the lower mechanical stiffness along the output axis yields a larger tuning range.

disk impacts the output electrode.

Fig. 2.26 plots measured  $Q$  as a function of  $AR$  for several elliptic disks spanning 82.4-96.5 MHz on three different dies, indicating similar  $Q$  variations regardless of their  $Q$  magnitudes. Interestingly, when  $AR = 1.2$   $Q$  drops consistently from that of a conventional circular wine glass disk ( $AR = 1$ ), but increases afterwards as the  $AR$  rises. Possible reasons that govern the  $Q$  fluctuations as a function of  $AR$  will be discussed in Chapter 4.6

## 2.5 Conclusions

This chapter demonstrated two designs of directional stiffness engineering to attain displacement gain necessary for preventing the resoswitch input port from impacting. Particularly, one technique strategically introduces slots into micromechanical disk structures that yield a larger displacement amplitude along the output axis than along the input axis but with the expense of  $Q$ . A better approach for high- $Q$  resoswitch is to use geometry ratioing rather

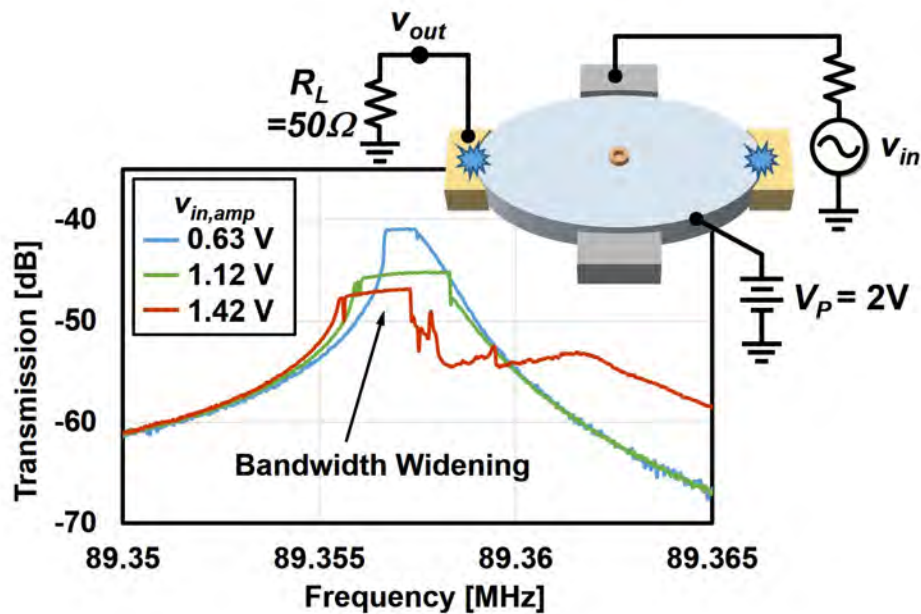


Figure 2.25: Measured input to output frequency response spectra as a function of input drive voltage, showing flattening and bandwidth widening of the response at the onset of impacting.

than  $Q$ -degrading slots. A single elliptical disk with an aspect ratio  $AR$  of 1.6 yielded a displacement gain of 2.04 with a measured  $Q > 100,000$  at 89 MHz.

By engineering stiffnesses via dimensional ratioing rather than slots, the demonstrated elliptic disks provide an alternative method to achieve displacement amplifying resoswitches that retain high resonator  $Q$ 's exceeding 100,000 that should improve the sensitivities of resoswitch-based zero-quiescent power radios at VHF. In fact, the almost  $10\times$  improvement in  $Q$  over previous disk array and slotted disk approaches should yield sensitivity reductions (i.e., improvements) on the order of 10dB. Of course, this work presented only polysilicon elliptic resoswitches with high contact resistances that preclude use in many desired applications. To be useful in an actual zero-quiescent power radio, next generation devices should employ metals or other more conductive materials at their contact interfaces. Methods for doing so without sacrificing  $Q$  are currently under study.

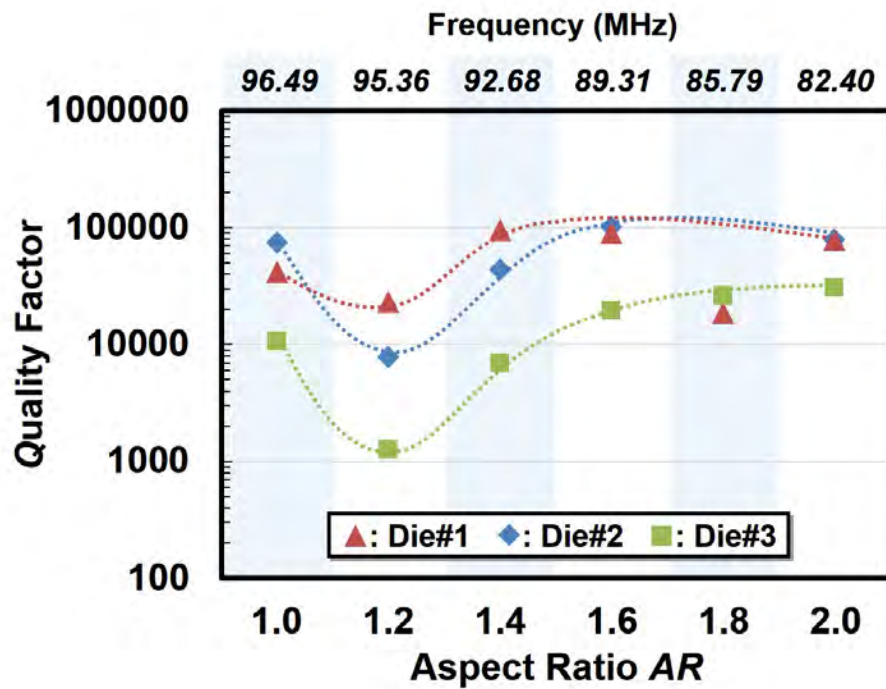


Figure 2.26: Measured  $Q$  versus aspect ratio from three dies. Here,  $AR = 1$  corresponds to a circular disk, while higher  $AR$ 's indicate ellipses.  $AR = 1.2$  presents the lowest  $Q$  while  $AR > 1.6$  seems to be able to recover  $Q$  back to that of a circular disk.

## Chapter 3

# Metal Micromechanical Frequency-Selective Power Amplifiers

The displacement-amplifying resoswitches described in Chapter 2 have been plagued by high contact and series resistances due to the use of polysilicon. This chapter first discusses a fabrication process used to achieve metal aluminum displacement-amplifying slotted-disk resoswitches that greatly reduces the contact and series resistances. Next, a filter-power amplifier circuit with the Al resoswitch embedded will be demonstrated with a 13.8 dB of power gain within a channel-selecting bandwidth.

### 3.1 Structure and Operation

Fig. 3.1 illustrates the architecture of a channel-selecting communication receiver front-end that utilizes a displacement-amplifying resoswitch embedded filter-amplifier to achieve signal filtering and power amplification using a FSK modulated signal as an example. The displacement-amplifying resoswitch used in the filter-amplifier essentially comprises a slotted disk identical to that discussed in Chapter 2. To operate the device as a filter-power amplifier, a supply voltage is tied to the conductive structure, and an input comprising a combined dc bias  $V_{P,in}$  and ac voltage  $v_{in}$ , similar to that used in the switched PA, are applied to the input electrodes. As seen in Fig. 3.2, when the frequency of  $v_{in}$  is within a small bandwidth around the resonance frequency with a magnitude larger than a prescribed threshold, the amplitude of vibration is then large enough to close the power supply  $V_{P,disk}$  to the output (periodically), thereby delivering power to the output. The resoswitch itself responds only over a small frequency bandwidth around its own resonance and rejects all other frequencies. In doing so, the device behaves as a very small percent bandwidth filter, i.e., a channel select filter, and it does its filtering before its amplification. In effect, the resoswitch realizes RF channel-selection and amplification, i.e., a filter-LNA function, in a single component, so stands to greatly alleviate the design complexity of low-power RF receiver front-ends.

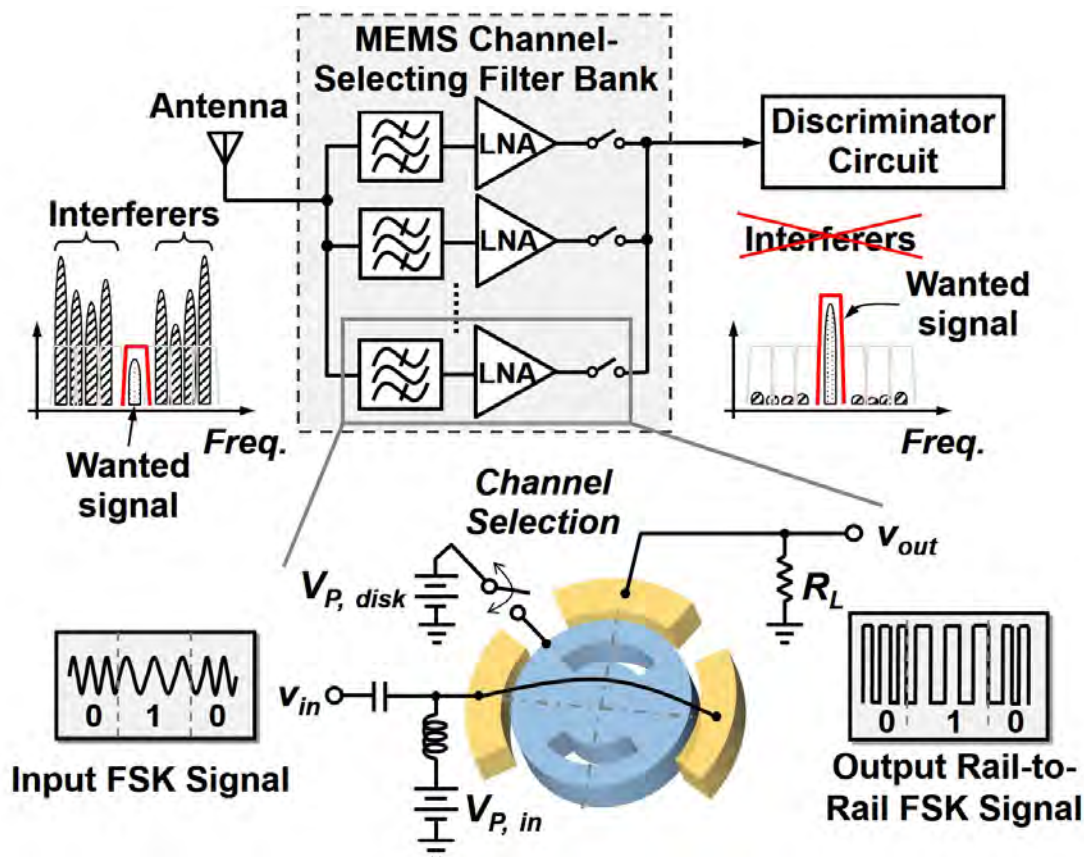


Figure 3.1: Schematic of the displacement-amplifying Al resoswitch-based filter-PA used in a FSK-based RF receiver chain, showing a highly nonlinear amplification while all other out-of-channel signals have been eliminated/filtered.

Obviously, the input-to-output transfer function of this device is quite nonlinear as a constant voltage value  $V_{P,disk}$  is delivered to the output once the switch is closed. Normally this would be problematic, since it would allow blockers to generate spurious signals that could interfere with the desired signal. But this is of little consequence now that the filtering function of the resoswitch has removed all blockers, i.e., there are no blockers to generate intermodulation distortion or any other spurious signals. Furthermore, no dc current flows when the resoswitch is not resonating. Thus, this device consumes no quiescent power when in standby! With this device, the design of an FSK channel-select receiver with zero quiescent power might be as simple as that depicted in Fig. 3.1. The trick, of course, will be in how small the threshold voltage amplitude that instigates periodic switching can be made, as this governs sensitivity.

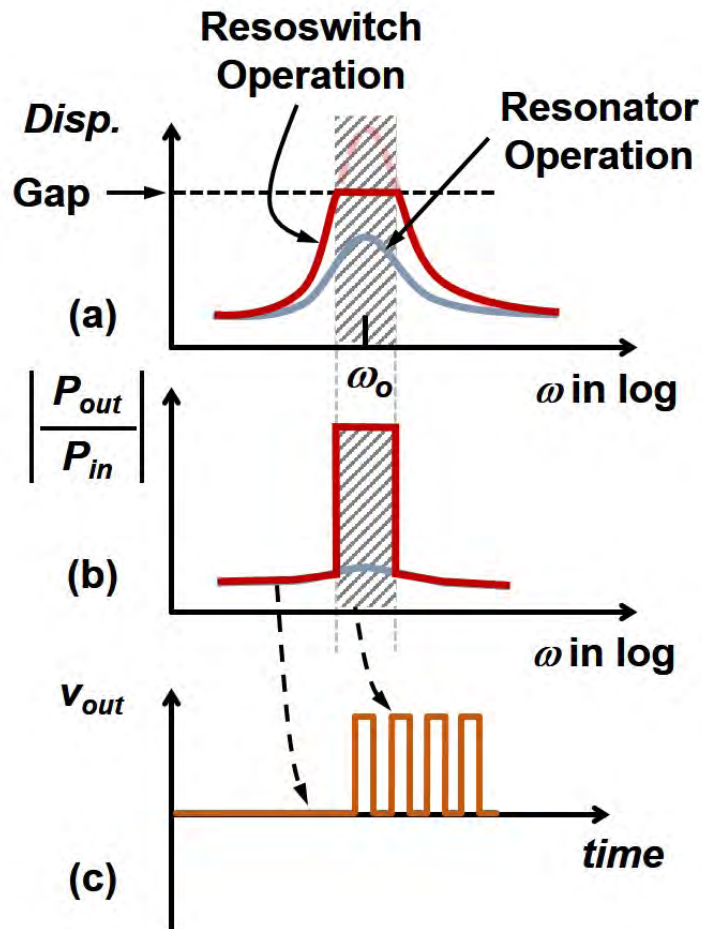


Figure 3.2: Illustrations of displacement amplifier operation that as the displacement of the vibrating structure is much higher and conventional disks and limited by the gap as of (a), the disk would close the gap and deliver power from the bias applied on the structure to the output around a small bandwidth of resonance frequency as of (b). In this switching bandwidth, a time domain waveform can be then measured, with a much higher amplitude than the capacitively vibrating ac signals as shown in (c).

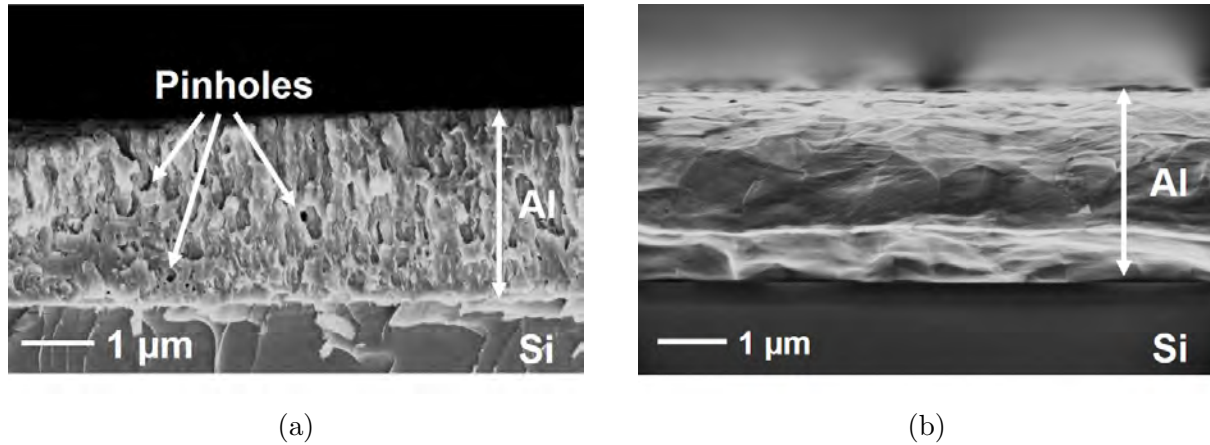


Figure 3.3: Cross-section of Al films deposited in (a) a contaminated conventional DC magnetron sputtering system and in (b) a clean S-gun sputtering system with an optimized recipe.

## 3.2 Fabrication Process

In order to achieve robust micromechanical vibrating devices, especially for those with sub-100 nm lateral gap spacings [13], a sophisticated etch process is key to achieve a smooth and straight structural sidewall that avoids any sharp points which otherwise may create short circuit paths between the structure and electrodes and cause pull-in failures. An inductively coupled plasma (ICP) based etcher was utilized to define the metal aluminum structure of the displacement-amplifying slotted disk, where a RF power is used to generate ions and reactive chemical species and another RF bias directs ions onto the substrates for more anisotropic etch profiles. This section first describes the Al deposition process used to achieve a void-free Al film to begin with. Next discusses effects of various process parameters on the resultant sidewall profiles in the TCP etch, namely bias power, chemical gas amounts/ratios, and process pressures. A vertical smooth structural sidewall was obtained based on the characterization. The Al fabrication processes finally achieved a one-mask folded-beam comb-driven micromechanical resonator and a displacement-amplifying slotted disk resonant switch.

### 3.2.1 Sputtering Deposition of Al Structural Material

Considering the desirable Al structure thickness (i.e., 2-3  $\mu\text{m}$ ) and availability of metal deposition tools in the laboratory, sputtering is used due to its fast deposition rate (i.e., less heat is being generated during deposition which otherwise would cause a milky Al film), and better film quality. To illustrate how the sputtering chamber clearness effects the sputtered film, Fig. 3.3 compares cleaved cross-sections of (a) a conventional DC magnetron sputtering system that contains three other co-existed metal targets, and (b) a S-gun sputtering system

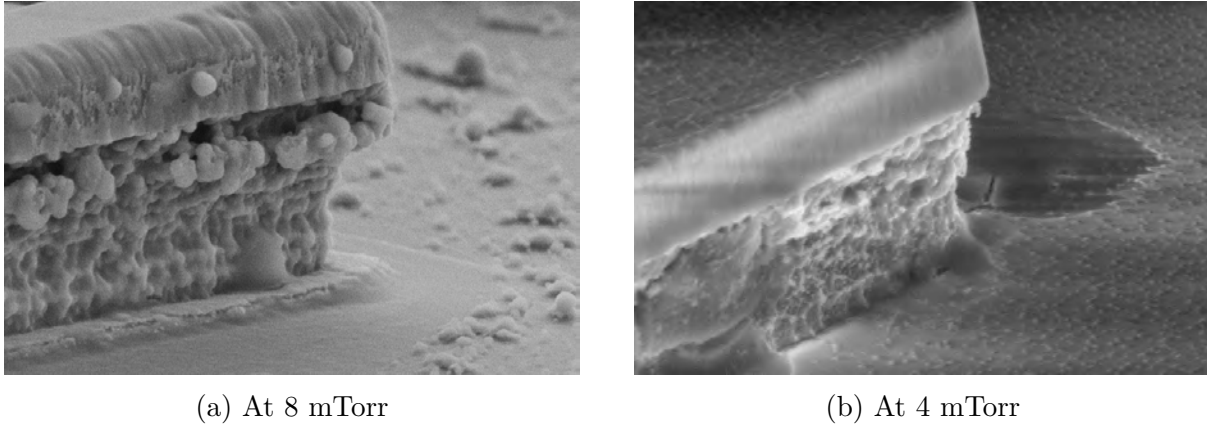


Figure 3.4: Cross-section of Al film etched in varying process pressures (RF/Bias Power = 800/100 W,  $\text{Cl}_2/\text{BCl}_3 = 90/45$  sccm).

(i.e., Endeavor ATTM, OEM Group). Obviously, the film obtained from the conventional chamber is not smooth and filled with voids resulted by contaminants as well as high substrate temperatures during deposition. The issues, however, are elevated in the S-gun sputtering tool, where with a base pressure  $\leq 5 \times 10^{-8}$  torr and a 0.5 mTorr process pressure (i.e., regulated by flowing Ar gas at 6 sccm), a 5-kW DC power sputters Al at a rate as quick as 333.3 nm/min, and a smooth, free-of-pinholes Al film is achieved. Splitting the total 540 seconds sputtering time for a 3- $\mu\text{m}$  Al into three runs with a 60-second rest between each run, much shorter deposition time and therefore much less heat generated compared to that in the conventional tool, together with a clean chamber condition, are key to realize such a high quality film with a measured compressive stress of  $< 100$  MPa.

### 3.2.2 Etching of Al Structural Material

To optimize the etching process to yield a smooth and vertical Al structural sidewall, test wafers that are first sputtered with a 3- $\mu\text{m}$  Al (using the S-gun system described above) followed by a 1.5- $\mu\text{m}$   $\text{SiO}_2$  (low-temperature LPCVD at 400°C) served as the etching hard mask are used to characterize various etching parameters, including process pressure, reactive gas ratio, and bias power. After undergoing photolithography and  $\text{SiO}_2$  hard mask etching, the test wafers that contain the thin film stack identical to the structural stack of actual disk devices are then ready for the Al etching characterization.

#### Process Pressure

Fig. 3.4 compares the Al structural sidewall etched under a process pressure of 8 mTorr in (a) (i.e., standard etching recipe of this specific etcher, with gases flow of  $\text{Cl}_2/\text{BCl}_3 = 90/45$  sccm) and a lower process pressure at 4 mTorr in (b). Here, it can be observed that the higher process pressure of 8 mTorr led to a rougher sidewall profile due to excessive ion scattering. In

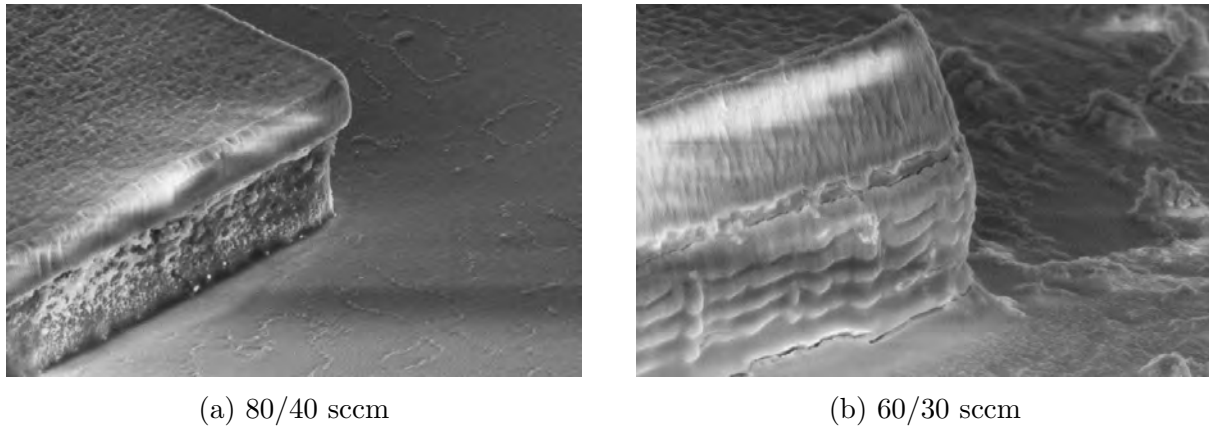


Figure 3.5: Cross-section of Al film etched with varying  $\text{Cl}_2/\text{BCl}_3$  ratios (RF/Bias Power = 800/100 W, process pressure = 4 mTorr)

general, a TCP etcher allows control of the process pressure independently from the plasma generation, whereby a relatively low process pressure can be applied reducing ion scattering to achieve more anisotropic etching.

### $\text{Cl}_2/\text{BCl}_3$ Flow Ratio

In a typical Al dry etch process,  $\text{Cl}_2$  and  $\text{BCl}_3$  are the two commonly used reactive gases as Al can form volatile product with Al. The purpose of  $\text{Cl}_2$  is used as the Al main etchant while  $\text{BCl}_3$  is mainly for etching/breaking through the native oxide and producing by-product to protect sidewall to enhance anisotropy. Fig. 3.5 compare the results of varying  $\text{Cl}_2/\text{BCl}_3$  gas flow ratio, 80/40 and 60/30 sccm, while keeping the  $\text{Cl}_2/\text{BCl}_3$  ratio at 2. The original 90/45 combination in Fig. 3.4 obviously creates too many reactive ions and causes a rough/undercut etching sidewall, and it gradually becomes smoother as the total gas flow reduces while keeping the same gas ratio (i.e.,  $\text{Cl}_2/\text{BCl}_3 = 2$ ). However, scalloped etching profiles are still observed for these etch conditions due to cycled etching. In fact, multiple cycles of etching are necessary in etching such thick metal layers to prevent excessive heat generated and to help remove corrosive etch byproduct such as  $\text{AlCl}_3$  during the initial chamber pumping down of each etching cycle that would otherwise cause under-cut etching.

To reduce the scalloping effect, given  $\text{BCl}_3$  assists compound generation for protecting the sidewall, the gas mixture ratio of  $\text{Cl}_2/\text{BCl}_3$  is then adjusted with increased  $\text{BCl}_3$  concentration. Fig. 3.6 (a) presents the result of using a higher  $\text{BCl}_3$  concentration of  $\text{Cl}_2/\text{BCl}_3 = 50/40$  sccm (i.e., a total flow of 90 sccm), yielding a less-scalloping profile with a considerable amount of undercut. This at least verifies the addition of  $\text{BCl}_3$  does help improve the smoothness of vertical sidewalls. Another trial with  $\text{Cl}_2/\text{BCl}_3 = 35/25$  sccm shown in Fig. 3.6 (b), a total gas flow of 60 sccm, then demonstrates a straight and smooth sidewall with much less undercut. Of course, this achievement requires a trade-off with etching selectivity (over the capped  $\text{SiO}_2$  hard mask) as a higher  $\text{BCl}_3$  make-up etches the

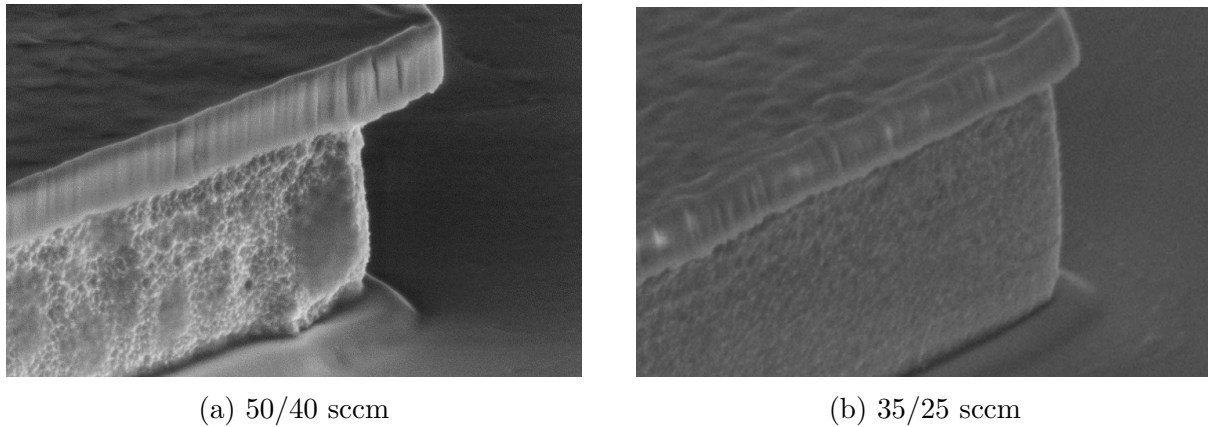


Figure 3.6: Cross-section of Al film etched with varying  $\text{Cl}_2/\text{BCl}_3$  ratio (Cont'd) (RF/Bias Power = 800/100 W, process pressure = 4 mTorr).

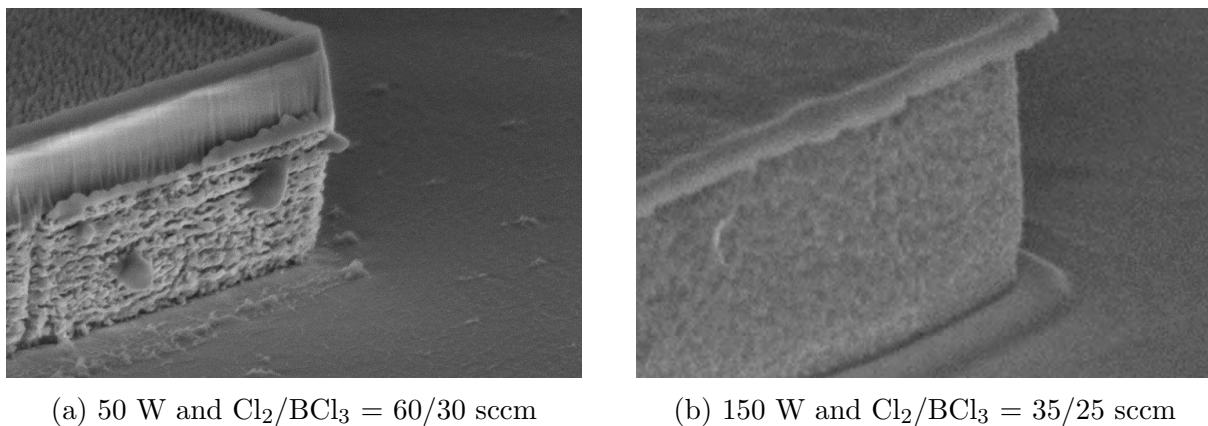


Figure 3.7: Cross-section of Al film etched with varying RF bias (RF power = 800 W, process pressure = 4 mTorr).

oxide faster. Fortunately, this compromise of selectivity can simply be accommodated by depositing a thicker oxide hard mask from the beginning.

### Bias Power

As mentioned, the bias power used to accelerate reactive ions can be controlled separately from the RF power in a TCP system, and generally a high bias power Fig. 3.7 (a) plots a case with  $\text{Cl}_2/\text{BCl}_3 = 60/30$  sccm at a lower bias power of 50 W to be compared with the previous 100-W bias power in Fig. 3.5 (b), where the etching process in the lower bias power of 50 W is dominated by chemical reaction of neutral reactive species and therefore leads to a non-uniform, scalloping sidewall.

Although a high bias power is desirable for anisotropic etching, the resultant non-deal

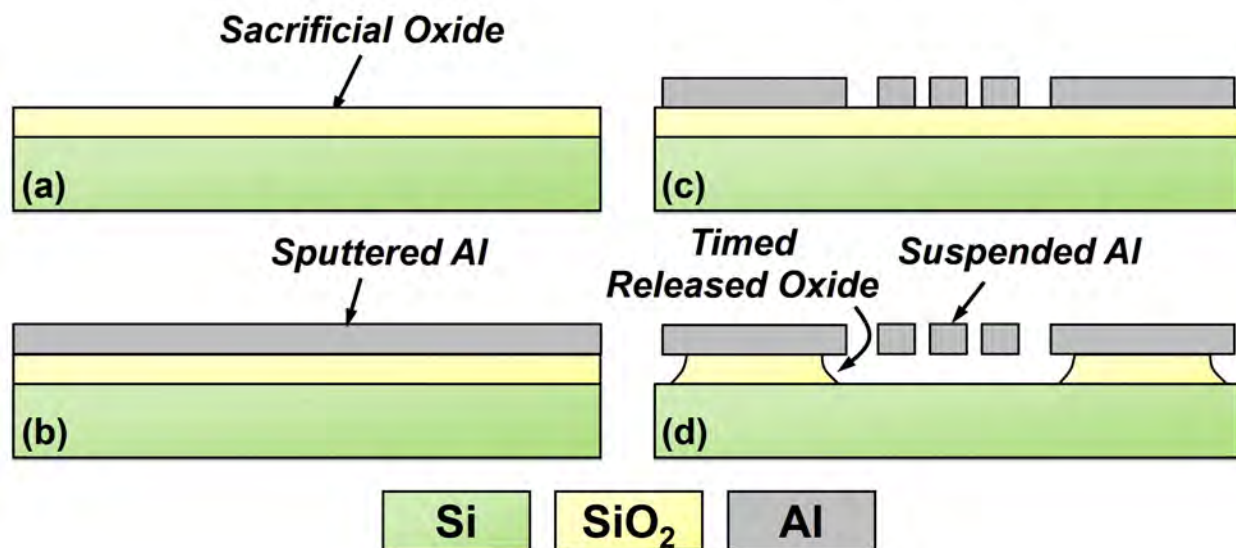


Figure 3.8: One-mask fabrication process flow used to achieve the folded-beam comb-driven micromechanical Al resonator, where the Si substrate was first doped and deposited a 2- $\mu\text{m}$  sacrificial oxide as in (a), followed by a 2- $\mu\text{m}$  Al sputtering of (b). The Al was then photolithographed and etched as in (c) and finally, a timed release of (d) was performed in a commercial Al-compatible solution to remain the oxide isolation island under the anchor areas.

effects, such as ion bombardment damage and/or selectivity degradation, also need to be considered in determining a suitable bias power. To illustrate this, Fig. 3.7 (b) shows the result that uses the same gas ratio of  $\text{Cl}_2/\text{BCl}_3 = 35/25$  sccm as that used in Fig. 3.5 (b) but with the bias power increased from 100 W to 150 W. As a result, the 150-W bias power case yields a thinner final hard mask oxide thickness, indicating that a higher bias power exhibits a poorer etching selectivity against the capping oxide.

### 3.2.3 Process Flow for Al Comb-Driven Resonators

To first identify if Al has a high mechanical  $Q$  needed for a low actuation voltage, a one-mask fabrication process as depicted in Fig. 3.8 is used to achieve a metal aluminum folded-beam comb-driven resonator. In particular, the process starts with a silicon wafer coated with a 2- $\mu\text{m}$  low temperature silicon dioxide (LTO) via LPCVD of Fig. 3.8 (a) serving as a sacrificial material. A 3- $\mu\text{m}$  Al layer is then sputtered on the wafer by the S-gun sputtering system described in III.A, followed by structure photolithography and etching (*cf.* Fig. 3.8 (b) and (c), respectively). Finally, a timed release is performed in Silox Vapox III<sup>®</sup> (Transene, Inc.), a commercial oxide etchant saturated with Al for enhanced selectivity [15], to partially remove the sacrificial LTO, yielding the final suspended structure anchored by the remaining oxide to the substrate (*cf.* Fig. 3.8 (d)). Again, the simplicity of the one-mask process allows

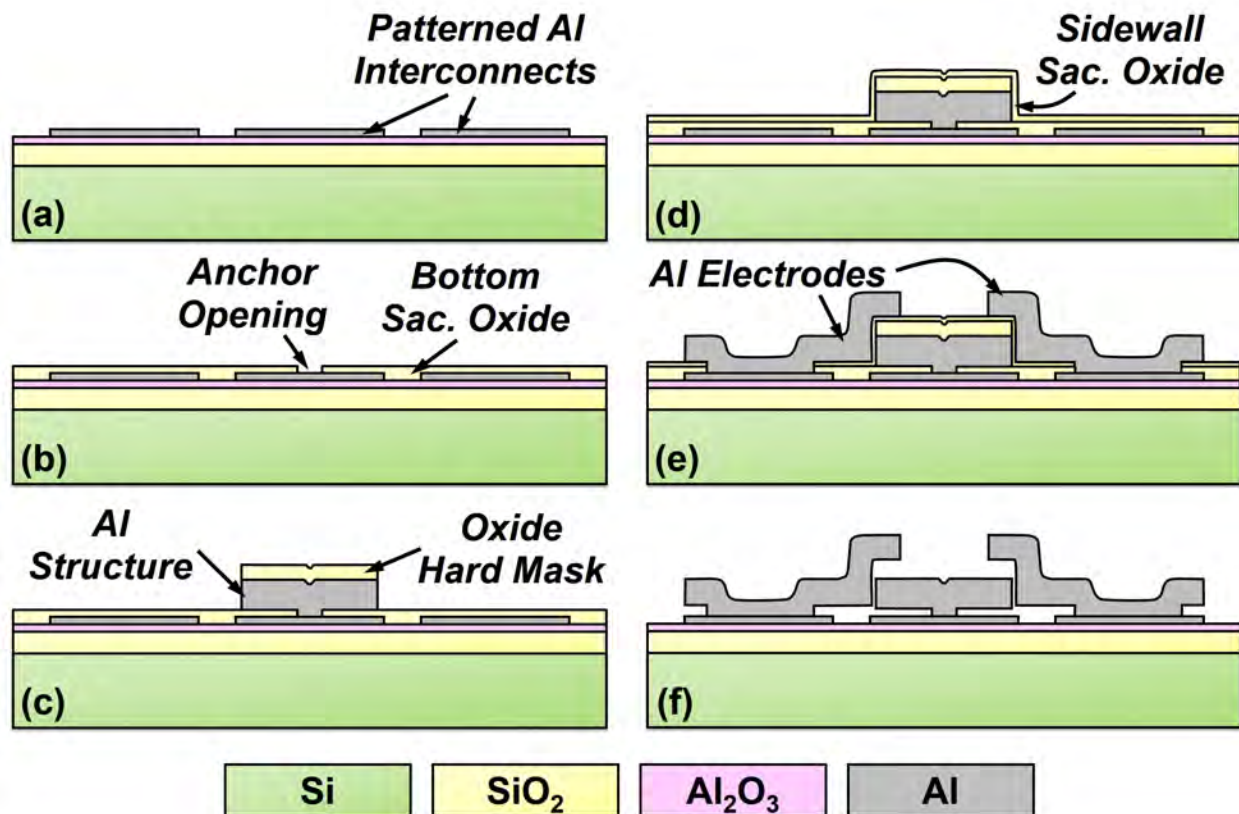


Figure 3.9: Surface micromachined fabrication process used to achieve the slotted Al displacement amplifiers.

a fast turnaround time to reveal the quality factor of materials as the structural layer of resonators.

### 3.2.4 Process Flow for Al Disk Resonators/Displacement Amplifiers

Fig. 3.9 presents the fabrication process flow used to achieve slotted disk resonators in metal aluminum structural material. The Al slotted resonant switch with an all-Al structure, including interconnects and the structure itself, allowing the device to be integrated directly over advanced CMOS.

The process begins with the growth of 2- $\mu\text{m}$  thermal oxide on a starting silicon substrate, followed by atomic layer deposition (ALD) of 100-nm Al<sub>2</sub>O<sub>3</sub>, both of which together serve as electrical insulation. A 100-nm thick pure aluminum film is then sputtered and patterned via plasma etching, as shown in Fig. 3.9 (a). Next, 750 nm of LPCVD oxide is deposited at 400 °C to act as a sacrificial layer, followed by photolithography and etching to form anchors (Fig. 3.9 (b)). Note that the 400°C deposition temperature is the lowest temperature

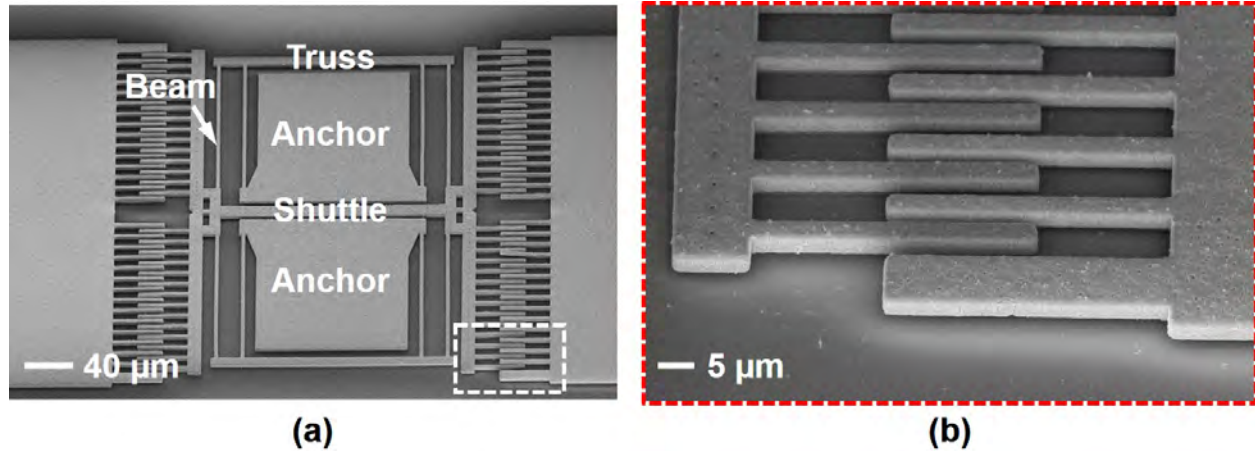


Figure 3.10: SEM images of (a) the fabricated Al comb-drive and (b) a zoom-in view on the comb structures.

limit of the deposition furnace and less than  $2/3$  of the Al melting point, chosen minimize impact on the first Al thin film. The second Al film (for the structure) is then sputtered  $2.5\text{-}\mu\text{m}$  thick, followed by deposition of a  $1.5\text{-}\mu\text{m}$ -thick oxide hard mask (Fig. 3.9 (c) (d)). The electrode-to-resonator spacing is then defined by depositing a  $70\text{-nm}$  sacrificial LPCVD oxide, again at  $400\text{ }^\circ\text{C}$ , as seen in Fig. 3.9 (e). The field oxide is then patterned to access interconnects (Fig. 3.9 (f)), followed by a  $1.5\text{-}\mu\text{m}$  Al deposition, which is patterned to form electrodes (Fig. 3.9 (g)). Finally, vapor phase HF (Primaxx<sup>®</sup> Etch System, SPTS) removes all sacrificial oxide to yield Fig. 3.9 (h). Here, vapor phase HF is chosen rather than Silox Vapox III<sup>®</sup> for the reasons that the Silox Vapox III<sup>®</sup> solution would still attack Al in a slow rate and the structure and interconnect Al cannot sustain such a long release time, much longer than that needed for the comb-driven devices, required to clean up the narrow gaps around the disk structure; plus, vapor phase HF exhibits a very high oxide:Al selectivity that ensures the Al structure remains intact after the release step.

## 3.3 Experimental Results

### 3.3.1 Al Comb-Driven Resonators

Fig. 3.10 presents SEMs of a fabricated one-mask Al comb-driven resonator. Tested in a typical two-port RF measurement with a commercial transimpedance amplifier IC (SA5211) connected at the output, the Al comb-drive resonator yields a measured frequency response as shown in Fig. 3.11 under a bias of  $50\text{ V}$  and a vacuum level of  $10^{-5}\text{ Torr}$ , showing a  $Q$  up to  $\sim 20,000$ . This as-fabricated  $Q$  value is essentially higher than the achieved  $Q$ s in electroplated Ni devices treated with post-fabrication annealing [16] and close to that demonstrated in polysilicon version [17], identifying that sputtered aluminum material indeed

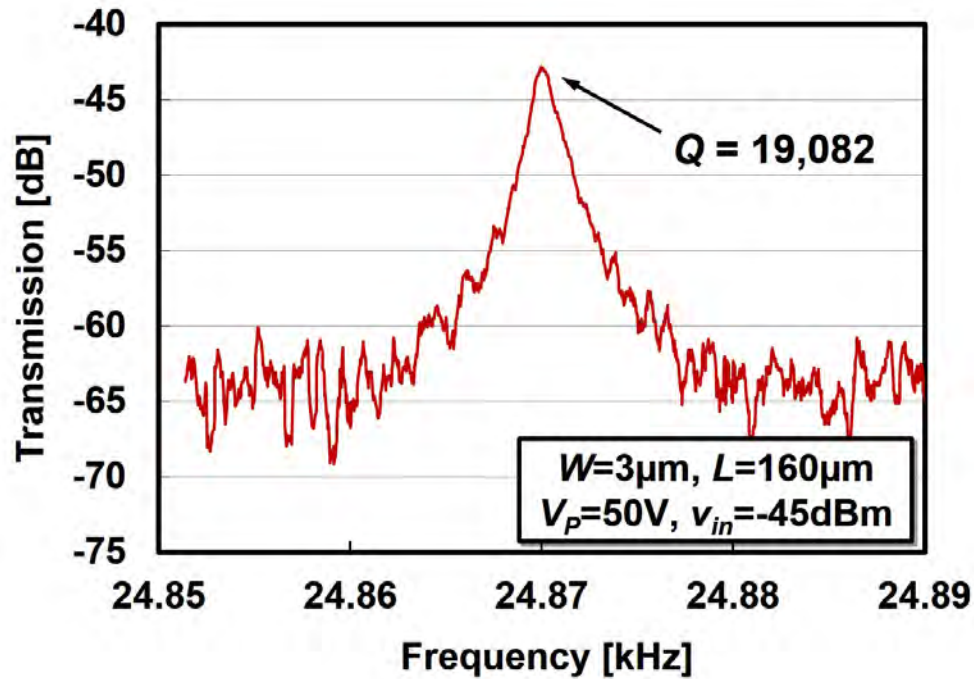


Figure 3.11: Measured frequency response of the Al comb-drive showing a high mechanical  $Q$  in Al structural material up to  $\sim 20,000$ .

has a high mechanical  $Q$ .

### 3.3.2 Al Disk Resonators/Displacement Amplifiers

Fig. 3.12 depicts the SEM of a fabricated Al slotted-disk displacement-amplifying resoswitch with a radius of  $32 \mu\text{m}$  and slots sized as  $(w_b, w_s, \theta_s) = (9 \mu\text{m}, 5 \mu\text{m}, 90^\circ)$ . The displacement gain of the slotted resoswitch was measured using the RF/LO mixing measurement setup described in Chapter 2 designed to simultaneously measure motional currents from any two ports on a capacitively transduced resonator (*cf.* Fig. 3.13). Particularly, the displacement gain, defined as the ratio of the displacement amplitude along the output axis to that along the input axis, can be extracted from the power levels measured from the input and output electrodes via

$$G = \frac{X_o}{X_i} \sim \frac{\sqrt{P_o}}{\sqrt{P_i}} \quad (3.1)$$

Fig. 3.14 plots the measured power waveforms generated at the electrodes of the Al slotted disk of Fig. 3.12, clearly showing a larger power level attained at the output compared to that along the input axes. Plugging the measured power values into (1) yields a displacement gain of  $5.38\times$  for the slotted displacement-amplifying resoswitch, confirming the efficacy of slot-based stiffness engineering. In contrast, Fig. 3.15 presents the measured power waveforms

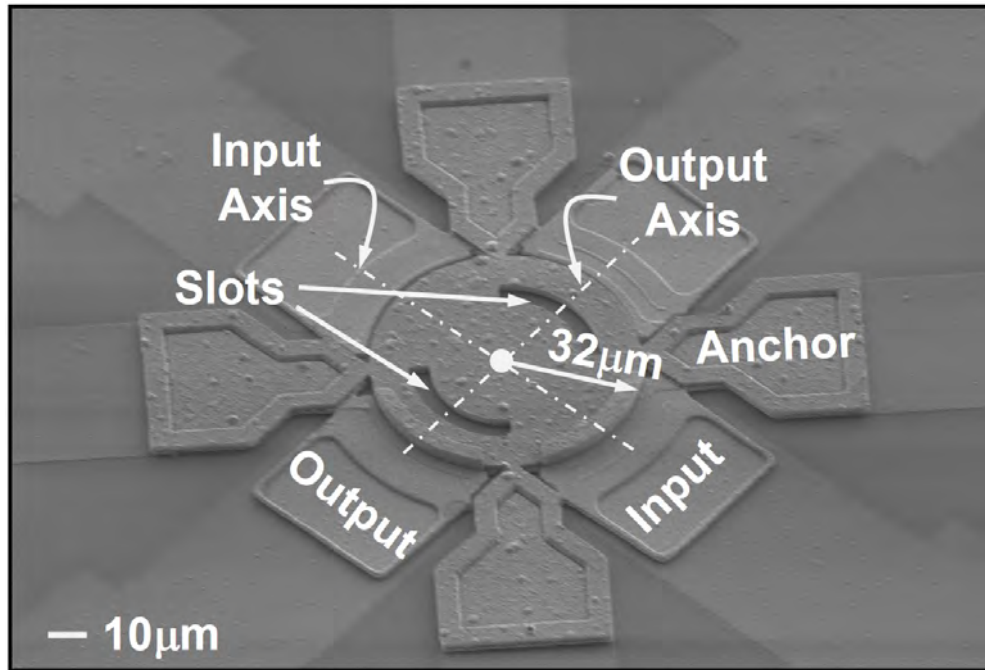


Figure 3.12: SEM of a fabricated Al slotted disk displacement amplifier.

of a conventional 32- $\mu\text{m}$ -radius Al wine-glass disk resonator with no slots introduced, where a similar power level is observed at both the input and output electrodes indicating the displacement amplitudes along the two axes are identical.

However, the  $Q$  in the Al wine glass disk resonator is only around 1,500 (*cf.* Fig. 3.15), much lower than the high- $Q$  observed in the one-mask Al comb-drives. The low- $Q$  could be contributed from several mechanisms among which the Al film quality degraded during the additional process steps in the disk fabrication perhaps is the dominant one. This hypothesis can be verified by measuring the  $Q$  of the comb-driven resonators available on the same wafer fabricated using the complete five-mask disk fabrication process (*cf.* Fig. 3.9), which also yields a  $Q$  round  $\sim 1,000$ .

As will be discovered and discussed in Chapter 4, the  $Q$  of slotted disks Al devices degrades. In particular, thermoelastic damping (TED) dominates the energy loss in slotted structures and TED could be even enhanced in metal materials. As a result, a  $Q \sim 500$  was observed in the measured frequency responses of Fig. 3.14.

Of course, further improvement of the fabrication process as well as investigation of other possible mechanisms that may cause the low- $Q$  issue are needed. If the  $Q$  in the conventional Al disk resonators can be recovered to a point around that measured in the one-mask Al comb-drives, then the array technique could be employed to achieve a certain desired displacement gain, consisted by multiplying the displacement gain of each individual slotted disks designed in a low-to-mid range aimed for retaining a reasonable high- $Q$ . For the demonstration purpose, however, a  $Q$  on the order of thousand is already enough to achieve

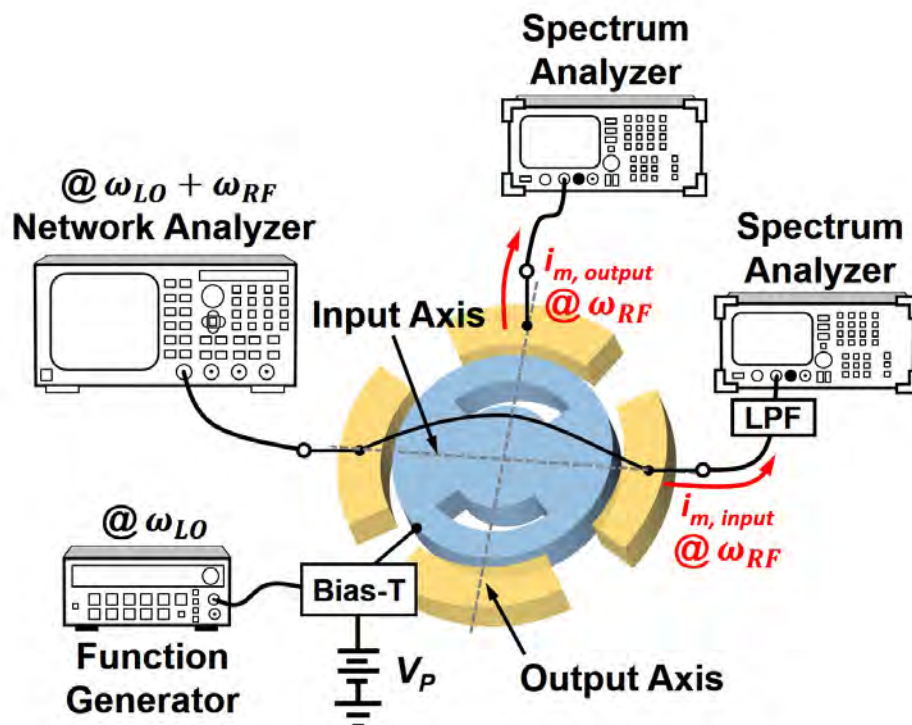


Figure 3.13: Schematic of the measurement setup that was used to characterize the motional currents simultaneously from two different electrodes of the slotted disk.

the desired filter-power amplifier circuit which will be discussed in the following section.

### 3.3.3 Al Switched-Mode Filter-Power Amplifiers

Fig. 3.16 plot the schematic of the circuit that was used to demonstrate the filter-power amplifier embedded with a slotted-disk Al resoswitch. The input signal was applied to the input axis via a network analyzer sweeping the frequency around the resonance frequency of the slotted resoswitch, the input electrodes were dc-biased at  $V_{P,in} = 21$  V separated from the  $v_{in}$  using a bias-T circuit, and the resoswitch structure was tied to a 2-V supply of  $V_P$ , disk. When  $v_{in} = 2$  V near the 23-MHz resonance frequency, the output displacement amplitude becomes large enough to impact the output electrode, thereby switching the 2-V  $V_P$ , disk supply to the output 50- $\Omega$  load to yield an output waveform as of Fig. 3.17 with a voltage amplitude of 0.15 V. When the input signal  $v_{in}$  is swept over a frequency span around the resonance frequency, the resoswitch responds and produces output signals only over a small bandwidth around the resonance peak. For input signals outside this bandwidth, the switch is at rest, and there is no output. Thus, as advertised, the device performs both frequency selection and power amplification, which is also illustrated in Fig. 3.2, where (a) plots the frequency domain displacement of the resoswitch structure, (b) shows its output power gain

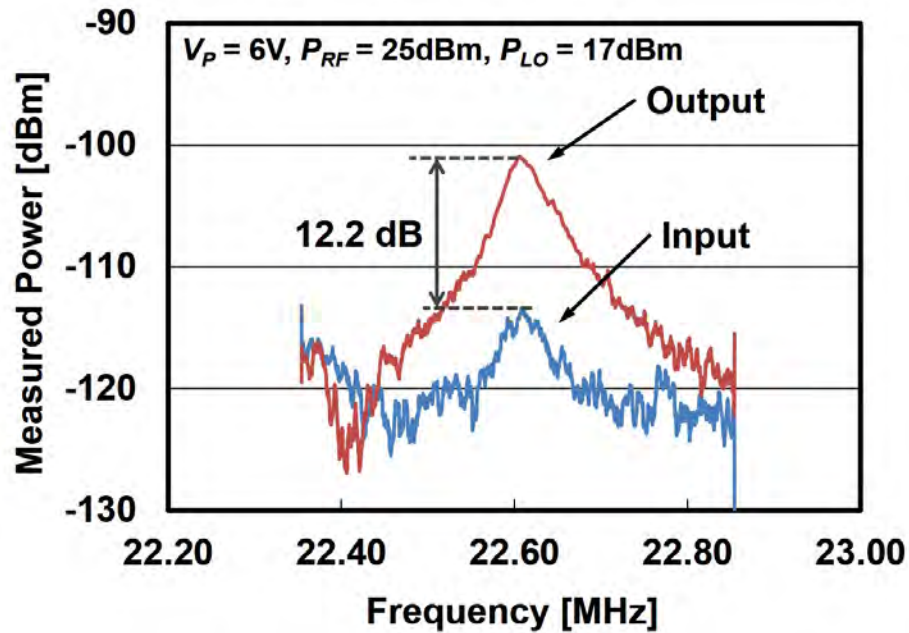


Figure 3.14: Measured frequency responses from the input and output ports of a slotted displacement-amplifying Al disk.

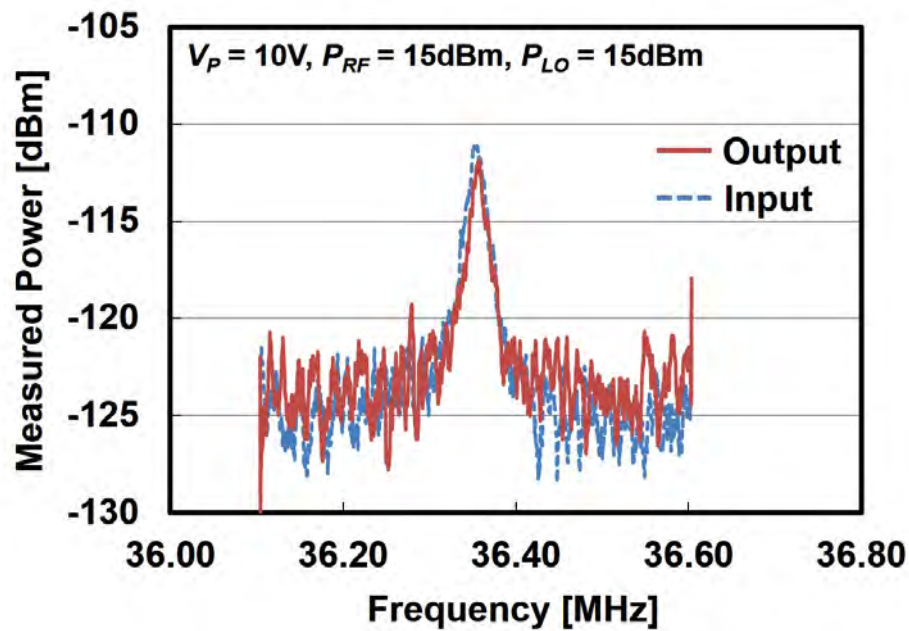


Figure 3.15: Measured frequency responses from the input and output ports of a non-slotted Al wine glass disk.

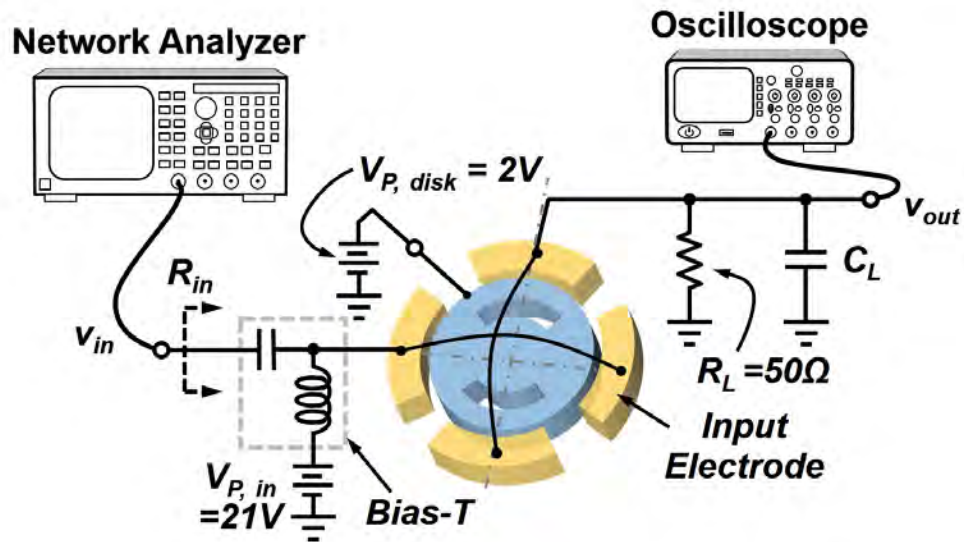


Figure 3.16: Schematic of the demonstrated Al filter-power amplifier together with the measurement setup.

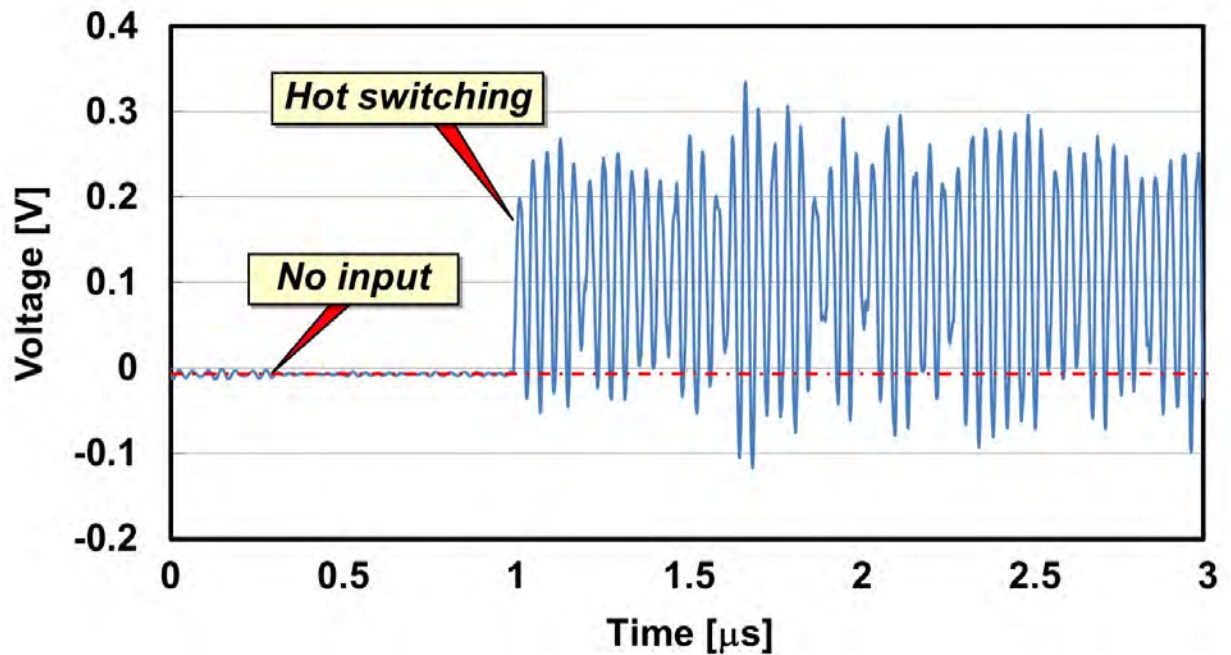


Figure 3.17: Measured hot switching waveform of the Al filter-power amplifier using the measurement setup of Fig. 3.16.

spectrum and finally (c) depicts the time domain waveforms. Particularly, the displacement of resoswitch is limited by the gap spacing and create a small bandwidth of switching (*cf.* Fig. 3.2 (a)), and within this bandwidth the device delivers power from the disk supply to the output to realize power amplification (*cf.* Fig. 3.2 (b)), where the output signal level is much higher than that outside the switching band (i.e., essentially a feedthrough signal) (*cf.* Fig. 3.2 (c))

Note that although there is no voltage gain, the input impedance of  $200\text{ k}\Omega$  determined by the device motional resistance is much higher than the output  $50\text{-}\Omega$  load, and thus, the input driving power and delivered output power can be calculated as

$$P_{in} = \frac{(v_{in}/\sqrt{2})^2}{R_{in}} = \frac{(2/\sqrt{2})^2}{200k} = 10\mu\text{W} \quad (3.2)$$

$$P_{out} = \frac{(v_{out}/\sqrt{2})^2}{R_L} = \frac{(0.15/\sqrt{2})^2}{50} = 238.6\mu\text{W} \quad (3.3)$$

The measured power gain can then be calculated to be 13.8 dB. Unfortunately, this power gain lasted only a short while. In particular, the device pulled into its electrode due to the need for a rather large  $V_{P,in}$ , brought about by a device  $Q$  of only 500, which is subject to be improved by tailoring its fabrication process.

### 3.4 Conclusions

The displacement-amplifying metal Al micromechanical resoswitch-equipped filter-power amplifier has been demonstrated a power amplification gain of 13.8 dB with simultaneous frequency selection function enabled by the vibrating resonant mechanical structure. This demonstration presents a novel method that can be utilized to greatly reduce the power consumption of RF front-end amplifiers towards ultra-low power wireless communications. In particular, the resoswitch-embedded amplifier circuit requires no standby power to operation while the input signal is out of band (i.e., while being in rest) which in turn eliminates the standby power that usually dominates the battery drain especially in the systems where the receive chain needs to be on at all times. With fabrication improvements to enhance the quality factors to improve the reliability, and with design options to reduce the input signal sensitivity and noise level, there seems to be plenty room for further performance improvement.

## Chapter 4

# Quality Factor of Micromechanical Resonators and Resoswitches

Since (as shown in [8]) the sensitivity of a resoswitch-embedded receiver is proportional to frequency and inversely proportional to the  $Q$  of its resoswitch,  $Q$  is apparently one of the most important attributes that determine the performances of such receivers. This chapter will discuss 1) intrinsic loss mechanisms of conventional wine-glass disk resonators; 2) annealing techniques to raise  $Q$  of micromechanical nickel as well as polysilicon-filled CNT composite comb-driven resonators; 3) loss mechanisms in slotted disks; and 4) loss mechanisms in elliptic disks.

### 4.1 Quality Factor Fundamentals

The energy loss mechanisms responsible for limiting the  $Q$ s of micromechanical resonators have been widely discussed and modeled [18] and include gas damping [19], thermoelastic dissipation (TED) [20], phonon-phonon interactions [21], phonon-electron interactions [22], and anchor loss [23], each of which is summarized pictorially in Fig. 4.1. The energy loss contributed by each of these mechanisms can be modeled as an individual  $Q_i$  that combines with the other  $Q_i$ 's to set the total  $Q$  of a given micromechanical resonator according to the expression

$$\frac{1}{Q} = \sum_i \frac{1}{Q_i} \quad (4.1)$$

where  $i$  is meant to indicate any one loss mechanism.

Among the listed loss mechanisms, gas damping is most easily rendered inconsequential by merely operating under vacuum something that will be necessary anyway when operating at cryogenic temperatures. All other listed mechanisms, however, are more difficult to eliminate, so must be considered. Table 4.1 provides analytical expressions from the open literature for some of the more well-researched ones.

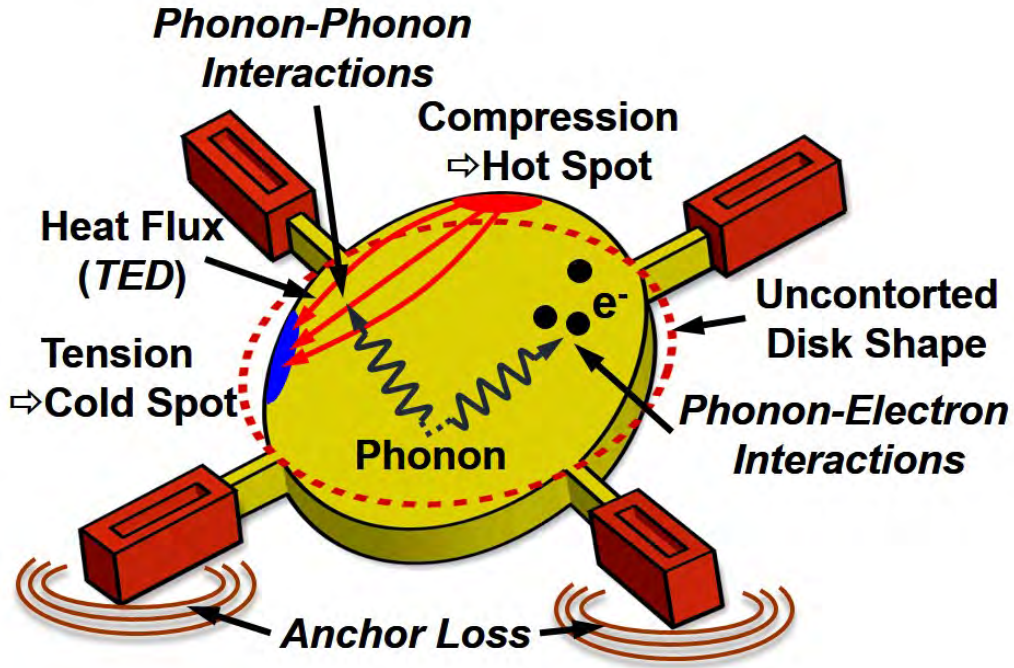


Figure 4.1: Schematic pictorially summarizing important loss mechanisms that constrain the  $Q$  of a wine-glass disk resonator.

Phonon-Phonon Interaction	$Q_{ph-ph} = \frac{\rho\nu^2}{CT\gamma^2} \frac{\omega\tau_{ph}^*}{1 + (\omega\tau_{ph}^*)^2}, \tau_{ph}^* = \frac{3\kappa}{CV_D^2}$
Thermoelastic Dissipation	$Q_{TED} = \frac{1}{\psi} \frac{C^2}{\kappa T \alpha^2 \rho \omega}$
Phonon-Electron Interaction	$Q_{ph-e} = \frac{15}{8} \frac{\rho\nu^2 e^2}{\epsilon_F m_e \sigma \omega}$
$\rho$ : density $\nu$ : sound velocity $C$ : heat capacity $\kappa$ : thermal conductivity $V_D$ : Debye sound velocity $\psi$ : mode shape-determined constant	$\alpha$ : thermal expansion coeff. $\sigma$ : electric conductivity $m_e$ : electron mass $\epsilon_F$ : Fermi energy $e$ : electron charge

Table 4.1: Expressions estimating the  $Q$  limits imposed by various loss mechanisms in micromechanical resonators

Among the mechanisms in Table 4.1, phonon-phonon interaction and thermoelastic dissipation are generally more dominant than phonon-electron interaction and have reciprocal dependences on temperature that encourages the use of cryogenic operation to raise  $Q$ . So far, however, these loss mechanisms have never been measured for micromechanical resonators at VHF and higher frequencies. Rather, for micromechanical resonators designed to avoid TED, anchor losses have always dominated; or at least they have set an upper bound on  $Q$  that is lower than that predicted by the expressions in Table 4.1. For this reason, it is quite possible (and even likely) that measurements of  $Q$  versus temperature for any existing VHF and higher micromechanical resonator will reveal more the dependency of anchor loss on temperature, rather than the dependencies of the mechanisms in Table 4.1. To maximize the chances of actually observing phonon-phonon interactions or thermoelastic dissipation, a resonator design that minimizes losses to the substrate via anchors is needed.

## 4.2 Cryogenic Operation to Raise $Q$

### 4.2.1 Test Devices—Wine-Glass Disk Resonators

In addition to anchor losses, transducer losses must also be minimized. For this reason, a resonator using capacitive transducers is perhaps most appropriate here, since such transducers intrude very little with resonator operation, so commonly allow the highest  $Q$ 's among transducer types. This work utilizes the capacitively transduced wine-glass disk resonator depicted in Fig. 4.2 (a) and (b), comprising a  $32\text{ }\mu\text{m}$ -radius,  $3\text{ }\mu\text{m}$ -thick disk surrounded by four closely spaced electrodes and supported by anchored beams attached at quasi-nodal locations, where radial displacements are negligible compared to other parts of the disk structure when the disk vibrates in its wine-glass mode shape shown in Fig. 4.2 (c). As shown, the device is excited to resonance via a combination of a dc-bias voltage  $V_P$  applied to its conductive resonant structure and an ac signal voltage  $v_i$  applied to two symmetrically placed input electrodes, both of which combine to induce a drive force at the frequency of  $v_i$ . Once vibrating, an output current  $i_o$  is generated by the ensuing  $V_P$ -biased time varying capacitance between the disk and its output electrodes. Attachment of supports at nodal locations helps to block the energy conduit from disk to support, thereby minimizing anchor losses to the substrate. Such losses are further reduced by making the supports as thin as permissible by lithography and sizing them to correspond to quarter-wavelength dimensions [12]. With careful support design, wine-glass disks generally exhibit the highest VHF  $Q$ s at room temperature among other available geometries, including free-free beams and contour mode disks, so are arguably the best vehicles with which to study temperature dependent loss mechanisms. The  $Q$  of this resonator design can be further increased by reducing the number of supports, which then further reduces anchor losses. As shown in [24], wine-glass disks exhibit their highest  $Q$ 's over 150,000 when using two  $1\text{ }\mu\text{m}$ -wide supports; and much lower  $Q$ 's 9,000 when supported by four  $3\text{ }\mu\text{m}$ -wide supports. Thus, by merely varying the number and orientation of supports, such as in Fig. 4.3, the  $Q$ 's of wine-glass disks can be

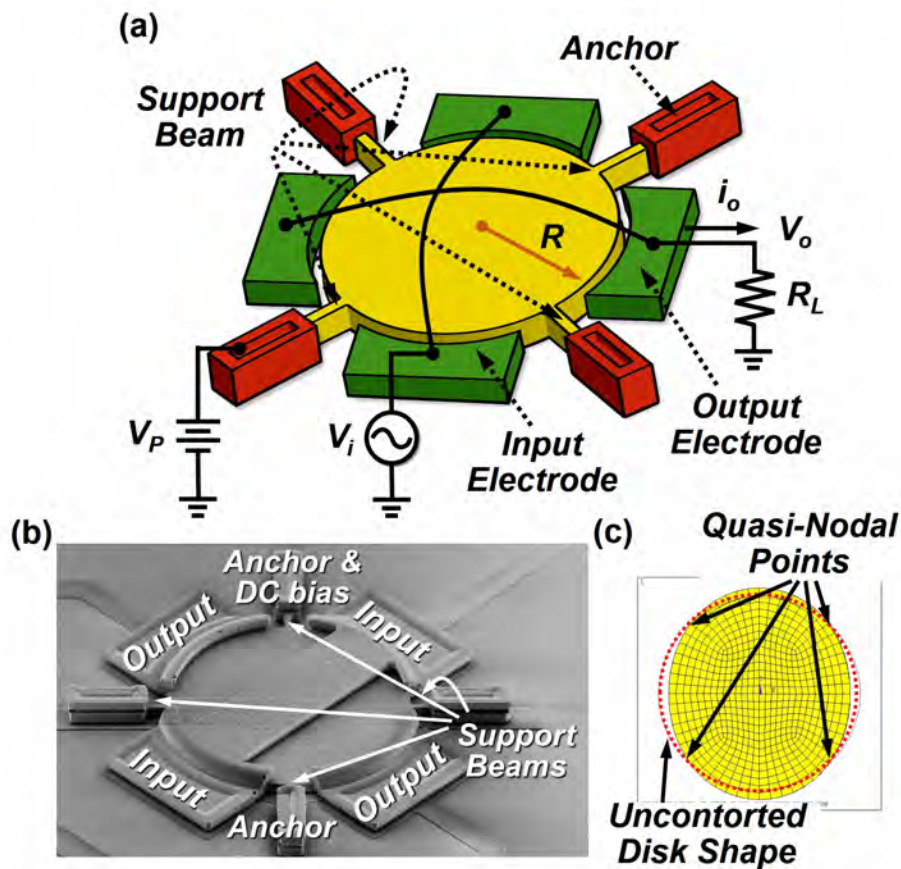


Figure 4.2: (a) Schematic of a wine-glass disk micromechanical resonator in a preferred two-port bias, excitation, and sense configuration. (b) SEM photo of a wine-glass disk resonator test device. (c) Wine-glass mode shape simulated via finite element analysis showing the locations of quasi-nodal points.

tailored to within specific ranges. In fact, the variation in  $Q$  among wine-glass disks with varying numbers of supports can be used to gauge the degree to which anchor losses still influence the  $Q$  at any given temperature.

## 4.2.2 Cryogenic Measurement

Fig. 4.4 presents a photo of the setup used to measure the frequency characteristics of micromechanical wine-glass disks under cryogenic temperatures. Here, a Suss MicroTec PMC150 cryogenic probe station is used that allows probing of chuck-mounted wafers under high vacuum while they are cooled via liquid helium (to the chuck). A turbo pump is used to provide vacuums down to  $6 \times 10^{-5}$  Torr, which practically eliminates air damping while providing thermal isolation against convection. A feedback control heating unit allows precise

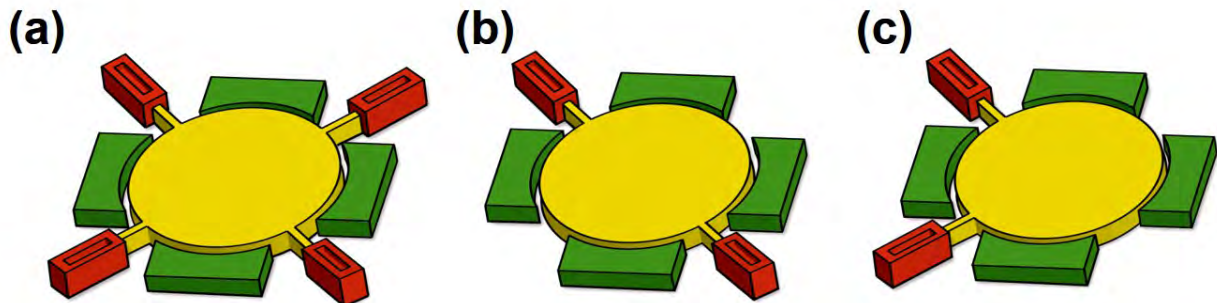


Figure 4.3: Schematic of wine-glass disk micromechanical resonators using various support configurations to vary anchor losses in this work: (a) four 1- $\mu\text{m}$  supports; (b) two 1.5- $\mu\text{m}$  supports oriented 180°; and (c) two 1.5- $\mu\text{m}$  90°-oriented support beams.

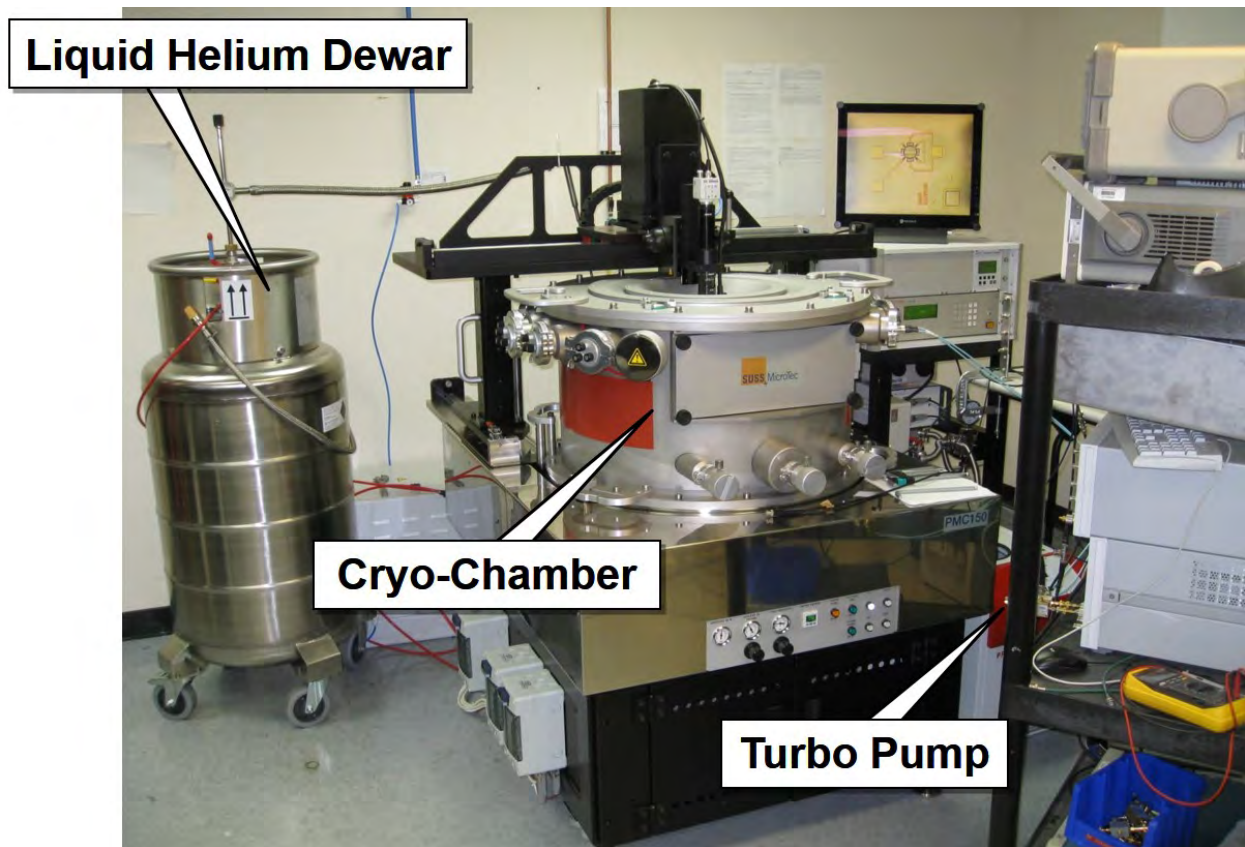


Figure 4.4: Photo of the Suss MicroTec PMC150 probe station used to measure micromechanical resonators at cryogenic temperatures.

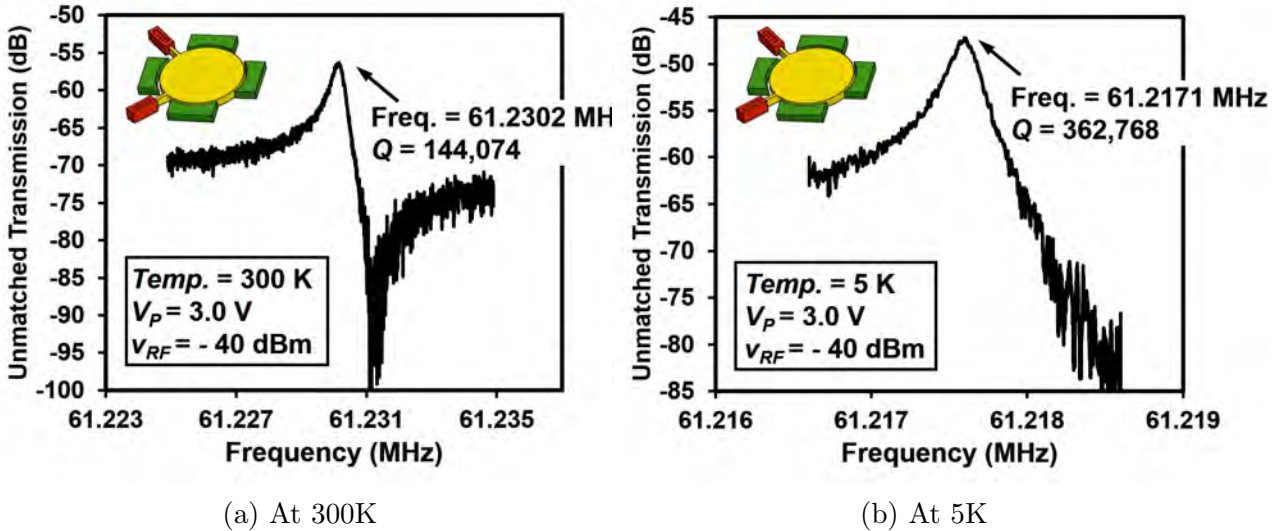


Figure 4.5: Measured frequency response for a 32  $\mu\text{m}$ -radius wine-glass disk with two asymmetric supports at room temperatures and at cryogenic temperatures with  $V_P = 3$  V.

control of the device temperature during measurement. Ideally, devices can be cooled to  $\sim 4.2$  K using this probe station, dependent upon several conditions, e.g., the lowest achievable pressure.

Fig. 4.5 (a) and (b) present frequency characteristics measured using this set-up for two-support 32  $\mu\text{m}$ -radius wine-glass disks with  $V_P = 3$  V at 300 K (i.e., room temperature) and at 5 K, where  $Q$ 's of 144,074 and 362,768, respectively, are observed. The increase in  $Q$  of  $2.5\times$  not only verifies the utility of cooling to increase micromechanical resonator  $Q$ , but would also result in a nearly 10-dB improvement in the phase noise performance of an oscillator referenced to the tested device. Fig. 4.6 presents a measured plot of  $Q$  versus temperature for 32  $\mu\text{m}$ -radius wine-glass disks with varying numbers and orientations of support beams. Here, the measured curves clearly show higher  $Q$ 's for devices employing fewer supports, and this even at cryogenic temperatures. Thus, although  $Q$ 's do rise with decreasing temperature, it is likely that anchor losses still dominate among loss mechanisms, and thus, still mask losses due to phonon-phonon interaction or other mechanisms.

Interestingly, the device employing an asymmetric two-support suspension performs better than that using a symmetric one, at least from a  $Q$  perspective. In addition, the  $Q$  of the symmetric two-support suspended device does not exceed that of the four-support device until the temperature drops below 20K. More study into this phenomenon is needed to identify the exact mechanism, but it is possible that over certain temperatures the symmetric two-support suspension imposes a more non-uniform stress field onto the disk than either the four-support or asymmetric two-support suspensions, thereby generating more loss over most of the low temperature range.

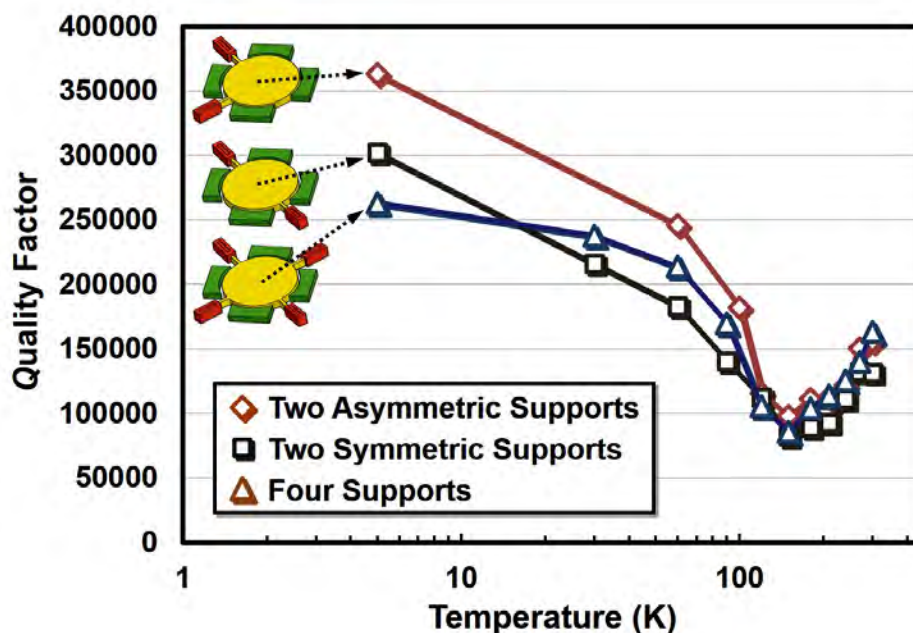


Figure 4.6: Measured  $Q$  vs. temperature for 32  $\mu\text{m}$ -radius wine-glass disks with varying numbers and orientations of support beams.

### 4.2.3 Measurement vs. Theory

Although impressive, the measured  $Q$  of 362,768 at 5 K is nowhere near the 300 million exhibited by quartz at a similar temperature. The question then arises: Why isn't the  $Q$  of the micromechanical resonator also in the millions? As already mentioned, it is likely that anchor losses are still dominant in this work, and the measured curves of Fig. 4.6 still do not convey the ultimate  $Q$  limited by phonon-phonon or other interactions. To convey the degree to which anchor losses (or some other loss) dominates, Fig. 4.7 plots the theoretically predicted  $Q$  limits imposed by TED, phonon-phonon interactions, and phonon-electron interactions, alongside the measured data of Fig. 4.6. Here, theoretical values are obtained via Table 4.1, using parameter values obtained from existing literatures [25][26][27][28]. From the plot, phonon-phonon interactions impose the highest energy dissipation among these loss mechanisms, so set the lower bound on  $Q$ . Clearly, however, this lower bound is still much higher than the measured data, further bolstering a suspicion that another loss mechanism, most likely anchor loss, still dominates the measured  $Q$ 's

Whatever the dominant loss mechanism is, the  $Q$  seems to show a relatively weak dependence on temperature for temperatures below 100K. Above 100K, on the other hand, a dip in the  $Q$  versus temperature curve is observed. Looking closely at Fig. 4.7, this dip seems to coincide with the predicted dip imposed by phonon-phonon interactions, suggesting that although other loss mechanisms mask much of the desired information on phonon-phonon interactions, the data of Fig. 4.7 might still confirm at least the portion and parameters of

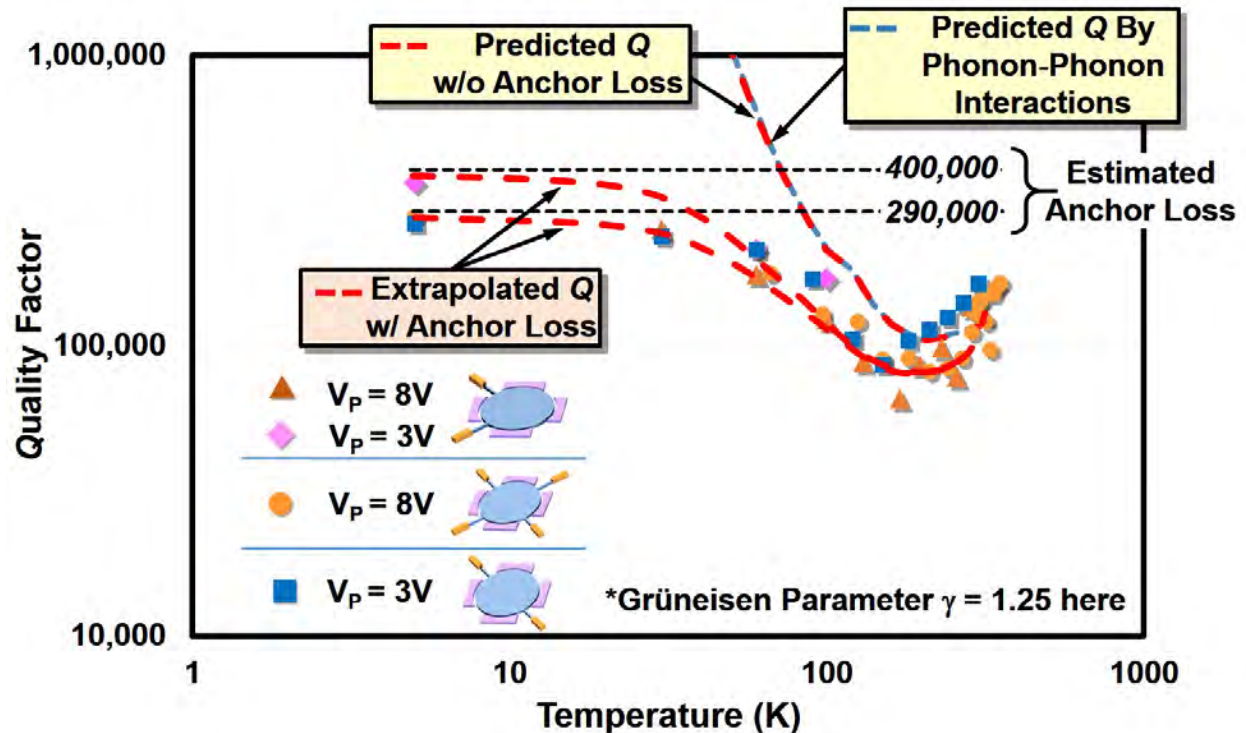


Figure 4.7: Plot of measured  $Q$  versus temperature alongside theoretical  $Q$  limits imposed by various loss mechanisms.

the theory that set the temperature where phonon-phonon-based losses peak

### 4.3 Annealing to Raise $Q$

An alternative approach to raise the  $Q$  is to anneal the as-fabricated devices. Here, a electroplated nickel comb-driven resonator is used to demonstrate this technique.

#### 4.3.1 Test Devices—Nickel Comb-Driven Resonators

Fig. 4.8 shows the electroplated nickel comb-driven resonator fabricated using a process similar to that in [16]. The as fabricated  $Q$  is in the range of 500. The possible reason for low  $Q$  might result from the low temperature process (i.e.,  $50^\circ$ ) which could lead to a less dense structural material. To density the material, as what is done for low-temperature oxide, the as fabricated Ni device is annealed using rapid thermal annealing (RTA) at  $400^\circ$  for a short 2 mins. Fig. 4.9 plots the measured frequency responses before and after annealing, showing that the  $Q$  dramatically increases from the initial 561 up to 11,000.

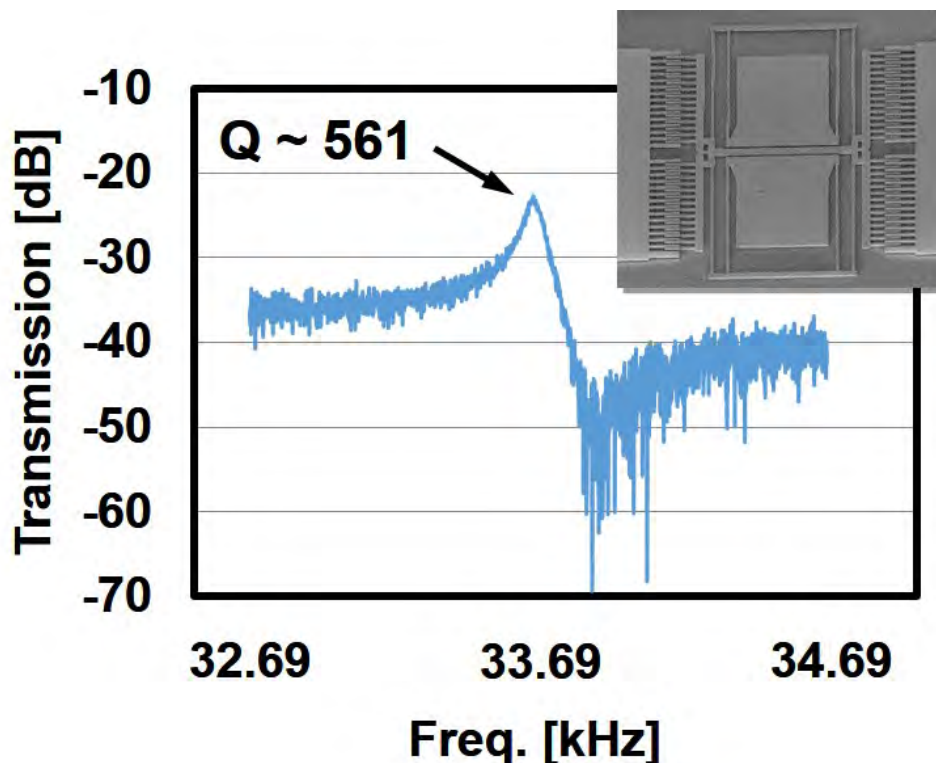


Figure 4.8: SEM and measured frequency spectrum of a micromechanical electroplated nickel folded-beam comb-driven resonator.

#### 4.4 Material Approach to Raise $Q$ : Polysilicon-Filled CNT Structural Material

To date, capacitively-transduced micromechanical resonators have posted the highest  $Q$ s among on-chip resonator technologies, with  $Q$  values exceeding 150,000 in the VHF range [29] and exceeding 11,000 in the GHz range [30]. However, the exceptional  $Q$ s of these resonators are available in concert with the sub-200  $\Omega$  impedances desired by off-chip board-level applications only when technologies that achieve tiny high aspect-ratio gaps are used, such as that of [31] or [32]. Aside from impedance issues, there are applications that demand even higher  $Q$ s at GHz frequencies [33], which means higher frequency- $Q$  products are also desired. To this last point, theoretical studies in literature generally predict that the material  $Q$  of SiC should exceed that of silicon at the same frequency [25][34]. So far, however, actual SiC devices have yet to best silicon in this area. This combined with higher electrical resistance and greater difficulty depositing low-stress doped SiC makes this material much less popular than silicon or polysilicon for high  $Q$ , high aspect-ratio applications.

Recently, Hutchinson [35] demonstrated a polysilicon-filled CNT grass structural material that combines carbon and polysilicon on the nanoscale in a process that achieves high

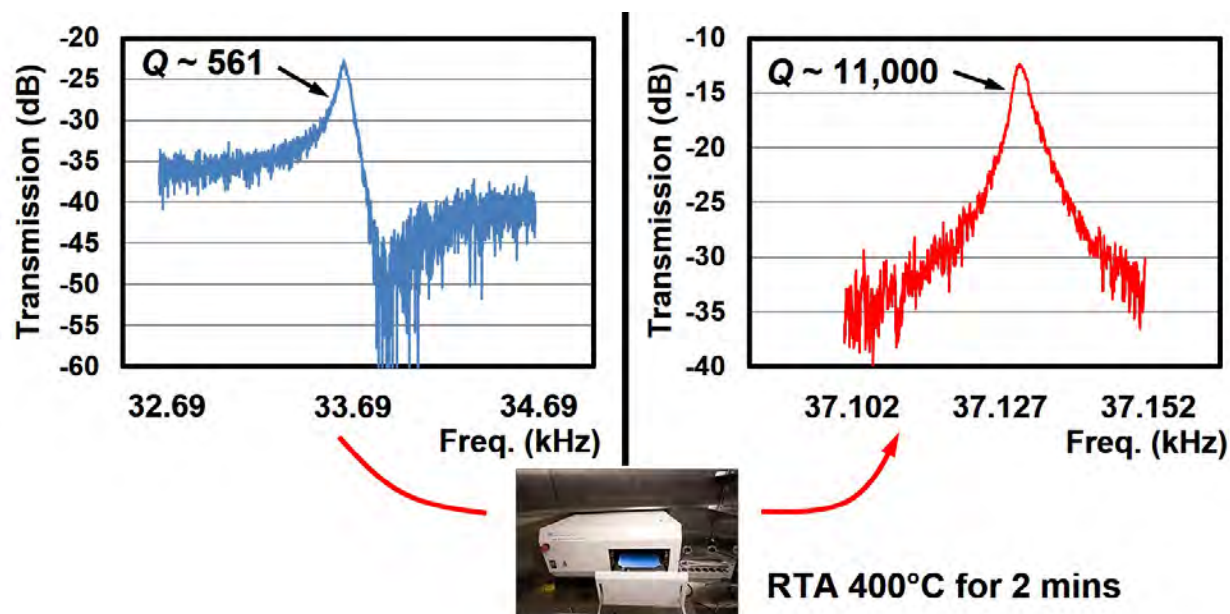


Figure 4.9: Measured frequency responses of the comb-driven resonator shown in 4.8 before and after a rapid thermal annealing for 2 mins at 400°, showing  $Q$  substantially increases from 561 to >10,000.

aspect-ratio microstructures more easily than conventional deposition and etch based methods. Although its combination of silicon and carbon are not at the molecular level, there is some interest in determining how closely this material mixture might approximate the material properties of molecular SiC. This work investigates this by first fabricating folded-beam capacitive-comb-driven micromechanical resonators in polysilicon-filled CNT material using a modified process that insures straighter sidewalls and adds post-fabrication in situ annealing of structures to improve material properties; then extracting material properties, such as  $Q$  and acoustic velocity, from their electrically measured resonance curves. Using this approach, a 28.658-kHz in situ localized annealed version yields a  $Q$  of 3,230 twice as high as that of an unannealed one; and an acoustic velocity of 9,042 m/s slightly higher than the 8,024 m/s of polysilicon, and inching towards the  $\sim 12,000$  m/s typical of SiC.

#### 4.4.1 Fabrication Process Flow

Fig. 4.10 presents the fabrication process flow used to achieve devices in polysilicon-filled CNT structural material. This process is based on that of [35] but modified to include an oxide mold that prevents CNTs at the edges of structures from growing sideways. This in turn allows for smaller widths and gaps than those achieved in [35].

The process begins with heavy doping of the silicon substrate using  $\text{POCl}_3$ , followed by a blanket deposition of 5- $\mu\text{m}$ -thick silicon dioxide to serve both as an insulating anchor and as the aforementioned CNT-guiding mold. The silicon dioxide layer is then patterned and

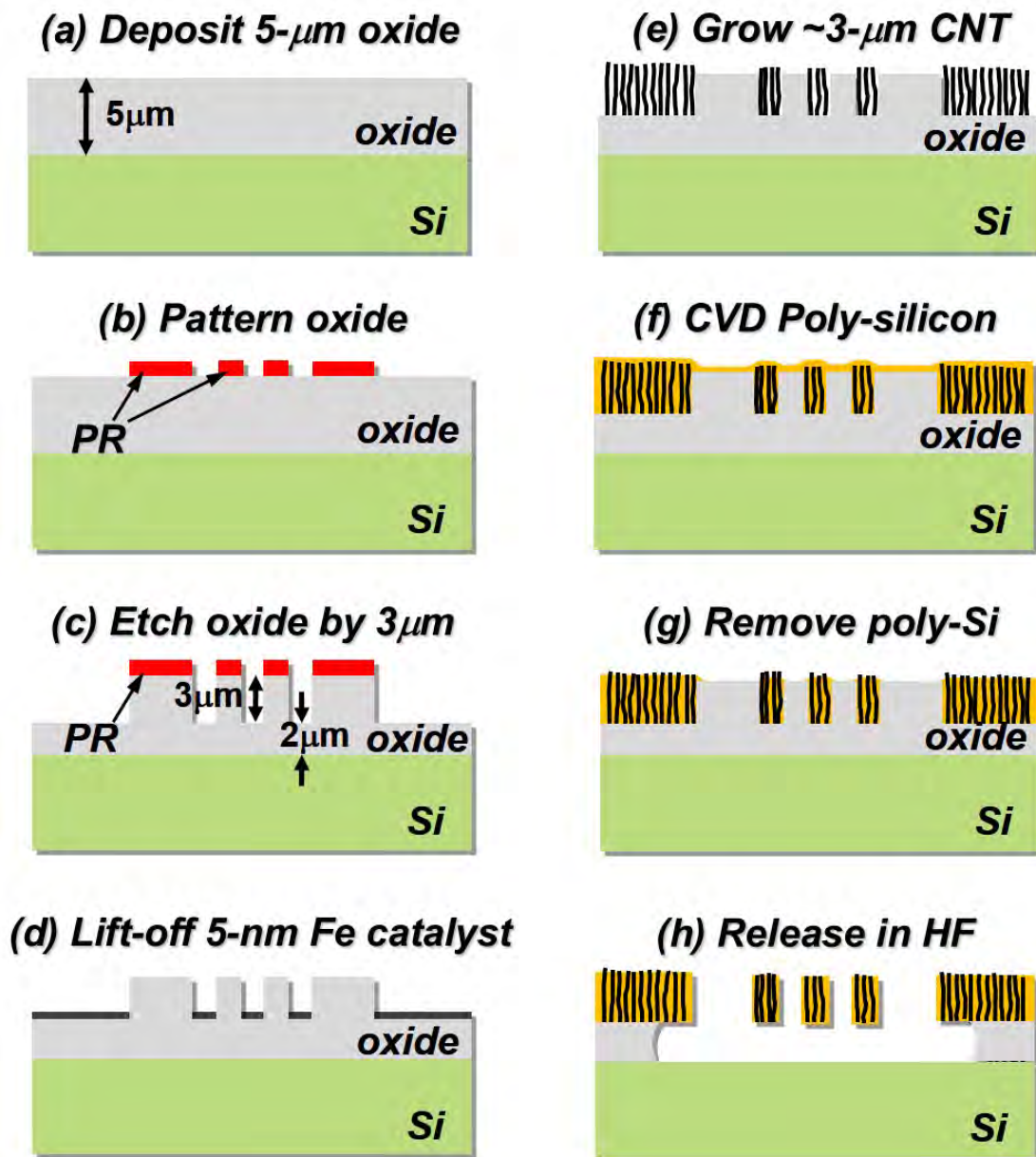


Figure 4.10: Fabrication process flow for folded-beam comb-driven microstructures in polysilicon-filled CNT material.

	PolySiC	PolySi-Filled CNTs
3 $\mu\text{m}$	7.5 hrs	2 mins+3 hrs
60 $\mu\text{m}$	6.2 days <sup>1</sup>	10 mins+3 hrs
Resistivity ( $\Omega\text{-cm}$ )	0.02	0.0016

Table 4.2: Deposition rate and resistivity comparison between CVD polySiC and polySi-filled CNT grass

timed-etched to achieve the cross-section of Fig. 4.10 (c), where battlement-like structures rise 3  $\mu\text{m}$  above a 2- $\mu\text{m}$  thick base of blanket oxide. Next, 5 nm of Fe seed layer (for later CNT growth) is evaporated and lifted off the tops of the battlements by removing the remaining photoresist to achieve the cross-section of Fig. 4.10 (d). CNTs are then grown using a gas mixture of  $\text{H}_2/\text{C}_2\text{H}_4$  at 720  $^\circ\text{C}$  in a custom CVD furnace. The lengths of the CNTs, which determine the eventual thick-ness of the structural layer, are controlled via the growth time—in this case, only two minutes to attain a desired CNT grass thickness of 3  $\mu\text{m}$  to achieve the cross-section of Fig. 4.10 (e). The as-grown CNTs are then filled by depositing a thin layer of LPCVD doped polysilicon, followed by a timed dry etch of polysilicon to remove the polysilicon layer on the surface, but keep the polysilicon in the composite material, to yield the cross-section of Fig. 4.10 (g). Finally, a timed HF dip releases the structures while preserving oxide mesas under large area features that serve as anchors.

It should be noted that the CNT growth rate is substantially faster than the deposition rate of conventional SiC CVD processes. To expand on this, Table 4.2 summarizes the required deposition time according to a reported deposition rate for polycrystalline SiC CVD [36] compared to the CNT growth time under the conditions described above, plus the fixed 3-hr deposition time for filling with polysilicon. Although the desired thickness for the devices designed here is around 3  $\mu\text{m}$ , this process provides even greater benefits for thicker structures, e.g., 60- $\mu\text{m}$  thick, for which the needed CNT grass requires only 10 minutes of deposition time under the growth conditions used here.

To gauge the efficacy of oxide molding, Fig. 4.11 compares SEMs of CNT structures grown with (right) and with-out (left) the oxide mold, before and after filling with polysilicon. Clearly, the sidewalls are uneven after polysilicon filling without the guiding oxide mold, while the oxide mold confines the growth towards straight sidewalls after filling. This process not only provides a relatively fast method for fabricating high-aspect ratio structures with small gap structures, it also does so with little stress compared with alternative methods.

<sup>1</sup>This is of course an unrealistically long deposition time. In practice, rather, a thinned SiC wafer can be used.

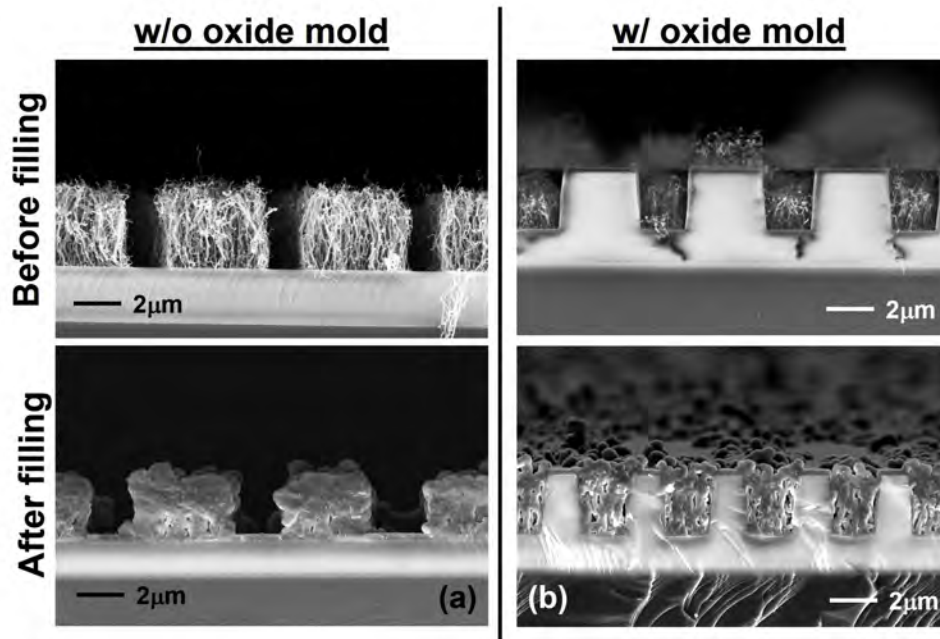


Figure 4.11: SEMs of CNT structures grown (a) with and (b) without the oxide mold, before and after polysilicon-filling.

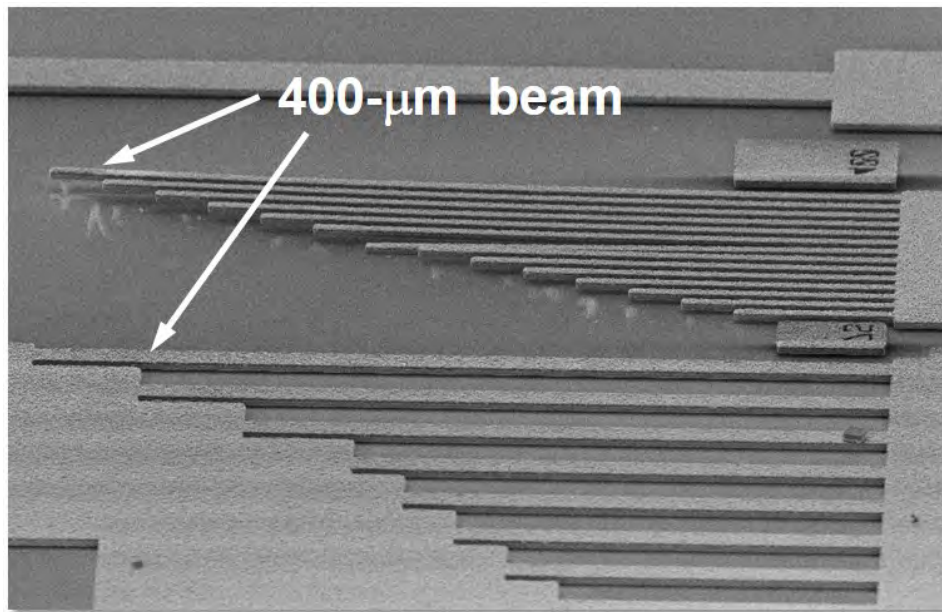


Figure 4.12: SEM of polysilicon-filled CNT clamped-clamped and cantilever beam arrays immediately after release, showing little or no curling or buckling.

Fig. 4.12 confirms this with a SEM showing released clamped-clamped and cantilever beam arrays constructed in polysilicon-filled CNT material with no apparent buckling and much less bending than other approaches. Thus, if this material does end up approximating SiC, it would do so while avoiding many of the stress issues often experienced by structures formed using CVD SiC. Indeed, stress control remains a major challenge for CVD SiC [37].

#### 4.4.2 As-Fabricated Polysilicon-Filled CNT Material Properties

To allow characterization via electrical measurement, this work employs one-mask folded-beam capacitive comb-driven resonators [38], such as shown in Fig. 4.13 (a), as measurement vehicles. As with previous one-mask devices, the anchors in this device are made much larger than any resonator features to allow complete undercutting of the resonator while retaining sufficient oxide under the anchors to hold the structures steadfast to the substrate. Fig. 4.13 (b) zooms in on the interdigitated fingers of the device's transducer, showing the 1- $\mu\text{m}$  gaps in  $\sim 3\text{-}\mu\text{m}$  thick polysilicon-filled CNT material achieved by this process. This SEM also reveals considerable surface roughness immediately after fabrication a problem to be addressed. To extract material properties, such as  $Q$  and acoustic velocity, the resonance behavior of this device must be measured, and this was done using conventional means, such as described in [39]. Fig. 4.14 presents the measured frequency response of a 28.482-kHz folded-beam comb-driven device using a 30V-bias under  $10^{-4}$  Torr immediately after fabrication, i.e., with no post-fabrication annealing (to be used later). Here, a  $Q$  of 1,636 is measured, which is lower than the  $Q$  of 10,000 exhibited by previous LPCVD polySiC comb-driven micromechanical resonators [40]. On first glance, the lower  $Q$  seems to arise at least partly from surface energy losses associated with the large surface roughness of the structure shown in Fig. 4.13 (b). One look at Fig. 4.15, however, which presents cross-sections of the polysilicon-filled CNT material, reveals voids that form during the polysilicon filling process and that could be major source of defect-based losses, where hysteretic movement of defects consumes energy, leading to loss and reducing  $Q$ . Although quite porous, the polysilicon-filled CNT material seems to still post a very good resistivity of  $1.610^{-3} \Omega \times \text{cm}$ , which is an order lower than reported for previous CVD polycrystalline SiC films [36].

To extract acoustic velocity, the well-known formula for the resonance frequency of a folded-beam comb-driven resonator is used, which can be expressed by [39]

$$f_o = \frac{\nu}{2\pi} \sqrt{2\left(\frac{W}{L}\right)^3 \frac{1}{A_{\text{equiv}}}}, \nu = \sqrt{\frac{E}{\rho}} \quad (4.2)$$

where  $\nu$  is the acoustic velocity of the material governed by its Young's modulus  $E$  and density  $\rho$ ;  $W$  and  $L$  are the width and length of the supporting beams, respectively; and  $A_{\text{equiv}}$  is the equivalent area of the shuttle, truss and beams, determined by considering their respective kinetic energies [39].

Table 4.3 summarizes measured frequencies for devices with varying beam lengths. By plotting measured frequency versus  $1/\sqrt{L^3}$ , as shown in Fig. 4.16, the acoustic velocity of

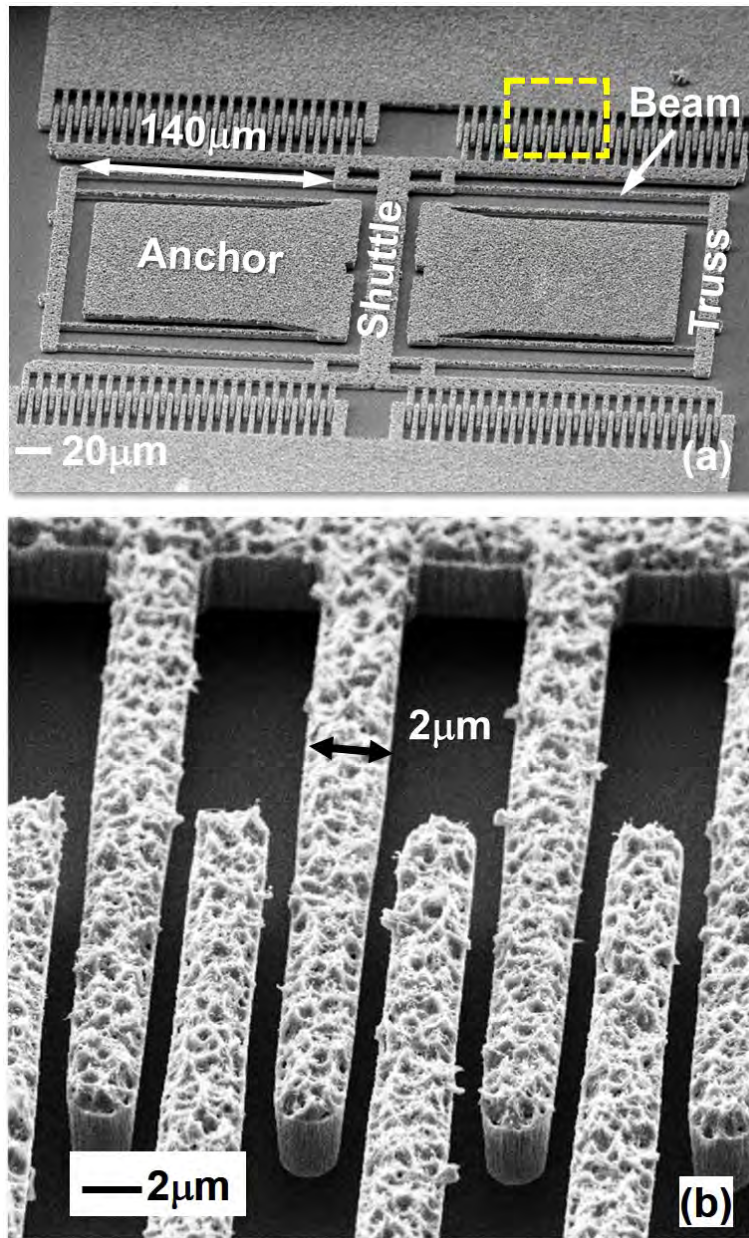


Figure 4.13: (a) Overview and (b) zoom-in SEMs of a fabricated polySi-filled CNT comb-driven resonator.

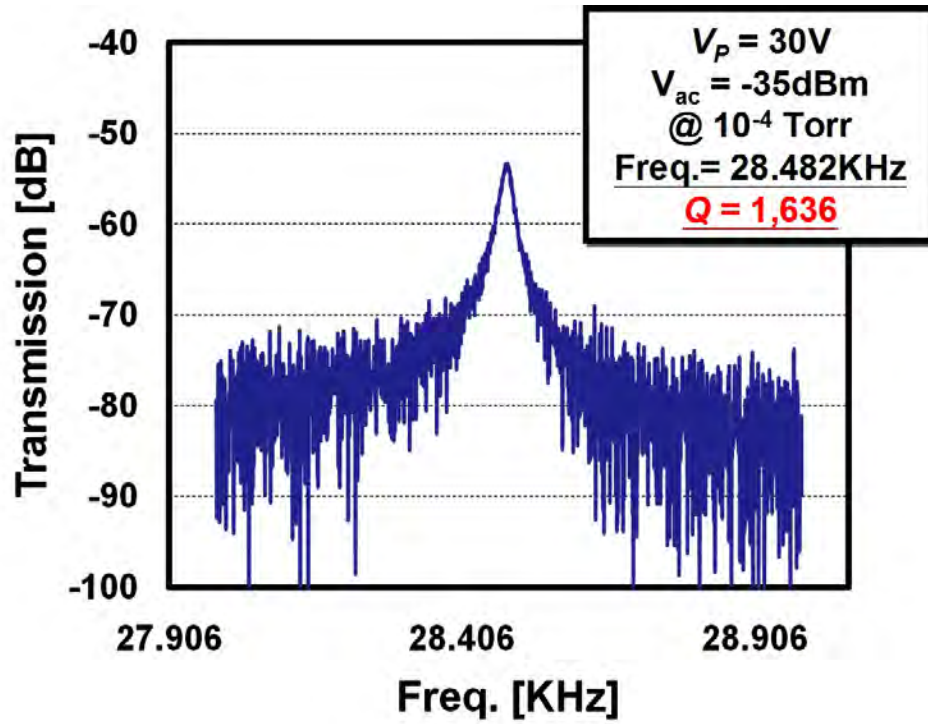


Figure 4.14: Electrically measured frequency response of the resonator of Fig. 4.13 before in situ localized annealing.

No.	Beam Size $L/W$ ( $\mu\text{m}$ )	Equiv. Area $A_{\text{equiv}}$ ( $\text{mm}^2$ )	Frequency (kHz)
1	140/2	0.0151	28.67
2	150/2	0.0152	25.95
3	160/2	0.0152	23.40

Table 4.3: Summary data for devices used in acoustic velocity extraction

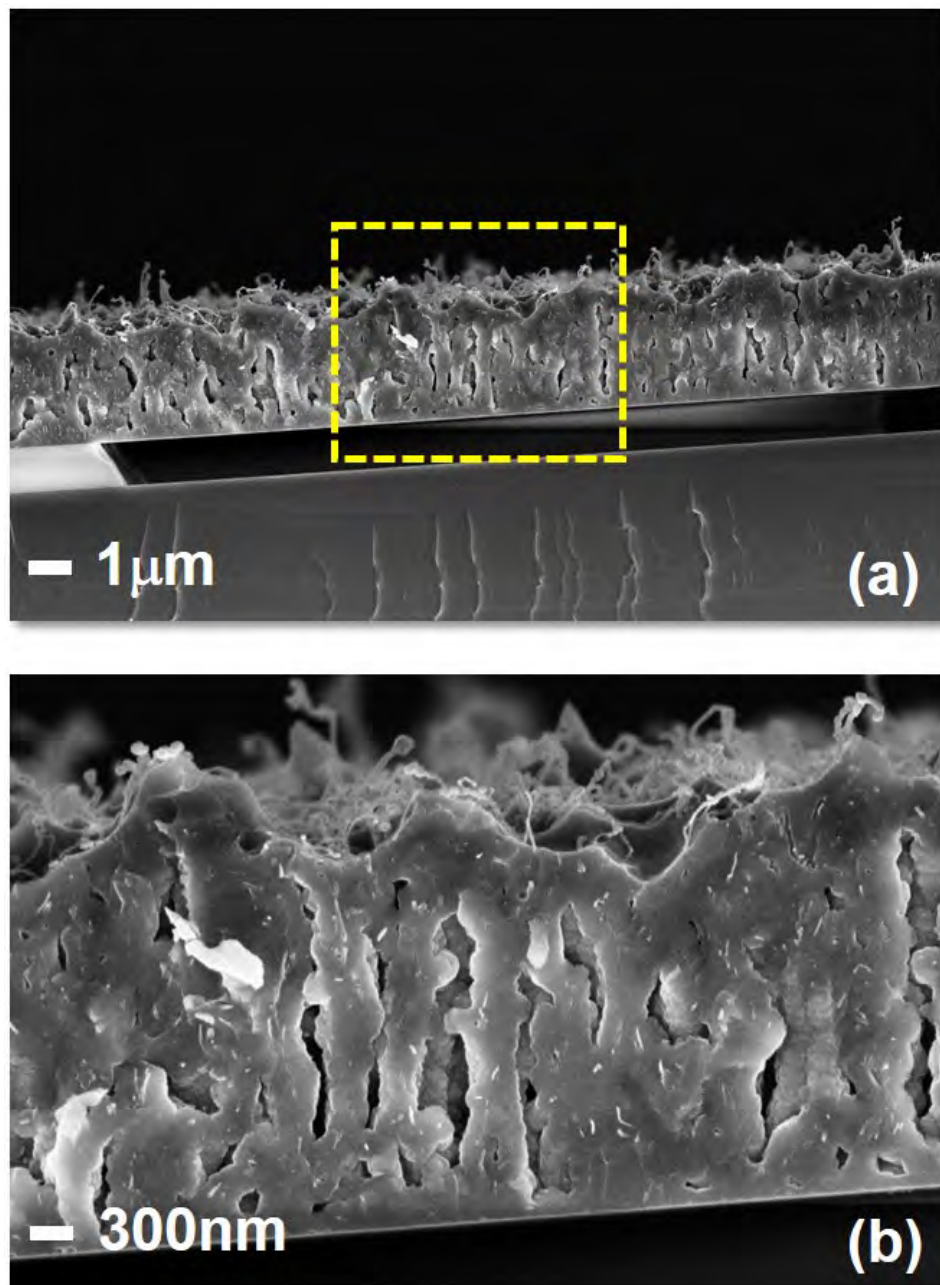


Figure 4.15: Zoom-in SEM of the cross-section view of a released structure showing the voids inside the material.

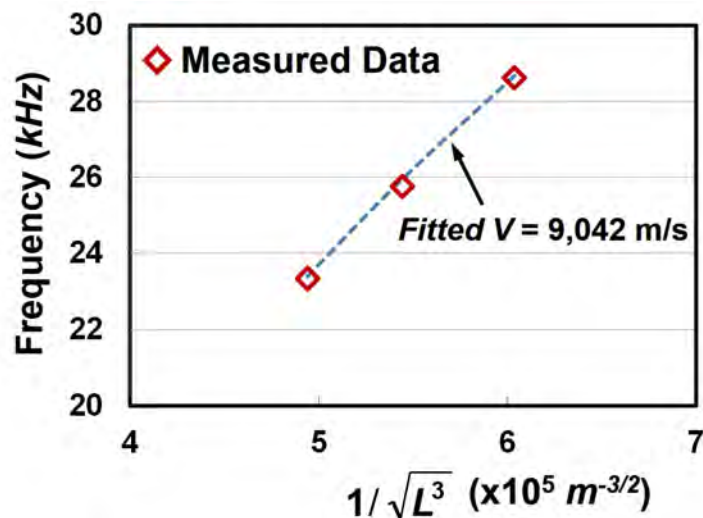


Figure 4.16: Curve fitting to extract the acoustic velocity of polysilicon-filled CNT material from frequency information.

this material is extracted to be 9,042 m/s from the slope. It should be noted that this direct electrical measurement of resonance provides a more accurate reading of material properties, especially for acoustic velocity, than the non-electrical, non-resonance methods used previously [35]. The fact that the measured value of acoustic velocity sits between the 8,024 m/s of polysilicon and the 12,000 m/s of SiC seems to suggest that the combination of silicon and carbon in the makeup of this material, although not at the molecular level, still approximates to some degree the behavior of SiC, at least from an acoustic velocity standpoint.

#### 4.4.3 *In Situ* Localized Annealing to Raise $Q$

As already stated, the measured  $Q$  of 1,636 is not reminiscent of previous CVD SiC, as it is too low. To raise the  $Q$  of the as-fabricated polysilicon-filled CNT material, an in situ localized annealing step was applied, which has been demonstrated previously to raise the  $Q$ 's of nickel comb-driven micromechanical resonators from 4,103 to 14,172 [16]. Fig. 4.17 describes the annealing setup: a voltage difference  $V_a$  sends electrical current into one anchor, through the structure and its supports, then out the other anchor, all while the device is driven into resonance vibration via an ac voltage provided by a network analyzer. The electrical current Joule-heats the structure and its supports to temperatures exceeding 1300°C when  $V_a = 4$  V (predicted by finite element simulation), allowing annealing of the structure while it operates. Fig. 4.18 presents measured frequency characteristics before and after in situ localized annealing under  $V_a = 4$  V for one hour and cooling down to room temperature (i.e.,  $V_a = 0$  V), revealing a doubling in  $Q$  over the original unannealed  $Q$  to a value of 3,230.

To provide some insight into the mechanism behind the observed of  $Q$  increase, Fig. 4.19

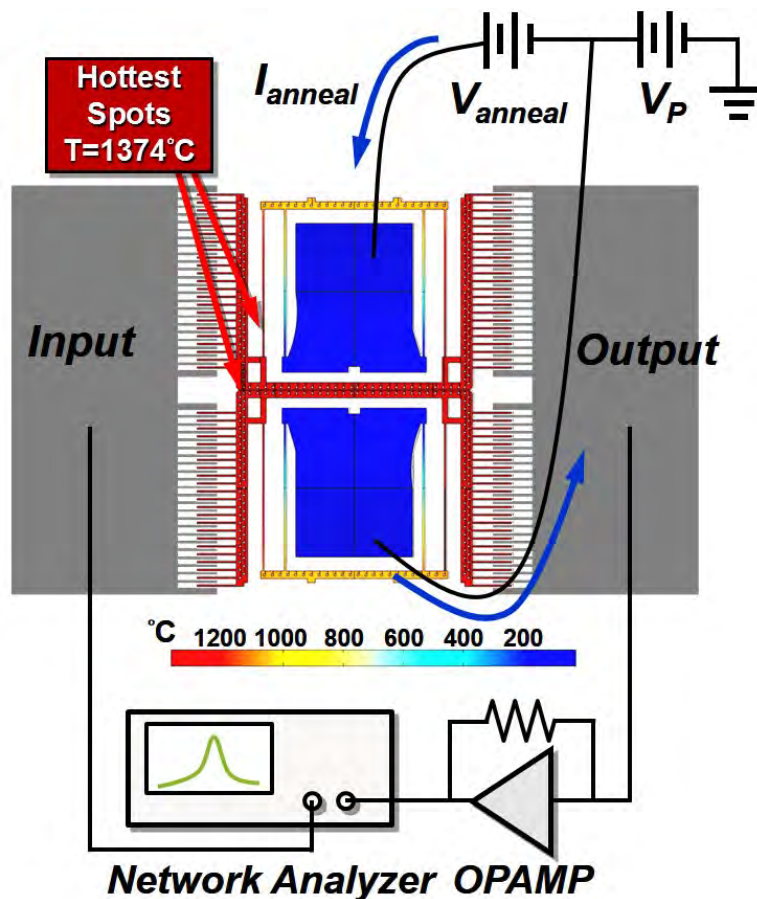


Figure 4.17: Setup for *in situ* localized annealing and measurement of frequency characteristics.

presents SEMs showing the surface morphology before and after *in situ* annealing, revealing a much smoother surface afterwards. That the  $Q$  is higher when the surface is smoother bolsters the suspicion that surface roughness-derived energy losses play a key role in limiting the  $Q$  of this material. However, there are other plausible reasons, such as 1) removal of contaminants from the surface and voids of the polysilicon-filled CNT material; 2) hardening of anchors after high temperature treatment; and 3) removal of material defects, which occurs more rapidly when high temperature raises defect diffusivity during device operation help to push them out toward the material surfaces. Whatever the mechanism, the observed doubling in performance is quite welcome.

#### 4.4.4 Conclusions

Although in no way polished at this time, polysilicon-filled CNT grass material seems to exhibit material properties commensurate with the needs of some lower end MEMS appli-

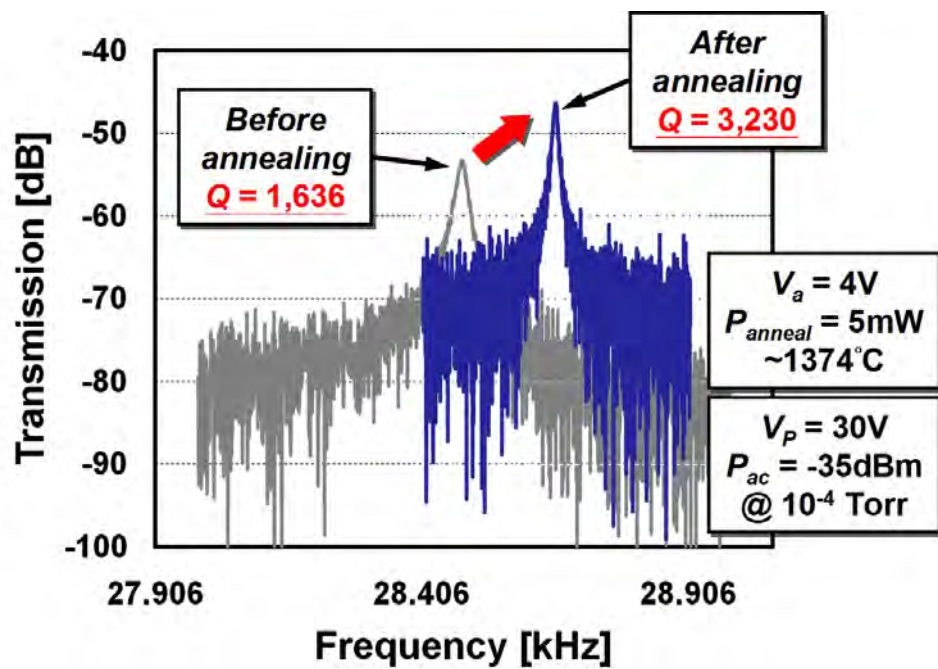


Figure 4.18: Measured frequency characteristics before and after in situ localized annealing under  $V_a = 4 V$ .

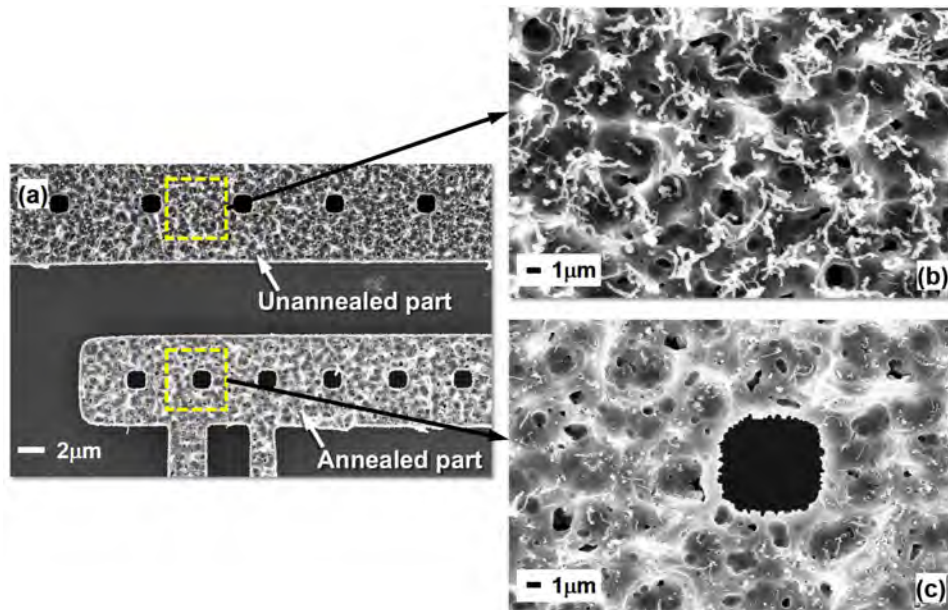


Figure 4.19: (a) SEMs of unannealed and annealed parts; and (b)-(c) respective zoom-in views.

cations. In particular, the measured frequency response for a 28.658-kHz in situ localized annealed folded-beam comb-driven resonator in this material yields a  $Q$  of 3,230, which is not unusable; and an extracted acoustic velocity of 9,042 m/s that sits right between the 8,024 m/s of polysilicon and the 12,000 m/s of SiC, suggesting that the makeup of this material, although not at the molecular level, might still approximate to some degree the behavior of SiC, at least from an acoustic velocity standpoint. If so, then it does so with the further benefits of a considerably faster fabrication process for low-stress high-aspect ratio structures with small gaps. Obviously, further improvements on film quality (e.g., its mechanical  $Q$ ) are needed before any conclusions can be made on whether or not this material really approximates SiC, and how closely (if at all).

## 4.5 Quality Factor of Slotted-Disk Displacement Amplifiers

### 4.5.1 Quality Factors vs. Varying Slot Geometry

Although slotted disks nicely provide the needed displacement amplification without complicated processing steps, they do so at the expense of  $Q$ . In particular, measurements indicate that slotted disks yield lower  $Q$  compared to that of conventional non-slotted disks. Fig. 4.20 plots measured  $Q$  for varying slot designs and support schemes. The support schemes include side supporting beams placed at the quasi-nodal locations with dimensions of  $W/L = 1\ \mu\text{m}/5.8\ \mu\text{m}$ ,  $2\ \mu\text{m}/3\ \mu\text{m}$ , and  $2\ \mu\text{m}/1\ \mu\text{m}$  (where  $W$  and  $L$  represent the support beam width and length, respectively), and a center stem with a diameter of  $4\ \mu\text{m}$  ( $D_{stem} = 4\ \mu\text{m}$ ). Among them the support beam of  $W/L = 1\ \mu\text{m}/5.8\ \mu\text{m}$  corresponds to a quarter-wavelength support (i.e., a clamped-guided beam) [41] [42]. In the ideal case, this configuration should confine the strain energy caused by disk vibration to the structure: none of this energy dissipates in the substrate, thereby maximizing  $Q$ . In practice, however, the quarter-wavelength-supported version does not the  $Q \sim 140,000$  seen in [13]. The finite tolerance in photolithography results in non-ideal quarter-wavelength supports leading to a non-slotted  $Q \sim 68,000$ . Other support beam sizes perform less well and ostensibly suffer larger anchor losses. On the other hand, the center stem supported disk yields a non-slotted  $Q \sim 110,000$ , even with a stem diameter of  $4\ \mu\text{m}$ . This result indicates that the wine-glass mode shape exhibits less susceptibility to the center stem support compared to radial mode devices [30], which often suffer low  $Q$  due to energy dissipation through the center stems. Nevertheless, slots induced to the disks reduce  $Q$  to a range of 1,500-15,000, depending upon the slot dimension and support scheme.

### 4.5.2 Energy Losses in Slotted Disks

The “beam” structure of the slotted area as illustrated in Fig. 4.21 suggests the presence of excessive thermoelastic damping (TED). This damping which typically exhibits little

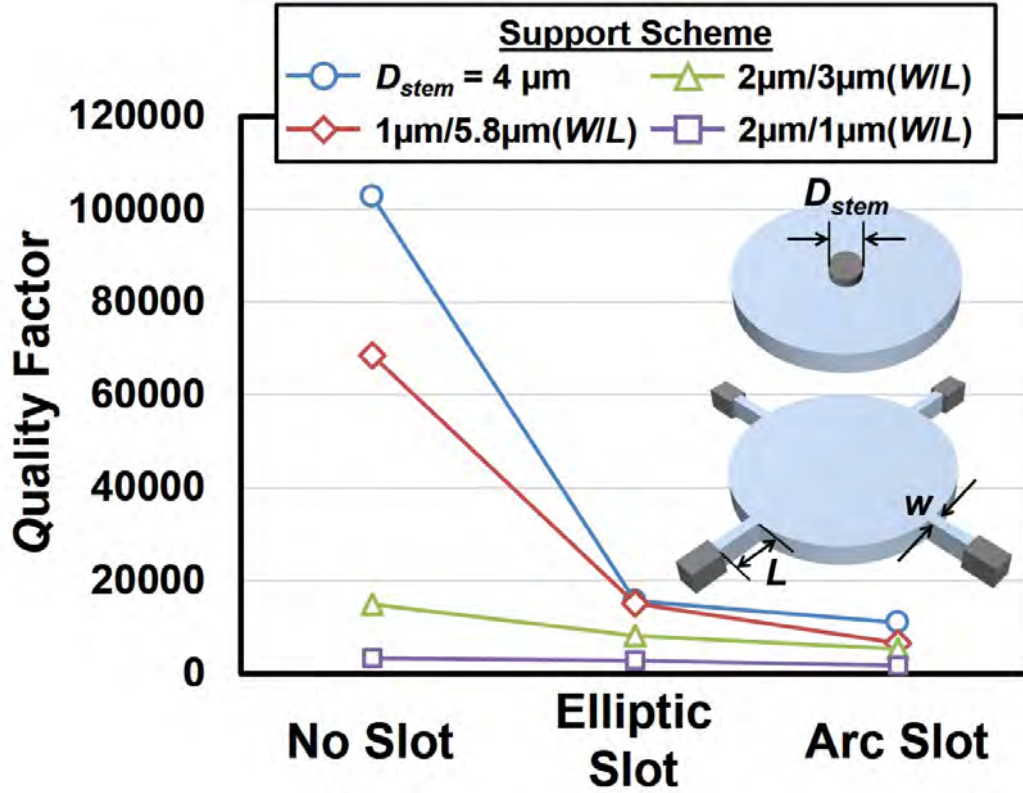


Figure 4.20: Measured  $Q$ 's for conventional non-slotted resonators and displacement amplifiers with elliptic and arc slots with varying support scheme as labeled.

influence on conventional wine-glass disks due to the long heat transfer path—thus, the TED characteristic frequency is much lower than the resonance frequency—seemingly becomes a dominant source of loss in slotted-disk displacement amplifiers. Additionally, as the actual mode shape changes and becomes asymmetric (no longer a pure wine-glass mode), energy loss through supporting beams is likely to increase. Other energy loss such as phonon-phonon interaction would also impose a geometry-independent energy loss [43]. The overall  $Q$ , therefore, takes a general form of

$$\frac{1}{Q} = \frac{1}{Q_{TED}} + \frac{1}{Q_{anchor}} + \frac{1}{Q_{phonon-phonon}} + \dots \quad (4.3)$$

Recent research focused on loss analysis identifies TED as the dominant loss factor for micromechanical beam resonators [20] [44] since its frequency-dependent magnitude incurs the maximum at frequencies in the vicinity of the resonance frequencies. TED-induced  $Q$  takes a general form of

$$\frac{1}{Q_{TED}} = \frac{1}{2\pi} \frac{\Delta W_{TED}}{W_{max}} \quad (4.4)$$

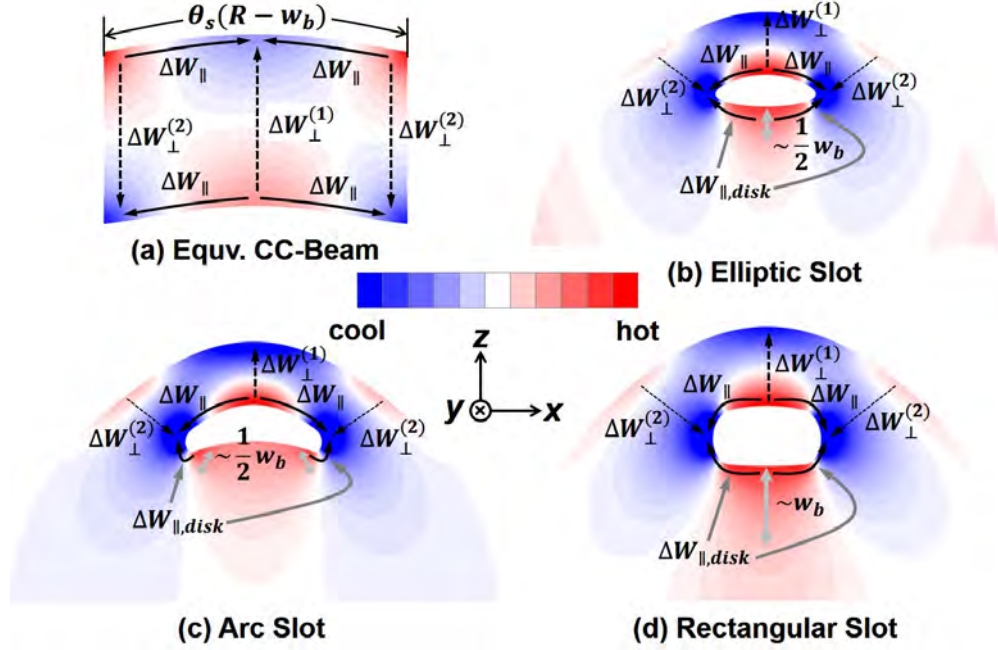


Figure 4.21: Simulated vibration-induced temperature deviations in (a) a CC-beam; (b) an elliptic-slot disk; (c) an arc-slot disk; and (d) rectangular-slot disk, illustrating the postulation of the thermoelastic loss in the slot region.

where  $W_{max}$  represents the maximum strain energy stored in the vibrating mechanical structure; and  $\Delta W_{TED}$  represent the TED-induced energy dissipation in one cycle. Fig. 4.22 presents the schematic of a slotted disk used to model the TED-induced  $Q$ . The figure approximates the slotted disk as a combination of a CC-beam and a disk portion operating in a wine-glass mode shape.

Most of the works on TED of micromechanical beam resonators consider the TED energy loss only along the beam thickness direction assumed much shorter, hence higher thermal gradient, than along the length direction [20] [45]. However, the equivalent beam length and thickness in slotted disks differ by only a factor of 2-3. Thus, TED-induced for slotted disks needs to incorporate TED-induced energy loss along both the length (in-plane) and thickness (transverse) directions. Additionally, the heat transfer around the slot area induces excessive energy loss distinct from those within the beam structure itself.

To do this, an analytic model developed in [46] that fully captures TED-induced energy loss along both length and thickness axes of a CC-beam resonator (*cf.* Fig. 25) is used here, taking the form of

$$\Delta W_{TED,beam} = \frac{4\pi E^2 \alpha^2 T_o}{C} \frac{h}{\theta_s r' w_b} \sum_{m=1}^{\infty} \sum_{p=1}^{\infty} \frac{\omega_n \frac{k}{C} (\beta_m^2 + \gamma_p^2)}{\omega_n^2 + \frac{k^2}{C^2} (\beta_m^2 + \gamma_p^2)^2} \chi_m^2 \eta_p^2 \quad (4.5)$$

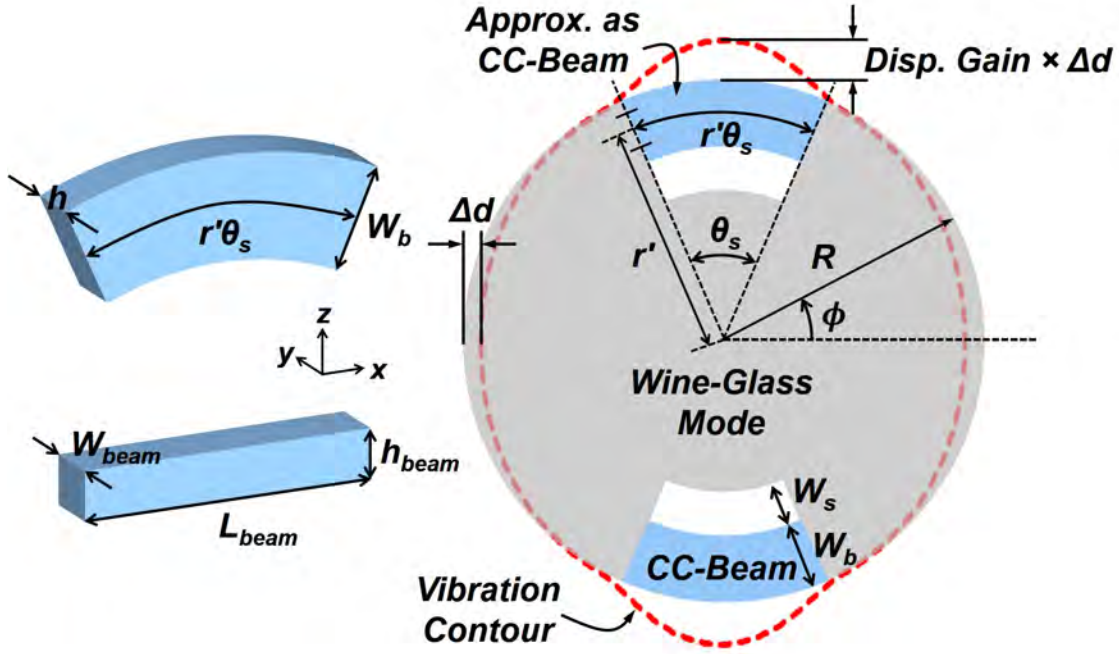


Figure 4.22: Schematic of a slotted disk used to calculate the thermoelastic damping in which the slotted disk is approximated as a composite of a partial wine-glass disk and CC-beams.

where

$$\beta_m = \frac{m\pi}{\theta_s r'}, m = 1, 2, \dots$$

$$\gamma_p = \frac{p\pi}{w_b}, p = 0, 1, 2, \dots$$

$$\chi_m = \int_{x=0}^{\theta_s r'} \sin \beta_m x \frac{\partial^2 Z'}{\partial x^2} dx$$

$$\eta_p = \int_{z=0}^{w_b} \cos \gamma_p z (z - w_b/2) dz$$

and where  $Z$  is the displacement of the CC beam along the  $z$  axis;  $E$ ,  $\alpha$ ,  $k$ , and  $C$  are the structure material's Young's modulus, thermal expansion coefficient, thermal conductivity, and heat capacity, respectively [41]. The use of  $\sin \beta_m x$  and  $\cos \gamma_p z$  accounts for the thermal boundary conditions of isothermal on the clamped-clamped ends along the  $x$ -axis and adiabatic on the free-free ends along the  $z$ -axis, respectively.

At frequencies of interest, the summation term in (4.5) which includes the addition of  $\beta_m^2$  and  $\gamma_p^2$  can be approximately split into two terms, representing energy losses along the beam thickness ( $\Delta W_{TED,\perp}$ ) and along the beam length ( $\Delta W_{TED,\parallel}$ ), and the TED-induced

energy loss takes a linear combination of the two losses:

$$\begin{aligned}
 W_{TED} &= \Delta W_{TED, \perp} + \Delta W_{TED, \parallel} \\
 &= \frac{4\pi E^2 \alpha^2 T_o}{C} \frac{h}{\theta_s r' w_b} \left[ \sum_{m=1}^{\infty} \sum_{p=1}^{\infty} \frac{\omega_n \frac{k}{C} (\gamma_p^2)}{\omega_n^2 + \frac{k^2}{C^2} (\gamma_p^2)^2} \chi_m^2 \eta_p^2 + \sum_{m=1}^{\infty} \sum_{p=1}^{\infty} \frac{\omega_n \frac{k}{C} (\beta_m^2)}{\omega_n^2 + \frac{k^2}{C^2} (\beta_m^2)^2} \chi_m^2 \eta_p^2 \right]
 \end{aligned} \tag{4.6}$$

Differing from  $\Delta W_{TED, \parallel}$ , TED inside the disk, where the boundary conditions are prescribed rather as free-clamped ends and the temperature linearly distributes over an equivalent width of  $w'_b$ , takes the form

$$\Delta W_{TED, disk} = \frac{4\pi E^2 \alpha^2 T_o}{C} \frac{h}{\theta_s r' w_b} \sum_{m=1}^{\infty} \sum_{p=1}^{\infty} \frac{\omega_n \frac{k}{C} (\beta_m^2)}{\omega_n^2 + \frac{k^2}{C^2} (\beta_m^2)^2} \chi_m^2 \eta_p^2 \tag{4.7}$$

where

$$\begin{aligned}
 \beta_m &= \frac{m\pi}{\theta_s r'}, m = 1, 2, \dots \\
 \gamma_q &= \frac{2q-1}{2} \frac{\pi}{w'_b}, q = 1, 2, \dots \\
 \eta_p &= \int_{z=0}^{w'_b} \sin \gamma_q z' (z' - w'_b) dz'
 \end{aligned}$$

where  $\sin \gamma_q z'$  accounts for the free-clamped thermal boundary conditions and  $z$  is defined starting from the free end, i.e., the edge of slots, towards the center of the disk.

On the other hand, the maximum strain energy  $W_{max}$  in (4.4) contains strain energy stored in the “beam” and remaining disk structures:

$$\begin{aligned}
 W_{max} &= 2W_{beam} + W_{remainingdisk} \\
 &= 2\kappa_{beam} W_{CCbeam} + \kappa_{disk} W_{partialWG-disk}
 \end{aligned} \tag{4.8}$$

where  $\kappa_{beam}$  and  $\kappa_{disk}$  represent the FEA-derived correction factors accounting for deviations from the strain energy calculated using the analytical formula described in the following;  $W_{CCbeam}$  and  $W_{partialWG-disk}$  represent the strain energy stored in the beam and in the remaining disk structure, respectively. According to Euler-Bernoulli beam theory,  $W_{CCbeam}$  takes the form

$$W_{CCbeam} = \frac{1}{2} EI \int_0^{\theta_s r'} \left( \frac{\partial^2 Z'}{\partial x^2} \right)^2 \tag{4.9}$$

As the beam length is shorter less than  $10\times$  the thickness, the actual strain energy in the beam reduces by the factor of  $\kappa_{beam}$  derived by FEA simulation:

$$\kappa_{beam} = \log_{10} \left( \frac{\theta_s r'}{w_b} \right) \tag{4.10}$$

$W_{partialWG-disk}$  takes the form

$$\begin{aligned}
 W_{WGdisk} &= 4 \times \frac{1}{2} \int_0^R \int_0^{\frac{\pi}{2} - \frac{\theta_s}{2}} (\sigma_r \varepsilon_r + \sigma_\theta \varepsilon_\theta + 2\sigma_{r\theta} \varepsilon_{r\theta}) r dr d\phi \\
 &+ 2 \times \frac{1}{2} \int_0^{R-w_b-w_s} \int_{\frac{\pi}{2} - \frac{\theta_s}{2}}^{\frac{\pi}{2} + \frac{\theta_s}{2}} (\sigma_r \varepsilon_r + \sigma_\theta \varepsilon_\theta + 2\sigma_{r\theta} \varepsilon_{r\theta}) r dr d\phi
 \end{aligned} \tag{4.11}$$

where

$$\begin{aligned}
 \sigma_r &= \frac{E}{1-\nu^2} (\varepsilon_r + \varepsilon_\phi), \sigma_\phi = \frac{E}{1-\nu^2} (\varepsilon_\phi + \nu \varepsilon_r), \sigma_{r\phi} = \frac{E}{1+\nu} \varepsilon_{r\phi} \\
 \varepsilon_r &= \frac{\partial U_r}{\partial r}, \varepsilon_\phi = \frac{1}{r} (U_r + \frac{\partial U_r}{\partial \phi}), \varepsilon_{r\phi} = \frac{1}{2} \left( \frac{1}{r} \frac{\partial U_\phi}{\partial \phi} + \frac{\partial U_\phi}{\partial r} - \frac{U_\phi}{r} \right),
 \end{aligned}$$

where  $U_r$  and  $U_\phi$  are the radial and tangential displacements of the wine glass mode shape, respectively. The following equations of the radial and tangential displacements used in (4.11) normalize the maximum radial amplitude to unity (i.e.,  $\Delta d = 1$  in Fig. 24) and use  $m = 2$  for wine glass mode [13]

$$\begin{aligned}
 U_r &= \frac{\left[ \frac{\partial}{\partial r} J_m \left( \frac{\zeta R}{\xi} r \right) + \frac{mB}{A} \frac{1}{r} J_m \left( \frac{\zeta}{R} r \right) \right]}{\left| \frac{1}{2} \left( J_{m-1} \left( \frac{\zeta}{\xi} \right) - J_{m+1} \left( \frac{\zeta}{\xi} \right) \right) + \frac{mB}{A} \frac{1}{R} J_m(\zeta) \right|} \cos(m\phi), \\
 U_\phi &= \frac{\left[ \frac{-1}{r} J_m \left( \frac{\zeta R}{\xi} r \right) - \frac{B}{mA} \frac{\partial}{\partial r} J_m \left( \frac{\zeta}{R} r \right) \right]}{\left| \frac{1}{2} \left( J_{m-1} \left( \frac{\zeta}{\xi} \right) - J_{m+1} \left( \frac{\zeta}{\xi} \right) \right) + \frac{mB}{A} \frac{1}{R} J_m(\zeta) \right|} \sin(m\phi),
 \end{aligned} \tag{4.12}$$

where

$$\zeta = 2\pi f_o R \sqrt{\frac{\rho(2+2\sigma)}{E}}, \xi = \sqrt{\frac{2}{1-\sigma}}, \text{ and } m = 2.$$

The amplitude of  $Z'$  in (4.5) and (4.9) depends on the achievable displacement gain and takes the form

$$|Z'| = Disp.Gain \times \Delta d - \left| \cos \left( 2 \left( \frac{\pi}{2} - \frac{\theta_s}{2} \right) \right) \right| \Delta d, \tag{4.13}$$

where the  $\cos(2\phi)$  term comes from the angular dependence of  $U_r$  along  $\phi$  and where the displacement at the input  $\Delta d$ , whose magnitude equals one, is kept here for clarity.

The correction factor  $\kappa_{disk}$  for  $W_{partialWG-disk}$  takes the form

$$\kappa_{disk} = D_3(1 - \cos \theta_s)^3 + D_2(1 - \cos \theta_s)^2 + D_1(1 - \cos \theta_s) + 1, \tag{4.14}$$

where

$$\begin{aligned}
 D_3 &= -23.814 \left( \frac{w_b + w_s}{w_b} \right) + 20.926, \\
 D_2 &= 24.18 \left( \frac{w_b + w_s}{w_b} \right) - 18.985,
 \end{aligned}$$

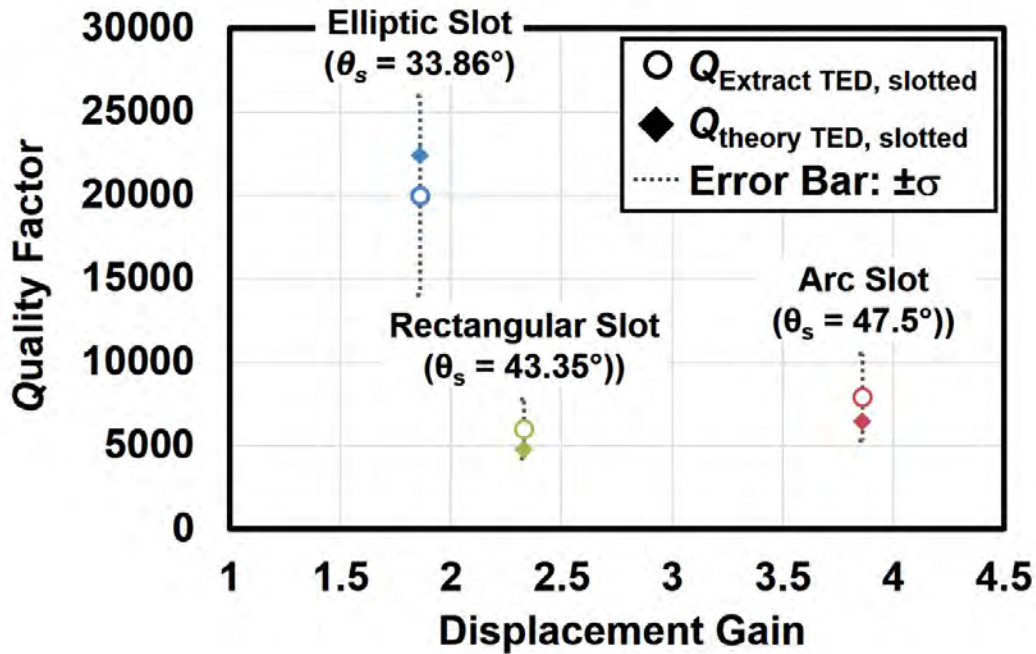


Figure 4.23: Theoretical  $Q_{TED}$  vs. extracted  $Q_{TED}$  showing that for a larger displacement gain suffers higher thermoelastic damping and thus, a lower  $Q_{TED}$  magnitude and that disks with rectangular slots exhibit higher TED compared to disks with other slot designs.

$$\text{and } D_1 = 1.455 \left( \frac{w_b + w_s}{w_b} \right)^3 - 5.118 \left( \frac{w_b + w_s}{w_b} \right)^2 + 2.497 \left( \frac{w_b + w_s}{w_b} \right) + 1.477$$

### 4.5.3 Theoretical versus Measured $Q_{TED}$

Fig. 4.21 plots the deformation-induced temperature deviation for an equivalent CC-beam and slotted disks with varying slot designs. Note that (1) the elliptic-slot case exhibits similar thermal distribution, hence similar TED, in the upper and lower halves of the slots; (2) the arc-slot (2) the elliptic- and arc-slot designs have a temperature distribution with an equivalent width around  $w_b/2$  while the rectangular slot exhibits a broader distribution of  $\sim w_b$ .

Measured  $Q$  of non-slotted and slotted disks can be used to estimate slot-induced  $Q_{TED}$  via

$$\frac{1}{Q_{ExtractTED,slotted}} = \frac{1}{Q_{Measure,slotted}} - \frac{1}{Q_{Measure,noslot}} \quad (4.15)$$

Fig. 4.23 plots  $Q_{ExtractTED,slotted}$  from (4.15) for the three slot designs alongside  $Q_{TED}$  from the theory given by (4.4). The arc-slot and rectangular-slot displacement amplifiers possess lower  $Q_{TED}$  magnitudes compared to the elliptic-slot counterpart. As shown in 4.21, compared to the elliptic-slot version, the arc-slot design has a larger thermal gradient in the

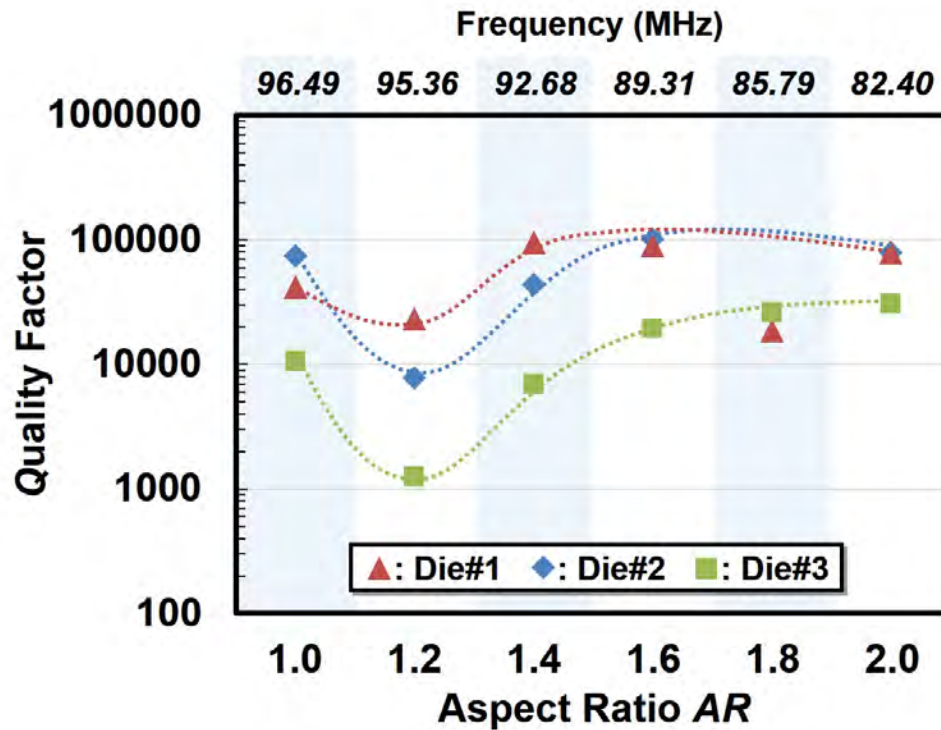


Figure 4.24: Measured  $Q$  versus aspect ratio from three dies. Here,  $AR=1$  corresponds to a circular disk, while higher ARs indicate ellipses.  $AR=1.2$  presents the lowest  $Q$  while  $AR > 1.6$  seems to be able to recover  $Q$  back to that of a circular disk. (Reprint of Fig. 2.26)

disk area while the rectangular-slot design has a wide thermal distribution that generates higher  $\Delta W_{TED,disk}$

#### 4.5.4 Conclusions

Slot-induced  $Q$  degradation of slotted-disk displacement amplifiers has been identified. Measurements on devices with varying slot designs and support schemes indicate that thermoelastic damping and anchor loss constitute the primary energy loss mechanisms decreasing  $Q$  in slotted-disk displacement amplifiers. Particularly, that a larger displacement gain suffers higher thermoelastic damping and thus, a lower  $Q_{TED}$  magnitude and that disks with rectangular slots exhibit higher TED compared to disks with other slot designs. Possible remedy to the trade-off between  $Q$  and displacement gain is coupling multiple displacement amplifiers with a low-to-medium displacement gain and acceptable  $Q$  into an array that supposedly ensures a high  $Q$  while achieves a higher displacement gain than a single device.

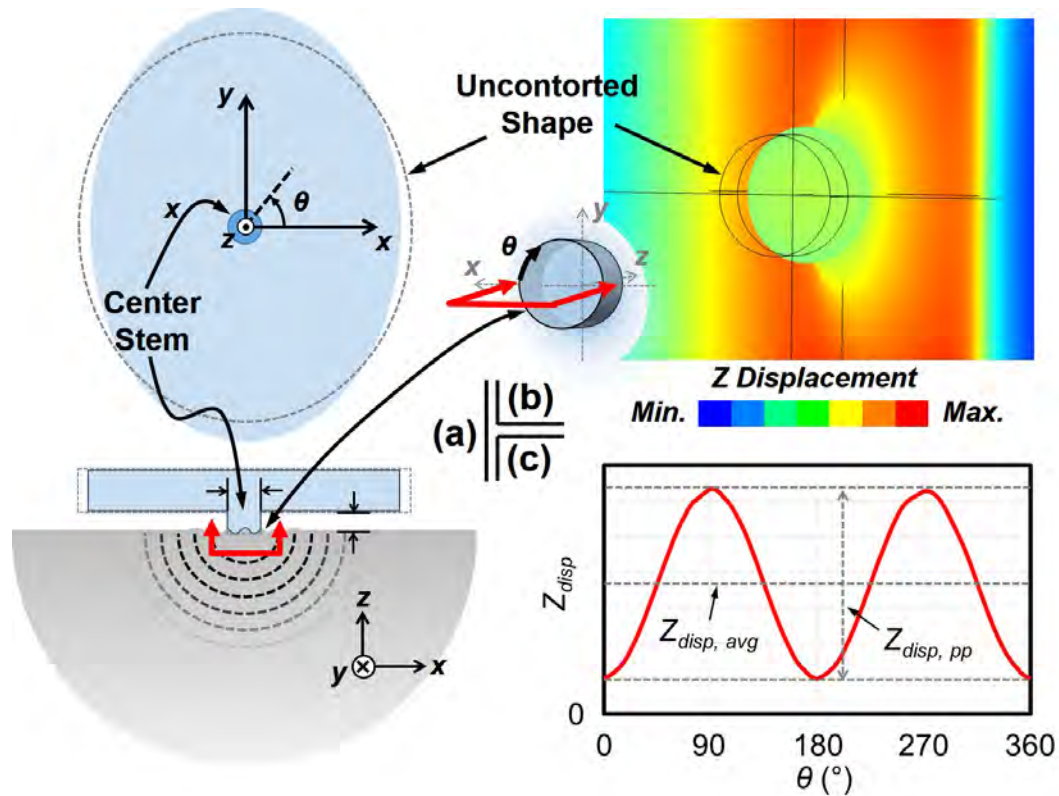


Figure 4.25: (a) Schematic of an elliptic disk dissipating energy into the substrate while vibrating. (b) FEA-simulated deformation of the center stem bottom (substrate is not shown for clarity). (c) Illustration of  $z$  displacement components versus rotating angle along the circumference at the bottom of the center stem when the elliptic disk vibrates in the wine glass mode shape.

## 4.6 Quality Factor of Elliptic-Disk Displacement Amplifiers

### 4.6.1 Quality Factor vs. Varying Ellipse Aspect Ratio $AR$

Fig. 4.24 reprints Fig. 2.26 of measured  $Q$  as a function of  $AR$  for several elliptic disks spanning 82.4-96.5 MHz on three different dies, indicating similar  $Q$  variations regardless of their  $Q$  magnitudes. Interestingly, when  $AR = 1.2$   $Q$  drops consistently from that of a conventional circular wine glass disk ( $AR = 1$ ), but increases afterwards as the  $AR$  rises.

### 4.6.2 $AR$ -Dependent Anchor Loss

The measured  $Q$  of 100,000 for a 96-MHz  $AR = 1$  circular disk is short of the expected intrinsic  $Q$  limit, most likely due to a combination of anchor loss and phonon-phonon in-

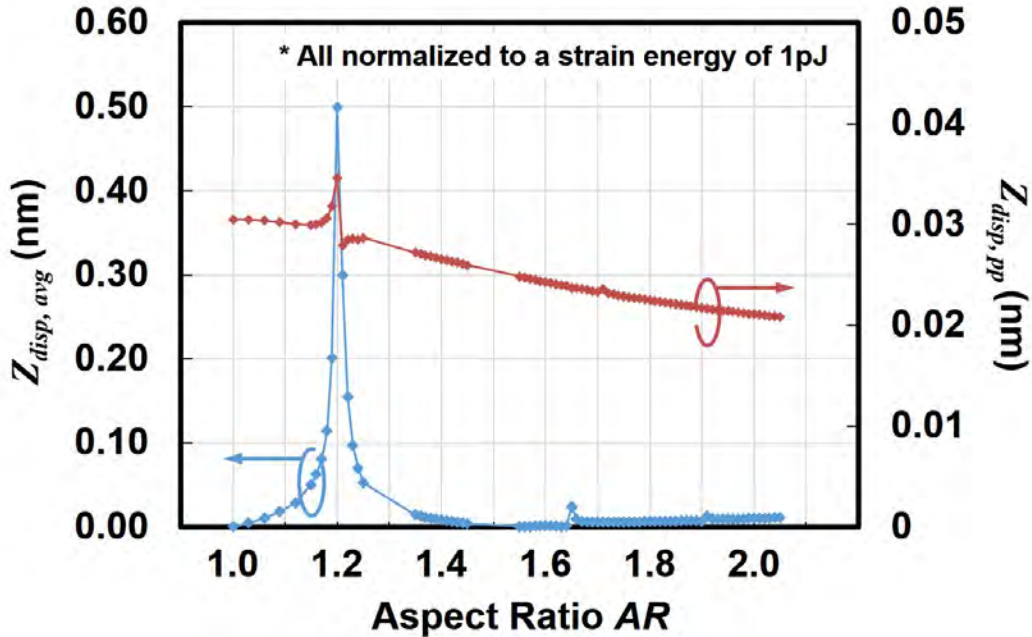


Figure 4.26: FEA-simulated z-displacement components versus aspect ratio, indicating a large vibration magnitude along the z axis when  $AR = 1.2$ .

teraction loss [34][47]. Since phonon-phonon interaction energy loss is less influenced by geometry, the reduction in  $Q$  as  $AR$  changes from 1 to 1.2 likely results from anchor dissipation. In particular, the center stem dissipates energy into the substrate via z-directed motion perpendicular to the substrate surface, as illustrated in Fig. 4.25(a).

4.25(b) and (c) plot the FEA-simulated mode shape around the anchor area and the z displacement amplitude as a function of angle  $\theta$  for a point along the circumference of the bottom of the center stem where it attaches to the substrate. Here, the z displacement comprises an average component “ $Z_{disp,avg}$ ” and a varying one with peak-to-peak magnitude “ $Z_{disp,pp}$ ”. An increase in either component raises the amount of energy lost to the substrate, thereby lowering  $Q$ .

4.26 plots the simulated z-displacement components, “ $Z_{disp,avg}$ ” and “ $Z_{disp,pp}$ ”, as a function of  $AR$  for elliptic disks with varying  $AR$  values. Here, the simulated  $1\ \mu\text{m}$ -radius,  $0.7\ \mu\text{m}$ -tall center stem seems to best couple the vibrating energy of the 95-MHz elliptic disk when the  $AR = 1.2$ , which produces the largest “ $Z_{disp,avg}$ ”, as shown in 4.26. This observation aligns well with the measurement results of 4.24 where the elliptic disks with an  $AR = 1.2$  yield the lowest  $Q$ ’s. In addition, aside from the circular disk case ( $AR = 1$ ),  $AR = 1.6$  yields the smallest “ $Z_{disp,avg}$ ”, which might explain why this  $AR$  yields the highest measured  $Q$ ’s for two of the curves in 4.24. For  $AR > 1.6$ , on the other hand, although “ $Z_{disp,avg}$ ” magnitudes rise as  $AR$  increases, “ $Z_{disp,pp}$ ”’s decrease, perhaps cancelling the former and allowing  $Q$ ’s on par with that of  $AR = 1.6$ , as shown in 4.24.

## Chapter 5

# Laser Frequency Trimming of Micromechanical Resonant Devices

In addition to  $Q$ , frequency accuracy of resoswitches is another important attribute as the resoswitch resonance frequency needs to align with the target radio frequency when used as a filter-power amplifier. This chapter will discuss laser frequency trimming technique for post-fabrication resonance frequency correction.

### 5.1 Overview

Over the past decade, vibrating high- $Q$  RF MEMS devices have played an important role in wireless communications. For example, piezoelectric film bulk acoustic resonators (FBARs) have served as front-end duplexers in CDMA phones since their introduction in 2001 [48]; timing oscillators referenced to capacitive gap-transduced micromechanical resonators have steadily increased their market share [49]; and new products that use single resonators to realize complete transceivers are on the horizon (this Thesis).

For applications enabled by vibrating MEMS technologies, resonator frequency stability and accuracy are two important attributes. To date, there are several solutions that attain adequate frequency stability. Examples of temperature compensation techniques that achieve thermal stability performance on par with AT-cut quartz crystals include introduction of silicon dioxide into structural materials [50], electrical stiffness compensation [51], and integrated micro-ovens combined with phase-locked loops [52]. On the short-term stability front, devices that satisfy GSM phase noise specifications have also been demonstrated [29][53]. On the other hand, an ultimate solution that enables accurate resonator frequency is still missing. A popular approach often used in commercial products is to embed vibrating devices in a fractional-N phase locked loop (PLL) circuit to produce an accurate output frequency [54][55]. This approach can generally yield frequency accuracy within 10 ppm via digital baseband control. However, fractional-N circuits inherently generate large spurs that can potentially interfere with other channel users. Although the spurs can be suppressed via

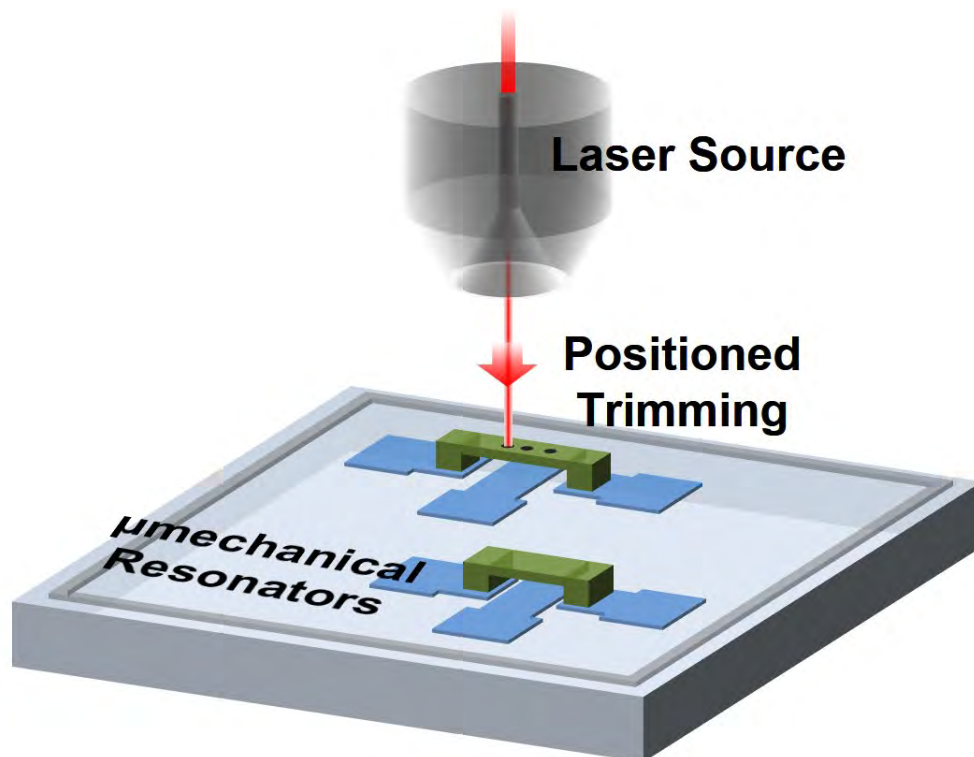


Figure 5.1: Schematic of laser trimming on micromechanical CC-beam resonators.

compensation circuits (i.e., narrowband loop filters, highly linear charge pumps, or advanced fractional modulators), the resultant excess phase noise, settling time, power consumption, and design complexity make this approach impractical for many communication applications.

Indeed, precise frequency trimming would obviate any need for fractional-N locking and rather allow direct embedding of a MEMS-based frequency-setting element into the closed-loop oscillator circuit within an integer-N PLL with resultant improvements in power consumption and noise performance. Beyond benefits to timing and frequency references, ppm-level trimming would also simplify the manufacture of very small percent bandwidth MEMS-based bandpass filters, such as needed for channel-selecting front-ends [56]. With percent bandwidths as small as 0.03%, such multiple-resonator mechanical circuits might require matching between adjacent resonators to within 10 ppm to avoid excessive passband distortion and spurious responses.

It is no surprise that there has been an abundance of re-search focused on trimming frequency by tailoring resonator structure mass and stiffness, including the use of metal diffusion [56], localized oxidation [57], or laser pulses [54][58]. However, these methods have faults. Although the metal diffusion technique is possible to trim up or down via different diffusion metals, it falls short of simultaneous bidirectional trimming flexibility. Additionally, metal diffusion and localized oxidation techniques require Joule heating through the structures, limiting applicable resonator geometries and materials—e.g., they will not work

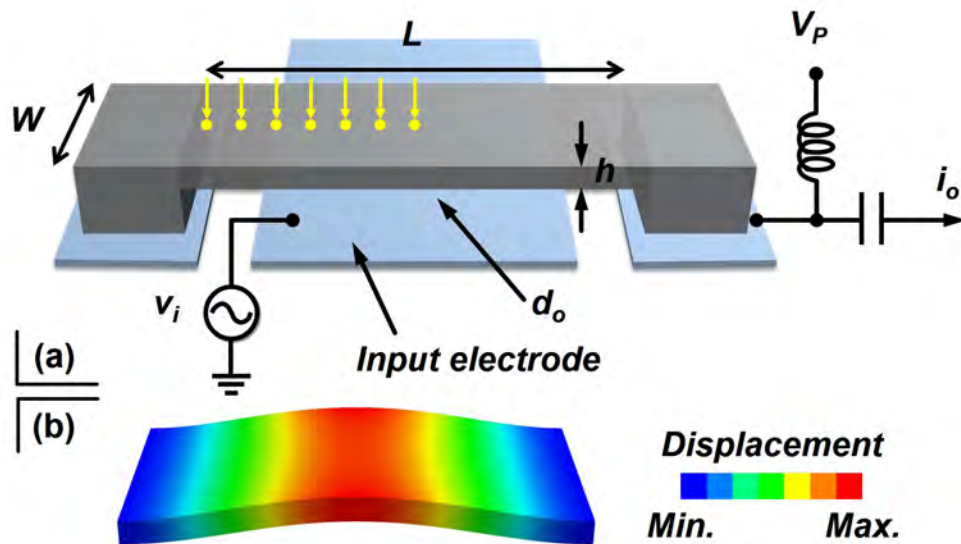


Figure 5.2: (a) Schematic of a CC-beam micromechanical resonator in a favored 2-terminal measurement setup. (b) Mode shape of fundamental transverse vibration by finite element analysis.

for nonconductive piezoelectric structural materials. In contrast, applying laser pulses to partially remove the structural material, as illustrated in Fig. 5.1, appears as a universal yet simple frequency trimming approach, as it enables bidirectional frequency tuning flexibility with no significant reduction in  $Q$  [58]. Unfortunately, the demonstrations of laser trimming so far lack a comprehensive analytical model that predicts the dependence of frequency shift on laser blast location, which otherwise would enable an efficient trimming sequence that consists of the minimum number of laser pulses for a target tuning amount.

To remedy this, an analytical model that employs rotational springs to model stiffness reduction induced by laser blasts captures well the frequency shift dependence on trimming location. Here, a fabricated micromechanical clamped-clamped beam (CC-beam) resonator trimmed by a Nd:YAG laser serves as the demonstration vehicle, verifying the efficacy of laser trimming and the accuracy of the analytical model. While presenting a good match to the measurement results of CC-beams, the theory enables a modeling framework for laser trimming on generic beam resonators. For instance, it would work for cantilevers or free-free beam resonators if the according boundary conditions are used in the theory.

## 5.2 Frequency Trimming Fundamentals

Fig. 5.2 (a) presents a schematic of a micromechanical CC-beam resonator in a typical bias and excitation configuration. The CC-beam resonator comprises a beam anchored at both ends, with an underlying electrode typically spaced 100 nm (i.e.,  $d_o$  in Fig. 5.2 (a))

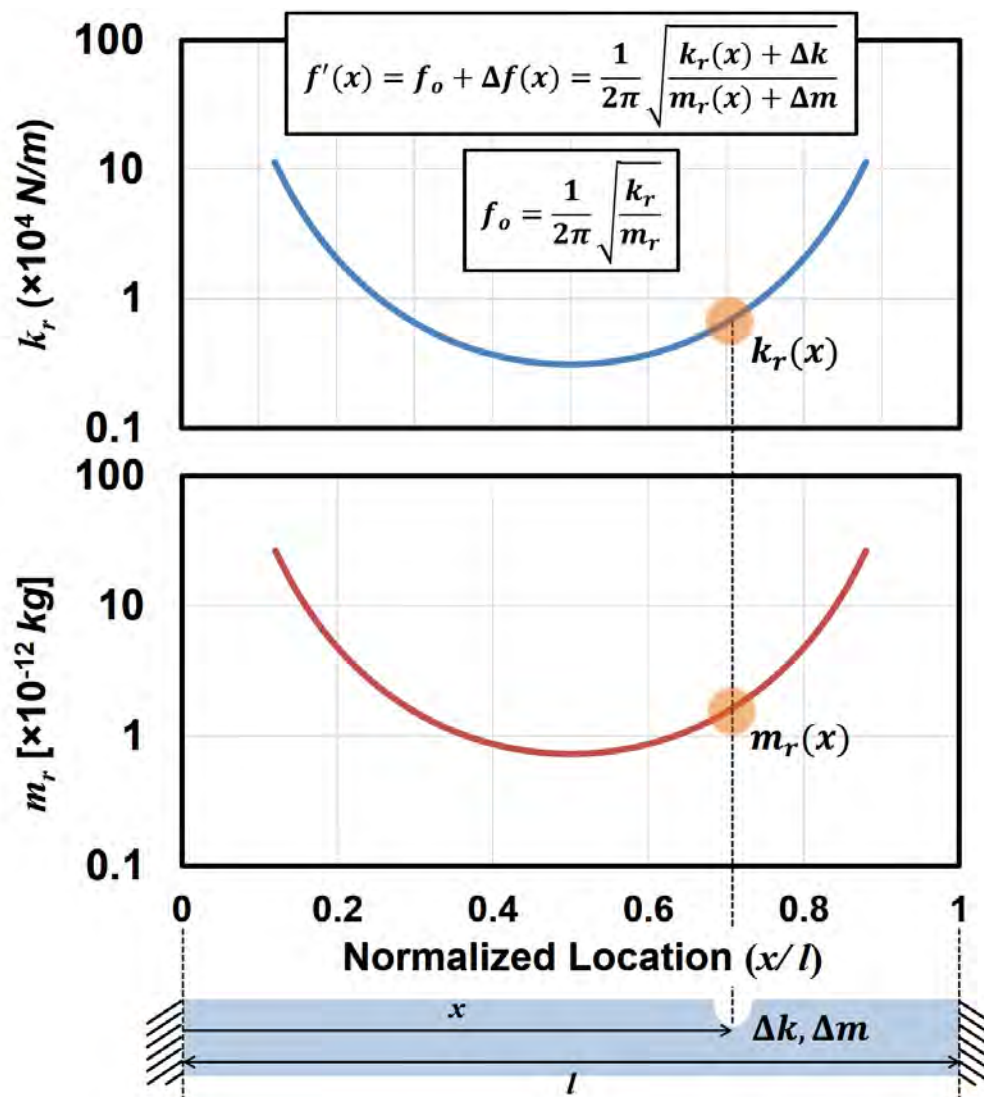


Figure 5.3: Effective mass and stiffness for a CC-beam ( $(l, w, h) = (40 \mu\text{m}, 10 \mu\text{m}, 2 \mu\text{m})$ ), showing a trimming hole generates location-dependent stiffness and mass deviations and therefore a location-dependent frequency shift.

below. Under normal operation, a dc-bias  $V_P$  is applied to the beam structure via a bias-T circuit, and ac excitation  $v_i$  to the underlying input electrode, where  $V_P \gg v_i$ . This combination of voltages generates an electrostatic force at the frequency of  $v_i$  that drives the beam into vertical resonance vibration (i.e., perpendicular to the plane of the substrate) as the simulated mode shape shown in Fig. 5.2 (b) when the frequency of  $v_i$  matches the beam resonance frequency [59]. The resonance frequency for CC-beam resonators (or for

any mechanical structure) takes a general form

$$f_o = \frac{1}{2\pi} \sqrt{\frac{k_r}{m_r}} \quad (5.1)$$

where  $k_r$  and  $m_r$  are the effective stiffness and mass, respectively, at a certain location along the beam. Fig. 5.3 plots the effective mass and stiffness as a function of normalized location for a polysilicon CC-beam resonator sized as  $(l, w, h) = (40 \text{ } \mu\text{m}, 10 \text{ } \mu\text{m}, 2 \text{ } \mu\text{m})$ , where both parameters exhibit symmetrical distribution and the minimum magnitudes at the midpoint.

As mentioned, laser pulses blasts induce deviations to the effective stiffness and mass of Fig. 5.3. The deviations shift the resonance frequency  $f_o$  by a magnitude of  $\Delta f$  to  $f'$ :

$$f' = f_o + \Delta f = \frac{1}{2\pi} \sqrt{\frac{k_r + \Delta k}{m_r + \Delta m}} \quad (5.2)$$

where  $\Delta f$  and  $\Delta m$  represent stiffness and mass offsets, respectively. The mass deviation  $\Delta m$ -induced frequency shift linearly proportional to the ratio between removed mass in magnitude over location-dependent  $m_r$  [59]. For a fixed size of removed mass, the dependence of  $\Delta m$ -induced frequency shift on location would follow the trend of  $m_r$  in Fig. 5.3. On the other hand, the magnitude of stiffness deviation  $\Delta k$  itself depends on the vibrating mode shape. As will be seen, instead of calculating the magnitude of  $\Delta k$ , a model that includes rotational springs at laser blast locations directly solves resultant resonance frequencies of trimmed CC-beams.

### 5.3 Modeling of Laser Trimming of CC-Beam Resonators

Fig. 5.4 depicts a trimmed CC-beam as an example where the beam has a width  $w$  of with three  $\frac{1}{5}w$ -diameter laser spots on the surface. The procedure used here to estimate the resonance frequency of such a CC-beam outlines as follows: first, divide the beam into several parallel beams separating the intact portions from the trimmed portions; then, calculate the resonance frequency of the trimmed portions using the model discussed in a bit; finally, combine the resultant frequency of the trimmed portions with that of the intact parts to estimate the overall frequency. Performing the first step to the CC-beam of Fig. 5.4 yields one  $1/5w$ -wide partial beam with the three laser blasts and two  $2/5w$ -wide intact beams, where the trimmed beam portion approximates the laser blasts as uniformly cut across the surface with a crack-like cross-section profile as indicated by the atomic force microscopy (AFM) image shown in [54]. For the fact that the cracks essentially soften the effective dynamic stiffness of the beam and thereby allow the structure to have extra bending while vibrating in the transverse modes, rotational springs would successfully capture stiffness modification induced by the laser blasts.

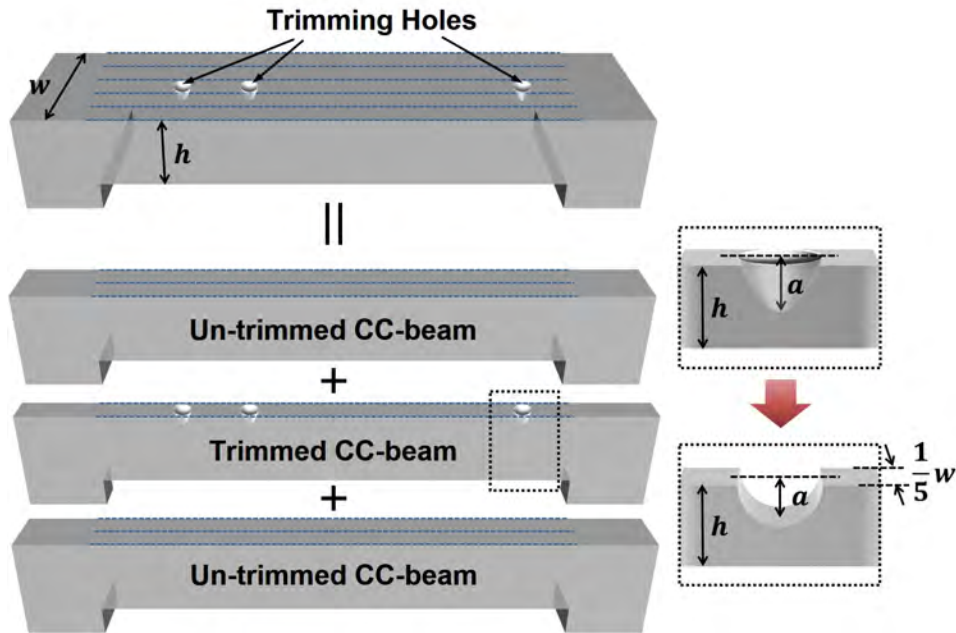


Figure 5.4: Schematic of a trimmed CC-beam where the CC-beam is decomposed by two intact CC-beams and one CC-beam that has the trimming holes across the width.

Fig. 5.4 depicts a CC-beam with a width of  $w$  and three  $\frac{1}{5}w$ -diameter laser blasts on the surface. The procedure to obtain  $\Delta k$ -induced resonance frequency change for such a CC-beam outlines as follows: (1) divide the beam into several parallel beams separating intact portions from trimmed portions; (2) calculate the resonance frequency of trimmed portions using a model discussed shortly; and (3) combine the resultant frequency with that of the intact parts to attain the final resonance frequency. Performing the first step to the CC-beam of Fig. 5.4 yields one  $\frac{1}{5}w$ -wide partial beam with three laser blasts and two  $\frac{2}{5}w$ -wide intact beams. AFM image provided in [54] shows that laser blasts exhibit crack-like cross-section profiles. Thus, for simplicity, the model represents laser blasts as cracks uniformly cut across the beam surface (*cf.* Fig. 5.4).

### 5.3.1 Stiffness Change—a Rotational Spring Model

The cracks introduce a spring softening effect, allowing extra bending when the beam vibrates in the transverse direction. The extra bending suggests that rotational springs to capture the stiffness modification [60]. Fig. 5.5 plots an equivalent mechanical model for the trimmed portion of Fig. 5.4, in which rotational springs ( $j = 1, 2, \text{ and } 3$ ) represent the corresponding laser blasts with depths of  $a_j$ . The beam now consists of  $n$  rotational springs and  $(n + 1)$  segments (i.e.,  $n = 3$  in this case). One possible way to attain the resonance frequency of such a mechanical model is to solve the boundary conditions, using the state vectors at junctions of beam segments and rotational springs and the state-vector transfer matrixes of

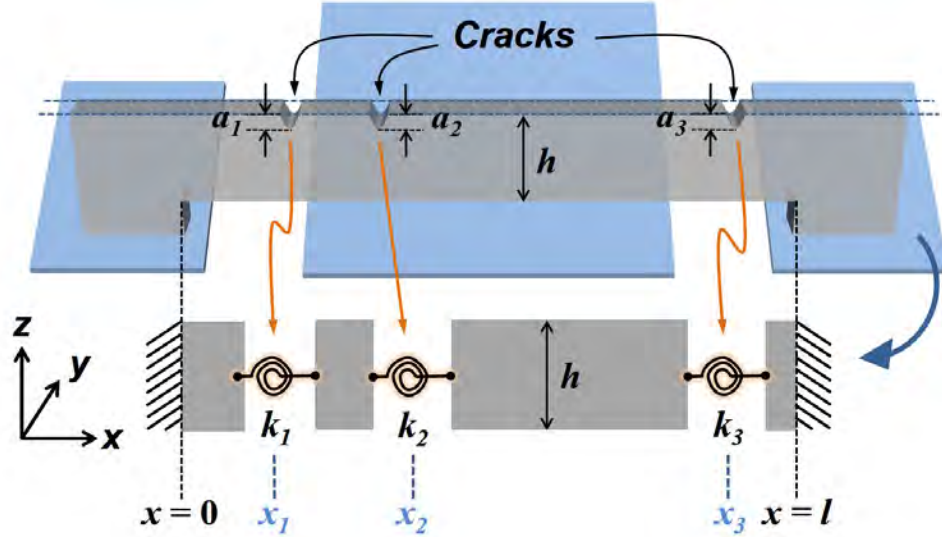


Figure 5.5: Schematic of a trimmed CC-beam and its mechanical model, where the trimming spots are modeled as cracks. Three cracks are shown in this example with depths of  $a_1$ ,  $a_2$ , and  $a_3$ , at locations  $x_1$ ,  $x_2$ , and  $x_3$ , respectively. Each of the cracks is modeled as a rotational spring ( $k_1$ ,  $k_2$ , and  $k_3$ ).

of beam segments and rotational springs [60].

Considering a beam structure in free transverse vibration governed by Euler-Bernoulli beam theory, the displacement  $\phi(x)$  takes on the form

$$\phi''''(x) - \lambda^4 \phi(x) = 0, \quad (5.3)$$

where  $\lambda$ , the frequency parameter, takes the form

$$\lambda^4 = \omega^2 \frac{\rho A}{EI} \quad (5.4)$$

in which  $\Omega$  is the angular resonance frequency;  $E$  and  $\rho$  are the Young's modulus and density of the structural material, respectively;  $A$  is the cross-section area of the beam;  $I$  is the area moment of inertia about  $x$  axis in Fig. 5.5. From (5.3), one possible set of state vectors at the left ( $x = 0$ ) and right ( $x = L$ ) ends of the entire beam takes the forms

$$\mathbf{S}_o^+ = \begin{bmatrix} \phi(0^+) \\ \phi'(0^+) \\ EI\phi'''(0^+) \\ -EI\phi''(0^+) \end{bmatrix} \text{ and } \mathbf{S}_L^- = \begin{bmatrix} \phi(L^-) \\ \phi'(L^-) \\ -EI\phi'''(L^-) \\ EI\phi''(L^-) \end{bmatrix}, \quad (5.5)$$

respectively. Similarly, the state vectors for the left and right ends of the beam segment

sandwiched by laser blasts at  $x_{j-1}$  and  $x_j$  are

$$\mathbf{S}_{j-1}^+ = \begin{bmatrix} \phi(x_{j-1}^+) \\ \phi'(x_{j-1}^+) \\ EI\phi'''(x_{j-1}^+) \\ -EI\phi''(x_{j-1}^+) \end{bmatrix} \text{ and } \mathbf{S}_j^- = \begin{bmatrix} \phi(x_j^-) \\ \phi'(x_j^-) \\ -EI\phi'''(x_j^-) \\ EI\phi''(x_j^-) \end{bmatrix}, \quad (5.6)$$

respectively.

### Rotational Spring Transfer Matrix

The magnitude of the additional rotational angle  $\Delta\theta(x_j)$  induced by the laser blast at  $x_j$  relates to the corresponding rotational spring  $k_j$  via

$$\theta(x_j^+) = \theta(x_j^-) + \Delta\theta(x_j) \quad (5.7)$$

where

$$\Delta\theta(x_j) = \frac{1}{k_j} M(x_j)$$

where  $M$  is the moment applied on the beam. Recalling that  $\theta(x) = \phi'(x)$  for small angles and that the differential equation governing an elastic curve

$$\phi''(x_j) = \frac{M}{EI}, \quad (5.8)$$

(5.7) becomes

$$\phi'(x_j^+) = \phi'(x_j^-) + \frac{EI}{k_j} \phi''(x_j^-). \quad (5.9)$$

Rewriting (5.9) using the state vectors yields

$$\begin{bmatrix} \phi(x_j^+) \\ \phi'(x_j^+) \\ EI\phi'''(x_j^+) \\ -EI\phi''(x_j^+) \end{bmatrix} = \begin{bmatrix} 1 & 0 & 0 & 0 \\ 0 & 1 & 0 & k_j^{-1} \\ 0 & 0 & -1 & 0 \\ 0 & 0 & 0 & -1 \end{bmatrix} \begin{bmatrix} \phi(x_j^-) \\ \phi'(x_j^-) \\ -EI\phi'''(x_j^-) \\ EI\phi''(x_j^-) \end{bmatrix} \quad (5.10)$$

$$\rightarrow \mathbf{S}_j^+ = \mathbf{J}_j \cdot \mathbf{S}_j^-,$$

where  $\mathbf{J}_j$  is the transfer matrix of the rotational spring  $k_j$ .

From Castiglianos second theorem, the additional rotation equals the first partial derivative of the strain energy in the rotational spring with respect to the applied moment, taking on the form

$$\Delta\theta = \frac{\partial U_T}{\partial M}, \quad (5.11)$$

where  $U_T$  represents the strain energy induced by the crack. The magnitude of the strain energy can be obtained by integrating the strain energy density  $J_S$  over the crack depth, yielding

$$U_T = w' \int_0^a J_S da, \quad (5.12)$$

where  $w'$  is the width of the cracked beam portion and the strain energy  $J_S$  takes the form

$$J_S = \frac{1 - \nu^2}{E} K_I^2, \quad (5.13)$$

where is the stress intensity factor of an opening mode fracture (i.e., Mode I). Here, based on an empirical function developed for macroscopic single-edge crack beam specimen under pure bending moment of  $M$  [61], the magnitude of the stress intensity factor  $K_I$  takes the form

$$K_I = \sigma_0 \sqrt{\pi a} \times F(\alpha), \quad (5.14)$$

where  $\sigma_0 = \frac{6M}{w'h^2}$ ,  $\alpha = \frac{a}{h}$ ,

where  $F(\alpha)$  is an adjusting factor based on empirical data

$$F(\alpha) = 1.12 - 1.40\alpha + 7.33\alpha^2 - 13.1\alpha^3 + 14.0\alpha^4. \quad (5.15)$$

Plugging (5.12) and (5.14) into (5.11) and then comparing with (5.7) finally yields

$$k_j^{-1} = \frac{6\pi h(1 - \nu^2)}{EI} I_C(\alpha_j), \quad (5.16)$$

where  $I_C(\alpha_j) = \frac{1}{2}\alpha_j^2 F^2(\alpha_j)$ .

### Beam Segment Transfer Matrix

Next, the beam segment between  $x_{j-1}$  and  $x_j$  can be described by a transfer matrix  $\mathbf{T}_j$  that links the state vectors at both ends of the beam segment, such as

$$\mathbf{S}_j^- = \mathbf{T}_j \cdot \mathbf{S}_{j-1}^+, \quad (5.17)$$

where the transfer matrix  $\mathbf{T}_j$  takes on the form

$$\mathbf{T}_j = \begin{bmatrix} K_1(\lambda_j) & K_2(\lambda_j)/\lambda & K_4(\lambda_j)/EI\lambda^3 & -K_3(\lambda_j)/EI\lambda^2 \\ \lambda K_4(\lambda_j) & K_1(\lambda_j) & K_3(\lambda_j)/EI\lambda^2 & -K_2(\lambda_j)/EI\lambda \\ -\lambda^3 EIK_2(\lambda_j) & -\lambda^2 EIK_3(\lambda_j) & -K_1(\lambda_j) & \lambda K_4(\lambda_j) \\ \lambda^2 EIK_3(\lambda_j) & \lambda EIK_4(\lambda_j) & K_2(\lambda_j)/\lambda & -K_1(\lambda_j) \end{bmatrix} \quad (5.18)$$

where  $l_j (= x_j - X_{j-1})$  is the segment length and  $K_1$  to  $K_4$  equal to

$$\begin{aligned} K_1(x) &= \frac{1}{2}(\cosh(x) + \cos(x)) \\ K_2(x) &= \frac{1}{2}(\sinh(x) + \sin(x)) \\ K_3(x) &= \frac{1}{2}(\cosh(x) - \cos(x)) \\ K_4(x) &= \frac{1}{2}(\sinh(x) - \sin(x)) \end{aligned} \quad (5.19)$$

Multiplying all transfer matrices of the rotational springs and the beam segments (i.e., as described by (5.10) and (5.18), respectively) renders the transfer matrix of the entire  $n$ -crack beam  $\mathbf{Q}$ , which links the state vectors of the right end (i.e.,  $\mathbf{S}_L^-$ ) and left end (i.e.,  $\mathbf{S}_0^+$ ) of the beam:

$$\begin{aligned} \mathbf{S}_L^- &= \mathbf{T}_{n+1} \cdot \mathbf{J}_n \cdot \mathbf{T}_n \cdot \mathbf{J}_{n-1} \cdots \mathbf{J}_2 \cdot \mathbf{T}_2 \cdot \mathbf{J}_1 \cdot \mathbf{T}_1 \cdot \mathbf{S}_0^+ \\ &\Rightarrow \mathbf{S}_L^- = \mathbf{Q} \cdot \mathbf{S}_0^+, \end{aligned} \quad (5.20)$$

On the other hand, the boundary conditions at both ends of the beam take on the matrix forms

$$\begin{aligned} \begin{bmatrix} B_{11}^0 & B_{12}^0 & B_{13}^0 & B_{14}^0 \\ B_{21}^0 & B_{22}^0 & B_{23}^0 & B_{24}^0 \end{bmatrix} \begin{bmatrix} \phi(0^+) \\ \phi'(0^+) \\ EI\phi'''(0^+) \\ -EI\phi''(0^+) \end{bmatrix} = 0 &\Rightarrow \mathbf{B}_0 \cdot \mathbf{S}_0^+ = 0 \\ \begin{bmatrix} B_{11}^L & B_{12}^L & B_{13}^L & B_{14}^L \\ B_{21}^L & B_{22}^L & B_{23}^L & B_{24}^L \end{bmatrix} \begin{bmatrix} \phi(L^-) \\ \phi'(L^-) \\ -EI\phi'''(L^-) \\ EI\phi''(L^-) \end{bmatrix} = 0 &\Rightarrow \mathbf{B}_L \cdot \mathbf{S}_L^- = 0 \end{aligned} \quad (5.21)$$

Combining (5.20) to (5.21) leads to

$$\begin{aligned} \mathbf{B}_0 \cdot \mathbf{S}_0^+ &= 0 \\ \mathbf{B}_L \cdot \mathbf{S}_L^- &= \mathbf{B}_L \cdot \mathbf{Q} \cdot \mathbf{S}_0^+ = 0 \\ \Rightarrow \begin{bmatrix} \mathbf{B}_0 \\ \mathbf{B}_L \mathbf{Q} \end{bmatrix} \mathbf{S}_0^+ &= \mathbf{A} \cdot \mathbf{S}_0^+ = 0, \end{aligned} \quad (5.22)$$

The determinant of the *4times4* matrix  $\mathbf{A}$  in 5.22 needs to vanish for the existence of non-zero solutions:

$$\det(\mathbf{A}) = 0 \quad (5.23)$$

Solving (5.23) yields the value of the frequency parameter  $\lambda$  and finally attain the natural frequency  $\omega$  of the  $n$ -crack beam via (5.4).

Here, in the case of clamped-clamped supports, the boundary condition matrices  $\mathbf{B}_0$  and  $\mathbf{B}_L$  in (5.21) are simply

$$\mathbf{B}_0 = \mathbf{B}_L = \begin{bmatrix} 1 & 0 & 0 & 0 \\ 0 & 1 & 0 & 0 \end{bmatrix}, \quad (5.24)$$

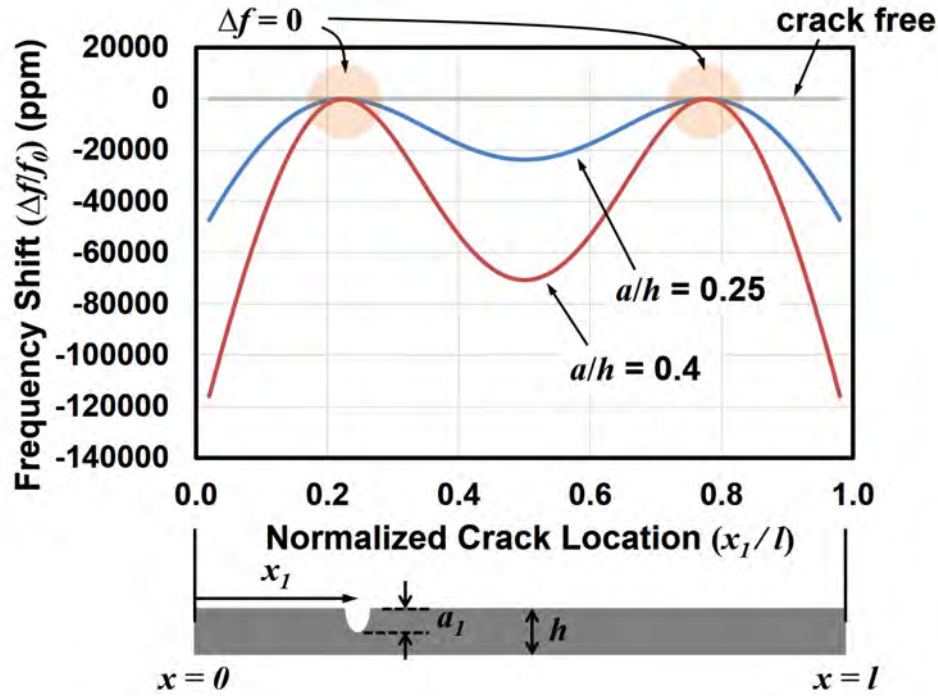


Figure 5.6: Frequency shift (relative to a crack-free version) versus crack location for a CC-beam resonator with dimensions of  $(l, w, h) = (40 \mu\text{m}, 10 \mu\text{m}, 2 \mu\text{m})$  estimated by the analytical model.

and there (5.23) reduces to

$$\det(\mathbf{A}) = Q_{13}Q_{24} - Q_{23}Q_{14} = 0, \quad (5.25)$$

where  $Q_{mn}$  represents the element in the overall transfer matrix  $\mathbf{Q}$  in (5.20). Fig. 5.6 plots the frequency shift as a function of normalized crack location for two normalized crack depth values for a single crack CC-beam with dimensions of  $(l, w, h) = (40 \mu\text{m}, 10 \mu\text{m}, 2 \mu\text{m})$ . For most beam locations, the amount of frequency shift increases as the crack depth increases due to a lowered magnitude of rotational spring stiffness. However, there are two particular spots, symmetrically located at  $x/l = 0.224$  and  $0.776$ , where the resonance frequency remains unaffected by laser blasts. Zero frequency change indicates no additional rotation at the two particular locations, where, according to (5.7) and (5.8), both the internal moment and second derivative of deflection of the fundamental flexural mode shape are zero. In other words, the two locations represent the inflection points of such a mode shape. Interestingly, it can be proved that the two locations also coincide with the nominal nodal line locations of the fundamental flexural mode of a free-free beam resonator [62]. Fig. 5.7 plots the resonance frequency shift estimated by the analytical model alongside the FEA simulations by CoventorWare<sup>®</sup>, showing that the theory matches FEA prediction fairly well.

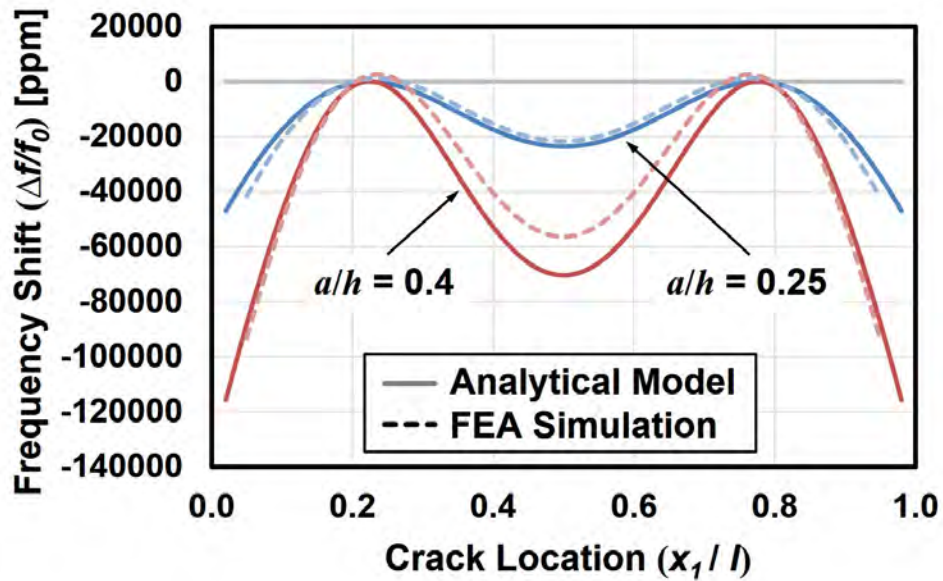


Figure 5.7: Comparison of frequency shift versus crack location using the analytical model and CoventorWare FEA for a CC-beam resonator with dimensions of  $(l, w, h) = (40 \mu\text{m}, 10 \mu\text{m}, 2 \mu\text{m})$ .

### 5.3.2 Combining Trimmed and Un-trimmed Beam Portions

Now, we are ready to combine the resultant resonance frequency of the cracked beam portion with the intact portions and attain the overall resonance frequency. The magnitudes of strain energy in (5.12) and crack-induced additional rotation in (5.11) are proportional to crack lateral dimension  $w$ . Thus, according to (5.7), for a first-order approximation, the compliance  $k_j^{-1}$  of the entire beam would be the compliance  $k_j^{-1}$  of the cracked beam portion multiplied by a dimension factor of  $\gamma_{dim} = w'/w$ . Here, we assume the laser blast has a semicircle cross-section profile with a depth of and an opening width of  $2a$  (i.e.,  $w' = 2a$ ).

In addition, edge cracks exhibit higher stress intensity factors compared to cracks with the same dimension but buried in the middle of the beam. The edge effect that further lowers the beam stiffness should be considered in the correction factor together with the dimension factor when combining the cracked beam portion with intact ones.

In fact, comparing the compliances of two single-crack beam specimens shown in Fig. 5.8–(upper) one with a single crack that only extends partially over the beam width to capture both the edge and dimension effects and (lower) one with an edge crack to represent the cracked beam portion developed in the previous section—directly yields the overall correction factor. Particularly, according to (5.16), the compliance (i.e.,  $k_j^{-1}$ ) is proportional to the magnitude of  $I_C$  and thereby an overall correction factor of the overall beam compliance

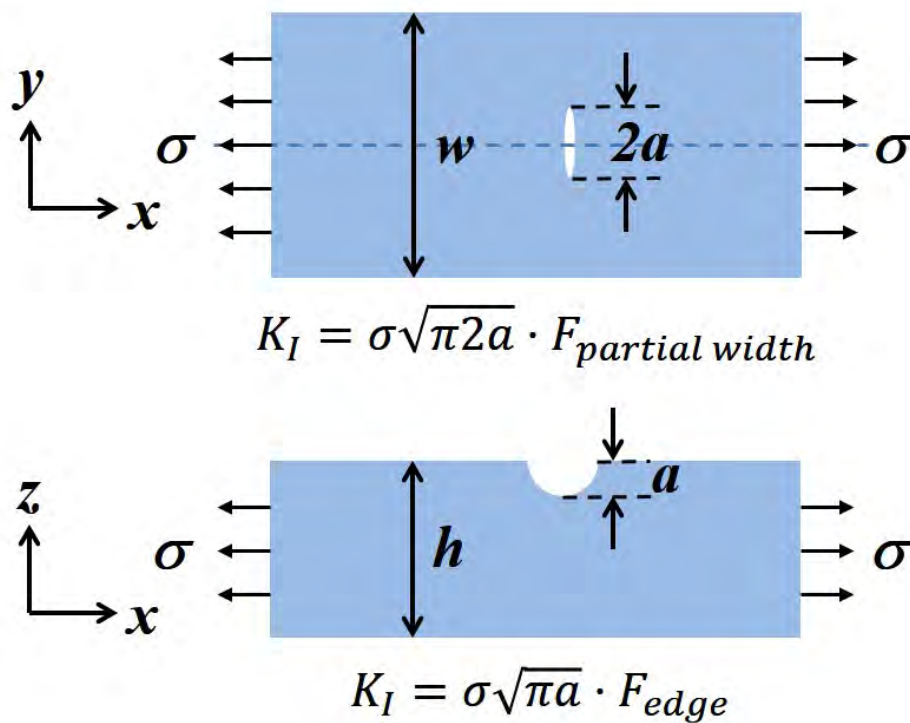


Figure 5.8: Stress intensity factor test specimen used to estimate the adjusting factors for partial-width trimming holes: (a) a partial-width central hole compared to (b) an edge hole.

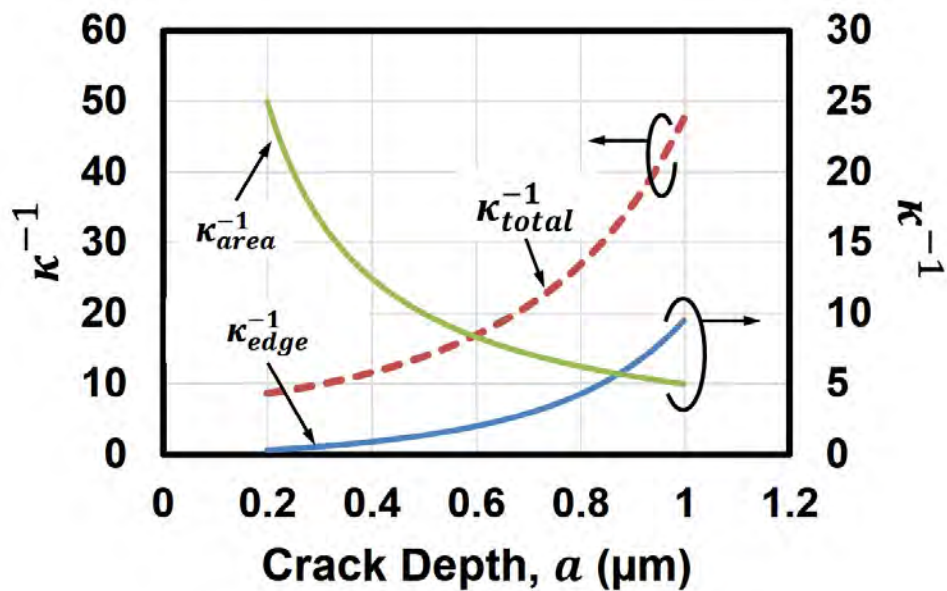


Figure 5.9: Adjusting factors (inverse) for partial-width trimming holes for varying crack depth, showing factors due to area and edge effects.

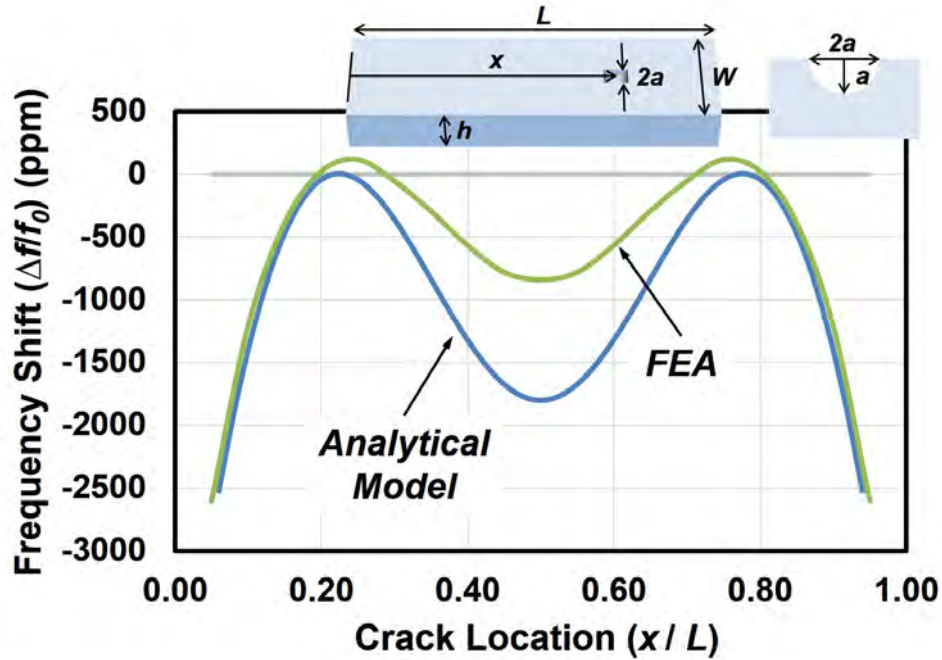


Figure 5.10: Frequency shift versus trimming location in a CC-beam  $((l, w, h) = (40 \mu\text{m}, 10 \mu\text{m}, 2 \mu\text{m}))$  resonator with a 1- $\mu\text{m}$ -diameter 0.5- $\mu\text{m}$ -deep circular hole estimated by FEA and the analytical model (only considering stiffness change).

takes the form [63]

$$\gamma_{total} = \gamma_{dim} \times \gamma_{edge} = \frac{I_{C, \text{partial width}}}{I_{C, \text{edge}}} = \frac{\left(\frac{2a}{w}\right)^2 F_{\text{partial width}}^2}{\left(\frac{a}{h}\right)^2 F_{\text{edge}}^2},$$

$$\text{where } F_{\text{partial width}} = \frac{1 - 0.5\left(\frac{2a}{w}\right) + 0.326\left(\frac{2a}{w}\right)^2}{\sqrt{1 - \left(\frac{2a}{w}\right)}}, \quad (5.26)$$

$$F_{\text{edge}} = 1.12 - 0.23\left(\frac{a}{h}\right) + 10.6\left(\frac{a}{h}\right)^2 - 21.7\left(\frac{a}{h}\right)^3 + 30.4\left(\frac{a}{h}\right)^4.$$

Fig. 5.9 plots the inverses of the dimension factor,  $\gamma_{dim}^{-1}$  (i.e.,  $(\frac{2a}{w})^{-1}$ ), of the edge effect correction factors,  $\gamma_{edge}^{-1}$ , and of the overall correction factor,  $\gamma_{total}^{-1}$ , showing that while the dimension correction factor reduces as the crack depth  $a$  increases, the overall correction factor in fact increases due to the edge effect factor.

Plugging in values into (5.26) for the 0.5  $\mu\text{m}$ -deep single-crack beam used in the previous section as an example gives a total correction factor  $\gamma_{total}$  of 0.0718 that consists of the dimension factor of 0.1 (i.e.,  $=1 \mu\text{m}/10 \mu\text{m}$ ) and the edge effect factor of 0.718. Fig. 5.10 plots the overall frequency shift of the entire cracked beam. The frequency shift reduces after combining the cracked portion with intact ones. For example, at the midpoint it reduces from the initial -23,642 ppm of Fig. 5.9 to -1,803 ppm. Note that the analytical model has

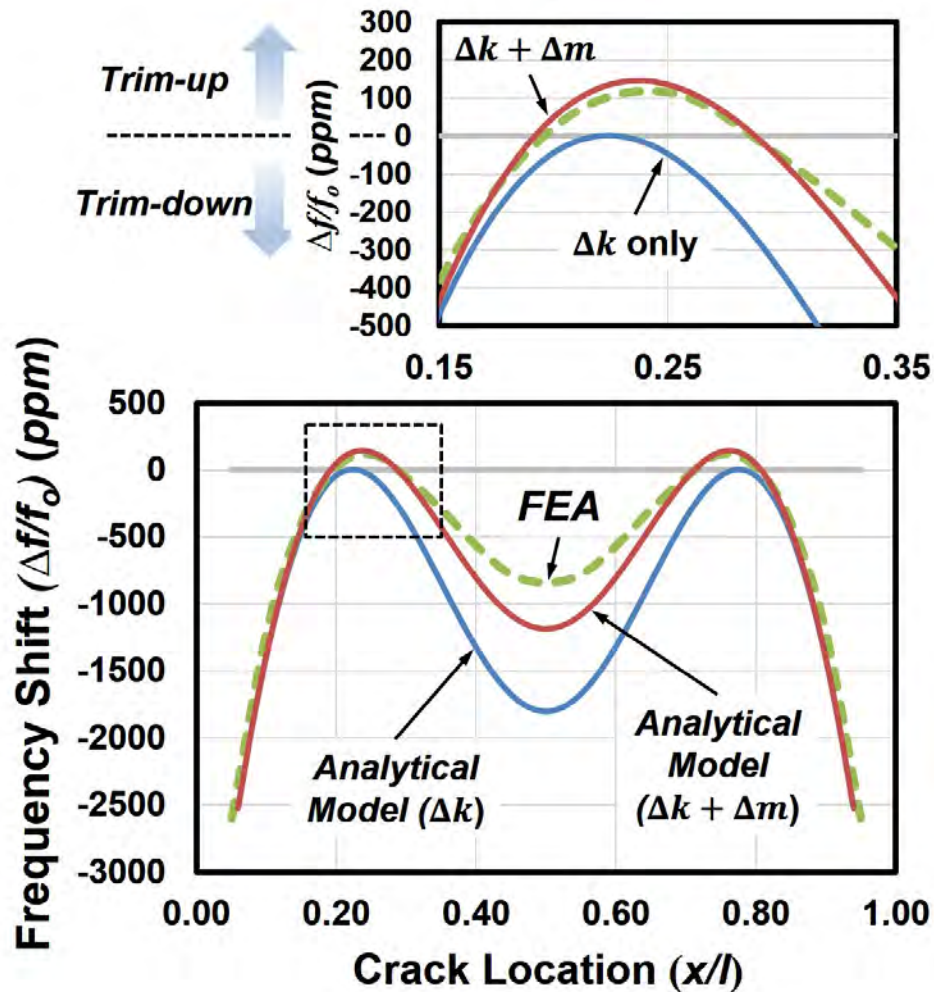


Figure 5.11: Frequency shift pattern using the analytical model added with mass removal effects, showing positive frequency shifts (i.e., trim-up) regions.

yet only emphasized stiffness-induced frequency shift, thereby resulting in an over-estimated frequency shift magnitude compared to FEA simulation, as shown in Fig. 5.10.

### 5.3.3 Mass Change

As denoted in 5.2, mass removal of structural material by laser pulses also accounts for frequency changes. Particularly, the magnitude of removed mass is usually much smaller than the effective mass  $m_r$  and therefore the amount of frequency shifts due to mass removal takes the approximated form (where  $\Delta m$  is a negative value)

$$\Delta f \approx -\frac{1}{2} \frac{\Delta m}{m_r} f_o. \quad (5.27)$$

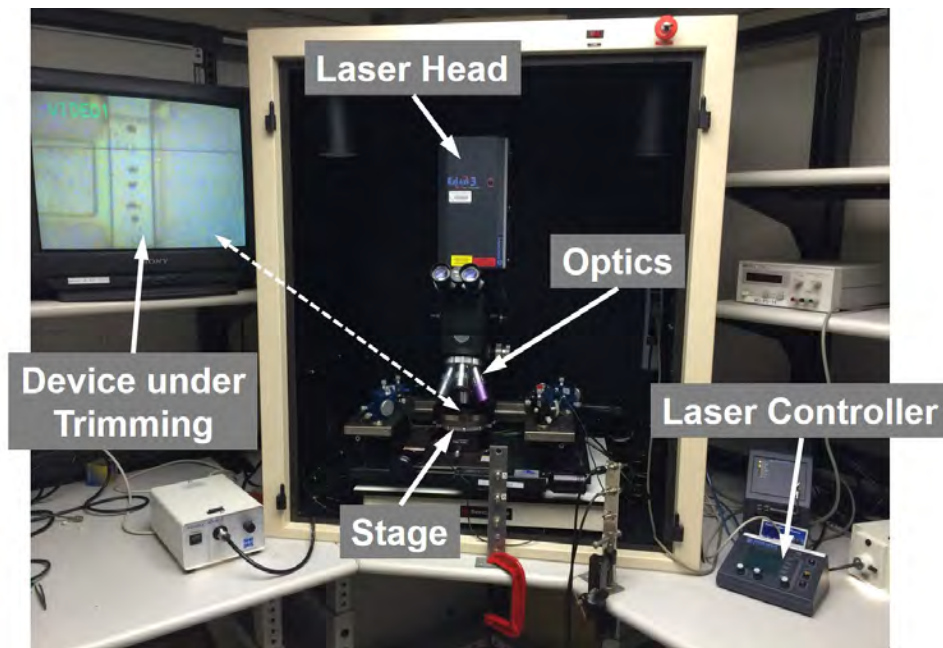


Figure 5.12: Photograph of the apparatus used to trim micromechanical CC-beam resonators.

For the laser blast profile shown in the inset of Fig. 5.11, the removed mass equals

$$\Delta m = \frac{1}{2}\pi a^2 w' \rho = \pi a^3 \rho, \quad (5.28)$$

where  $\rho$  is the material density. Adding the mass-induced frequency shift to the result of Fig. 5.10 yields a better match to what FEA predicts, shown in Fig. 5.11.

More importantly, Fig. 5.11 indicates that mass removal effects a net *positive* frequency shift (i.e., trim-up) in the vicinity of the two specific locations where, as mentioned before, the stiffness model predicts zero frequency changes. This allows coexisting bidirectional frequency trimming controlled by targeting laser pulses, much more flexible than the metal diffusion method in [56], which requires different add-on metal materials for either trim-up or trim-down.

## 5.4 Experimental Results

To demonstrate, micromechanical CC-beam resonators were first fabricated by a micro-fabrication process identical to that of [59], and then trimmed using a laser system (EZLaze 3) based on Nd:YAG laser (Class 3b). Fig. 5.12 presents the experimental apparatus used in this work, where the laser head mounted onto the microscope unit of a probe station allows a controllable laser spot size as small as 1.5-2  $\mu\text{m}$ . A drawback of this apparatus is that

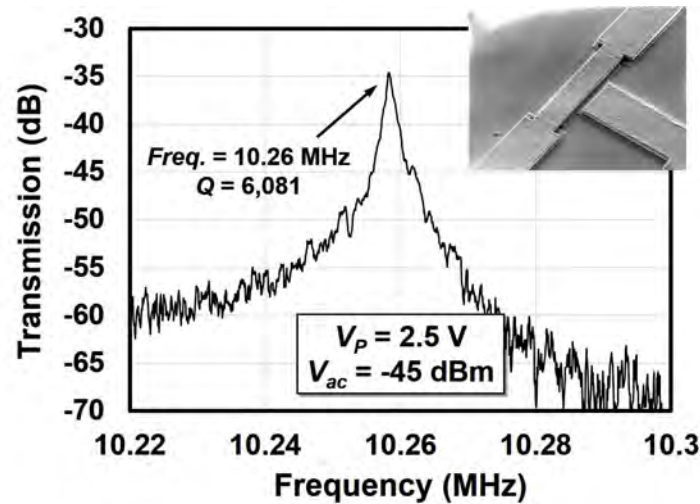


Figure 5.13: Measured frequency response of a fabricated CC-beam resonator with dimensions of  $(l, w, h) = (40 \mu\text{m}, 10 \mu\text{m}, 2 \mu\text{m})$ .

the positioning stage is manual, which lacks precision control. Results with better match to theory would probably be more attainable than the measured data to be shown if automatic positioning system were available [54]. Nevertheless, the experimental set-up is sufficient to demonstrate the laser trimming technique.

#### 5.4.1 Location-Dependent Frequency Trimming

Fig. 5.13 plots a measured frequency response of a fabricated CC-beam resonator sized as  $(l, w, h) = (40 \mu\text{m}, 10 \mu\text{m}, 2 \mu\text{m})$  with its SEM image inserted as an inset. Fig. 5.14 presents the SEM of the CC-beam after being trimmed with a fixed energy level at  $300 \mu\text{J}$  at varying locations, where the numbers indicate the applied laser pulse sequence.

Fig. 5.15 plots the measured frequency shift against laser trim location for the CC-beam of Fig. 5.14 alongside that predicted by the analytical model and by FEA, in which the laser blasts are  $0.5 \mu\text{m}$  in depth. Note that for blasts close to the edges of the beam, both measured data and FEA simulation (the one without topography) yield smaller frequency shift magnitudes than those predicted by the theory. The reason for less frequency shift results perhaps from the actual topography due to the support scheme that makes the beam more compliant and thereby mitigates the effect of stiffness change by laser blasts. As shown in Fig. 5.15, FEA with topography considered predicts a better match with measured data.

Another measurement performed on a longer CC-beam sized as  $(l, w, h) = (49 \mu\text{m}, 10 \mu\text{m}, 2 \mu\text{m})$  with with a laser applying sequence different from the previous case. Fig. 5.17 presents a similar result as Fig. 5.15, verifying that the theory is applicable to various beam dimensions and that the frequency shift magnitude induced by a laser pulse depends only on the location regardless of any previous pulses.

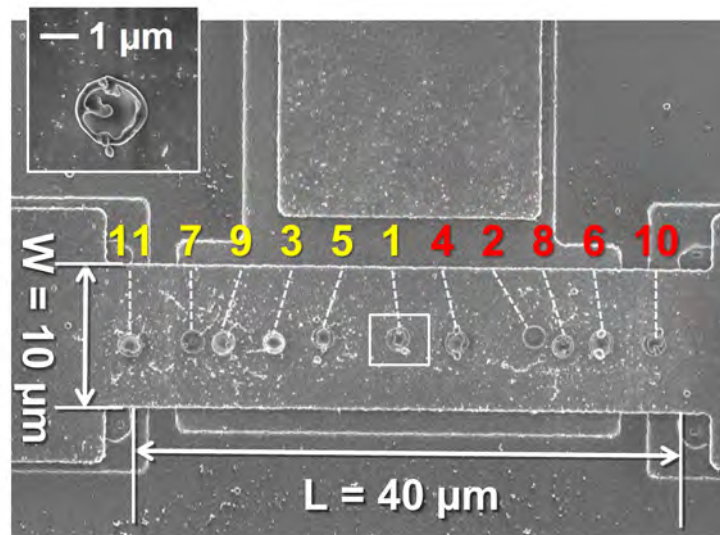


Figure 5.14: SEM of the trimmed CC-beam resonator with dimensions of  $(l, w, h) = (40 \mu\text{m}, 10 \mu\text{m}, 2 \mu\text{m})$ , showing regions ablated by the applied laser pulses and with a inset of zoom-in view of the laser trimming spot.

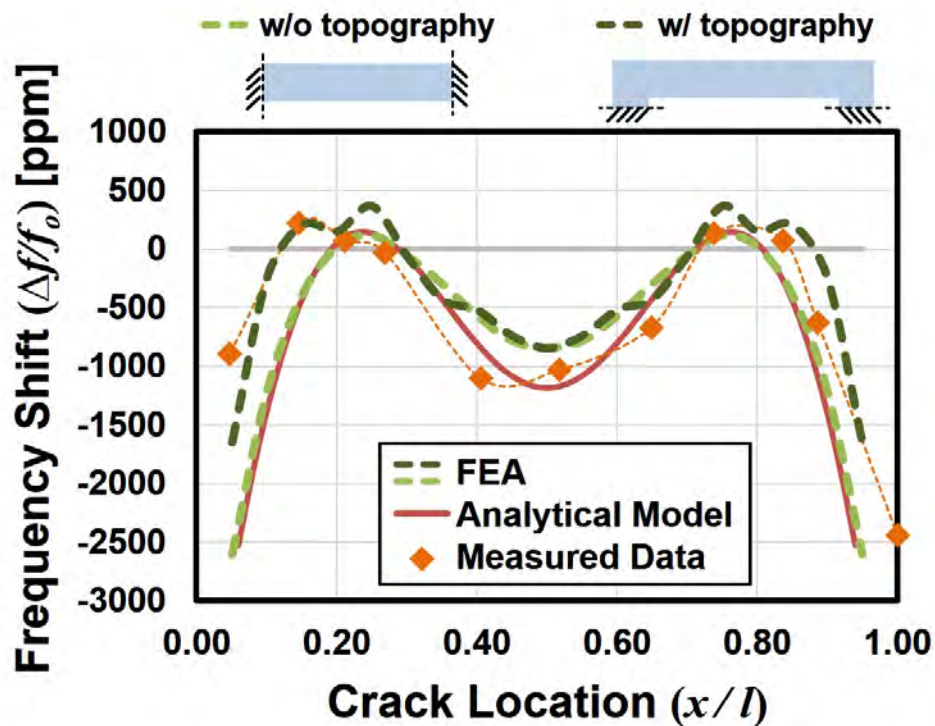


Figure 5.15: Measured frequency shift versus trimming location for the CC-beam resonator of Fig. 5.14 alongside with that obtained from the analytical model and FEA simulation.

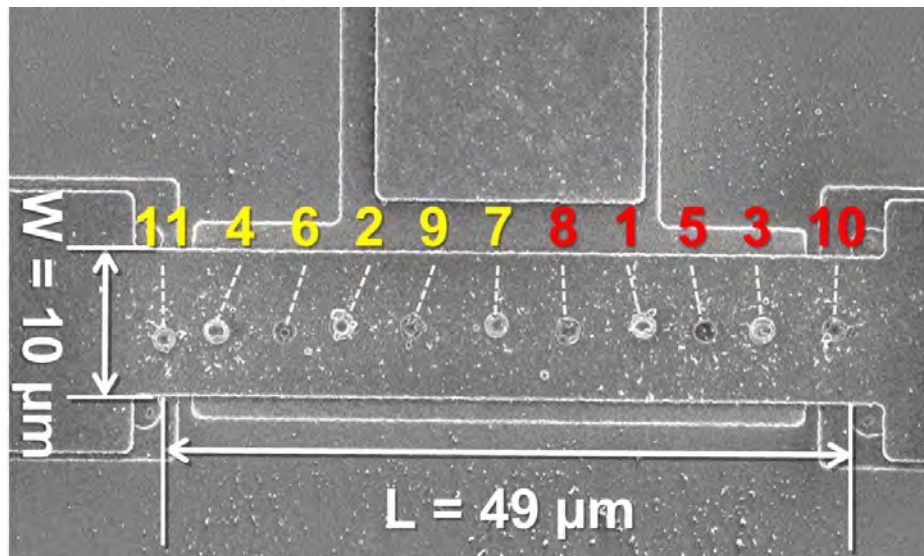


Figure 5.16: SEM of the trimmed CC-beam resonator with dimensions of  $(l, w, h) = (49 \mu\text{m}, 10 \mu\text{m}, 2 \mu\text{m})$ .

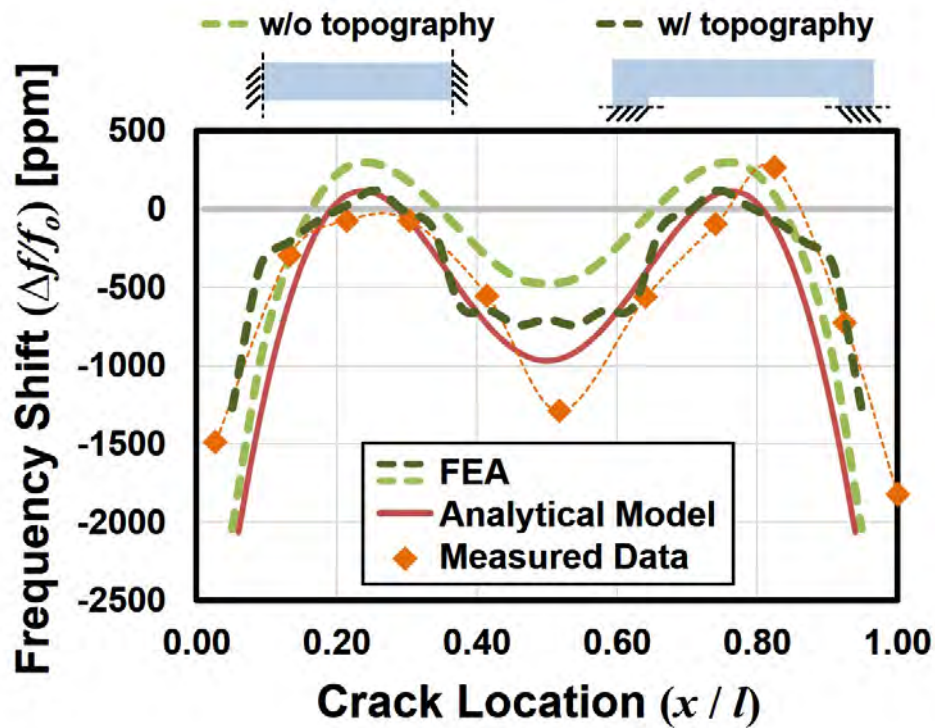


Figure 5.17: Measured frequency shift versus trimming location for the CC-beam resonator of Fig. 5.16 alongside with that obtained from the analytical model and FEA simulation.

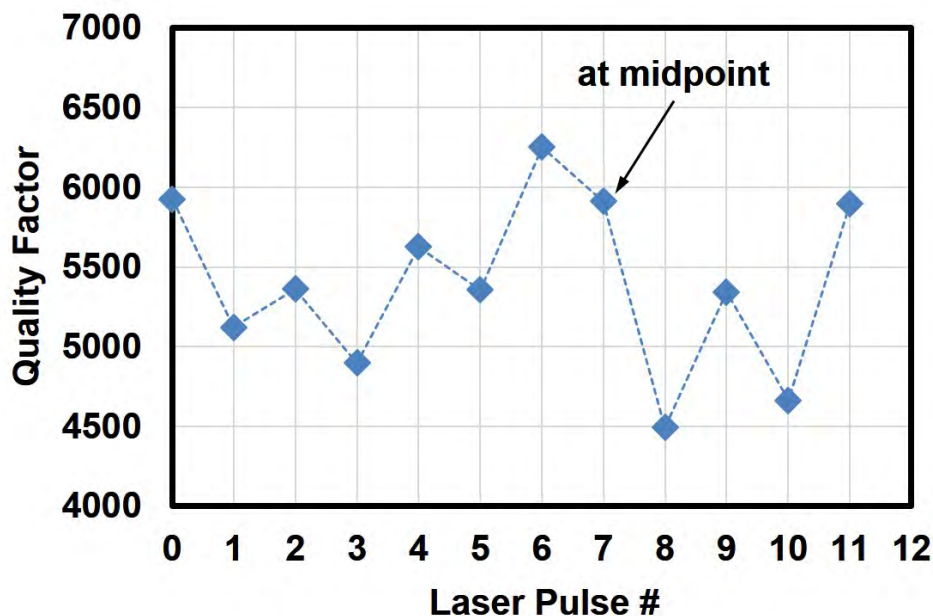


Figure 5.18: Measured  $Q$  versus laser pulse sequence for the device of Fig. 5.16, illustrating how symmetric trimming maintains the CC-beam  $Q$ .

#### 5.4.2 Symmetrical Trimming to Preserve $Q$

Fig. 5.18 plots the measured  $Q$  over eleven laser pulses applied on the CC-beam of Fig. 5.16, showing no significant degradation. In particular,  $Q$  decreases after an asymmetrical trim, but then restores to certain degree after another pulse applied at the mirrored location of the previous shot with respect to the midpoint, suggesting that symmetrical trimming helps maintain the  $Q$ . One possible mechanism of  $Q$  preservation is that symmetrical laser blasts balance crack-induced stress. Other possible mechanisms, such as laser-induced annealing or intrinsic stress relaxation, would also help preserve (or even raise)  $Q$ . As a result, the  $Q$  of the CC-beam in Fig. 5.16 merely drops from its initial 5,927 to 5,898 after eleven laser shots.

Another point of view for the  $Q$  degradation caused by an asymmetrical trim might be the fact that an asymmetrical trim results in an asymmetrical mode shape, which could induce larger energy dissipation through anchors during vibrating. To illustrate this, Fig. 5.19 plots FEA-simulated vertical displacements (i.e.,  $z$ -axis) at either ends of a CC-beam along the beam width while vibrating in the fundamental transverse mode shape with (a) no trims; (b) single trim at midpoint; (c) single trim at  $15\ \mu\text{m}$  away from midpoint; and (d) two mirrored trims with each  $15\ \mu\text{m}$  away from midpoint. As shown, the single unbalanced trim exhibits uneven displacements at two ends (Fig. 5.19 (c)), while the cases with no trim or with symmetrical trims present a balanced movement, which might be key to preserving high  $Q$ .

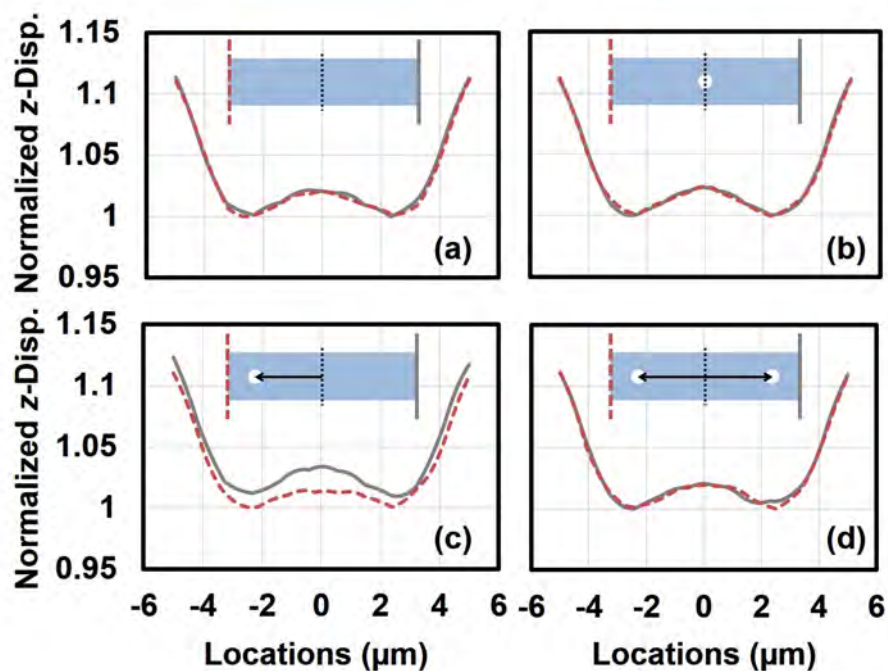


Figure 5.19: FEA-simulated mode shapes of vertical  $z$ -displacement at either ends of a CC-beam ( $(l, w, h) = (40 \mu\text{m}, 10 \mu\text{m}, 2 \mu\text{m})$ ) with (a) no trimming holes; (b) a single trimming hole at midpoint; (c) a single trimming hole away from midpoint by  $15 \mu\text{m}$ , and (d) two trimming holes symmetrically away from midpoint by  $15 \mu\text{m}$ .

### 5.4.3 Deterministic Trimming of a CC-beam Resonator

As discussed, simultaneous bidirectional frequency trimming allows one to tune the resonance frequency to a desirable target more flexibly—can still reach the target if missing it. To illustrate, a CC-beam resonator (*cf.* Fig. 5.20) is trimmed from its as-fabricated 10.27612-MHz resonance frequency towards 10 MHz, a typical resonance frequency available in quartz crystal oscillators. It should be noted that the overall frequency tuning range of 27,612 ppm is in fact much larger than the range in practical cases, which is usually within 1,000 ppm [54].

Measurement results from the previous section suggest targeting on locations close to either ends of the CC-beam for large frequency shifts and on locations around the two “trim-up” spots for small or positive shifts. Fig. 5.21 plots the resonance frequency versus laser pulse index. After the first eight pulses, the resonance frequency effectively reduces to 9.99991 MHz, less than 10 ppm away from the 10-MHz target. Next, pulse#9 intends to move the resonance frequency to a lower value of 9.99535 MHz, -465 ppm away from 10 MHz. The following pulses target on the trim-up spots intended to bring the frequency back. With additional nine pulses, the resonance frequency finally returns to a frequency value of 10.00098 MHz, less than 100 ppm from 10 MHz. Although the results are seemingly

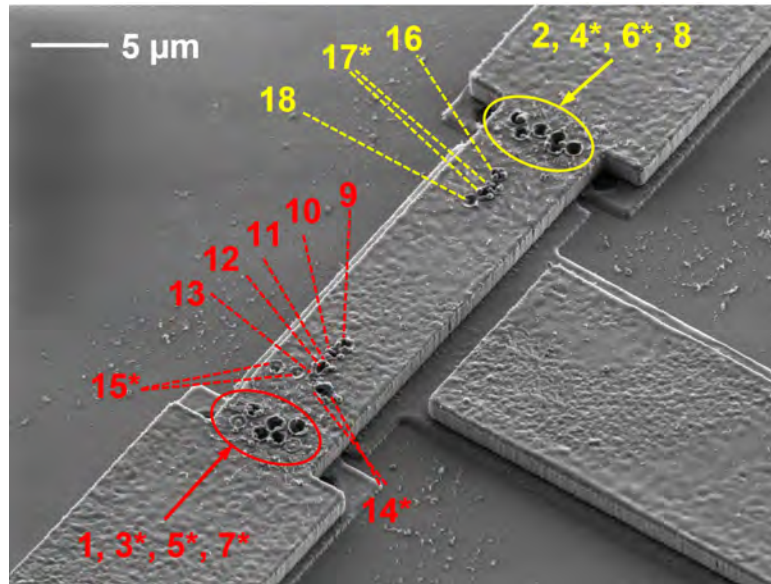


Figure 5.20: SEM of a CC-beam ( $(l, w, h) = (40 \mu\text{m}, 10 \mu\text{m}, 2 \mu\text{m})$ ) labeled with the sequence of applied pulses that is used to demonstrate deterministic trimming from its initial resonance frequency of 10.27612 MHz to the 10-MHz target frequency.

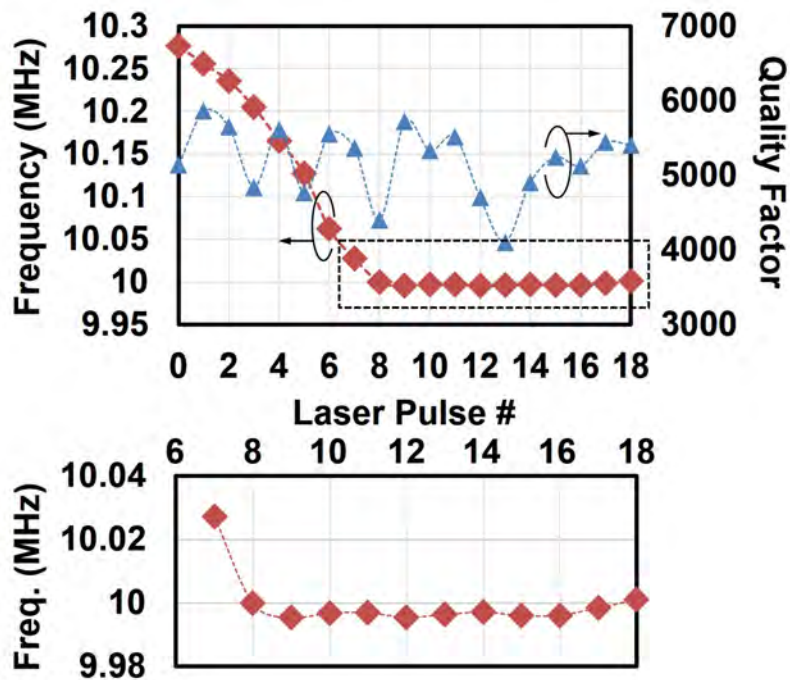


Figure 5.21: Resonance frequency and the corresponding  $Q$  as a function of the applied laser pulse number for the deterministic trimming of the CC-beam resonator of Fig. 5.20 towards a 10-MHz target frequency.

Table 5.1: Pulse sequence used for deterministic trimming of a CC-beam resonator targeted to a desired frequency of 10 MHz

#	Power* [mJ]	Distance from Center [ $\mu\text{m}$ ]	Frequency [MHz]	Freq. Shift [ppm]
0	NA	NA	10.27612	NA
1	0.6	20	10.25556	2000.9
2	0.6	20	10.23563	1944.1
3	0.6**	20	10.20464	3017.1
4	0.6**	20	10.16509	3876.3
5	0.6**	20	10.12708	3738.6
6	0.6**	20	10.06203	6424.1
7	0.51**	20	10.02722	3459.1
8	0.51	20	9.99991	2723.5
9	0.3	9.03	9.99535	456.0
10	0.27	10.3	9.99679	+144.4
11	0.27	12.1	9.99686	+6.8
12	0.27	12.8	9.99542	143.8
13	0.27	13.7	9.99630	+87.5
14	0.27**	14.1	9.99705	+75.0
15	0.3**	13.7	9.99595	109.5
16	0.3	14.8	9.99608	+12.5
17	0.3**	12.4/13.4	9.99842	+234.5
18	0.3	11.0	10.00098	+256.2

\*Note that the power specified here is the power output from the laser aperture, not the laser power that arrives onto the CC-beam resonators, which is believed to be much lower than the values indicated here.

\*\*Indication for those pulses, which have two shots performed at same distance away from the center, unless otherwise specified (i.e., #17).

impressive, the returning resonance frequency could be even closer to the 10 MHz target, and the number of pulses needed to bring the frequency back could be less if a precise positioning stage were available. Table 5.1 summarizes the laser pulse index, the corresponding location and energy, and the resultant resonance frequency. It is worthwhile to mention that the  $Q$  changes from its initial 5,138 to 4,400 after the first eight pulses, and to an even higher value of 5,402 after all eighteen pulses, possibly enhanced by laser-induced annealing and/or stress releasing.

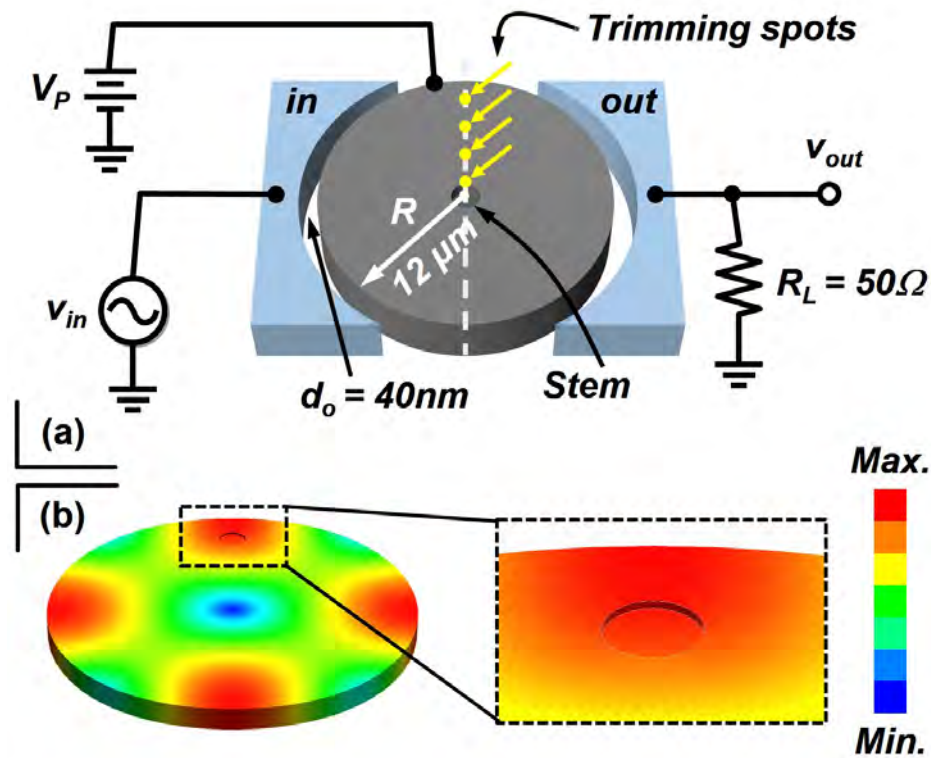


Figure 5.22: (a) Schematic of a center stem supported disk resonator showing the measurement setup and targeted trimming locations. (b) The FEM simulated wine glass mode shape showing a hole on the disk solid model (mass removal) to imitate the trimmed spot.

## 5.5 Laser Trimming of Micromechanical Wine-Glass Disk Resonators

Wine-glass disk resonators (*cf.*, Fig. 5.22 (a)) [13] are expected to have potentials being applied in more applications than their CC-beam counterparts, having been demonstrated with  $Q$ 's  $> 145,000$  at 60 MHz with phase noise performance nearly satisfying GSM specifications when being embedded in a oscillator circuit [13]. These resonators, however, are typically  $350\times$  stiffer than CC-beams, so cannot be tuned as easily via dc-bias-induced electrical stiffness. Thus, laser trimming is quite desirable for wine-glass disk resonators, much more than for the CC-beams.

Fig. 5.22 (a) presents a schematic of the micromechanical disk resonator, along with the two-port measurement set up used in the work. The disk has a radius of  $12 \mu\text{m}$  with center stem size of  $2 \mu\text{m}$  in diameter and gap spacing of  $40 \text{nm}$  and is tied to a dc bias on its structure, and excited/sensed via the two surrounding electrodes. The preferred wine glass mode shape (with higher measured  $Q$  over radial contour mode [30]) is illustrated in Fig. 5.22 1(b) with a hole on the disk solid model to mimic a trimmed spot.

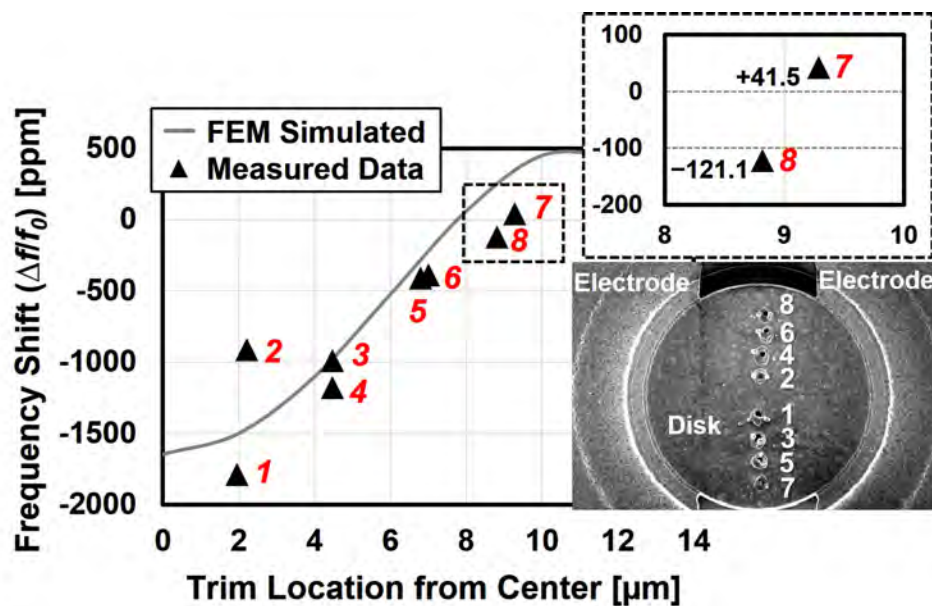


Figure 5.23: Measured frequency shift versus the trim location measured from the center of disk, presenting a good matching against the FEM simulated data. The SEM of the trimmed disk is shown in the inset with pulse sequence number labeled.

### 5.5.1 Experimental Results of Laser Trimming of Disk Resonators

The disk resonators were first fabricated using a micro-fabrication process similar to that in [30] of a conventional polysilicon disk resonator supported by a center stem, except that instead of opening the stem anchor throughout the polysilicon structure, the bottom sacrificial oxide was first opened for the stem layer and then structural polysilicon layer refilled, chemical-mechanical polished (CMP'ed) and patterned. The use of CMP has also been applied to the electrode polysilicon after deposition to ensure less topography in the following photolithography step, as well as to remove the overhead of electrodes, which were believed as one of the factors that limit the pull-in voltage of the devices. Then, the fabricated devices were trimmed using the same manual positioning laser system for CC-beam resonators.

Fig. 5.23 presents the frequency shift versus the pulse location of a fabricated 155-MHz center stem supported wine glass disk resonator with a radius of 12  $\mu\text{m}$ . The device SEM image is shown in the inset of Fig. 5.23 with labeled laser pulse sequences. The disk resonator was trimmed along the zero-tangential-movement axis (*cf.* Fig. 5.22) from the center and towards the edge of disk, presenting a coarse negative frequency shift up to 1787 ppm for targeting at 2  $\mu\text{m}$  away from the center and a fine positive shift as precise as +41.5 ppm when trimming at 9.3  $\mu\text{m}$  from center, together exhibits a flexible bidirectional frequency trimming as also observed in the CC-beam devices.

However, unlike the CC-beams and side supported disks in [58] where the  $Q$ 's degraded

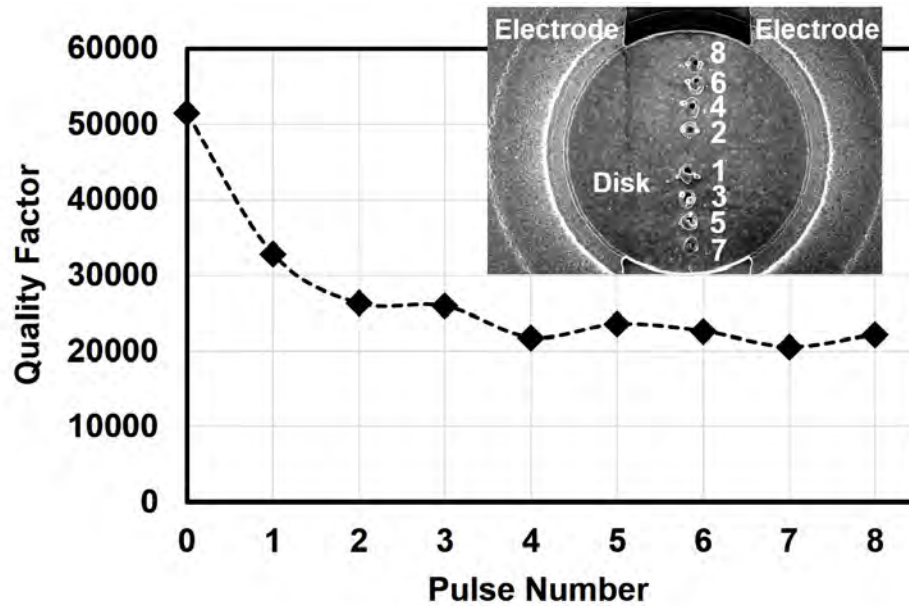


Figure 5.24: Measured  $Q$ s versus the pulse number that has been applied sequentially, exhibiting  $Q$  degradation for trims of #1 and #2, which are closest to the center.

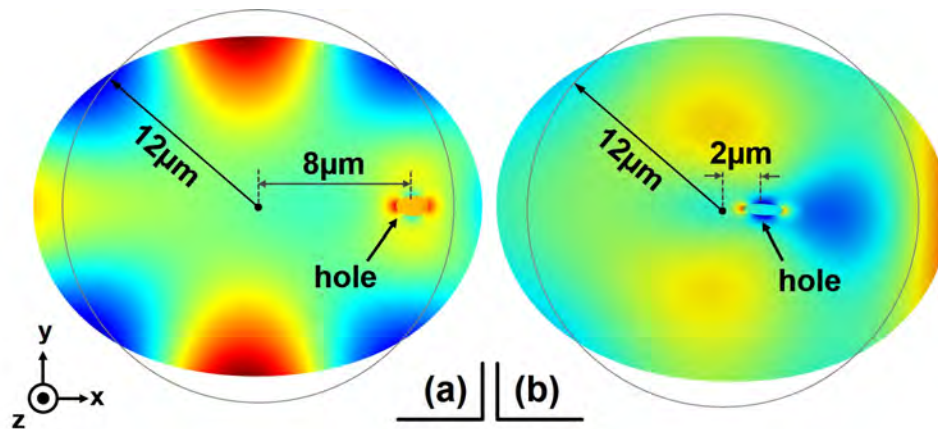


Figure 5.25: FEM simulation for comparison of vertical displacement (shown as the color legend) for trimming location occurred at (a)  $8\ \mu\text{m}$ , and (b)  $2\ \mu\text{m}$  from the center, illustrating unbalanced movement/stress was introduced by a close-to-center laser pulse.

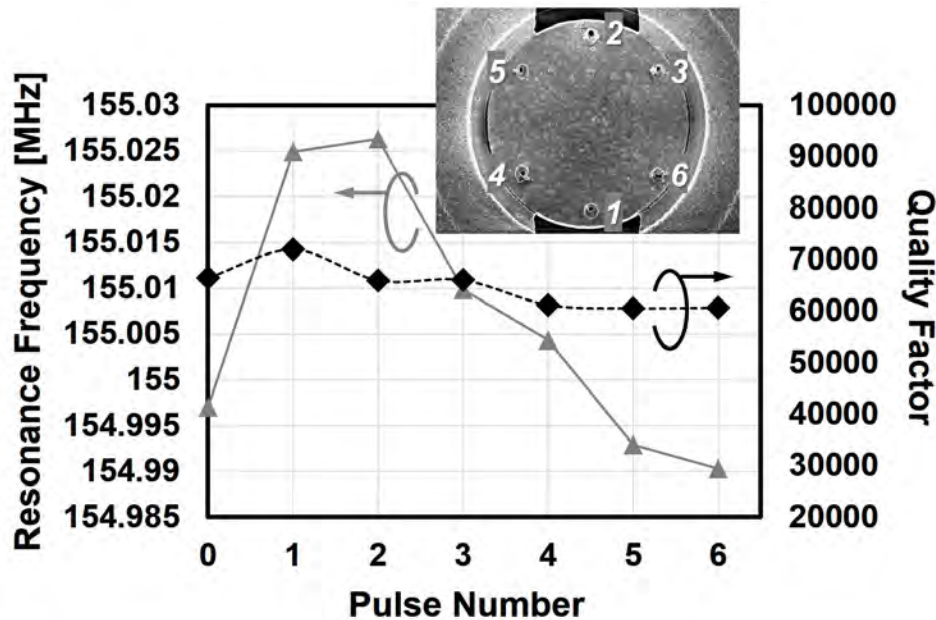


Figure 5.26: Measured frequencies and  $Q$ s for a trimming sequence with all pulses being applied on the edge of disk, verifying the postulation that  $Q$  can be kept as long as pulses are away from the center.

by asymmetric trims, the measured  $Q$ 's of the center stem supported disk (*cf.* Fig. 5.24) drops during the first two shots (i.e., location 1 and 2 in the SEM) for which the laser pulses were targeted in the vicinity of disk center and then remains visually unchanged after-wards. In other words, once the laser pulse is away from the center stem, the  $Q$  in a center stem supported disk seems immune to the laser trimming process. As a result, the  $Q$ -reduction in a side supported disk caused by unbalanced trimming is possibly resolved by the center stem support scheme, where the stress introduced by laser pulses can be relieved even with unbalanced trims. One of the possible mechanisms that lead to the degradation of  $Q$  might be the laser pulse-induced stress causes unbalanced support of disk, and it could be better illustrated by Fig. 5.25 of the FEM simulated out-of-plane displacement (along z-axis) for two cases of trimming location such as (a) 8  $\mu\text{m}$  and (b) 2  $\mu\text{m}$  away from center. The case of Fig. 5.25 (b) clearly shows a much more asymmetrical vertical movement occurred for entire disk as well as on the center stem and therefore dissipates more energy (i.e., low- $Q$ ) through the stem. To further verify this observation, another experiment presented in Fig. 5.26 performed only trims around the edge of the disk and again confirmed that the  $Q$  almost remains unchanged after each pulse and the overall reduction of  $Q$  after six laser pulses is only 8.7% of the initial value.

## 5.6 Conclusions

Permanent frequency trimming of vibrating micromechanical CC-beam and radial disk resonators has been demonstrated using location-dependent laser trimming with additional geometrical targeting measures that allow bidirectional frequency shifts and that suppress variations in resonator  $Q$ . In particular, an analytical model developed to capture the frequency trimming location dependency shows a good agreement with measured trimming results on micromechanical CC-beam resonators with varying dimensions. Additionally, laser trimming preserves  $Q$  of micromechanical resonators by symmetrically targeting the pulses that help redistribute the localized stress and restore the unbalanced mode shape generated by uneven pulses.

Although only CC-beams serve here as the demonstration vehicle, it is quite straightforward to employ the analytical model on beam resonators with differing support schemes, e.g., free-free beams or cantilevers, by simply altering the boundary condition matrices (i.e., (5.24)) accordingly. Yet, it is possible to apply the theory on other resonator geometries, such as disk and extensional ring resonators that are perhaps more useful in RF reference applications, given that their stress intensity factors are available. Work towards this continues.

# Chapter 6

## Conclusions

By harnessing the nonlinear dynamics of micromechanical vibrating devices, the resoswitch technology as applied to resonant switching applications indeed enables new horizons in ultra-low power (zero-quiescent power receivers) and on-chip high voltage (charge pump) applications. This dissertation focuses on the development of the very first zero-quiescent power filter-amplifier that employs a metal aluminum surface micromachined displacement amplifying resoswitch. The beauty of the approach towards near-zero receivers is that the device not only draws zero power while in stand-by but also functions as a channel-selecting filter—essentially combining the filter and amplifier in a receiver front-end.

As a typical switch, the resoswitch wishes the input terminal controls the operation and remains isolated from other parts of the device. Therefore, the vibrating displacement of the structure along the output axis is necessarily at least larger than that along the input axis—in this case, the input signal remains intact as the structure switches only to the output. To achieve this, here utilizes the slotted disk approach first demonstrated in [11], which yields directional stiffness differences by cutting slots into the structure of a wine glass disk resonator. This approach successfully effects displacement gain in a single mechanical disk rather than using the area-consuming coupled disk array seen in [6]. A FEA-based semi-empirical model for displacement gain prediction allows the first-hand estimation of achievable displacement gains for given disk and slot dimensions.

Although slotted disks nicely provide displacement differences, they do so at expense of  $Q$ . Because  $Q$  perhaps is the most important attribute in resonant devices that determines performances such as frequency selectivity, receiver sensitivity, and actuation voltage, a lowered  $Q$  is typically unacceptable. Before looking into the mechanisms that cause low  $Q$ 's in slotted-disks, one might wonder what the energy loss mechanisms that limit typical disk resonators'  $Q$ 's are. Thanks to the abundance research efforts in micromechanical resonators, several loss mechanisms have been identified as possible dominant ones in vacuum-operated disk resonators including anchor loss and phonon-phonon interaction (Akheiser effect). Operating at cryogenic temperatures reduces the temperature-dependent phonon-phonon interaction and reveals the anchor loss at 5K, presenting a  $Q > 360,000$ . The measurements indicate that once the support scheme is designed correctly room temperature  $Q$  of disk

resonators is typically determined by phonon-phonon interaction. In other words, although the presented support beam design is good enough to make the anchor loss a secondary loss mechanism in addition to phonon-phonon interaction at room temperatures, anchor loss starts to dominate the overall  $Q$  rather than phonon-phonon interaction when operating the device at cryogenic temperatures.

In fact, one might not be able to easily attain an as-fabricated  $Q$  of more than 100,000 even with perfect support design. Other mechanisms that would (often) limit  $Q$  include the structural material, intrinsic stress, and vibrating mode shape. As a direct result when these additional losses take place, the presented as-fabricated  $Q$  is typically lower than what theory predicts by orders of magnitudes. Fortunately, annealing, a well known technique in transistor industry used for restoring damaged lattice structure and interfaces, seems to be also helpful in restoring  $Q$  for MEMS devices. *In situ* annealing has been demonstrated to recover  $Q$  of micromechanical nickel comb-driven resonators. Here, the technique demonstrates its  $Q$ -restoring efficacy again to a comb-driven resonators that use polysilicon-filled carbon nanotube (CNT) composite as the structural material. Another experiment that uses rapid thermal annealing also shows to restore nickel resonators'  $Q$ 's from  $\sim 500$  to  $>10,000$  for 2 mins at a temperature as low as  $400^\circ$ , which should be low enough to be qualified as a CMOS-compatible process.

Slotted-disk resonators exhibit much lower  $Q$ 's compared to conventional disk resonators. Measurement results of  $Q$  with varying slot design and support scheme identify that  $Q$  is always lower in slotted disks compared to non-slotted ones no matter their support schemes and that a higher displacement gain would induce a lower  $Q$ . The reason for the  $Q$  degradation is mostly likely due to slot-induced thermoelastic damping (TED). A TED theory based on an already-developed 2-D TED model predicts the theoretical TED that matches well the measured data. Because of the trade-off observed between the displacement gain and  $Q$ , one way to accommodate the slot-induced low- $Q$  is using a slotted disk array which couples multiple slotted-disks with a low displacement gains. Or, one can try to realize displacement gains in different ways. Here, elliptic disks are demonstrated that achieve stiffness differences along the orthogonal axes by geometry ratioing rather than  $Q$ -degrading slots. As a direct result of eliminating the  $Q$ -degrading slots, hence the slot-induced TED, the  $Q$ 's of elliptic disks retain and somehow is even higher than that of regular wine glass disks, reaching  $Q > 100,000$  with a displacement gain of 2.14 demonstrated by an elliptic disk with an aspect ratio of 1.6.

Additionally, because the filter-amplifier would serve as a radio receiver, how accurately the resoswitch resonance frequency matches with the target radio frequency would be another primary concern. Although device design techniques such as use of arrayed disks have been demonstrated that help reduce the matching tolerance [6], they fail to address the absolute tolerance. In this regard, laser trimming that removes the material from the resonator structures and allows flexible bidirectional trimming via controlling laser blast location serves as a great candidate for post-fabrication frequency trimming. In particular, laser trimming of the resonance frequency of micromechanical clamped-clamped beam resonators is demonstrated in steps as small as 6.8 ppm over a range of 26,879 ppm, and with

targeting measures that suppress unwanted variations in  $Q$  and series motional resistance. A model that divides the beam into several parallel beams, using stiffness-modifying cracks in those receiving laser blasts, captures well the frequency shift dependence on laser blast location. The accuracy of this theory further enables a deterministic trimming protocol that specifies the laser targeting sequence to attain a needed frequency trim with minimal  $Q$  reduction.

## 6.1 Future Research Directions

Although this dissertation demonstrated the resoswitch-based filter amplifier, a bunch of issues need to be solved before it becomes practical. Here lists some possible future research directions that may provide solutions towards this goal.

### 6.1.1 Reliability

The demonstrated Al resoswitch typical fails when the disk pulls in and fuses to one of the electrodes due to high short current. A current limiting circuit is definitely needed in such conductive devices. Resoswitches in polysilicon, however, do not seem to fuse to electrodes after pulling in. Instead, in most of the cases measured, smaller motional current can still be observed in the frequency spectrum (i.e., the resoswitch is still alive!) after the resoswitch stops performing switch. It would be useful if we can understand how the structure changes to cause the “smaller peaks” after switching. Laser Doppler vibrometry measurements may be helpful to this. Another important direction is the electrode design [8]. According to the work, more compliant electrodes help minimize variation of  $Q$ , hence allow more reliable contact, during switching. It would be great to see comparisons of more varying electrode designs, e.g., varying electrode stiffness as well as dynamically adapting electrode stiffness.

### 6.1.2 Resoswitch-Based Switched-Mode Power Amplifiers

Although currently demonstrated resoswitch-based radio components focus on the receive path, resoswitches in fact can be even more powerful if they are employed in transmit amplifiers. For example, resoswitches can be integrated into Class-E switched-mode power amplifiers. Class-E power amplifiers use LC resonance networks and current switches to yield non-overlapped current and voltage waveforms across the switching devices, which theoretically can achieve 100% efficiency. However, practical Class-E power amplifiers only achieve  $\sim 50\%$  efficiency due to the large parasitic capacitances of transistor switches. If the transistor switches of Class-E power amplifiers can be replaced by resoswitches which have much smaller parasitic capacitances compared to transistor counterparts, the efficiency should increase dramatically. In this case, the circuit better integrates the resoswitch with on-chip inductors and capacitances to eliminate any parasitics as if using off-chip reactive components.

### 6.1.3 Integrated Resoswitch-Based Radios

To date, the demonstrations of zero-quiescent power receivers are merely component level. It would be more promising and convincing if the devices are integrated with baseband transistor circuits. This would allow the ground-breaking technology more prominent to areas other than MEMS. For the first phase, it can be done using a two-chip solution that connects the resoswitches with CMOS circuits by wire bonding. Then, the monolithically integrated version that could truly benefit sensor applications would rely on the low-temperature metal fabrication technologies.

### 6.1.4 Laser Frequency Trimming of Other Types of Resonators

Laser frequency trimming of CC-beam resonators have been demonstrated together with the frequency prediction model presenting an universal yet simple post-fabrication frequency trimming approach. In fact, it certainly can be applied to other types of resonators such as disk resonators and extensional ring resonators which might be actually more favorable for frequency and timing applications. While the model can be employed for other beam resonators by simply altering the boundary conditions, it may be necessary to replace the rotational spring model by other springs and blast-induced stress intensity factors accordingly. For example, regular springs should apply to extensional vibrating mode shapes.

## 6.2 Conclusion Remarks

To summarize, prototype micromechanical filter-power amplifiers based upon the novel resoswitch technology have been demonstrated in this dissertation. Two of the most important attributes of resoswitches and resonant devices,  $Q$  and frequency accuracy, have been discussed and solutions to some issues observed have been demonstrated. Although many works still need to be done before all of this becomes practical, the resoswitch-based zero-quiescent power radios present great promise for one day being the paradigm-shifting components of ultra-low power communication devices.

# Appendix A

## All-Al Disk Process Outline

The following comprises a step-by-step outline of the all-Al disk process, as run for the metal Al resoswitches of this dissertation.

### All-Al Disk Process

0.7- $\mu\text{m}$  substrate gap, 3- $\mu\text{m}$  thickness, Sputtered pure-Al

---

0.0 Starting material: n-type, <100> prime wafers, w/ no minor flat!

Process wafers: 3

---

1.0 Zero layer alignment mark photo mask (mask#0)

1.1 PR coating

1.1.1 HMDS prime, svgcoat6, 100°C, 60 secs

1.1.2 PR spin, svgcoat6, UV210, 1.48krpm, 30 secs, target = 900 nm

1.1.3 soft bake, svgcoat6, 130°C, 60 secs

1.2 Photolithography

1.2.1 expose, asml, 15-18 mJ

1.2.2 post-expose bake, svgdev6, 130°C, 60 secs

1.2.2 develop, svgdev6, MF26A, 60 secs

1.2.4 hard bake, uvbake, U recipe, 140°C

- 1.3 Si etch, lam8, 8001 Cl<sub>2</sub>/HBr, 20 secs, target = 120 nm
  - 1.4 PR strip, matrix, O<sub>2</sub>, 2.5 mins
- 

## 2.0 Substrate doping

- 2.1 Standard wafer clean
  - 2.2 n<sup>+</sup> diffusion, tystar13, POCL<sub>3</sub>, 900°C, 30-min ramp, 30-min anneal
- 

## 3.0 Insulation layer

- 3.1 Transfer directly from tystar13 to tystar2
  - 3.2 Wet oxidation, tystar2, O<sub>2</sub>, H<sub>2</sub>O, 1050°C, 12 hrs, target = 2 μm
  - 3.3 Al<sub>2</sub>O<sub>3</sub> ALD, picosun (or cambridge), TMA (Al(CH<sub>3</sub>)<sub>3</sub>), H<sub>2</sub>O, 1000 cycles, target = 100 nm
- 

## 4.0 Al ground plane (metal1) deposition

- 4.1 Transfer directly from tystar17 to aln2 in a clean cassette
  - 4.2 Al sputtering, aln2, PM3, (5-6-19), 0.55 mTorr, 5 kW, 27 secs, 1 cycle, target = 170 nm
  - 4.3 Measure Rsh, cde-resmap, target < 0.2 Ω/sq
- 

## 5.0 Al metal1 photo mask (mask#1)

### 5.1 PR coating

- 5.1.1 HMDS prime, svgcoat6, 100°C, 60 secs
- 5.1.2 PR spin, svgcoat6, UV210, 1.48krpm, 30 secs, target = 900 nm
- 5.1.3 soft bake, svgcoat6, 130°C, 60 secs

### 5.2 Photolithography

- 5.2.1 expose, asml, 13 mJ
- 5.2.2 post-expose bake, svgdev6, 130°C, 60 secs
- 5.2.3 develop, svgdev6, MF26A, 60 secs
- 5.2.4 hard bake, uvbake, U recipe, 140°C

5.3 Al etch, lam7, Cl2/BCl3 = 35/25 sccm, \*\* secs;  
Or, centura-met, Cl2/BCl3 = 60/10 sccm, 10 mTorr, 20 secs), target =  
150 nm, visual inspection

5.4 PR strip, matrix, O2, 2.5 mins

---

6.0 Bottom sacrificial oxide layer, w/ one ctrl wafer

6.1 metal clean, self prepared, SVC-14, 110°C (water bath), 15 mins

6.2 LT0 deposition, tystar12, SiH4, 400°C, 60 mins, target = 700 nm

---

7.0 Device anchor (anchor1) photo mask (mask#2)

7.1 PR coating

7.1.1 HMDS prime, svgcoat6, 100°C, 60 secs

7.1.2 PR spin, svgcoat6, UV210, 1.48krpm, 30 secs, target=900 nm

7.1.3 soft bake, svgcoat6, 130°C, 60 secs

7.2 Photolithography

7.2.1 expose, asml, 25 mJ

7.2.2 post-expose bake, svgdev6, 130°C, 60 secs

7.2.3 develop, svgdev6, MF26A, 60 secs

7.2.4 hard bake, uvbake, U recipe, 140°C

7.3 Oxide etch, lam6, 6001, CHF3/CF4, \*\* secs, (Or, centura-mxp, 2+1 mins),  
target = 700 nm

7.4 test opening, probe station

7.5 PR strip, matrix, O2, 2.5 mins

7.6 metal clean, self prepared, SVC-14, 110°C (water bath), 15 mins (prior  
to Al deposition)

---

8.0 Al structure (metal2) and oxide hard-mask deposition

8.1 Transfer directly from msink1 to aln2 in a clean cassette

8.2 Al sputtering, aln2, PM3, 0.55 mTorr, 5 kW, 150 secs, 4 cycle, target  
= 3 µm, first run at least two dummy wafers

- 8.2.1 Rsh measurement, cde-resmap, target  $<13 \text{ m}\Omega/\text{sq}$ , on the last dummy wafer prior to the process wafers
  - 8.3 LTO deposition, tystar12,  $\text{SiH}_4$ ,  $400^\circ\text{C}$ , 2.5 hrs, target =  $1.5 \mu\text{m}$ 
    - 8.3.1 place two ctrl wafers to sandwich the process wafers, may run only two process wafer at this step
    - 8.3.2 oxide thickness measurement, nanospec, target =  $1.5 \mu\text{m}$ , on the two ctrl wafers that sandwich the process wafers
- 

## 9.0 Al disk structure photo mask (mask#3)

### 9.1 PR coating

- 9.1.1 HMDS prime, svgcoat6,  $100^\circ\text{C}$ , 60 secs
- 9.1.2 PR spin, svgcoat6, UV210, 1.48krpm, 30 secs, target=900 nm
- 9.1.3 soft bake, svgcoat6,  $130^\circ\text{C}$ , 60 secs

### 9.2 Photolithography

- 9.2.1 expose, asml, 10 mJ
- 9.2.2 post-expose bake, svgdev6,  $130^\circ\text{C}$ , 60 secs
- 9.2.3 develop, svgdev6, MF26A, 60 secs
- 9.2.4 hard bake, uvbake, U recipe,  $140^\circ\text{C}$

9.3 oxide hard-mask etch, STS oxide,  $\text{Cl}_2/\text{BCl}_3$ , \*\* secs, 10 cycles target =  $1.5 \mu\text{m}$

9.4 Al etch, lam7,  $\text{Cl}_2/\text{BCl}_3 = 35/25\text{sccm}$ , 4 mTorr, \*\* secs, (or, centura-met,  $\text{Cl}_2/\text{BCl}_3 = 40/20 \text{ sccm}$ , 10 mTorr, 30 sec/cycle, 8 cycles) target =  $3 \mu\text{m}$

9.5 test opening, probe station

9.6 PR strip, matrix,  $\text{O}_2$ , 2.5 mins

9.7 metal clean, self prepared, SVC-14,  $110^\circ\text{C}$  (water bath), 15 mins

9.8 metal clean, self-prepared, EKC-270,  $180^\circ\text{C}$  water bath, 10 mins (ready for sidewall sacrificial oxide deposition)

---

## 10.0 Sidewall sacrificial layer

10.1 Transfer directly from msink1 to tystar12

10.2 LTO deposition, tystar12,  $\text{SiH}_4$ ,  $400^\circ\text{C}$ , 5 mins, target  $\sim 70 \text{ nm}$

10.2.1 may run one process wafer at this step, place process wafer(s)  
around the center slot (slot#7)

10.2.2 oxide thickness measurement, nanospec, target = 70 nm at slot#7

---

## 11.0 Electrode anchor (anchor2) photo mask (mask#4)

### 11.1 PR coating

11.1.1 HMDS prime, svgcoat6, 100°C, 60 secs

11.1.2 PR spin, svgcoat6, UV26 3.0, 1krpm, 30 secs, target = 5.5  $\mu\text{m}$

11.1.3 soft bake, svgcoat6, 130°C, 60 secs

### 11.2 Photolithography

11.2.1 expose, asml, 50 mJ

11.2.2 wait, at least 10 mins

11.2.3 post-expose bake, svgdev6, 110°C, 90 secs

11.2.4 develop, svgdev6, MF26A, 60 secs

11.2.5 hard bake, vwroven, 120°C, overnight

11.3 oxide etch, lam6, Cl<sub>2</sub>/BCl<sub>3</sub>, 60 secs per cycle, 3 cycles target = 800  
nm

11.4 test opening, probe station

11.6 metal clean, self prepared, SVC-14, 110°C (water bath), 15 mins

---

## 12.0 Al electrode (metal3) deposition

12.1 Transfer directly from msink1 to Al evaporator in a clean cassette

12.2 Al deposition, dw (or cha), target=1.5  $\mu\text{m}$

---

## 13.0 Electrode photo mask (mask#5)

### 13.1 PR coating

13.1.1 HMDS prime, svgcoat6, 100°C, 60 secs

13.1.2 PR spin, svgcoat6, UV26 3.0, 1krpm, 30 secs, target = 5.5 $\mu\text{m}$

11.1.3 soft bake, svgcoat6, 140°C, 60 secs

### 13.2 Photolithography

- 13.2.1 expose, asml, 50 mJ
  - 13.2.2 wait, at least 10 mins
  - 13.2.3 post-expose bake, svgdev6, 105°C, 90 secs
  - 13.2.4 develop, svgdev6, MF26A, 60 secs
  - 13.2.5 hard bake, vwroven, 120°C, overnight
  - 13.3 Al etch, lam7, Cl2/BCl3 = 35/25sccm, 4 mTorr, \*\* secs;  
Or, centura-met, Cl2/BCl3 = 60/30 sccm, 10 mTorr, 30 secs per cycles,  
4 cycles or till visually clear, then 50/40 sccm, 30 secs per cycles,  
6 cycles for over-etch, target = 1.5  $\mu\text{m}$
  - 13.4 Al wet dip, msink8, Al etchant, 50°C, 30 secs
  - 13.5 SEM, stringer (if any) possibly is polymer, not Al
  - 13.6 metal clean, self-prepared, EKC-270, 180°C water bath, 25 mins (can  
divide into 10+15 mins, SEM after each dip)
- 

#### 14.0 Device release

- 14.1 PR strip, acetone and then heated SVC-14, 20 mins
  - 14.2 release
    - 14.2.1 vapor HF, primaxx, recipe2, 10 mins per cycle, 15 cycles
    - 14.2.2 need a clean wafer carrier, clean with pirahna regularly.
- 

Wei-Chang Li

last revision: 8/23/12

# Bibliography

- [1] N. O. Sokal and A. D. Sokal, "Class e-a new class of high-efficiency tunes single-ended switching power amplifiers," *IEEE Journal of Solid-State Circuits*, vol. SC-10, no. 3, pp. 168–176, 1975. DOI: [10.1109/JSSC.1975.1050582](https://doi.org/10.1109/JSSC.1975.1050582).
- [2] S. Jee, J. Moon, J. Kim, J. Son, and B. Kim, "Switching behavior of class-e power amplifier and its operation above maximum frequency," *Microwave Theory and Techniques, IEEE Transactions on*, vol. 60, no. 1, pp. 89–98, 2012. DOI: [10.1109/TMTT.2011.2173208](https://doi.org/10.1109/TMTT.2011.2173208).
- [3] Z. J. Yao, S. Chen, S. Eshelman, D. Denniston, and C. Goldsmith, "Micromechanical low-loss microwave switches," *IEEE/ASME Journal of Microelectromechanical Systems*, vol. 8, no. 2, pp. 129–134, 1999. DOI: [10.1109/84.767108](https://doi.org/10.1109/84.767108).
- [4] C. T.-C. Nguyen, "Frequency-selective MEMS for miniaturized low-power communication devices," *Microwave Theory and Techniques, IEEE Transactions on*, vol. 47, no. 8, pp. 1486–1503, 1999. DOI: [10.1109/22.780400](https://doi.org/10.1109/22.780400).
- [5] Y. Lin, W.-C. Li, Z. Ren, and C. T.-C. Nguyen, "The micromechanical resonant switch (resoswitchi)," in *Tech. Digest, 2008 Solid-State Sen., Act., & Microsyst. Workshop*, Hilton Head, SC, 2008, pp. 40–43.
- [6] Y. Lin, W.-C. Li, I. Gurin, S.-S. Li, Y.-W. Lin, Z. Ren, B. Kim, and C. T.-C. Nguyen, "Digitally-specified micromechanical displacement amplifiers," in *Solid-State Sensors, Actuators and Microsystems Conference, 2009. TRANSDUCERS 2009. International*, Denver, CO, 2009, pp. 781–784. DOI: [10.1109/SENSOR.2009.5285651](https://doi.org/10.1109/SENSOR.2009.5285651).
- [7] Y. Lin, T. Riekkinen, W.-C. Li, E. Alon, and C. T.-C. Nguyen, "A metal micromechanical resonant switch for on-chip power applications," in *Electron Devices Meeting (IEDM), 2011 IEEE International*, 2011, pp. 20.6.1–20.6.4. DOI: [10.1109/IEDM.2011.6131593](https://doi.org/10.1109/IEDM.2011.6131593).
- [8] R. Liu, J. Naghsh Nilchi, Y. Lin, T. Naing, and C.-C. Nguyen, "Zero quiescent power vlf mechanical communication receiver," in *Solid-State Sensors, Actuators and Microsystems (TRANSDUCERS), 2015 Transducers - 2015 18th International Conference on*, 2015, pp. 129–132. DOI: [10.1109/TRANSDUCERS.2015.7180878](https://doi.org/10.1109/TRANSDUCERS.2015.7180878).
- [9] J. Jöhler, "Propagation of the low-frequency radio signal," *Proceedings of the IRE*, vol. 50, no. 4, pp. 404–427, 1962, ISSN: 0096-8390. DOI: [10.1109/JRPROC.1962.288037](https://doi.org/10.1109/JRPROC.1962.288037).

- [10] Y. Chen, Q. Wang, M. Chang, and A. Terzis, "Ultra-low power time synchronization using passive radio receivers," in *Information Processing in Sensor Networks (IPSN), 2011 10th International Conference on*, 2011, pp. 235–245.
- [11] B. Kim, Y. Lin, W.-L. Huang, M. Akgul, W.-C. Li, Z. Ren, and C. T.-C. Nguyen, "Micromechanical resonant displacement gain stages," in *Micro Electro Mechanical Systems, 2009. MEMS 2009. IEEE 22nd International Conference on*, Sorrento, Italy, 2009, pp. 19–22. DOI: [10.1109/MEMSYS.2009.4805308](https://doi.org/10.1109/MEMSYS.2009.4805308).
- [12] R. Johnson, *Mechanical Filter in Electronics*. New York: John Wiley & sons, 1983.
- [13] Y.-W. Lin, S. Lee, S.-S. Li, Y. Xie, Z. Ren, and C. T.-C. Nguyen, "Series-resonant vhf micromechanical resonator reference oscillators," *Solid-State Circuits, IEEE Journal of*, vol. 39, no. 12, pp. 2477–2491, 2004. DOI: [10.1109/JSSC.2004.837086](https://doi.org/10.1109/JSSC.2004.837086).
- [14] W.-C. Li, Y. Lin, and C. T.-C. Nguyen, "Metal micromechanical filter-power amplifier utilizing a displacement-amplifying resonant switch," in *Solid-State Sensors, Actuators and Microsystems (TRANSDUCERS EUROSENSORS XXVII), 2013 Transducers Eurosensors XXVII: The 17th International Conference on*, Barcelona, Spain, 2013, pp. 2469–2472. DOI: [10.1109/Transducers.2013.6627306](https://doi.org/10.1109/Transducers.2013.6627306).
- [15] W.-C. Chen, W. Fang, and S.-S. Li, "A generalized cmos-mems platform for micromechanical resonators monolithically integrated with circuits," *Journal of Micromechanics and Microengineering*, vol. 21, no. 6, p. 065012, 2011. DOI: [10.1088/0960-1317/21/6/065012](https://doi.org/10.1088/0960-1317/21/6/065012).
- [16] W.-T. Hsu, S. Lee, and C. T.-C. Nguyen, "In situ localized annealing for contamination resistance and enhanced stability in nickel micromechanical resonators," in *Dig. Tech. Papers, 10th Int. Conf. Solid-State Sensors and Actuators*, 1999, pp. 932–935.
- [17] C. T.-C. Nguyen and R. Howe, "Quality factor control for micromechanical resonators," in *Electron Devices Meeting, 1992. IEDM '92. Technical Digest., International*, 1992, pp. 505–508. DOI: [10.1109/IEDM.1992.307411](https://doi.org/10.1109/IEDM.1992.307411).
- [18] B. Kim, M. Hopcroft, R. Candler, C. Jha, M. Agarwal, R. Melamud, S. A. Chandorkar, G. Yama, and T. Kenny, "Temperature dependence of quality factor in mems resonators," *Microelectromechanical Systems, Journal of*, vol. 17, no. 3, pp. 755–766, 2008, ISSN: 1057-7157. DOI: [10.1109/JMEMS.2008.924253](https://doi.org/10.1109/JMEMS.2008.924253).
- [19] W. E. Newell, "Miniaturization of tuning forks," *Science*, vol. 161, no. 3848, pp. 1320–1326, 1968. DOI: [10.1126/science.161.3848.1320](https://doi.org/10.1126/science.161.3848.1320).
- [20] C. Zener, "Internal friction in solids ii. general theory of thermoelastic internal friction," *Phys. Rev.*, vol. 53, pp. 90–99, 1938. DOI: [10.1103/PhysRev.53.90](https://doi.org/10.1103/PhysRev.53.90).
- [21] H. E. Bommel and K. Dransfeld, "Excitation and attenuation of hypersonic waves in quartz," *Phys. Rev.*, vol. 117, pp. 1245–1252, 5 1960. DOI: [10.1103/PhysRev.117.1245](https://doi.org/10.1103/PhysRev.117.1245).

- [22] D. I. Bolef, *Physical Acoustics. Principles and methods. vol. 1, part A. Warren P. Mason, Ed.* 3639. Academic Press, New York, 1964, vol. 145, pp. 1424–1425.
- [23] D. Binder, E. Quevy, T. Koyama, S. Govindjee, J. Demmel, and R. Howe, “Anchor loss simulation in resonators,” in *Micro Electro Mechanical Systems, 2005. MEMS 2005. 18th IEEE International Conference on*, 2005, pp. 133–136. DOI: [10.1109/MEMSYS.2005.1453885](https://doi.org/10.1109/MEMSYS.2005.1453885).
- [24] Y.-W. Lin, L.-W. Hung, S.-S. Li, Z. Ren, and C. T.-C. Nguyen, “Quality factor boosting via mechanically-coupled arraying,” in *Solid-State Sensors, Actuators and Microsystems Conference, 2007. TRANSDUCERS 2007. International*, 2007, pp. 2453–2456. DOI: [10.1109/SENSOR.2007.4300667](https://doi.org/10.1109/SENSOR.2007.4300667).
- [25] S. Chandorkar, M. Agarwal, R. Melamud, R. Candler, K. Goodson, and T. Kenny, “Limits of quality factor in bulk-mode micromechanical resonators,” in *Micro Electro Mechanical Systems, 2008. MEMS 2008. IEEE 21st International Conference on*, 2008, pp. 74–77. DOI: [10.1109/MEMSYS.2008.4443596](https://doi.org/10.1109/MEMSYS.2008.4443596).
- [26] A. McConnell, S. Uma, and K. E. Goodson, “Thermal conductivity of doped polysilicon layers,” *Microelectromechanical Systems, Journal of*, vol. 10, no. 3, pp. 360–369, 2001, ISSN: 1057-7157. DOI: [10.1109/84.946782](https://doi.org/10.1109/84.946782).
- [27] P. Flubacher, A. J. Leadbetter, and J. A. Morrison, “The heat capacity of pure silicon and germanium and properties of their vibrational frequency spectra,” *Philosophical Magazine*, vol. 4, no. 39, pp. 273–294, 1959. DOI: [10.1080/14786435908233340](https://doi.org/10.1080/14786435908233340).
- [28] S. Ghaffari, S. A. Chandorkar, S. Wang, E. J. Ng, C. H. Ahn, V. Hong, Y. Yang, and T. W. Kenny, “Quantum limit of quality factor in silicon micro and nano mechanical resonators,” *Scientific Reports*, 2013; 3: 3244.
- [29] Y.-W. Lin, S.-S. Li, Z. Ren, and C. T.-C. Nguyen, “Low phase noise array-composite micromechanical wine-glass disk oscillator,” in *Electron Devices Meeting, 2005. IEDM Technical Digest. IEEE International*, 2005, 4 pp.–281. DOI: [10.1109/IEDM.2005.1609328](https://doi.org/10.1109/IEDM.2005.1609328).
- [30] J. Wang, Z. Ren, and C. T.-C. Nguyen, “1.156-ghz self-aligned vibrating micromechanical disk resonator,” *Ultrasonics, Ferroelectrics, and Frequency Control, IEEE Transactions on*, vol. 51, no. 12, pp. 1607–1628, 2004, ISSN: 0885-3010. DOI: [10.1109/TUFFC.2004.1386679](https://doi.org/10.1109/TUFFC.2004.1386679).
- [31] M. Akgul, B. Kim, Z. Ren, and C. T.-C. Nguyen, “Capacitively transduced micromechanical resonators with simultaneous low motional resistance and  $q > 70,000$ ,” in *Tech. Digest, 2008 Solid-State Sensor, Actuator, and Microsystems Workshop, Hilton Head*, 2010.
- [32] L.-W. Hung and C. T.-C. Nguyen, “Capacitive-piezo transducers for higher q contour-mode aln resonators at 1.2 ghz,” in *Tech. Digest, 2008 Solid-State Sensor, Actuator, and Microsystems Workshop, Hilton Head*, 2010.

- [33] C. T.-C. Nguyen, “Integrated micromechanical rf circuits for software-defined cognitive radio (invited plenary),” in *Proceedings, the 26th Symposium on Sensors, Micromachines & Applied Systems*, 2009, pp. 1–5.
- [34] R. Tabrizian, M. Rais-Zadeh, and F. Ayazi, “Effect of phonon interactions on limiting the f.q product of micromechanical resonators,” in *Solid-State Sensors, Actuators and Microsystems Conference, 2009. TRANSDUCERS 2009. International*, 2009, pp. 2131–2134. DOI: [10.1109/SENSOR.2009.5285627](https://doi.org/10.1109/SENSOR.2009.5285627).
- [35] D. Hutchison, N. Morrill, Q. Aten, B. W. Turner, B. D. Jensen, L. Howell, R. Vanfleet, and R. Davis, “Carbon nanotubes as a framework for high-aspect-ratio mems fabrication,” *Microelectromechanical Systems, Journal of*, vol. 19, no. 1, pp. 75–82, 2010, ISSN: 1057-7157. DOI: [10.1109/JMEMS.2009.2035639](https://doi.org/10.1109/JMEMS.2009.2035639).
- [36] M. B. Wijesundara, D. Gao, C. Carraro, R. T. Howe, and R. Maboudian, “Nitrogen doping of polycrystalline 3c-sic films grown using 1,3-disilabutane in a conventional {lpcvd} reactor,” *Journal of Crystal Growth*, vol. 259, no. 12, pp. 18–25, 2003, ISSN: 0022-0248. DOI: [http://dx.doi.org/10.1016/S0022-0248\(03\)01573-2](http://dx.doi.org/10.1016/S0022-0248(03)01573-2).
- [37] C. S. Roper, R. T. Howe, and R. Maboudian, “Stress control of polycrystalline 3c-sic films in a large-scale lpcvd reactor using 1,3-disilabutane and dichlorosilane as precursors,” *Journal of Micromechanics and Microengineering*, vol. 16, no. 12, p. 2736, 2006. [Online]. Available: <http://stacks.iop.org/0960-1317/16/i=12/a=029>.
- [38] T. Hirano, T. Furuhashi, K. Gabriel, and H. Fujita, “Design, fabrication, and operation of submicron gap comb-drive microactuators,” *Microelectromechanical Systems, Journal of*, vol. 1, no. 1, pp. 52–59, 1992, ISSN: 1057-7157. DOI: [10.1109/84.128056](https://doi.org/10.1109/84.128056).
- [39] W. C. Tang, T.-C. H. Nguyen, and R. T. Howe, “Laterally driven polysilicon resonant microstructures,” *Sensors and Actuators*, vol. 20, no. 12, pp. 25–32, 1989, A Special Issue Devoted to Micromechanics, ISSN: 0250-6874. DOI: [http://dx.doi.org/10.1016/0250-6874\(89\)87098-2](http://dx.doi.org/10.1016/0250-6874(89)87098-2).
- [40] W.-T. Chang, M. Mehregany, and C. Zorman, “Energy dissipation in folded-beam mems resonators made from single crystal and polycrystalline 3c-sic films,” in *Nano/Micro Engineered and Molecular Systems, 2007. NEMS '07. 2nd IEEE International Conference on*, 2007, pp. 740–744. DOI: [10.1109/NEMS.2007.352124](https://doi.org/10.1109/NEMS.2007.352124).
- [41] R. D. Blevins, *Formulas for natural frequency and mode shape*. New York: Van Nostrand Reinhold Co., 1979.
- [42] Y. Xie, S.-S. Li, Y.-W. Lin, Z. Ren, and C. T.-C. Nguyen, “1.52-ghz micromechanical extensional wine-glass mode ring resonators,” *Ultrasonics, Ferroelectrics, and Frequency Control, IEEE Transactions on*, vol. 55, no. 4, pp. 890–907, 2008, ISSN: 0885-3010. DOI: [10.1109/TUFFC.2008.725](https://doi.org/10.1109/TUFFC.2008.725).
- [43] V. B. Braginsky, V. P. Mitrofanov, and V. I. Panov, *Systems with Small Dissipation*. University of Chicago Press, 1985.

- [44] A. Duwel, R. Candler, T. Kenny, and M. Varghese, “Engineering mems resonators with low thermoelastic damping,” *Microelectromechanical Systems, Journal of*, vol. 15, no. 6, pp. 1437–1445, 2006, ISSN: 1057-7157. DOI: [10.1109/JMEMS.2006.883573](https://doi.org/10.1109/JMEMS.2006.883573).
- [45] R. Lifshitz and M. L. Roukes, “Thermoelastic damping in micro- and nanomechanical systems,” *Phys. Rev. B*, vol. 61, pp. 5600–5609, 8 2000. DOI: [10.1103/PhysRevB.61.5600](https://doi.org/10.1103/PhysRevB.61.5600).
- [46] S. Prabhakar and S. Vengallatore, “Theory of thermoelastic damping in micromechanical resonators with two-dimensional heat conduction,” *Microelectromechanical Systems, Journal of*, vol. 17, no. 2, pp. 494–502, 2008, ISSN: 1057-7157. DOI: [10.1109/JMEMS.2008.916316](https://doi.org/10.1109/JMEMS.2008.916316).
- [47] W.-C. Li, Y. Lin, B. Kim, Z. Ren, and C.-C. Nguyen, “Quality factor enhancement in micromechanical resonators at cryogenic temperatures,” in *Solid-State Sensors, Actuators and Microsystems Conference, 2009. TRANSDUCERS 2009. International*, 2009, pp. 1445–1448. DOI: [10.1109/SENSOR.2009.5285815](https://doi.org/10.1109/SENSOR.2009.5285815).
- [48] P. Bradley, R. Ruby, I. Larson J.D., Y. Oshmyansky, and D. Figueredo, “A film bulk acoustic resonator (fbar) duplexer for uspcs handset applications,” in *Microwave Symposium Digest, 2001 IEEE MTT-S International*, vol. 1, 2001, 367–370 vol.1. DOI: [10.1109/MWSYM.2001.966908](https://doi.org/10.1109/MWSYM.2001.966908).
- [49] A. Partridge, H.-C. Lee, P. Hagelin, and V. Menon, “We know that mems is replacing quartz. but why? and why now?” In *European Frequency and Time Forum International Frequency Control Symposium (EFTF/IFC), 2013 Joint*, 2013, pp. 411–416. DOI: [10.1109/EFTF-IFC.2013.6702311](https://doi.org/10.1109/EFTF-IFC.2013.6702311).
- [50] J. Clark, A. Brown, G. He, and W.-T. Hsu, “Temperature compensated overtone resonators,” in *Solid-State Sensors, Actuators and Microsystems (TRANSDUCERS EUROSENSORS XXVII), 2013 Transducers Eurosensors XXVII: The 17th International Conference on*, 2013, pp. 794–797. DOI: [10.1109/Transducers.2013.6626886](https://doi.org/10.1109/Transducers.2013.6626886).
- [51] W.-T. Hsu and C. T.-C. Nguyen, “Stiffness-compensated temperature-insensitive micromechanical resonators,” in *Micro Electro Mechanical Systems, 2002. The Fifteenth IEEE International Conference on*, 2002, pp. 731–734. DOI: [10.1109/MEMSYS.2002.984374](https://doi.org/10.1109/MEMSYS.2002.984374).
- [52] J. Salvia, R. Melamud, S. A. Chandorkar, S. Lord, and T. Kenny, “Real-time temperature compensation of mems oscillators using an integrated micro-oven and a phase-locked loop,” *Microelectromechanical Systems, Journal of*, vol. 19, no. 1, pp. 192–201, 2010, ISSN: 1057-7157. DOI: [10.1109/JMEMS.2009.2035932](https://doi.org/10.1109/JMEMS.2009.2035932).
- [53] Z. Wu, V. Thakar, A. Peczkalski, and M. Rais-Zadeh, “A low phase-noise pierce oscillator using a piezoelectric-on-silica micromechanical resonator,” in *Solid-State Sensors, Actuators and Microsystems (TRANSDUCERS EUROSENSORS XXVII), 2013 Transducers Eurosensors XXVII: The 17th International Conference on*, 2013, pp. 490–493. DOI: [10.1109/Transducers.2013.6626810](https://doi.org/10.1109/Transducers.2013.6626810).

- [54] W.-T. Hsu and A. Brown, “Frequency trimming for mems resonator oscillators,” in *Frequency Control Symposium, 2007 Joint with the 21st European Frequency and Time Forum. IEEE International*, 2007, pp. 1088–1091. DOI: [10.1109/FREQ.2007.4319247](https://doi.org/10.1109/FREQ.2007.4319247).
- [55] F. Lee, J. Salvia, C. Lee, S. Mukherjee, R. Melamud, N. Arumugam, S. Pamarti, C. Arft, P. Gupta, S. Tabatabaei, B. Garlepp, H.-C. Lee, A. Partridge, M. Perrott, and F. Assaderaghi, “A programmable mems-based clock generator with sub-ps jitter performance,” in *VLSI Circuits (VLSIC), 2011 Symposium on*, 2011, pp. 158–159.
- [56] A. Samarao and F. Ayazi, “Postfabrication electrical trimming of silicon micromechanical resonators via joule heating,” *Microelectromechanical Systems, Journal of*, vol. 20, no. 5, pp. 1081–1088, 2011, ISSN: 1057-7157. DOI: [10.1109/JMEMS.2011.2162489](https://doi.org/10.1109/JMEMS.2011.2162489).
- [57] A. Hajjam and S. Pourkamali, “Self-contained frequency trimming of micromachined silicon resonators via localized thermal oxidation,” *Microelectromechanical Systems, Journal of*, vol. 22, no. 5, pp. 1066–1072, 2013, ISSN: 1057-7157. DOI: [10.1109/JMEMS.2013.2263218](https://doi.org/10.1109/JMEMS.2013.2263218).
- [58] M. Abdelmoneum, M. Demirci, Y.-W. Lin, and C. T.-C. Nguyen, “Location-dependent frequency tuning of vibrating micromechanical resonators via laser trimming,” in *Frequency Control Symposium and Exposition, 2004. Proceedings of the 2004 IEEE International*, 2004, pp. 272–279. DOI: [10.1109/FREQ.2004.1418464](https://doi.org/10.1109/FREQ.2004.1418464).
- [59] F. Bannon, J. Clark, and C.-C. Nguyen, “High-Q HF microelectromechanical filters,” *Solid-State Circuits, IEEE Journal of*, vol. 35, no. 4, pp. 512–526, 2000, ISSN: 0018-9200. DOI: [10.1109/4.839911](https://doi.org/10.1109/4.839911).
- [60] N. Khiem and T. Lien, “A simplified method for natural frequency analysis of a multiple cracked beam,” *Journal of Sound and Vibration*, vol. 245, no. 4, pp. 737–751, 2001, ISSN: 0022-460X. DOI: <http://dx.doi.org/10.1006/jsvi.2001.3585>.
- [61] H. Tada, *Stress Analysis of Cracks Handbook*. ASME, 2000.
- [62] K. Wang, A.-C. Wong, and C. T.-C. Nguyen, “Vhf free-free beam high-q micromechanical resonators,” *Microelectromechanical Systems, Journal of*, vol. 9, no. 3, pp. 347–360, 2000, ISSN: 1057-7157. DOI: [10.1109/84.870061](https://doi.org/10.1109/84.870061).
- [63] D. P. Rooke and D. J. Cartwright, *Compendium of stress intensity factors*. HMSO Ministry of Defence. Procurement Executive., 1976.